

ABSTRACT

Title of Dissertation: OPTIMIZING JWST EXOPLANETARY
ATMOSPHERIC CHARACTERIZATION
THROUGH PRIORITIZATION AND
VALIDATION OF TESS-DISCOVERED
EXOPLANETS AND
PANCHROMATIC STUDIES

Dana R. Louie
Doctor of Philosophy, 2021

Dissertation Directed by: Professor Drake Deming
Department of Astronomy

The approaching launch of the James Webb Space Telescope (JWST), coupled with the recent all-sky search of the Transiting Exoplanet Survey Satellite (TESS), heralds a new era in exoplanetary atmospheric characterization, with TESS projected to detect over one thousand transiting exoplanets smaller than Neptune, and JWST offering unprecedented spectroscopic capabilities.

My work focuses on optimizing future observations in three ways. First, JWST time and resources will not allow observations of all TESS discoveries, so we must prioritize exoplanets for atmospheric characterization. I simulated JWST transmission spectroscopy observations of the anticipated TESS planet yield and compared the results to simulated transmission spectroscopy observations of already known exoplanets. My most significant finding is that several hundred TESS 1.5 to 2.5 Earth radii sub-Neptunes can be observed at higher signal-to-noise than currently

known similarly-sized exoplanets. My work was used as the basis in developing the [Kempton et al. \(2018\)](#) Transmission Spectroscopy Metric (TSM), which is widely used by the exoplanet atmosphere community in prioritizing which exoplanets to observe with JWST.

Second, predictions show that TESS will detect thousands of astrophysical false positives that mimic exoplanet discoveries by also producing periodic decreases in starlight. A common scenario occurs when light from the target star blends with that of nearby eclipsing binary stars. Thus, TESS discoveries must be validated as true exoplanets using additional instruments or techniques. I designed software codes to predict how well two multi-band photometry instruments can discriminate between blended eclipsing binary false positives and true exoplanets. I found that the instruments can validate hundreds of candidate exoplanets smaller in size than Neptune.

Finally, previous atmospheric characterization studies have shown that observations using only infrared instruments—such as those used by JWST—may produce ambiguous atmospheric compositions. An exoplanet atmosphere may be more clearly understood by analyzing observations across multiple wavelength regimes. I analyzed Hubble Space Telescope (HST) transmission spectroscopy data for the hot Jupiter KELT-7b across wavelengths from the near ultraviolet to near infrared. This panchromatic analysis helps us better understand observations we can use to complement the near and mid-infrared observations of JWST, which is particularly important while HST is still operational.

OPTIMIZING JWST EXOPLANETARY ATMOSPHERIC
CHARACTERIZATION THROUGH PRIORITIZATION AND
VALIDATION OF TESS-DISCOVERED EXOPLANETS AND
PANCHROMATIC STUDIES

by

Dana R. Louie

Dissertation submitted to the Faculty of the Graduate School of the
University of Maryland, College Park in partial fulfillment
of the requirements for the degree of
Doctor of Philosophy
2021

Advisory Committee:
Professor Drake Deming, Chair/Advisor
Professor Kayo Ide, Dean's Representative
Professor Eliza Kempton
Professor Norio Narita
Professor Derek Richardson

© Copyright by
Dana R. Louie
2021

Preface

The research presented in Chapters 3 and 4 of this dissertation has been previously published.

Chapter 3 is presented with only minimal modification since appearing in Publications of the Astronomical Society of the Pacific (PASP) as “Simulations Predicting the Ability of Multi-color Simultaneous Photometry to Distinguish TESS Candidate Exoplanets from False Positives” ([Louie et al., 2020](#)). Paper authors are Dana R. Louie, Norio Narita, Akihiko Fukui, Enric Palle, Motohide Tamura, Nobuhiko Kusakabe, Hannu Parviainen, and Drake Deming.

Sections [4.1](#) through [4.6](#) of Chapter 4 are presented with only minimal modification since appearing in PASP as “Simulated JWST/NIRISS Transit Spectroscopy of Anticipated TESS Planets Compared to Select Discoveries from Space-based and Ground-based Surveys” ([Louie et al., 2018](#)). Paper authors are Dana R. Louie, Drake Deming, Loic Albert, L. G. Bouma, Jacob Bean, and Mercedes Lopez-Morales. In addition, I have added Section [4.7](#) to describe application of this work since publication.

Dedication

I dedicate this thesis to my Grandma and Grandpa Fankhauser, whose excited enthusiasm for the early space program first inspired me to reach for the stars; to my parents, John (“Hans”) and Nancy Schindler, whose dedicated effort in building and expanding a small-town Ohio business taught me the value of persistence in realizing your dreams; and to my husband and best friend Jeff Louie, who has joined me with unconditional love in life’s journey.... I begin my life as a professional astronomer today because of the love and support all of you have given me.

Acknowledgments

In 2012, I concluded the Air Force chapter of my career. My entire life, I'd been excited by space exploration, and for at least a decade I had dreamt of becoming a professional astronomer. Jumping onto a new career path as a nontraditional student brings with it unique challenges. Yet, I made the leap and today I begin my new path as a nascent scientist. Through all the twists and turns of fate, so many people have brought me to this point in my journey. Here, I would like to acknowledge those people who have contributed most directly to my success at University of Maryland (UMD): my committee members, my fellow graduate students, the Astronomy Department support staff, and my family.

First, I'd to thank my advisor, Prof Drake Deming. It was truly an honor to be guided by one of the founders of exoplanet science! During my second year as a graduate student, Drake began taking me with him to TESS Science Team meetings, where he introduced me to other pioneers in the field and gave me opportunities to present my research. Throughout my years at UMD, Drake has continually offered sage research advice and has never hesitated from wading knee-deep in my research difficulties. He accompanied me on my first observing run to the Lowell Discovery Telescope (LDT), which was unfortunately snowed out. Then, after we literally dug our rental car out from a foot of snow, he went with me again during

a more successful second observing run. Thank you for your continual support, encouragement, patience, and instruction. It has truly been a pleasure working with you, and I hope we can continue to collaborate in the future!

Next, I would like to acknowledge my other committee members—Prof Kayo Ide, Prof Eliza Kempton, Prof Norio Narita, and Prof Derek Richardson—for taking the time to advise me and serve on my committee. Prof Ide, thank you for serving as the Dean’s representative on my committee. Since Atmospheric Science is vital in understanding exoplanet atmospheres, I hope that we can continue collaborating in the future. Eliza, I’m continually amazed at all the projects you have your hands in. You serve as a role model for the type of scientist that I strive to become, and I look forward to working with you on exoplanet atmosphere projects in the future. Narita-san, thank you for welcoming me into your MuSCAT research group and taking care of me during my summer in Japan. I hope that I can continue to work with your group for years to come. Derek, thank you for inviting me to audit your computational astrophysics class and helping me to further develop my coding skills. It’s been a pleasure to gain some insight into your impressive coding and teaching skills. I hope that I can continue to work with all of you in the future!

I’d like to thank *all* of the graduate students for creating such a welcoming, diverse, and supportive graduate student community. One of my great (but too infrequent) pleasures in graduate school has been spending time with each of you and learning about your unique walks through life. I would especially like to acknowledge my graduate school classmates: Amy, Pradip, Thomas, and Zeeve. It was wonderful to begin our graduate school journey together! In particular, I’d like to thank Amy

for spending time with me during Panera Bread and late-night Skype study sessions the first two years of the program. I must admit that I also hold a special place in my heart for those graduate students and members of the Department who have joined me in Star Trek watch groups or who went with me to the Cherry Hill, NJ Star Trek convention in 2016. Thank you Amy, Elizabeth Warner, Kathleen & Eric, Krista & Ray, Mahmuda, Ron & Kellie, Sara & Alex, Thomas & Bernadette, and Vicki & Wes. Thanks again to *everyone* for your support and companionship throughout the program. I look forward to continuing to keep in touch with you and perhaps working with you on astronomical research throughout the coming years!

Finally, I'd like to thank the professional staff members of the Department for their prompt and tireless support. I would especially like to thank those department members (past and present) who I have worked most closely with. Thank you John Cullinan, Olivia Dent, Dorinda Kimbrell, Barbara Hansborough, Susan Lehr, Eric McKenzie, Adrienne Newman, Mary Ann Phillips, and Mona Susanto. Your support over the years is much appreciated!

I don't think I'd be here today without the loving support of my family. I'd like to begin by thanking my parents, my late father "Hans" Schindler and my mom, Nancy, for always loving and supporting me, even when I served in the Air Force half-way around the World. I've recently come to realize that Mom has served as an example to me of what it is like to not grow old... I, too, plan to be climbing fences well past the age when others think it's no longer possible to do so. Also, thank you Mom for joining us the first time we hosted fellow graduate students for Thanksgiving in 2015, and thank you for helping me bake my first turkey and trying

to teach me how to make mashed potatoes!

To my other family members—siblings, in-laws, niece, nephews, and extended family—please know that your love and support have helped fuel me through these transformative years. I cherish having all of you in my life!

My most important debt of gratitude goes to my husband Jeff Louie. I am blessed to be married to a man who shows such faithful devotion to others. Thank you for believing in me enough to buy a house a mile from UMD before I was admitted to the Astronomy program, thank you for retiring from the Air Force rather than taking a prominent assignment to Yokota Airbase, Japan (and not telling me about it until my second year mid-terms were over), thank you for often treating my fellow graduate students to restaurant quality barbecue dishes made on your Big Green Egg(s), and.... Your acts of love are endless, and I am so fortunate to have you in my life. I look forward to our continuing adventures!

Table of Contents

Preface	ii
Foreword	iii
Dedication	iii
Acknowledgements	iv
Table of Contents	viii
List of Tables	xi
List of Figures	xii
List of Abbreviations	xv
Chapter 1: Introduction	1
1.1 Exoplanet Transit Discoveries	4
1.1.1 Ground-based Transit Surveys	9
1.1.2 Space-based Transit Surveys	12
1.1.3 Astrophysical False Positives	17
1.1.4 Validation and Confirmation of Transiting Exoplanets	18
1.1.5 The M-Dwarf Advantage	24
1.2 Exoplanet Atmospheres – Theory and Modeling	27
1.2.1 Fundamental Concepts	27
1.2.2 Exo-Transit – Forward Modeling Transmission Spectra	37
1.2.3 Exoplanet Atmospheric Retrievals	39
1.3 Hot Jupiters	46
1.3.1 Kepler Occurrence Rates	46
1.3.2 Hot Jupiter Formation	47
1.3.3 Hot Jupiter Atmospheres – Theory and Observations	48
1.4 $R_{\text{pl}} < 4R_{\oplus}$ Planets	54
1.4.1 Kepler Occurrence Rates and the Radius Valley	55
1.4.2 Atmospheres of $R_{\text{pl}} < 4R_{\oplus}$ Planets – Theory and Observations	57

Chapter 2: Supplemental Background Regarding TESS Predicted Planet Yield and Validation using Multi-Color Photometry	62
2.1 Overview	62
2.2 TESS Predicted Planet Yields	63
2.3 Distinguishing False Positives with Multi-Band Photometry	68
Chapter 3: Simulations Predicting the Ability of Multi-Color Simultaneous Photometry to Distinguish TESS Candidate Exoplanets from False Positives	75
3.1 Overview	75
3.2 Introduction	76
3.3 Methods	80
3.3.1 Predicted TESS Exoplanet Discoveries	81
3.3.2 MuSCAT and MuSCAT2 Simulation Tools	83
3.3.3 Comparison of Simulation Results to Observations	90
3.3.4 Blended Eclipsing Binary False Positives	93
3.3.5 Distinguishing BEBs with MuSCAT/MuSCAT2	97
3.4 Results and Discussion	98
3.4.1 MuSCAT/MuSCAT2 Ability to Distinguish BEBs	100
3.4.2 Application to TESS Objects of Interest	107
3.5 Summary and Conclusion	114
Chapter 4: Simulated JWST/NIRISS Transit Spectroscopy of Anticipated TESS Planets Compared to Select Discoveries from Space-Based and Ground-Based Surveys	117
4.1 Overview	117
4.2 Introduction	118
4.3 Methods	124
4.3.1 Predicted Properties of TESS Discoveries	124
4.3.2 Selection of Known Exoplanets for Comparison	127
4.3.3 Spectra	132
4.3.4 Description of NIRISS Simulator	140
4.4 Results and Discussion	151
4.4.1 S/N for Anticipated TESS Discoveries	152
4.4.2 Sensitivity to Planetary Composition	157
4.4.3 Observational Overhead Effects	161
4.4.4 Cloud Effects	161
4.4.5 Analysis Of 50 Trials of TESS Primary Mission	163
4.4.6 Sensitivity to Systematic Noise	167
4.5 JWST Follow-Up Observation Program	170
4.6 Summary and Conclusion	176
4.7 Addendum	178
4.7.1 NIRISS S/N for Barclay et al. (2018) TESS Planet Yield	179

4.7.2	NIRISS S/N and Transmission Spectroscopy Metric for TESS Confirmed Planets	183
4.7.3	Summary and Additional Conclusions	189
Chapter 5: Transmission Spectroscopy of the Hot Jupiter KELT-7b		191
5.1	Overview	191
5.2	Introduction	192
5.3	Observations	194
5.4	Data Analysis	198
5.4.1	WFC3 Data Analysis	198
5.4.2	STIS Data Analysis	202
5.4.3	TESS Data Analysis	204
5.5	White Light Transit Curves	205
5.5.1	WFC3 White Light Transit Curves	207
5.5.2	STIS White Light Transit Curves	209
5.6	Transmission Spectrum	210
5.6.1	WFC3 Transmission Spectrum	210
5.6.2	STIS Transmission Spectrum	216
5.7	Results and Discussion	225
5.7.1	KELT-7b Atmospheric Retrievals	225
5.7.2	Discussion of Retrieval Results	236
5.7.3	Comparison to Previous Results	240
5.7.4	Implications for Planet Formation	241
5.8	Summary and Conclusion	243
5.9	Future Work	244
Appendix A: Facilities and Software		247
A.1	Facilities	247
A.2	Software	247
Bibliography		249

List of Tables

1.1	Advantages of Searching for Earth-sized Planets Orbiting M Dwarfs	25
3.1	MuSCAT Ability to Distinguish <i>Bona Fide</i> Exoplanets - Barclay et al. (2018) Systems	102
3.2	MuSCAT2 Ability to Distinguish <i>Bona Fide</i> Exoplanets - Barclay et al. (2018) Systems	103
3.3	MuSCAT2 Ability to Distinguish <i>Bona Fide</i> Exoplanets - TOIs	111
3.4	MuSCAT Ability to Distinguish <i>Bona Fide</i> Exoplanets - TOIs	111
3.5	TOIs for which MuSCAT2 Can Distinguish BEBs from True Exoplanets in 100% of Trials	114
4.1	Space-based Exoplanet Discoveries Used for Comparison	130
4.2	Ground-based Exoplanet Discoveries Used for Comparison	133
4.3	Masses for Select Exoplanets Assuming an Earthlike Composition	133
4.4	Terrestrial-Sized Anticipated TESS Planets with High NIRISS S/N	155
4.5	NIRISS Atmospheric Characterization Predictions for Sullivan et al. (2015) and Barclay et al. (2018) TESS Planet Yields	181
4.6	Probable Subgiant Stars in Barclay et al. (2018) TESS Planet Yield	182
4.7	Small Barclay et al. (2018) Simulated TESS Planets with Highest NIRISS S/N	183
4.8	TESS Confirmed Planets with Highest NIRISS S/N	186
5.1	System Parameters for KELT-7b	193
5.2	KELT-7b TESS and Spitzer Transit Depths and Uncertainties	205
5.3	KELT-7b WFC3 G141 Grism Transit Depths and Uncertainties	215
5.4	KELT-7b STIS G430L Grating Transit Depths and Uncertainties	222
5.5	KELT-7b STIS G750L Grating Transit Depths and Uncertainties	223
5.6	Prior Parameter Distribution for Fiducial Model	227
5.7	Prior Parameter Distributions - Scattering Slope and WFC3 Offset	230
5.8	Comparison of Fiducial and More Complicated Model Retrievals	230
5.9	Detection of Various Atomic and Molecular Species	234
5.10	Examination of STIS and WFC3 Data for Various Species	234

List of Figures

1.1	Cumulative Exoplanet Discoveries	5
1.2	Depiction of Exoplanet Transit	6
1.3	Confirmed Exoplanet Discoveries from Ground-Based Surveys	11
1.4	Confirmed Exoplanet Discoveries from Space-Based Surveys	14
1.5	TESS Primary Mission Observation Sectors	16
1.6	Common Astrophysical False Positives in Transit Surveys	17
1.7	TESS Validation and Mass Measurement Process	22
1.8	Radius Valley in $R_{\text{pl}} < 4R_{\oplus}$ Planets	56
2.1	Sullivan et al. (2015) and Barclay et al. (2018) TESS Planet Yields	66
2.2	Sullivan et al. (2015) and Barclay et al. (2018) J-band Magnitudes	67
2.3	Sullivan et al. (2015) and Barclay et al. (2018) J-band Magnitudes— Small Planets	69
2.4	Sullivan et al. (2015) and Barclay et al. (2018) Host Star Temperatures	70
2.5	Sullivan et al. (2015) and Barclay et al. (2018) Host Star Temperatures— Small Planets	71
2.6	Comparison of TESS and MuSCAT2 Bandpasses	73
2.7	MuSCAT2 and TESS Bandpasses Overlaid on Blackbody Curves at Three Temperatures	74
3.1	MuSCAT/MuSCAT2 Simulation Block Diagram	82
3.2	Illustration of MuSCAT/MuSCAT2 Criterion to Distinguish Between BEB False Positives and <i>Bona Fide</i> Exoplanets	101
3.3	Histograms Showing Fraction of Barclay et al. (2018) Systems Dis- tinguishable as BEB False Positives using MuSCAT	105
3.4	Histograms Showing Fraction of Barclay et al. (2018) Systems Dis- tinguishable as BEB False Positives using MuSCAT2	106
3.5	Percentage of Trials Where MuSCAT Can Distinguish Between BEB False Positives and <i>Bona Fide</i> Exoplanets	108
3.6	Percentage of Trials Where MuSCAT2 Can Distinguish Between BEB False Positives and <i>Bona Fide</i> Exoplanets	109
3.7	Percentage of Trials Where MuSCAT2 Can Distinguish Between BEB False Positives and <i>Bona Fide</i> Exoplanets - TOIs	113
4.1	Comparison of Empirical and Theoretical Exoplanet Mass-Radius Re- lationships	128

4.2	Comparison of Our Transmission Spectroscopy Code with Exo-Transmit	138
4.3	Graphical Illustration Showing Calculation of Integrated Signal-to-Noise	146
4.4	Comparison of Our NIRISS Simulator to Instrument Team NIRISS Simulator	147
4.5	Suitability of Anticipated TESS Planets to JWST Atmospheric Characterization	153
4.6	Suitability of Potentially Habitable Anticipated TESS Planets to JWST Atmospheric Characterization	154
4.7	Examination of Cold and Temperate Planets Suitable for Atmospheric Characterization	156
4.8	Influence of Planet Radius on Detectability of Planetary Atmosphere	158
4.9	Effect of Planet Composition on Detection of Planetary Atmosphere	160
4.10	Impact of Observational Overhead on Our Calculations	162
4.11	Impact of Clouds on Suitability of TESS Planets to JWST Atmospheric Characterization	164
4.12	Suitability of Anticipated TESS Planets to JWST Atmospheric Characterization by Examining 50 Realizations of TESS Primary Mission Yield	166
4.13	Impact of Systematic Noise on JWST Atmospheric Characterization	168
4.14	K2-3c Simulated NIRISS Transmission Spectra with and without Systematic Noise	169
4.15	Two Example Trials from Our Synthetic JWST/NIRISS Observing Programs	172
4.16	Cumulative Distribution of the Difference in Bayesian Information Criteria for Our Two Models	174
4.17	Suitability of Barclay et al. (2018) Anticipated TESS Planets to JWST Atmospheric Characterization	180
4.18	Suitability of TESS Confirmed Planets to JWST Atmospheric Characterization	185
4.19	Comparison of NIRISS Signal-to-Noise to Transmission Spectroscopy Metric (TSM)	187
4.20	Comparison of NIRISS Signal-to-Noise to Transmission Spectroscopy Metric (TSM)	188
5.1	Example HST STIS and WFC3 Spectra	197
5.2	Example WFC3 Spatial Scan Image	201
5.3	Example STIS Array Images	203
5.4	KELT-7b Transits Observed by TESS in Sector 19	206
5.5	Uncorrected Normalized WFC3 White Light Curve	208
5.6	Corrected Normalized WFC3 White Light Curve	209
5.7	Uncorrected Normalized STIS White Light Curves	211
5.8	Corrected Normalized STIS White Light Curves	212
5.9	HST WFC3 Transmission Spectrum	216
5.10	Spectroscopic Light Curves for STIS G430L Data	219

5.11 Spectroscopic Light Curves for STIS G750L Data	220
5.12 HST STIS Transmission Spectrum	221
5.13 Composite Transmission Spectrum	224
5.14 Best Fit Models for PLATON Retrievals	232
5.15 PLATON Retrieval Corner Plot	233

List of Abbreviations

Astronomical Symbols and Units:

AU	Astronomical Unit (1.496×10^{11} m)
M_{\oplus}	Earth mass (5.972×10^{24} kg)
M_{J}	Jupiter mass (1.899×10^{27} kg)
M_{\odot}	Solar mass (1.988×10^{30} kg)
R_{\oplus}	Earth radius (6.378×10^6 m)
R_{J}	Jupiter radius (7.149×10^7 m)
R_{\odot}	Solar radius (6.957×10^8 m)

Chemical Symbols and Formulae:

Ca	Calcium
C/H	Carbon-to-Hydrogen ratio
CH ₄	Methane
CO	Carbon Monoxide
CO ₂	Carbon Dioxide
C/O	Carbon-to-Oxygen ratio
Cr	Chromium
Fe	Iron
FeH	Iron Hydride
H ⁻	Negative Hydrogen Ion
H ₂	Molecular Hydrogen
H ₂ O	Water
He	Helium
K	Potassium
MgSiO ₃	Pervoskite
Mn	Manganese

Na	Sodium
N/C	Nitrogen-to-Carbon ratio
Ni	Nickel
O/H	Oxygen-to-Hydrogen ratio
SiO	Silicon Monoxide
Ti	Titanium (chemical symbol)
X_{CO_2}	Dry-Air Mole Fraction of CO_2

Acronyms:

ACOS	Atmospheric CO_2 Observations from Space
ADU	Analog Digital Unit
ARIEL	Atmospheric Remote-Sensing Infrared Exoplanet Large-survey
BEB	Blended Eclipsing Binary
BIC	Bayesian Information Criterion
CCD	Charge-Coupled Device
CoRoT	COncvection, ROTation and planetary Transits
CP	Confirmed Planet
CTL	Candidate Target List
EB	Eclipsing Binary
ELT	Extremely Large Telescope
EM	Electromagnetic
EOS	Equation of State
ExoFOP-TESS	Exoplanet Follow-up Observing Program for TESS
FFI	Full Frame Image
FITS	Flexible Image Transport System
FWHM	Full Width Half Maximum

GO	General Observer
HATNet	Hungarian-made Automated Telescope Network
HEB	Hierarchical Eclipsing Binary
HST	Hubble Space Telescope
HZ	Habitable Zone
ID	Identification
IR	Infrared
IRAC	Infrared Array Camera
IRS	Infrared Spectrograph
JWST	James Webb Space Telescope
KELT	Kilodegree Extremely Little Telescope
LDT	Lowell Discovery Telescope
LTE	Local Thermodynamic Equilibrium
MAST	Mikulski Archive for Space Science
MCMC	Markov Chain Monte Carlo
MIPS	Multiband Imaging Photometer for Spitzer
MuSCAT	Multi-color Simultaneous Camera for Studying Atmospheres of Transiting Planets
NAOJ	National Astronomical Observatory of Japan
NASA	National Aeronautics and Space Administration
NEB	Nearby Eclipsing Binary
NICMOS	Near Infrared Camera and Multi-Object Spectrometer
NIR	Near Infrared
NIRISS	Near InfraRed Imager and Slitless Spectrograph
NIRSpec	Near InfraRed Spectrograph
NUV	Near Ultraviolet

OAC	Okayama Astro-Complex
OCO-2	Orbiting Carbon Observatory 2
OGLE	Optical Gravitational Lensing Experiment
OOT	Out-Of-Transit
PanCET	Panchromatic Comparative Exoplanet Treasury
PASP	Publications of the Astronomical Society of the Pacific
PC	Planet Candidate
PI	Principal Investigator
PLATON	PLanetary Atmospheric Tool for Observer Noobs
PRV	Precision Radial Velocity
RM	Rossiter-McLaughlin
RV	Radial Velocity
S/N	Signal-to-Noise
SOSS	Single Object Slitless Spectroscopy
STIS	Space Telescope Imaging Spectrograph
STScI	Space Telescope Science Institute
TD	Transit Depth
TESS	Transiting Exoplanet Survey Satellite
TFOF	TESS Follow-up Observing Program
TIC	TESS Input Catalog
TOI	TESS Object of Interest
T-P	Temperature-Pressure
TRAPPIST	TRAnsiting Planets and PlanetesImals Small Telescope
TRES	Tillinghast Reflector Echelle Spectrograph
TRILEGAL	TRIdimensional modeL of thE GALaxy
TSM	Transmission Spectroscopy Metric
UMD	University of Maryland
UV	ultraviolet
WASP	Wide-Angle Search for Planets
WFC3	Wide Field Camera 3

Chapter 1: Introduction

Extrasolar planets, or exoplanets, are planets that orbit stars other than our Sun. Michel Mayor and Didier Queloz launched the field of exoplanet science in 1995 when they discovered 51 Pegasi b, the first exoplanet detected orbiting a main sequence star (Mayor & Queloz, 1995), an achievement for which they shared the 2019 Nobel Prize in Physics (Gibney & Castelvetti, 2019). Mayor and Queloz detected 51 Pegasi b by measuring the planet’s gravitational tugs on its host star using the so-called *radial velocity* technique. Since then, the *transit* technique has become the workhorse exoplanet detection method, with the majority of the > 4,000 exoplanets detected since 1995 relying upon this method for discovery (Figure 1.1). In particular, exoplanet discoveries made using the transit method exploded with the launch of the Kepler Space Telescope in 2009, and continue at a rapid pace following the launch of the Transiting Exoplanet Survey Satellite (TESS) in 2018.

Exoplanet transit surveys discover new exoplanets by observing a large number of potential exoplanet host stars at a predetermined cadence. During an exoplanet transit, the planet passes in front of its host star as viewed by a distant observer (e.g. on Earth), thereby causing a measurable decrease in the amount of electromagnetic (EM) radiation we receive. An exoplanet on a closed orbit will cause repeatable, pe-

riodic dips in the measured stellar flux (Figure 1.2). The exoplanet transit technique is powerful because it allows us to measure the radius of the transiting exoplanet with respect to its host star. The *transit depth*, δ_{tra} , or fractional decrease in flux as an exoplanet passes in front of its host star, may be expressed as the ratio of cross sectional areas of the planet and host star, or (e.g., Seager & Mallén-Ornelas, 2003)

$$\delta_{\text{tra}} \equiv \frac{F_{\text{OOT}} - F_{\text{MT}}}{F_{\text{OOT}}} = \frac{R_{\text{pl}}^2}{R_{\star}^2}, \quad (1.1)$$

where F_{OOT} is the out-of-transit baseline flux received from the host star, F_{MT} is the flux measured at mid-transit, R_{pl} is the radius of the planet, and R_{\star} is the radius of the host star.¹ Thus, with knowledge of the host star radius, the planetary radius may be determined. Furthermore, if the exoplanet maintains an atmosphere, we can imagine that atmosphere appearing as an annulus surrounding the planet during transit. That atmospheric annulus will absorb some of the stellar flux. The amount of starlight absorbed is wavelength-dependent and varies with the properties of the atmosphere. By measuring the transit depth at a variety of wavelengths, we can thus discern properties of the exoplanet’s atmosphere.

In this dissertation, I present three scientific studies I have led that all make use of the advantages inherent in the transit geometry. This first introductory chapter places these projects in context by explaining the necessary historical and scientific background. I begin in Section 1.1 by reviewing key exoplanet transit discoveries from ground-based and space-based surveys, focusing on those aspects

¹Note that equation 1.1 is an idealized equation that does not take into account such effects as limb darkening, grazing transits, star spots, etc.

that are relevant to this work. I continue by describing astrophysical false positives that complicate our efforts to detect transiting exoplanets, and methods employed to *validate* and *confirm* exoplanet detections. I close Section 1.1 by discussing the advantages of searching for transiting planets orbiting M-dwarf host stars. In Section 1.2, I discuss the theory and modeling of planetary atmospheres. I begin with fundamental concepts, then describe the open-source code Exo-Transmit as an example modeling code for transmission spectra. I close Section 1.2 by discussing atmospheric retrievals. In Sections 1.3 and 1.4, I take a deeper look at two populations of planets that do not exist in our own Solar System by reviewing their Kepler occurrence rates, looking at possible formation mechanisms, and examining theory and observations regarding their atmospheres. These two populations are hot Jupiters (§1.3), which are highly-irradiated Jupiter-sized planets that orbit their stars in ~ 10 days or less, and $R_{\text{pl}} < 4R_{\oplus}$ ² planets, or planets that range in size between Earth and Neptune (§1.4).

After this introductory chapter, in Chapter 2, I present supplemental background information to assist the reader in understanding the studies described in Chapters 3 and 4. My work in both Chapters 3 and 4 relies upon predictions of the exoplanets that will be discovered by the Transiting Exoplanet Survey Satellite (TESS). In Chapter 2, I quantify some key differences between the Sullivan et al. (2015) and Barclay et al. (2018) TESS planet yield predictions.

Chapter 3 is a refereed, published study I led to predict the ability of the Multi-color Simultaneous Camera for Studying Atmospheres of Transiting Planets

²The unit R_{\oplus} refers to an Earth radius, which is approximately 6.378×10^6 m.

(MuSCAT) instrument, as well as the MuSCAT2 instrument, to distinguish *bona fide* exoplanets from false positives. Chapter 2 includes further background information on the MuSCAT/MuSCAT2 instruments and multi-band photometry.

Chapter 4 contains a refereed, published study which employs simulations to determine the suitability of TESS-discovered exoplanets to atmospheric characterization using the James Webb Space Telescopes (JWST). In Section 4.7, I add to this published work by applying the simulation tools to recently-discovered TESS confirmed planets and the [Barclay et al. \(2018\)](#) TESS planet yield predictions.

Chapter 5 contains a preliminary study concerning transit spectroscopy observations of the hot Jupiter KELT-7b. The planet’s atmosphere has been observed across wavelengths ranging from the near ultraviolet to near infrared (NIR) regime. For the first time, I combine near ultraviolet and optical Hubble Space Telescope (HST) observations of this planet with previous NIR observations.

1.1 Exoplanet Transit Discoveries

Detection of an exoplanet transit requires that observer and host star be aligned such that the exoplanet passes between them. In other words, the planet’s orbit is viewed nearly edge-on by the observer. Thus, in a long-term monitoring campaign, transits will *not* be detected for the majority of stars, even if many of those stars indeed host exoplanets. For a circular orbit, the probability that a transit will be observable, p_{transit} , is given by ([Winn, 2010](#))

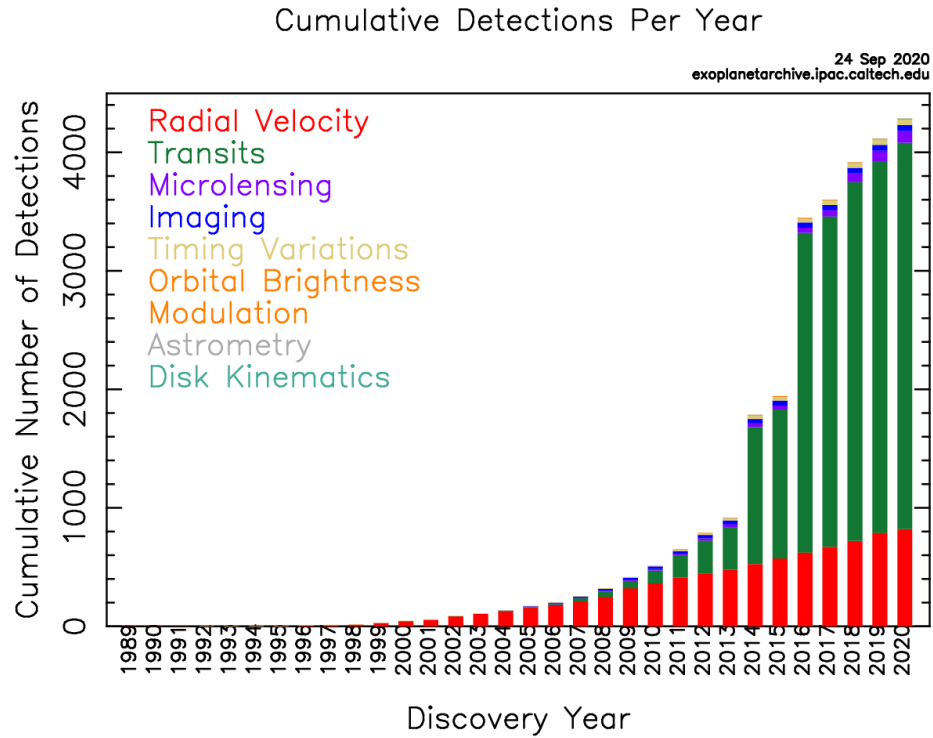


Figure 1.1: Cumulative number of exoplanets discovered using various techniques. The Kepler Space Telescope, launched in 2009, boosted the number of detections made via the *transit* method. The number of exoplanets discovered via the *transit* technique will continue to grow as exoplanet candidate detections from the Transiting Exoplanet Survey Satellite (TESS) are validated and confirmed (§1.1.4). Figure from NASA Exoplanet Archive: <https://exoplanetarchive.ipac.caltech.edu/>.

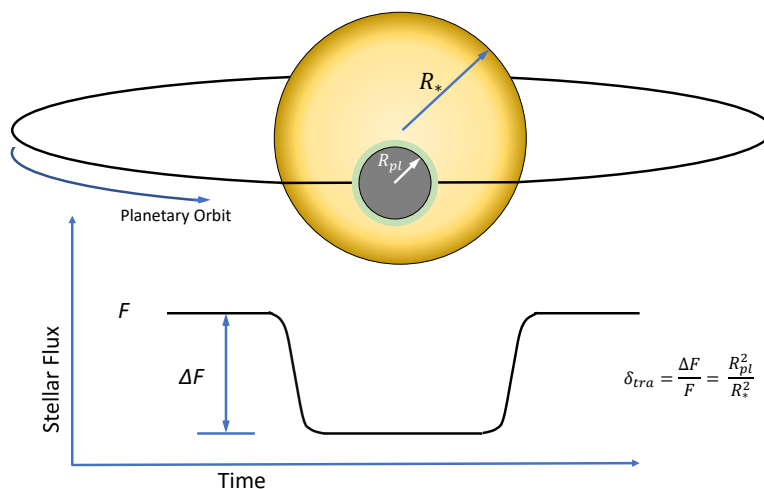


Figure 1.2: Diagram showing an exoplanet transit. We measure the flux from the exoplanet’s host star over time. As the planet passes in front of its host star as viewed by a distant observer, the flux we collect from the host star decreases. Assuming that the planet itself appears dark during transit (i.e., emits no electromagnetic radiation), and ignoring the effects of stellar limb darkening and the exoplanet’s atmosphere, the drop in flux during transit is proportional to the cross sectional area of the planet divided by that of the host star. Thus, with knowledge of the host star radius, we can determine the radius of the exoplanet. In this diagram, the exoplanet atmosphere is represented by an annulus surrounding the exoplanet. If an exoplanet maintains an atmosphere, atoms and molecules in that atmosphere will absorb light at certain wavelengths. In turn, the opacity of the atmospheric annulus and thus the overall cross sectional area of the planet varies with wavelength. Examination of the wavelength-dependent transit depth thus allows us to estimate atmospheric composition and other properties such as cloud cover. Note that most of the electromagnetic radiation emitted by an exoplanetary system during transit emanates from the host star.

$$p_{\text{transit}} = \left(\frac{R_*}{a}\right) \approx 0.005 \left(\frac{R_*}{R_\odot}\right) \left(\frac{a}{1 \text{ AU}}\right)^{-1}, \quad (1.2)$$

where R_* is the stellar radius in units of solar radii (R_\odot),³ and a is the semi-major axis of the planetary orbit in astronomical units (AU).⁴ Thus, the probability that our Earth would pass in front of the Sun as viewed by an extraterrestrial observer is only ~ 0.005 , or $\frac{1}{2}\%$. Since Jupiter orbits at $a \sim 5.203$ AU, the probability of transit drops to a mere $\sim 0.1\%$. Even Mercury, our Sun’s closest orbiting planet at $a \sim 0.0129$ AU, only has a $\sim 1.3\%$ probability of transit as viewed by an extraterrestrial observer. In contrast, the hot Jupiter 51 Pegasi b, which orbits its $1.2R_\oplus$ host star at $a \sim 0.0527$ AU, has an $\sim 11\%$ probability of transit.

Realization that planets could exist on ultra-short-period orbits resulted in a paradigm shift, prompting astronomers to begin searching for planets on such orbits. By the late 1990s, scientists had discovered 11 candidate⁵ hot Jupiters (§1.3) through radial velocity surveys. Knowing that the probability of these hot Jupiters transiting was $\sim 10\%$ motivated astronomers to search for evidence of exoplanet transits, which would allow measurement of the planet candidate’s radius and better constraint of its mass. The mass and radius in turn would allow estimates of the planet candidate’s bulk density, as well as confirmation of its planetary nature (§1.1.4). Charbonneau et al. (2000) reported the first full exoplanet transit light curve, that of HD 209458b.

³The unit R_\odot refers to a solar radius, which is approximately 6.957×10^8 m.

⁴The unit AU refers to an astronomical unit, which is approximately 1.496×10^{11} m. It was originally conceived as the average orbital distance of the Earth about the Sun.

⁵An astrophysical signal which could be produced by an exoplanet is referred to as an exoplanet *candidate*. We conduct additional observations or analyses to *validate* or *confirm* (§1.1.4) the planetary nature of such candidates.

That same year, [Henry et al. \(2000\)](#) reported observations of partial transits of the same planet.

As early as 1971, [Rosenblatt \(1971\)](#) described an automated exoplanet transit survey that would use 3 wide-field telescopes slaved to a central computer. Based upon the detectability of planets like those in our solar system to a distant observer, he estimated that his two color photometric transit survey would detect one or more planets in a given year. Later, [Borucki & Summers \(1984\)](#) revised the concept for a ground-based photometric survey that would result in the same estimated planet yield. [Borucki & Summers \(1984\)](#) also stated that detection of terrestrial-sized planets was not yet possible with state-of-the-art photometers of the time, and would require a spaceborne platform to avoid the atmospheric effects of scintillation and variation in sky transparency. The first transit surveys were implemented within a decade of discovering hot Jupiter exoplanets, and at last began to yield detections in the early 2000s.

I begin this section with a review of ground-based (§1.1.1) and space-based (§1.1.2) transit surveys, focusing on those surveys that have been most productive, as well as those yielding planets that are referenced in Chapters 4 and 5. Next, I discuss those astrophysical phenomena that may mimic the signals of transiting exoplanets, producing false positives (§1.1.3). The possibility of false positive detection requires us to *validate* and/or *confirm* transiting exoplanets as *bona fide* exoplanets, which I describe in Section 1.1.4. I conclude this section on transit discoveries by explaining the advantages of searching for transiting exoplanets orbiting small, M-dwarf host stars (§1.1.5).

1.1.1 Ground-based Transit Surveys

The first exoplanet discovered in a ground-based transit survey was OGLE-TR-56 b. The planet was detected in the third phase of the Optical Gravitational Lensing Experiment (OGLE-III) (Udalski et al., 2002a,b), and later confirmed via radial velocity to be a $0.9M_{\text{J}}$ ⁶ hot Jupiter on a 1.2-day orbit around its host star (Konacki et al., 2003). The OGLE-III survey yielded the earliest new transiting planets, finding five out of six transiting planet candidates discovered before 2006.⁷

The most productive ground-based surveys have been HAT/HATNet (Bakos, 2018) and WASP/SuperWASP (Collier Cameron et al., 2009; Pollacco et al., 2006). To date, the NASA Exoplanet Archive lists 127 confirmed exoplanets discovered by HAT/HATNet, and 156 confirmed exoplanets discovered by WASP/SuperWASP. The Hungarian-made Automated Telescope Network (HATNet) began Northern operations in 2003, with telescopes in Arizona and Hawaii, and began Southern operations in 2009 at facilities spread out longitudinally in Chile, Namibia, and Australia. HATNet discoveries range in size from $0.389R_{\text{J}}$ ⁸ to $2.085R_{\text{J}}$, with a median value of $1.239R_{\text{J}}$. The planets are on short orbital periods, ranging from 1.2 to 16.2 days, orbiting stellar hosts with T_{eff} ranging from 3,405 K to 8,450 K. The Wide-Angle Search for Planets (WASP) consortium, with eight-camera arrays operated robotically in both the Canary Islands and South Africa, began observa-

⁶The unit M_{J} refers to a Jupiter mass, which is approximately 1.899×10^{27} kg.

⁷Unless otherwise noted, all statistical information regarding planet discoveries in Section 1.1, to include planet properties, was found using the NASA Exoplanet Archive, <https://exoplanetarchive.ipac.caltech.edu/>, accessed 28 October 2020.

⁸The unit R_{J} refers to a Jupiter radius, which is approximately 7.149×10^7 m.

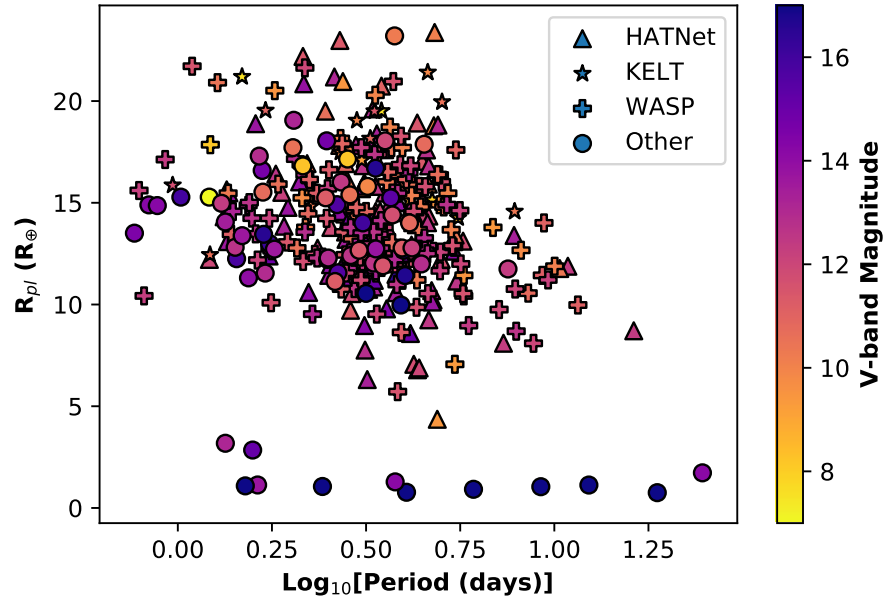
tions in 2004. WASP discoveries range in size from $0.51R_{\oplus}$ to $1.937R_{\oplus}$, with a median value of $1.22R_{\oplus}$. The planets are on short orbital periods, ranging from 0.79 to 11.6 days, orbiting stellar hosts with T_{eff} ranging from 4,143 K to 9,360 K. In general, as can be seen in Figure 1.3, ground-based transit surveys show strong selection effects in favor of large planets on short-period orbits. The surveys also favor small, bright host stars (Haswell, 2010).

Bieryla et al. (2015) announced confirmation of KELT-7b, the $1.28M_{\oplus}$ hot Jupiter I analyze in Chapter 5. The planet was discovered using the Kilodegree Extremely Little Telescope (KELT) project, comprised of two 5-cm aperture, wide-field, robotic telescopes referred to as KELT-North in Arizona, and KELT-South in South Africa (Pepper et al., 2004, 2012, 2007). To date, KELT has discovered 21 Jupiter-sized planets on short period orbits. KELT discoveries range in size from $1.11R_{\oplus}$ to $1.91R_{\oplus}$, with a median value of $1.57R_{\oplus}$. The orbital periods range from 0.97 to 7.85 days, with host star effective temperatures T_{eff} varying from 5,375 K to 10,170 K.

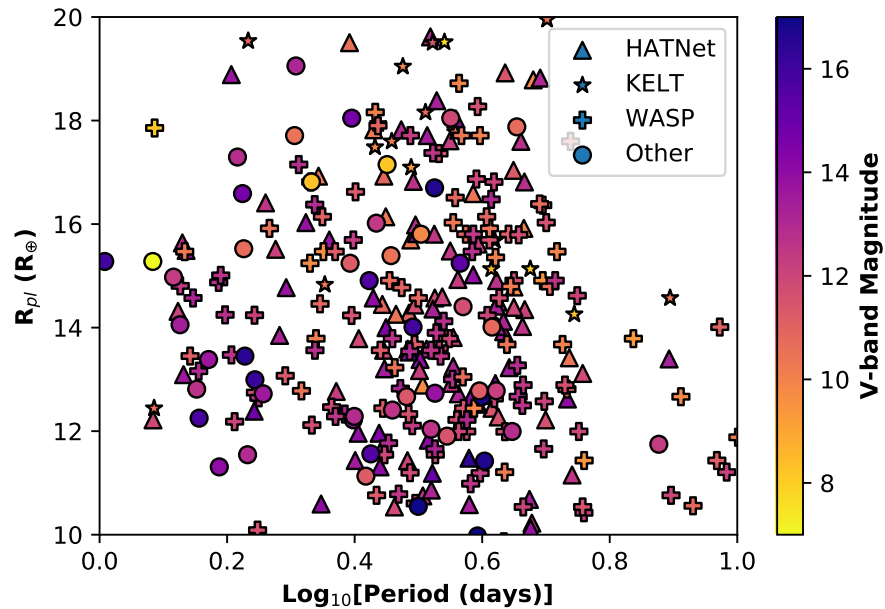
Two surveys of interest searching for smaller planets are MEarth⁹ (Irwin et al., 2009; Nutzman & Charbonneau, 2008) and TRAPPIST¹⁰ (Gillon et al., 2011). Unlike traditional wide-field surveys, the MEarth project telescopes employ narrower 25 arcmin \times 25 arcmin fields of view, and employ a unique observing strategy specifically targeting pre-selected M-dwarf stars. Since 2008, MEarth-North has specifically targeted $\sim 2,000$ pre-selected bright nearby M-dwarf stars (§1.1.5) us-

⁹<https://www.cfa.harvard.edu/MEarth/Welcome.html>

¹⁰https://www.trappist.uliege.be/cms/c_5006023/fr/trappist



(a)



(b)

Figure 1.3: Confirmed exoplanet discoveries from ground-based surveys. Panel (a) displays all exoplanets reported by the NASA Exoplanet Archive, accessed 28 October 2020. Panel (b) zooms in on highly irradiated giant planets on orbital periods $P \leq 10$ days. In general, ground-based transit surveys are more sensitive to large planets orbiting bright host stars on short periods. The 12 smallest planets shown in panel (a) include discoveries by the MEarth and TRAPPIST surveys, which were specifically designed to search for small planets orbiting cool, low mass host stars.

ing 8 identical 0.4-m telescopes on an automated array at Mt Hopkins, Arizona. Since 2014, the MEarth-South array has surveyed M-dwarfs within 33 pc from its location in Chile. To date, MEarth has announced 3 exoplanet discoveries: the super-Earth GJ1214b (Charbonneau et al., 2009), the $1.2R_{\oplus}$ rocky planet GJ1132b (Berta-Thompson et al., 2015), and the $1.7R_{\oplus}$ LHS1140b (Dittmann et al., 2017b). The Belgian TRAnsiting Planets and PlanetesImals Small Telescope (TRAPPIST) is a 0.6-m robotic telescope that began operations in Chile in 2010. The TRAPPIST-North 0.6-m telescope began operations in 2016 (Perryman, 2018). To date, the only TRAPPIST exoplanet discoveries are TRAPPIST-1 b, c, and d—3 temperate Earth-sized planets orbiting a $T_{eff} \sim 2,550 K$ ultra-cool dwarf star at 12 pc distance (Gillon et al., 2016). Both MEarth and TRAPPIST have played a role in the discovery of other planets as well, such as LHS1140c (Ment et al., 2019) and TRAPPIST-1 e, f, g, and h (Gillon et al., 2017). I use GJ1132b, LHS1140b, and the TRAPPIST-1 planets in my analysis in Chapter 4.

1.1.2 Space-based Transit Surveys

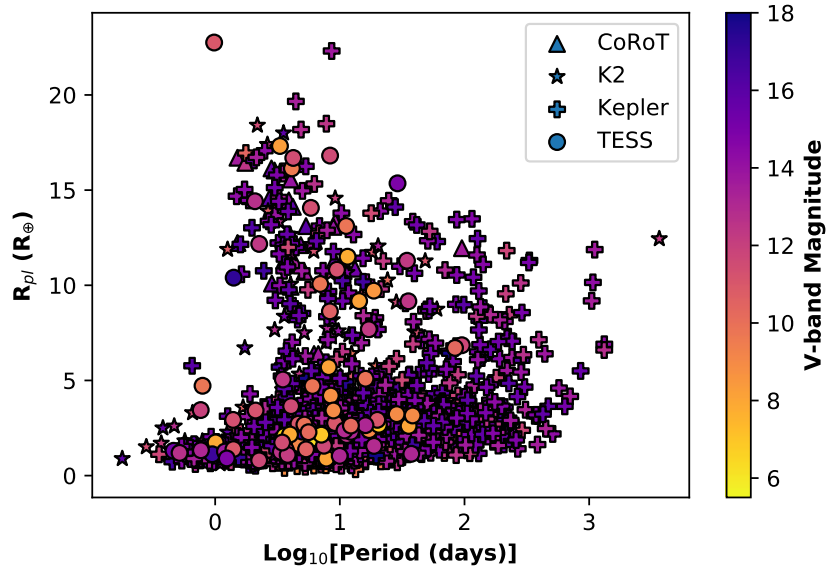
The CONvection, ROTation and planetary Transits (CoRoT) satellite, launched in 2006 and dedicated to asteroseismology as well as the search for transiting exoplanets, detected the first transiting exoplanets from space (Auvergne et al., 2009; Moutou et al., 2013). Notably, the satellite detected the $1.68R_{\oplus}$ CoRoT-7b, the first super-Earth planet with a measured radius (Léger et al., 2009), which I use in my analysis of Chapter 4. The 32 CoRoT discoveries range in size from $0.15R_{\oplus}$

(CoRoT-7b) to $1.49R_{\oplus}$, with a median value of $1.07R_{\oplus}$. The orbital periods range from 0.85 to 95.3 days, orbiting stellar hosts with T_{eff} ranging from 4,950 K to 6,740 K . As is evident by comparing Figures 1.3 and 1.4, space-based transit surveys can detect planets on longer orbital periods than ground-based surveys.

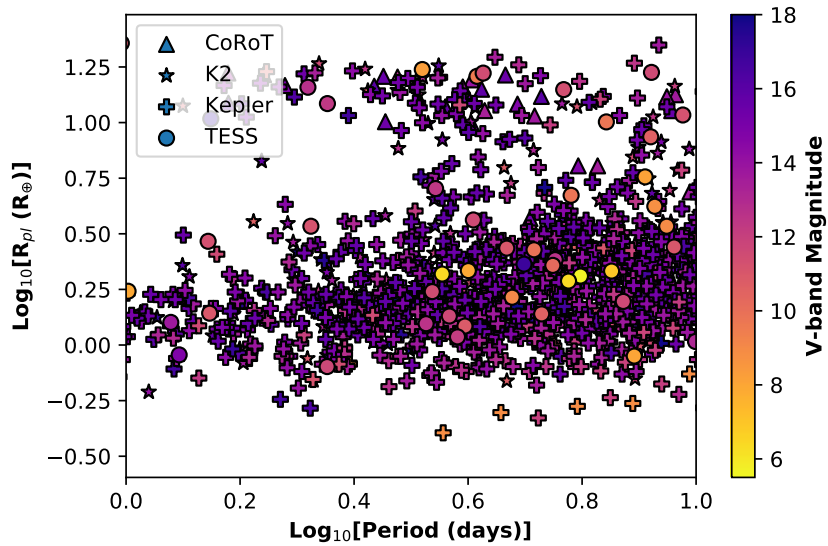
The Kepler satellite, which conducted its primary mission between May 2009 and May 2013, was the first space-based platform dedicated to detecting and understanding transiting exoplanet systems (Borucki et al., 2010, 2007; Howell, 2020). Over its 4-year primary mission, the satellite stared at a 115 square degree field-of-view in the constellations Cygnus and Lyra, monitoring $\sim 150,000$ main sequence stars for the tell-tale dips in brightness indicative of transiting exoplanets. The primary objective of the Kepler mission was to determine the frequency of Earth-sized planets ($1R_{\oplus}$) orbiting within the habitable zones (Kasting et al., 1993; Kopparapu et al., 2013, 2014) of Sun-like stars. To accomplish this mission, the Kepler program was designed to continuously monitor a large number of main sequence stars. Sub-objectives of the program included determining the distribution of sizes and semi-major axes of $R_{pl} \geq 1R_{\oplus}$ planets and the frequency of multi-planetary systems (Borucki et al., 2007). Kepler detected 2,384 of 3,290 ($\sim 72\%$)¹¹ confirmed transiting exoplanet discoveries currently listed in the NASA Exoplanet Archive. Many scientists have analyzed the results of Kepler, producing studies on important topics such as exoplanet occurrence rates and planetary system architectures. I defer a discussion of those results relevant to my work to Sections 1.3 and 1.4.

After losing two of its four reaction wheels, the Kepler satellite was repurposed

¹¹This number does not include K2 discoveries, described briefly in the next paragraph.



(a)



(b)

Figure 1.4: Confirmed exoplanet discoveries from space-based surveys. Panel (a) displays all exoplanets reported by the NASA Exoplanet Archive, accessed 28 October 2020. Panel (b) zooms in on highly irradiated planets with orbital periods $P \leq 10$ days. We can see that space-based transit surveys allow us to detect planets on longer orbital periods than ground-based surveys. The plot confirms the Kepler discovery that planets between the sizes of Earth ($1R_{\oplus}$) and Neptune ($4R_{\oplus}$) are common (see §1.4), as we can see from the clustering of planets between those two radii. In addition, TESS is designed to detect planets which are 30 to 100 times brighter than those detected during the Kepler mission. This too is evident, as the V-band magnitudes for TESS discoveries are brighter than those of Kepler.

to complete the K2 mission (Howell et al., 2014). During the K2 mission, the satellite stared at successive fields of view along the ecliptic plane for ~ 83 -day periods, with 75 days of each campaign devoted to science observations. The K2 mission detected 422 of 3,290 ($\sim 13\%$) confirmed transiting exoplanet discoveries currently listed in the NASA Exoplanet Archive. Thus, Kepler and K2 combined are responsible for $\sim 85\%$ of the confirmed transiting exoplanet discoveries listed. By design, K2 searched for planets orbiting stars brighter than those searched by Kepler,¹² and K2 targeted some interesting sub-groups of planets, such as those in bright open clusters and star-forming regions (Howell et al., 2014). In Chapter 4, I use the following Kepler and K2 discoveries in my analysis: Kepler-138b, c, and d; HIP-116454b; K2-3b and c; K2-95b; and WASP-47d and e.¹³

The Transiting Exoplanet Survey Satellite¹⁴ (TESS, see Ricker et al., 2015, 2014) was launched in April 2018 and completed its primary mission in July 2020. The TESS primary mission level 1 science requirement was to measure the masses of 50 transiting $R_{\text{pl}} < 4R_{\oplus}$ exoplanets. To accomplish this goal, TESS stared at 26 observation sectors for successive 27-day observing periods, monitoring a total of $\sim 200,000$ pre-selected target stars at 2-minute cadence. Due to overlap in sectors, regions near each ecliptic pole were viewed continuously for almost a year throughout the primary mission, while regions closer to the ecliptic plane were only observed for 27-day periods (Figure 1.5). TESS targeted stars are 30 to 100 times brighter

¹²The median V-band magnitude for Kepler host stars is 14.7, while that for K2 is 12.8.

¹³Analysis of K2 data revealed the presence of WASP-47d and WASP-47e—Neptune and super-Earth-sized planets, respectively—orbiting the known hot Jupiter host star WASP-47 (Becker et al., 2015).

¹⁴MIT TESS website: <https://tess.mit.edu/>; NASA TESS website: <https://heasarc.gsfc.nasa.gov/docs/tess/>

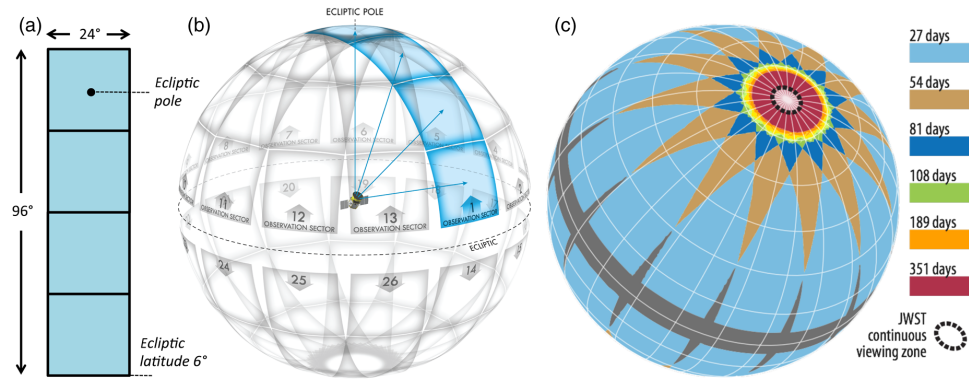


Figure 1.5: TESS primary mission observation sectors. (a) The TESS field-of-view for each sector covers 24 deg by 96 deg. (b) During the primary mission, TESS observed 26 sectors, 13 in each ecliptic hemisphere. Each sector was observed for 27 days. A 12-deg swath surrounding the ecliptic equator was not observed. (c) Due to overlap between observation sectors, regions near the ecliptic poles were observed for periods longer than 27 days. The dashed black circle near the ecliptic pole indicates the James Webb Space Telescope (JWST) continuous viewing zone. Note that this diagram was produced prior to the TESS mission. During the actual mission, observations sectors 14-16 and 24-26 were slightly modified to avoid contamination by stray Earth and moonlight. See <https://tess.mit.edu/observations/> for details. Figure from Ricker et al. (2015).

than those observed during the Kepler mission, thus facilitating follow-up observations such as those to measure planetary masses, determine stellar properties, or characterize planetary atmospheres. The TESS primary mission survey observed $\sim 85\%$ of the sky, which is 400 times larger than the region surveyed by Kepler. Members of the TESS Follow-up Observing Program (TFOP) are continually validating and confirming TESS discoveries. Currently, TESS detections comprise 81 of 3,290 ($\sim 2\%$) confirmed transiting planet discoveries listed in the NASA Exoplanet Archive. The TESS extended mission is ongoing. In Chapter 2, I will discuss some predictions for TESS exoplanet discoveries that I used for my work in Chapters 3 and 4.

1.1.3 Astrophysical False Positives

The arrival of the first ground-based transit surveys was accompanied by the detection of many stellar systems that produced the transit durations, depths, and periods expected from transiting hot Jupiters (Brown, 2003; Charbonneau et al., 2004). The most common sources of astrophysical false positives were blended eclipsing binary (BEB) systems, grazing eclipsing binary systems with equal mass components, and transits by planet-sized stars such as brown dwarfs or white dwarfs (e.g., Evans & Sackett, 2010; Haswell, 2010). Figure 1.6 depicts each of these cases.

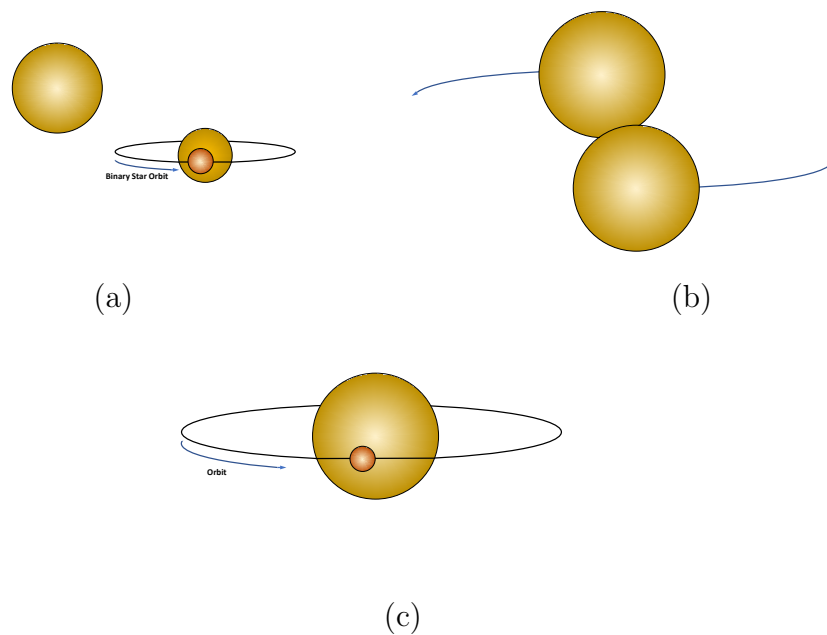


Figure 1.6: Astrophysical sources that commonly cause false positives in transit surveys. In each situation, the signal produced mimics the expected transit duration, depth, and period of a transiting exoplanet. (a) Light from the targeted stellar system blends with light from an eclipsing binary stellar system. (b) A binary star system comprised of two main sequence stars of similar masses and colors produces grazing eclipses. (c) Planet-sized stars such as brown dwarfs or white dwarfs transit a main sequence star.

In the BEB scenario, the binary star system may be gravitationally bound

to the stellar system, but more likely the binary system is located along the same sightline as the targeted star, but in the foreground or background. In Chapter 3, following [Sullivan et al. \(2015\)](#), I refer to the gravitationally bound case as a hierarchical eclipsing binary (HEB), and to the foreground/background case as a blended eclipsing binary (BEB), which is also known as a nearby eclipsing binary (NEB). Generally, the problems caused by blended light from eclipsing binaries become progressively worse with larger pixel scale (e.g., [Collins et al., 2018](#)). Thus, since the TESS satellite has a large pixel scale of $21 \text{ arcsec pixel}^{-1}$, candidate TESS exoplanet discoveries require extensive vetting, analysis, and follow-up observations to eliminate false positives, validate exoplanet candidates, and to confirm the best exoplanet candidates as true exoplanets.

1.1.4 Validation and Confirmation of Transiting Exoplanets

Detection of large numbers of astrophysical false positives in early transit surveys necessitated the development of various schemes to optimize the identification of *bona fide* exoplanets ([Alonso et al., 2004](#); [Brown, 2003](#); [Charbonneau et al., 2004](#)). Some astrophysical false positives may be identified by photometric data from the transit survey itself, thus ensuring that only the highest-quality exoplanet candidates are analyzed further (e.g., [Sullivan et al., 2015](#); [Torres et al., 2011](#)). The term *validation* refers to a process by which we establish that the probability for a candidate planet being a *true* exoplanet is much higher than the probability that it is a false positive. The process may include deeper statistical analyses of tran-

sit data (e.g., [Fressin et al., 2013](#); [Morton, 2012](#); [Morton et al., 2016](#); [Torres et al., 2011](#)), as well as follow-up observations (e.g., [Colón & Ford, 2011](#); [Colón et al., 2012](#); [O’Donovan et al., 2007, 2006](#); [Parviainen et al., 2020](#)). Ultimately, we more firmly establish the planetary nature of the very best validated exoplanet candidates by measuring their masses, a process known as *confirmation* (e.g., [Bluhm et al., 2020](#); [Jenkins et al., 2019](#); [Nielsen et al., 2020](#)). In this section, using the TESS program as an example, I explain the procedures used to identify false positives, and then to further *validate* and *confirm* exoplanet discoveries.

[Torres et al. \(2011\)](#) described four diagnostics applied to transit survey photometric data in order to eliminate clear false positives. [Sullivan et al. \(2015\)](#) later simulated these methods to predict their efficacy in the TESS mission. Following [Sullivan et al. \(2015\)](#), I refer to the diagnostics as (1) ellipsoidal variations, (2) secondary eclipses, (3) lengthy ingress and egress durations, and (4) centroid motion. These four tests are currently being successfully applied to TESS data via the vetting process ([Guerrero, 2020, submitted](#)). In the TESS program, TESS detections that pass the four tests are considered planet *candidates* (PCs) and are assigned a TESS object of interest (TOI) number. Note that failure of a single diagnostic test will not necessarily preclude a TESS detection from becoming a TOI. I briefly describe each test below.

Ellipsoidal Variations. Eclipsing binaries in close orbits are subject to gravitational tidal forces that break the spherical symmetry of each star, distorting their shapes into ellipsoids ([Mazeh, 2008](#)). As a result, the cross-sectional area of each star presented towards a distant observer varies with the phase of the binary orbit.

The stellar flux measured from the binary system thus varies periodically with orbital phase, and the apparent transits in the light curve will be synchronized with this variation in flux. Appearance of such synchronization in the light curve for a TESS detection is thus indicative that the detection may be of an eclipsing binary.

Secondary eclipses. Binary star systems differ from a system comprised of a star and transiting exoplanet because each component of the binary star system emits significant starlight of its own. In the case where the surface brightnesses of the two stars differ,¹⁵ and when both transit and secondary eclipse are captured in TESS observations, then we can expect to see significant secondary eclipses in the TESS light curve that are ~ 180 degrees out-of-phase with the apparent planetary transits. I note that secondary eclipses are visible in some planetary systems as well (e.g., [Wong et al., 2020](#)). Thus, consideration must be given to the equilibrium temperature of the planet (equation 1.18) and the possibility that the planet itself would produce secondary eclipses in the TESS light curve.

Lengthy ingress and egress durations. Eclipsing binaries generally have more prolonged ingress and egress durations than transiting exoplanets. As shown in Figure 1.2, the exoplanet transit light curve is normally U-shaped, with a relatively flat bottom throughout mid-transit. In contrast, eclipsing binaries are composed of two stars that are closer in size, so the resulting light curve is more likely to be V-shaped. In particular, for two stars that are the same size viewed nearly edge-on, half of the transit curve will be comprised by the ingress, and half by the egress.

¹⁵In the case where the two stars have nearly the same surface brightness, a secondary eclipse may be mistaken for an additional planetary transit.

Centroid motion. We can compare the amount of baseline stellar flux, or out-of-transit flux, falling upon TESS pixels to the amount of light falling upon the pixels during a putative planetary transit, the in-transit flux. The difference between the out-of-transit and in-transit flux provides the centroid of the difference image, which indicates the spatial location of the detected transit. If the difference image centroid shifts greatly from the centroid of the baseline flux, then the source of the putative transit is not the targeted star, and is likely to be a nearby eclipsing binary star.

Those TESS detections assigned a TOI number are passed on to the TESS Follow-up Observing Program (TFOP) for further validation and confirmation. The TFOP working group¹⁶ includes astronomers leading efforts on multiple observatories to support the TESS mission through such activities as identifying false positives, refining ephemerides, and confirming the most promising TESS PCs as true exoplanets by measuring their masses through precise radial velocity (PRV) follow-up.

As shown in Figure 1.7, planet candidates are successively filtered through various stages of validation, such that approximately 6% of $R_{\text{pl}} < 4R_{\oplus}$ TESS planet candidates are selected by the TESS team for PRV follow-up. In general, those observations conducted at earlier stages are the least time and resource intensive, with PRV observations consuming the most effort. In Chapter 3, I analyze the ability of multi-band photometry to distinguish BEB false positives from true transiting exoplanets. Multi-band photometry is one of the first observational steps applied to

¹⁶<https://tess.mit.edu/followup>

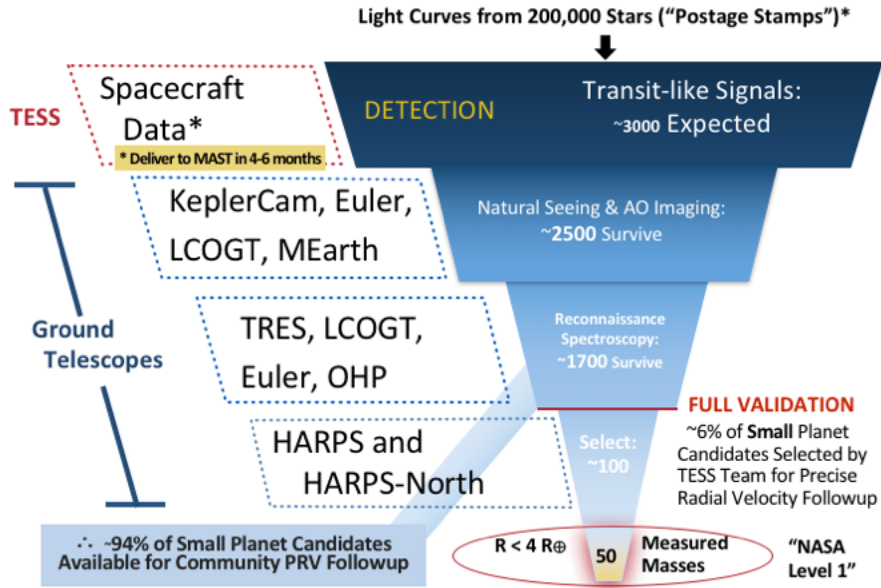


Figure 1.7: TESS validation and mass measurement process. TESS monitored $\sim 200,000$ pre-selected target stars throughout its primary mission, searching for signals indicative of transiting exoplanets. After eliminating those detections that are most likely false positives, promising TESS planet candidates are observed using ground-based facilities, and are successively filtered through more stringent stages of validation. Multi-band photometry observations, which I examine in Chapter 3, take place as part of the “Natural Seeing and AO Imaging” step. Ultimately, approximately 6% of $R_{\text{pl}} < 4R_{\oplus}$ planet candidates are analyzed using precision radial velocity (PRV) facilities. Figure from <https://tess.mit.edu/followup/>.

eliminate false positives, taking place as part of “Natural Seeing and AO Imaging.”

Determination of $R_{\text{pl}} < 4R_{\oplus}$ exoplanet masses through confirmation is not only one of the prime objectives of the TESS program, but is also key to later exoplanet atmospheric characterization (Batalha et al., 2017a, 2019). Radial velocity (RV) observations are the gold standard in determining transiting exoplanet masses. Radial velocity refers to velocity along our line-of-sight, and we measure it by de-

tecting Doppler shifts in the absorption lines of stellar atmospheres. If a star hosts an exoplanet, the radial velocity for that star will vary repeatedly over time due to gravitational tugs from the planet. For example, the radial velocity curve for a star hosting a planet on a perfectly circular orbit would have a sinusoidal shape. Denoting the radial velocity as v_r , the RV semiamplitude, K , is defined as $\frac{1}{2}(v_{r,\max} - v_{r,\min})$. The RV semiamplitude is related to the stellar mass M_* and planetary mass M_{pl} , both expressed in units of solar radii M_\odot ,¹⁷ through (Lovis & Fischer, 2010)

$$K = \frac{28.4329 \text{ m s}^{-1}}{\sqrt{1 - e^2}} \frac{M_{\text{pl}} \sin i}{M_\oplus} \left(\frac{M_* + M_{\text{pl}}}{M_\odot} \right)^{-2/3} \left(\frac{P}{1 \text{ yr}} \right)^{-1/3}, \quad (1.3)$$

where the orbital period P , eccentricity e , and the RV semiamplitude K can all be derived from analysis of radial velocity data, as long as observations are taken at all orbital phases. Assuming that $M_{\text{pl}} \ll M_*$, we can thus find the value of $M_{\text{pl}} \sin i$ from radial velocity observations. When the planet transits, the inclination i is near 90 degrees, so the radial velocity observations essentially provide the planetary mass.

Exoplanet scientists envision a day when they can study the atmospheres of Earth-like planets orbiting Sun-like stars. Assuming a circular orbit, equation 1.3 tells us that such planets will have RV semiamplitudes of $\sim 9 \text{ cm s}^{-1}$. In comparison, a Jupiter-mass planet on a 1.0 AU orbit would create an RV semiamplitude of $\sim 28 \text{ m s}^{-1}$, while a $5M_\oplus$ planet on a 1.0 AU orbit would create an RV semiamplitude of $\sim 45 \text{ cm s}^{-1}$. Recently developed PRV facilities provide RV precisions of 1 m

¹⁷The solar mass M_\odot is approximately $1.988 \times 10^{30} \text{ kg}$.

s^{-1} or better (Fischer et al., 2016; Wright & Robertson, 2017), thus allowing the confirmation of planets as small as Earth orbiting a mid-to-late M-dwarf host star.¹⁸

1.1.5 The M-Dwarf Advantage

Low-mass M-dwarf stars comprise 70% of all stars in our galaxy (Bochanski et al., 2010), and thus are ubiquitous in the solar neighborhood. The masses of M-dwarfs range from $0.08M_{\odot} < M_{*} < 0.6M_{\odot}$ (Reid & Hawley, 2005). The lower mass limit corresponds to the lowest mass stars able to fuse hydrogen into helium in their central cores (Chabrier & Baraffe, 1997). The magnitude of the stellar radius has approximately a one-to-one correspondence with stellar mass for M-dwarfs,¹⁹ and thus ranges from $0.08R_{\odot} < R_{*} < 0.6R_{\odot}$ (Boyajian et al., 2012).

Charbonneau & Deming (2007) described the multiple advantages of searching for exoplanets orbiting M-dwarfs. They illustrate the benefits of searching for Earth-sized planets orbiting in the habitable zones of M-dwarf host stars of stellar types M4V ($0.25M_{\odot}$, $0.25R_{\odot}$, $3,200 K$) and M8V ($0.10M_{\odot}$, $0.10R_{\odot}$, $2,400 K$), rather than Sun-like stars. Table 1.1 summarizes the results of their investigation.

Compared to transits of Earth-sized planets orbiting Sun-like stars, Table 1.1 shows that Earth-sized planets orbiting within the habitable zones of M-dwarf host stars are three to five times more likely to transit, their transit depths are 15 to

¹⁸A partial list of facilities includes MAROON-X (Seifahrt et al., 2018), NIRPS (Wildi et al., 2017), GIARPS (Claudi et al., 2016), NEID (Schwab et al., 2016), ESPRESSO (Mégévand et al., 2014) and KPF (Gibson et al., 2016).

¹⁹Boyajian et al. (2012) developed an empirical relationship between the mass and radius of M-dwarfs, and the exact equation is a second-degree polynomial. However, the relationship is consistent with a one-to-one correspondence between M-dwarf mass and radius, when measured in solar units.

R_* (R_\odot)	M_* (M_\odot)	a (AU)	p_{transit}^i (%)	δ_{tra}^{ii} (ppt)	K^{iii} (m s^{-1})	P^{iv} (days)	t_{transit}^v (hrs)	transits/yr
1.0	1.0	1.0	0.5	0.084	0.089	365.25	13	1
0.25	0.25	0.077	1.6	1.3	0.64	15.6	1.80	23
0.10	0.10	0.017	2.9	8.4	2.17	2.56	0.536	142

NOTES:

ⁱ Equation 1.2

ⁱⁱ Equation 1.1

ⁱⁱⁱ Equation 1.3, assuming $M_{\text{pl}} \ll M_*$, $i = 90$ deg, and $e = 0$. Also, note that $1M_\oplus \approx 318M_\oplus$.

^{iv} Equation 1.5

^v Equation 1.6

Table 1.1: Advantages of Searching for Earth-sized Planets Orbiting Within Habitable Zones of M Dwarfs

100 times greater, and their RV semi-amplitudes are 7 to 24 times larger. In addition, while our Earth spends ~ 13 hours in transit each year, a planet orbiting an M4V host star will spend 41.4 hours in transit (total of ~ 23 transits), while an M8V host star will spend 76 hours in transit (total of ~ 142 transits). Similarly, large planet-to-star radius ratios make M-dwarf host stars favorable for atmospheric characterization as well. For these reasons, recent transit surveys such as TESS, MEarth, and TRAPPIST have targeted low mass stars. In Chapter 2, I review predictions for the TESS survey planet yield, and in Chapter 4, I discuss my work in determining how well we can characterize the atmospheres of TESS-discovered exoplanets with the James Webb Space Telescope (JWST). Despite the advantages of studying exoplanets orbiting M-dwarfs, I note that the habitability of planets orbiting M-dwarf host stars is still an active field of investigation (e.g., [Shields et al., 2016](#)).

Equations 1.1–1.3, as well as the useful equations I present in this section,

allow quick duplication of the [Charbonneau & Deming \(2007\)](#) results, as well as easy comparisons of the requirements to detect planets orbiting various stellar types. Note that the semi-major axis shown in [Table 1.1](#) is calculated assuming that the equilibrium temperature ([equation 1.18](#)) and albedo of the planet are the same as that of Earth.

The orbital period P of a planet is related to its semi-major axis a through the general form of Kepler’s third law, given by (e.g., [Perryman, 2018](#))

$$P^2 = \frac{4\pi^2}{G(M_* + M_{\text{pl}})} a^3, \quad (1.4)$$

where G is Newton’s gravitational constant. If $M_{\text{pl}} \ll M_*$, [equation 1.4](#) can more conveniently be expressed as (e.g., [Perryman, 2018](#))

$$P \simeq 1\text{yr} \left(\frac{a}{\text{AU}} \right)^{3/2} \left(\frac{M_*}{M_\odot} \right)^{-1/2} \quad (1.5)$$

where M_* is in units of solar masses, and a is in AU. Additionally, for an edge-on transit at 90 degrees inclination, [Perryman \(2018\)](#) conveniently expresses the transit duration t_{transit} as

$$t_{\text{transit}} \simeq 13 \left(\frac{M_*}{M_\odot} \right)^{-1/2} \left(\frac{a}{1 \text{ AU}} \right)^{1/2} \left(\frac{R_*}{R_\odot} \right) \text{ hours}. \quad (1.6)$$

1.2 Exoplanet Atmospheres – Theory and Modeling

When we examine exoplanet atmospheres using the transit technique, we study the effects of the exoplanet upon the observed spectrum of the host star. The planet’s *transmission spectrum* is found by dividing the spectrum of the star recorded during transit—with the features of the planetary atmosphere imprinted upon it—by the spectrum of the star recorded out-of-transit. The resulting transmission spectrum reveals the wavelength-dependence of the transit depth.

To analyze a planetary transmission spectrum, we begin with our knowledge of planetary atmospheres, derived largely from theoretical analyses and observations of planets in our own solar system. In this section, I begin by explaining basic concepts from physics and chemistry that are necessary to describe planetary atmospheres (§1.2.1). I next illustrate how these concepts are applied in the open-source modeling code Exo-Transmit (§1.2.2), which I have used in portions of my work. I conclude this section by explaining how atmospheric retrieval codes can be used to estimate exoplanet atmospheric properties that are most consistent with observed planetary transmission spectra. (§1.2.3).

1.2.1 Fundamental Concepts

Since we examine exoplanet atmospheres in transmission by looking at the effects of those atmospheres on electromagnetic radiation from the host star, I begin this section by reviewing the radiative transfer equation. To understand the complexities involved in radiative transfer, I define and discuss the topics of optical

depth, opacity, absorption coefficient, chemical equilibrium, and local thermodynamic equilibrium. This discussion leads naturally to the understanding that the temperature and pressure of planetary atmospheres are critical to understanding radiative transfer. Thus, I next present the concepts of hydrostatic equilibrium, planetary scale height, and equilibrium temperature. I conclude this section by explaining the confounding effect of aerosols, clouds, and hazes on exoplanet transmission spectra. This section is necessarily brief, but an in-depth explanation of exoplanet atmospheres can be found in the two textbooks by [Seager \(2010\)](#) and [Heng \(2017\)](#).

I begin by presenting the one-dimensional (1D) form of the *radiative transfer equation* for a plane-parallel atmosphere, which is (e.g., [Seager & Deming, 2010](#))

$$\mu \frac{dI(z, \nu, \mu)}{dz} = -\kappa(z, \nu)I(z, \nu, \mu) + \epsilon(z, \nu, \mu). \quad (1.7)$$

Equation 1.7 describes how the intensity of a beam of electromagnetic radiation at frequency ν changes over distance due to absorption and emission. We may think of the beam of radiation as comprised of photons. In this equation, I is the intensity in $\text{J m}^{-2} \text{s}^{-1} \text{ster}^{-1} \text{Hz}^{-1}$, z is the vertical distance in m, and $\mu = \cos(\theta)$, where θ is the angle between the beam of radiation and the normal to the plane-parallel atmosphere. The first term on the right-hand side of equation 1.7 quantifies absorption of photons from the beam, to include scattering. The second term on the right-hand side quantifies photons added to the beam through both emission and scattering. The absorption coefficient κ is in units of m^{-1} , and the emission ϵ

is in $\text{J m}^{-3} \text{s}^{-1} \text{Hz}^{-1}$.

We use the definition of *optical depth*, $d\tau = \kappa dz$, to convert the radiative transfer equation to an alternative form that depends upon optical depth. This form of the radiative transfer equation, often used in atmospheric modeling codes, is given as

$$\mu \frac{dI(z, \nu, \mu)}{d\tau} = -I(z, \nu, \mu) + S(z, \nu, \mu), \quad (1.8)$$

where the *source function* is defined as $S = \epsilon/\kappa$. In modeling transmission spectra, emission is often negligible so that the last term in the radiative transfer equation can be ignored. Thus, the solution to the equation may be simply expressed using Beer's or Lambert's Law, given by (e.g., [Seager, 2010](#))

$$I(\tau_\nu, \mu, \nu) = I(0, \mu, \nu)e^{-\tau_\nu/\mu}, \quad (1.9)$$

where τ_ν is the frequency-dependent optical depth. When applied to a transmission spectrum, $I(\tau_\nu, \mu, \nu)$ is the stellar intensity attenuated by absorption in the planetary atmosphere, while $I(0, \mu, \nu)$ is the stellar intensity incident upon the atmosphere.

Although Beer's Law is simple in form, its application to a planetary atmosphere relies upon complex physics and laboratory experiments related to the determination of the atmospheric absorption. The opacity κ may be separated into a pure absorption term and a scattering term as ([Seager, 2010](#))

$$\kappa(z, \nu) = \alpha(z, \nu) + \sigma_s(z, \nu), \quad (1.10)$$

where $\alpha(z, \nu)$ is the pure absorption coefficient for an atomic or molecular species, and $\sigma_s(z, \nu)$ is the scattering coefficient, which represents removal of photons from a beam of incident light via a change of direction. We calculate these quantities at a given vertical height z in the planetary atmosphere, which may be specified by the temperature T and pressure P at that height. For example, the pure absorption coefficient may be expressed as (Seager, 2010)

$$\alpha(T, P, \nu) = \sum_j \alpha_j(T, P, \nu) = \sum_j \sum_i n_{ji}(T, P) \sigma_{ji}(T, P, \nu), \quad (1.11)$$

where n refers to the number density in m^{-3} , and σ refers to the absorption cross section in m^2 . Here, the summation over j refers to different atomic and molecular species, while the summation over i refers to different energy level populations. Atmospheric models typically employ temperature-pressure (T-P) profiles for planetary atmospheres in order to compute absorption cross sections and number densities for atomic and molecular species. Modelers use publicly available line lists, such as ExoMol²⁰ (Tennyson et al., 2020) or HITEMP²¹ (Rothman et al., 2010), to determine the positions and cross sections of absorption lines for each species. Such line lists are developed using quantum mechanical computations supplemented with laboratory observations. Heng (2017) describes meticulously the computations involved in transforming a line list into an atmospheric opacity.

Chemical equilibrium is often assumed in atmospheric modeling codes to compute number densities n of various species. Given an atmospheric layer with a spec-

²⁰<http://www.exomol.com/>

²¹<https://hitran.org/hitemp/>

ified temperature, pressure, and elemental abundance, chemical equilibrium refers to the state where the number densities of particles do not change. A method to determine the number densities of particles in chemical equilibrium is by minimizing the Gibbs free energy (e.g., [Heng, 2017](#); [Seager, 2010](#)). The Gibbs free energy is not a physical property of matter, but is a restatement of the first law of thermodynamics (conservation of energy) in terms of temperature and pressure. The quantities that Gibbs free energy depend upon—temperature and pressure—may be inferred directly from spectral data. [Mbarek & Kempton \(2016\)](#) explain in detail how Gibbs free energy minimization calculations are performed in the context of an exoplanet atmospheric modeling code to determine chemical equilibrium abundances. Chemical equilibrium is generally a good assumption in the deeper, hotter layers of an atmosphere. The higher temperatures and pressures of these layers speed up chemical reactions, so that the time scale for the reactions is shorter than any disequilibrium process.

Situations where chemical equilibrium may *not* be achieved include cases where heat is transported by convection rather than radiation. In these cases, the time scale for a chemical reaction to occur takes more time than the time scale for upwelling in the atmosphere. An example of chemical disequilibrium which is important for exoplanets—and indeed which has been observed in the solar system planet Jupiter—concerns the dominant carbon species in an atmosphere. The reaction governing the amount of CO and CH₄ in an atmosphere is ([Seager, 2010](#))



Because CO has a strong double bond that is difficult to break apart, the reaction proceeds more slowly to the right than to the left. CO is the dominant form of carbon at higher temperatures, whereas CH₄ is the dominant carbon species at lower temperatures. In Jupiter, we would thus expect to predominantly detect CH₄ in the cooler, upper layers of the atmosphere, while CO should not exist. Contrary to these expectations, CO has been detected, which is evidence of deep vertical mixing in the atmosphere (Seager, 2010).

In atmospheric modeling codes, the planetary atmosphere is divided into multiple layers, with temperatures and pressures determined in accordance with the T-P profile. Computing atmospheric opacity for a model transmission spectrum may be considered a complex geometric problem where we must consider multiple sightlines through the limb of the planetary atmosphere. Along each sightline, we view only portions of the atmospheric annulus from each layer as seen during transit. The optical depth along these sightlines is often referred to as the *slant optical depth* (Kempton et al., 2017).

Modeling codes may handle vertical mixing by employing the concept of a *quench level* (e.g., Zhang et al., 2020). We expect that in lower levels of the atmosphere (i.e. at higher pressures), chemical reactions will proceed at a faster rate than vertical mixing. Conversely, there may be higher levels in the atmosphere (i.e. lower pressures) where vertical mixing occurs more rapidly than chemical reactions can take place. Since modeling codes divide the atmosphere into multiple layers, we can define a pressure level—the *quench level*—in the atmosphere where the rate for vertical mixing will equal the rate of a given chemical reaction, thus leading

to chemical disequilibrium at lower pressure levels (i.e., higher in the atmosphere). Note that the quench level will differ with each chemical species.

An important fundamental concept in radiative transfer is that of *local thermodynamic equilibrium*, or LTE. In general, the radiation field, which we solve for in the radiative transfer equation, is coupled to the energy level populations of various chemical species (equation 1.11). By assuming LTE in radiative transfer calculations, we can use Boltzmann statistics to calculate energy level populations. Essentially, the energy levels will only depend upon the local conditions in a given layer of the atmosphere (e.g., Heng, 2017; Seager, 2010). LTE is valid in any region of the atmosphere where changes in pressure, temperature, and chemistry are small compared to the photon mean free path. The atmospheric density must be high enough that collisional processes dominate over any radiative processes. An obvious situation where LTE does not apply is the upper region of an atmosphere, where radiation freely escapes into space.

In addition to radiative transfer, we describe exoplanets and their atmospheres using several basic quantities that were first applied in our own solar system. Next, I describe the concepts of *hydrostatic equilibrium*, *equilibrium temperature*, and *scale height*, which can help us better understand the temperatures and pressures at work in planetary atmospheres.

Hydrostatic equilibrium refers to the stable state of an atmosphere where the pressure gradient and gravitational forces are balanced, so that the atmosphere is neither collapsing due to gravity, nor expanding/escaping due to pressure. Mathematically, this concept is expressed as (e.g., Seager, 2010)

$$\frac{dP}{dz} = -g\rho, \quad (1.13)$$

where g is the gravitational acceleration in units of m s^{-2} and ρ is the density in kg m^{-3} . Using the definition of optical depth introduced previously, hydrostatic equilibrium may also be expressed as

$$\frac{dP}{d\tau} = \frac{g\rho}{\kappa}. \quad (1.14)$$

Equation 1.13 may be combined with an equation of state to derive an expression for the pressure *scale height* H , which is a characteristic length scale for a planetary atmosphere, and describes the exponential drop in pressure with altitude.

For the equation of state we use the ideal gas law, given by

$$P = nkT = \frac{\rho kT}{\mu m_H}, \quad (1.15)$$

where k is Boltzmann's constant in J K^{-1} , μ is the mean molecular weight in atomic mass units, and m_H is the mass of the hydrogen atom in kg . If we assume an isothermal atmosphere with constant μ , and neglect variations in g with altitude, then the pressure lapse rate is calculated to be

$$P = P_0 e^{-z/H}, \quad (1.16)$$

where P_0 is the pressure at the base of the atmosphere in Pa , and H is the atmospheric scale height given by

$$H \equiv \frac{kT}{\mu m_H g}. \quad (1.17)$$

Thus, *scale height* is the e-folding vertical distance for pressure. Through the ideal gas law (Equation 1.15), we can see that density also varies exponentially with altitude in an isothermal atmosphere. Note that even in non-isothermal and non-uniform composition atmospheres, the scale height can be calculated locally and is still a useful quantity.

The *equilibrium temperature* is a theoretical number that describes the temperature of a planet with no internal energy flux which has reached a state of equilibrium between energy received from its host star and energy re-radiated by the planet. Equilibrium temperature is expressed as (e.g., Seager, 2010)

$$T_{\text{eq}} = T_{\text{eff},*} \left(\frac{R_*}{a} \right)^{1/2} \left[f'(1 - A_B) \right]^{1/4}, \quad (1.18)$$

where $T_{\text{eff},*}$ is the effective temperature of the host star, A_B is the Bond albedo of the planet, and f' is a factor that accounts for redistribution of heat around the planet before it is re-emitted. If heat is uniformly redistributed throughout the entire surface area of the planet (i.e., 4π sr), then $f = 1/4$ and equation 1.18 may be written as

$$T_{\text{eq}} = T_{\text{eff},*} \left(\frac{R_*}{2a} \right)^{1/2} \left[(1 - A_B) \right]^{1/4}. \quad (1.19)$$

Equilibrium temperature is often used to describe a planet's temperature when

we have no data concerning that planet. For example, in Chapter 4, I use the equilibrium temperature to distinguish between various TESS-discovered exoplanets.

I conclude this section with a discussion of the complicating effects of aerosols, clouds, and hazes upon our interpretation of planetary transmission spectra. I begin by presenting the definition of these terms, as explained by Prof Sarah Hörst.²² The term *aerosol* is the most general term, and refers to solid or liquid particles in an atmosphere that absorb or scatter light differently from gaseous species. Thus, *aerosols* describes both clouds and hazes, which can be distinguished from each other via their formation mechanisms. Prof Hörst defines a cloud as “a visible mass of liquid and/or solid particles suspended in an atmosphere that form from condensation of atmospheric gases.” We can expect clouds to form at a pressure level where the partial pressure of a given species exceeds the saturation vapor pressure for that species (Seager, 2010). Prof Hörst defines haze as “particles produced from chemistry in the atmosphere that results in the formation of involatile solids.” Whereas clouds can move back and forth between the solid and liquid state depending upon atmospheric conditions, hazes *cannot*.

Aerosols affect a planetary atmosphere in many ways. For example, clouds may be very reflective, thus increasing the planetary albedo A_B and lowering the planetary equilibrium temperature (equation 1.18), which in turn affects the T-P profile of the planet. Clouds may also trap infrared radiation—as in the solar system planets Venus and Earth—thus raising the surface temperature of the planet. In planetary transmission spectroscopy, clouds that form at a given pressure level will

²²<https://www.planetary.org/articles/0324-clouds-and-haze-and-dust-oh-my>

obscure our observations at higher pressures (i.e., lower in the atmosphere). I will return to the topic of aerosols during my discussion of theory and observations of hot Jupiter and $R_{\text{pl}} < 4R_{\oplus}$ planet atmospheres in Sections 1.3.3 and 1.4.2.

1.2.2 Exo-Transmit – Forward Modeling Transmission Spectra

Many planetary atmosphere codes have been developed that rely upon the fundamental concepts described in Section 1.2.1 to produce plausible model spectra that can explain our observations. The term *forward model* refers to an atmospheric model that is produced by assuming values for all input quantities. Here, I briefly describe the usage and functionality of the open-source Exo-Transmit forward modeling code (Kempton et al., 2017), which I used as part of my work in Chapter 4. Exo-Transmit is also the basis for the transmission model in the PLATON retrieval code (Zhang et al., 2019, 2020) described in Section 1.2.3, which I used in my work in Chapter 5.

Exo-Transmit is an easy-to-use, well documented software package that creates model transmission spectra for exoplanets ranging in size from hot Jupiters down to super-Earths. The code solves the radiative transfer equation (equation 1.8) for pure absorption (equation 1.9) in each layer of the model atmosphere, with the line-of-sight optical depth computed based upon the opacities (equation 1.10) of the absorbing species (equation 1.11).

The Exo-Transmit package supplies isothermal T-P profiles with temperatures ranging from 300 to 1500 K in 100 K increments. Unlike emission spectra, trans-

mission spectra are not strongly dependent on gradients in the T-P profile, making isothermal profiles a good first-order modeling choice (Miller-Ricci et al., 2009). For each temperature, the T-P profile is specified at pressures ranging from 10^3 to 10^{-9} bars in logarithmic steps. Wavelengths are computed at a resolving power $R = 1000$ from 0.3 to 30 μm . The opacities and abundances of 30 individual atomic and molecular species are tabulated on a T-P-wavelength grid. The package also supplies equation of state (EOS) files for various chemical species and abundances. Some choices for EOS files include metallicities ranging from 0.1 to 1000x solar (Lodders, 2003), and C/O ratios ranging from 0.2 to 1.2. The user may also specify an atmospheric composition of solely a single molecular type, such as CO_2 or H_2O . This is particularly useful for super-Earth atmospheres, which may be produced by outgassing of higher mean molecular weight molecules (Elkins-Tanton & Seager, 2008). The user may supply their own T-P profiles or EOS files, as long as they maintain the same format as the files supplied by the Exo-Transmit software package.

In atmospheres of mixed composition, Exo-Transmit provides pre-computed chemical equilibrium tables that were calculated using the Gibbs free energy minimization code described in Mbarek & Kempton (2016). The code provides an option to include condensation chemistry and rainout. In rainout, a condensed species settles to the lowest level of the atmosphere where it first appeared, which depletes upper levels in the atmosphere of its constituent atomic species (Mbarek & Kempton, 2016). The user may include ad-hoc clouds in the model by indicating the pressure level where clouds are formed. Exo-Transmit will then only complete the radiative transfer calculations for pressure levels higher in the atmosphere (i.e., at

lower pressures than the cloud deck). The resulting transmission spectrum therefore has muted features, since starlight passes through a thinner atmospheric annulus. The user can specify whether or not to include Rayleigh scattering, and can also indicate to enhance Rayleigh scattering by some factor. Enhanced Rayleigh scattering alters the slope of the continuum in the optical and near infrared regime, and also reduces the strength of atomic spectral features. This allows the user to simulate the presence of additional scattering aerosols that are not explicitly included in the code otherwise.

To use Exo-Transmit, the user modifies a single input file, specifying the following quantities: planetary and stellar radii, planet surface gravity, pressure level for clouds (if desired), a factor for excess Rayleigh scattering (if desired), desired T-P profile, and desired EOS file. The user should specify an isothermal T-P profile with the temperature selected to coincide with the base of the transmission spectrum, which is typically near 1 mbar.

1.2.3 Exoplanet Atmospheric Retrievals

Retrieval codes use atmospheric models in a Bayesian framework to indicate the most probable atmospheric model consistent with an observed spectrum. Atmospheric retrieval methods allow us to statistically examine observed planetary atmosphere spectra to infer atmospheric properties such as chemical compositions, T-P profiles, and presence of clouds or hazes. [Madhusudhan & Seager \(2009\)](#) pioneered application of the method to exoplanet atmospheres in 2009, when they

analyzed Spitzer and Hubble Space Telescope (HST) data to estimate the T-P profiles and molecular abundances in the atmospheres of two transiting hot Jupiters, HD 189733b and HD 209458b. Here, I describe how atmospheric retrievals are performed and highlight some of their key features. I emphasize some of the characteristics of the PLATON (Zhang et al., 2019, 2020) retrieval code, which I use to analyze the KELT-7b transmission spectrum in Chapter 5. I conclude this section by comparing and contrasting atmospheric retrieval methods used within our Solar System to those used on Exoplanets. A more complete pedagogical review of exoplanet atmospheric retrievals was recently written by Madhusudhan (2018).

To perform an atmospheric retrieval, we first require a data set. For observations taken during exoplanet transit, an atmospheric *transmission spectrum* constitutes that data set. The atmospheric retrieval code itself consists of 1.) a parametric model, and 2.) an optimization algorithm.

Parametric models are designed to vary *parameters* within the model to produce an output *model atmospheric spectrum* that can be compared with the *observed transmission spectrum*. Parameters may include the T-P profile, atmospheric chemical composition, and presence of aerosols. The atmospheric models generally assume spherical symmetry, hydrostatic equilibrium, and LTE. Computations to produce the *model atmospheric spectrum* are similar to those used in Exo-Transmit (§1.2.2), although subtle differences exist between codes.

The goal of the optimization algorithm is to extensively and efficiently sample the parameter space to search for the model solution space that best fits the data (transmission spectrum). Recent retrieval codes employ Bayesian inference

techniques such as Markov Chain Monte Carlo (MCMC) and Nested Sampling as optimization algorithms (e.g., [Evans et al., 2017](#); [Waldmann et al., 2015](#); [Zhang et al., 2020](#)).

Bayesian inference techniques originate from Bayes' Theorem, which may be written (e.g., [Trotta, 2017](#); [Wall & Jenkins, 2012](#))

$$p(\theta|d) = \frac{p(d|\theta)p(\theta)}{p(d)}. \quad (1.20)$$

In this equation, d is our data—the transmission spectrum, and θ represents our model parameters. $p(\theta|d)$ is the posterior probability of our model, given the data. $p(d|\theta)$ is the likelihood function, which we can describe as the probability of the data given a set of parameters θ . $p(\theta)$ is the prior probability distribution of the parameters, and represents our knowledge about the parameters before examining the data. For example, when performing a retrieval on a transmission spectrum, we may have some prior knowledge about the radius of a planet and its host star, as well as their estimated errors, based upon other observations. Finally, $p(d)$ is a normalizing constant referred to as the evidence, which ensures the posterior distribution is normalized to unity. Given a transmission spectrum (data), and considering our priors $p(\theta)$, the goal of Bayesian inference is to determine the posterior distribution $p(\theta|d)$ of the model parameters. Techniques such as MCMC and Nested Sampling differ in their methods to sample the model parameter space and estimate the posterior distributions and evidences.

The PLanetary Atmospheric Tool for Observer Noobs (PLATON²³, Zhang et al., 2019, 2020) is a fast, easy-to-use, open-source Python package that produces model exoplanet transmission and emission spectra, and also computes atmospheric retrievals based upon observed spectra. The PLATON Bayesian optimization algorithm incorporates either MCMC, via the *emcee* package (Foreman-Mackey et al., 2013), or Nested Sampling, via the *dynesty* package (Speagle, 2020).

PLATON’s transmission code is based upon Exo-Transmit, but the most recent version has incorporated several upgrades. Opacities for chemical species were updated with the most recent and complete public line lists, such as ExoMol (Tennyson & Yurchenko, 2018) and HITRAN (Gordon et al., 2017), and are available at $R = 1000$ and $R = 10,000$ over the wavelength regime from 0.3 - 30 μm . For example, water opacities, which have proven to be an important opacity source in exoplanet transmission spectra (§1.3.3, §1.4.2), have been updated with the most recent POKAZATEL water line list (Polyansky et al., 2018). PLATON also allows incorporation of H^- opacity. In addition, the user can download additional opacities for metallic species, to include Ca, Fe, Ni, and Ti. The user can also download the more accurate line profiles produced for K (Allard et al., 2016) and Na (Allard et al., 2019) that more accurately estimate the far wings of the lines for these atoms. These recent improvements are particularly important in retrievals of hot Jupiter transmission spectra (§1.3.3).

Exoplanet atmospheric retrievals are rooted in techniques developed for use on Earth and within our Solar System (e.g., Irwin et al., 2008; Rodgers, 2000).

²³<https://platon.readthedocs.io/en/latest/>

However, exoplanet atmospheric retrievals differ because the data for exoplanets generally result from spatially unresolved observations taken at relatively low signal-to-noise (S/N), and the exoplanetary atmosphere may be at conditions not found in our Solar System. For example, many exoplanets discovered to date are highly irradiated by their host stars, and thus the planetary atmospheres are much hotter than those of solar system planets. Furthermore, observations of Earth and other planets within our Solar System often allow collection of in-situ data to further inform our analyses. Such data collection is not possible with exoplanet atmospheres using currently available technologies. In what follows, I briefly discuss an example of Earth remote sensing observations and the corresponding retrievals, comparing and contrasting techniques applied to Earth’s atmosphere with the methods applied in exoplanetary science.

Recent work in atmospheric remote sensing of Earth’s atmosphere has dealt with changes in the quantity of greenhouse gases such as carbon dioxide (CO₂). For example, the Orbiting Carbon Observatory 2 (OCO-2, see [Crisp et al., 2017](#)) is a NASA dedicated science satellite designed to detect and track variations in CO₂ levels within Earth’s atmosphere across time (e.g, seasons) and space (i.e., geographic regions).²⁴ Whereas exoplanet atmosphere data is derived from analysis of spatially unresolved observations from the combined light of the planet and host star, OCO-2 satellite measurements are spatially-resolved, high resolution observations, allowing us to locate CO₂ sources and sinks upon the Earth. Furthermore, OCO-2 observations are supplemented by a global network of ground-based measurement stations.

²⁴<https://ocov2.jpl.nasa.gov/mission/>

[Crisp et al. \(2017\)](#) report that since its mission began in 2014, OCO-2 has typically delivered almost 1 million soundings per day across Earth’s sunlit hemisphere, where each sounding is observed at high resolving power $R \equiv \frac{\lambda}{\Delta\lambda} > 17,500$, and where single-sounding random errors and biases are between 0.5 and 1.0 ppm. In comparison, exoplanet atmospheres observed through the transit method may only be observed for at most a few transits, and at much lower resolving powers and with higher instrumental systematic noise values. For example, [Kreidberg et al. \(2014a\)](#)’s historic analysis of GJ1214b (see §1.4.2) consisted of 12 exoplanet transit observations across 22 spectral channels at $R \equiv \frac{\lambda}{\Delta\lambda} = 70$, with a systematic noise floor ~ 30 ppm. The duration of a single transit for GJ1214b is less than an hour, and typically astronomers observe an equal amount of time in and out of transit. Thus, the [Kreidberg et al. \(2014a\)](#) results were derived from approximately a single day of relatively low resolution observations.

[O’Dell et al. \(2012\)](#) describe the Atmospheric CO₂ Observations from Space (ACOS) retrieval algorithm, which may be used to retrieve the column-averaged dry-air mole fraction of CO₂, denoted X_{CO_2} . The retrieval algorithm itself operates similarly to retrieval algorithms applied to exoplanet atmospheres. However, the high quality of remote sensing observations on Earth, as well as data supplied using ancillary measurements, offer many advantages. For example, meteorological data such as surface pressure, temperature, and water vapor content are used to inform the prior parameters for ACOS retrievals. The accuracy of surface pressure measurements is 2-3 hectoPascals, so ACOS retrievals typically use 4 hectoPascals as the $1\text{-}\sigma$ prior error width for surface pressure. Without in-situ measurements, prior

information such as this is simply unobtainable in exoplanet atmospheric retrievals.

OCO-2 data are pre-filtered to eliminate soundings that may result in spurious X_{CO_2} estimates. As one example, an empirically-calibrated cloud-screening algorithm eliminates soundings with thick clouds or aerosols. For the soundings not eliminated with pre-filters, ACOS retrieves for a mixture of 4 specific optical path scattering agents: water clouds, ice clouds, dust, and a carbonaceous mixture. On the exoplanet front, although aerosols are complex phenomena, our lack of prior information about their structure and composition (e.g., lack of in-situ measurements), combined with limited information content in our observations, compels us to represent clouds using parametrized models in our retrievals. Parameters commonly used to describe clouds in exoplanet retrievals include opacity, scattering index, cloud-top or base pressure level, shape, and particle size (Barstow, 2020). Some retrieval codes are able to account for partial cloud coverage (e.g., MacDonald & Madhusudhan, 2017). The low information content of exoplanet atmosphere observations often prevents us from disentangling the presence of clouds in an atmosphere from other atmospheric properties, such as high mean molecular weight (e.g., Line & Parmentier, 2016).

O'Dell et al. (2012) used realistic simulations to evaluate systematic and random errors in the ACOS retrieval algorithm, to include the effects of cloud screening and post-retrieval filters. They concluded that the ACOS X_{CO_2} retrieval algorithm is accurate to 1-2 ppm, thus enabling accurate monitoring of carbon fluxes on regional scales.

1.3 Hot Jupiters

The term *hot Jupiter* refers to a gas giant exoplanet on a short period orbit, such that the planet is heated significantly by stellar irradiation. [Gaudi et al. \(2005\)](#) defined these exoplanets as Jupiter-mass planets with semi-major axes $a \leq 0.1AU$, corresponding to orbital periods $3 < P < 9$ days depending upon stellar type. [Gaudi et al. \(2005\)](#) further distinguished *very hot Jupiters* as those gas giant planets on $P < 3$ day orbits. Recently, the term *ultra-hot Jupiter* has entered the exoplanet lexicon, and may be defined as those hot Jupiters with dayside temperatures $\geq 2,200 K$, and which exhibit distinct atmospheric characteristics (e.g., [Parmentier et al., 2018](#)). In Section [1.3.1](#), I briefly present hot Jupiter occurrence rates found using Kepler data. Next, in Section [1.3.2](#), I motivate the discussion of hot Jupiter atmospheres by briefly describing how the planetary atmosphere may constrain their formation and migration mechanisms. Finally, in Section [1.3.3](#), I review key insights into our knowledge of hot Jupiter atmospheres based upon theory and observations. This section serves as a prelude to Chapter 5, where I add to our understanding of this unique planet category when I present my analysis of the optical and near infrared (NIR) transmission spectrum for the hot Jupiter KELT-7b.

1.3.1 Kepler Occurrence Rates

Based upon a 6-year radial velocity follow-up campaign of Kepler-discovered Jupiter-sized exoplanets with orbital periods of up to 400 days, [Santerne et al. \(2016\)](#) estimated the overall occurrence rate of giant planets on orbits $P \leq 400$ days to be

$4.6 \pm 0.6\%$. They further estimated the occurrence rate of hot Jupiters, which they defined as those giant exoplanets on orbital periods $P < 10$ days, to be $0.47 \pm 0.08\%$.

1.3.2 Hot Jupiter Formation

Gas giant planets form in protoplanetary disks through either core accretion (e.g., [Pollack et al., 1996](#)) or gravitational disk instability (e.g., [Boss, 1997](#); [Helled et al., 2014](#)). Hot Jupiters (or their progenitor cores) most likely formed beyond the snow line ($a \gtrsim 3$ AU) and then arrived on short orbital periods through either 1.) inward disk-driven migration (e.g. [Rice et al., 2012](#)), or 2.) production of a highly eccentric orbit with small periapse, followed by tidal circularization (e.g., [Perryman, 2018](#)).

One motivation for studying hot Jupiter atmospheres is to gain insight into planet formation. The atmospheric composition encodes information about the formation and evolutionary history of a hot Jupiter. [Öberg et al. \(2011\)](#) demonstrated that the C/O ratio of the solids and gases in a protoplanetary disk vary depending upon the radial location within the disk due to the presence of various snowlines (H₂O, CO₂, CO). Their models showed that measuring the C/O and C/H ratios in a giant planet atmosphere, and determining whether those ratios were substellar, stellar, or superstellar, would place constraints on the formation mechanism (core accretion or gravitational instability), the formation location (within or beyond the water snowline), and the degree of atmospheric pollution by evaporating

planetesimals during the late stages of planet formation.

[Öberg & Bergin \(2016\)](#) refined the earlier [Öberg et al. \(2011\)](#) model predictions to include dynamics such as grain growth and pebble drift. They focused on the effects of CO redistribution to show that both superstellar C/O and C/H ratios could exist in the gas between the H₂O and CO snowlines of a protoplanetary disk. They proposed that the N/C ratio could be used in conjunction with C/O and C/H ratios to distinguish between giant planet formation locations.

Recently, [Eistrup et al. \(2018\)](#) have shown that protoplanetary disk chemistry evolves over time during the era of planet formation—up to 7 Myr. Thus, to properly interpret planetary atmosphere C/O ratios, disk chemistry must be incorporated into planet formation models.

[Madhusudhan et al. \(2014\)](#) proposed chemical tests to constrain the migration pathway for gas giant exoplanets. Two hypotheses for hot Jupiter migration are interactions with the protoplanetary disk, or some type of disk-free process such as gravitational interaction with a third body. [Madhusudhan et al. \(2014\)](#) demonstrated that sub-solar carbon and oxygen abundances likely indicated disk-free migration processes. Such planets would also have solar or super-solar C/O ratios.

1.3.3 Hot Jupiter Atmospheres – Theory and Observations

Soon after [Mayor & Queloz \(1995\)](#) announced the first discovery of hot Jupiter 51 Pegasi b, theorists began to expand our planetary atmosphere models to predict

the properties of these unique worlds. Early work focused on modeling the atmospheres of these highly irradiated planets to predict their chemical composition, emergent flux, and observational features (e.g., [Burrows et al., 1997](#); [Burrows & Sharp, 1999](#); [Guillot et al., 1996](#); [Saumon et al., 1996](#); [Seager & Sasselov, 1998](#)). With the detection of the first exoplanet transit ([Charbonneau et al., 2000](#); [Henry et al., 2000](#)), theorists touted the benefits of transmission spectroscopy and began to lay the foundations for later observational work (e.g., [Brown, 2001](#); [Hubbard et al., 2001](#); [Seager & Sasselov, 2000](#)).

In an early study, [Seager & Sasselov \(2000\)](#) derived the analytical transmission spectrum for HD 209458 b to foretell the strongest absorption features of giant exoplanets on short-period orbits. Their predictions of strong alkali metal lines—in particular the KI resonance doublet ($4^2\text{p}-4^2\text{s}$) at 7670 \AA and the NaI resonance doublet ($3^2\text{p}-3^2\text{s}$) at 5893.6 \AA —were later borne out by observations. In addition, they accurately predicted strong absorption of stellar photons at $1.083 \mu\text{m}$ due to the He I $2^3\text{s}-2^3\text{p}$ triplet transition line, an observational diagnostic that has only been recently exploited (e.g., [Allart et al., 2018](#); [Mansfield et al., 2018](#); [Nortmann et al., 2018](#); [Salz et al., 2018](#)).

[Brown \(2001\)](#) wrote an early pedagogical description of transmission spectroscopy, and developed a rigorous model spectrum for HD 209458 b. His work agreed with that of [Seager & Sasselov \(2000\)](#), with his spectrum showing strong KI and NaI lines in the optical, as well as strong signatures of CO, CH₄, and H₂O in the infrared. [Brown \(2001\)](#) noted the advantages of avoiding the contaminating effects of Earth’s atmosphere via space-based observations, particularly in the in-

frared. He also illustrated the obfuscating effects of clouds on transmission spectra. He cautioned that although transmission spectroscopy would allow insight into the properties of planetary atmospheric properties, some of these properties are degenerate. For example, high altitude clouds and higher heavy element abundances could produce similar effects on planetary atmosphere spectra.

[Charbonneau et al. \(2002\)](#) published the first detection of an atmospheric feature attributable to atomic absorption—namely, they reported detection of atomic sodium near 5893.6 Å in the atmosphere of HD 209458 b, based upon analysis of HST Space Telescope Imaging Spectrograph (STIS)²⁵ spectra. They noted that the features were not as strong as expected from their solar metallicity cloud-free model. They postulated four potential causes of the muted sodium feature: formation of molecules using sodium in the atmosphere, photoionization of sodium in the upper atmosphere, low primordial sodium abundance, or high-altitude clouds.

Soon HST transit spectroscopy observations shifted to the infrared regime, where astronomers sought evidence of molecular features. Unfortunately, the first NICMOS²⁶ detections of H₂O and CH₄ ([Swain et al., 2008](#)), as well as CO₂ ([Tinetti et al., 2010](#)) were deemed questionable ([Gibson et al., 2011](#)). However, after its installation on HST servicing mission 4, the Wide Field Camera 3 (WFC3)²⁷ has become the mainstay instrument for near infrared space-based transmission spectroscopy.

[Deming et al. \(2013\)](#) analyzed HST/WFC3 G141 grism spectra for the two

²⁵<https://www.stsci.edu/hst/instrumentation/stis>

²⁶The Near Infrared Camera and Multi-Object Spectrometer (NICMOS) has been inoperative since 2008. See <https://stsci.edu/hst/instrumentation/legacy/nicmos>.

²⁷<https://www.stsci.edu/hst/instrumentation/wfc3>

hot Jupiters XO-1b and HD 209458b using the (then) newly available *spatial scan* mode (McCullough & MacKenty, 2012).²⁸ In spatial scan mode, HST is moved at a small constant rate back and forth perpendicular to the dispersion direction of the spectrum, such that the target starlight spreads across the detector array in the spatial direction. When observing bright exoplanet host stars, spatial scan mode allows selection of longer exposure times without saturating subarray pixels. Deming et al. (2013) found water absorption of ~ 200 ppm near the $1.38 \mu\text{m}$ H₂O bandhead in the transmission spectra for both XO-1b and HD 209458b. Similar to the Charbonneau et al. (2002) sodium features, Deming et al. (2013) noted that the water spectral features were muted compared to expectations from models of clear atmospheres, and attributed this attenuation to continuous opacity from haze and/or dust. Following the Deming et al. (2013) analysis of WFC3 spatial scan data, many other scientists reported detection of NIR H₂O features in hot Jupiters (e.g., Kreidberg et al., 2014b, 2015; McCullough et al., 2014; Wakeford et al., 2013).

The spectral region probed by the HST/WFC3 G141 grism is dominated by H₂O features. Spitzer Space Telescope observations complement those of HST/WFC3 by providing data further into the IR regime. Spitzer began its mission in 2003, and during its cryogenic phase was able to simultaneously observe in four photometric bandpasses (centered at 3.6, 4.5, 5.8, and $8 \mu\text{m}$) with the Infrared Array Camera (IRAC), complemented by broadband observations at $24 \mu\text{m}$ using the Multiband Imaging Photometer for Spitzer (MIPS, e.g., Deming & Knutson, 2020; Perryman,

²⁸I applied the procedures of Deming et al. (2013), as well as Wilkins et al. (2014), in analyzing WFC3 spectra for KELT-7b, and summarize those procedures further in Section 5.4.1.

2018). The Infrared Spectrograph (IRS, [Houck et al., 2004](#)) also supported low and high resolution spectroscopy. However, after March 2009, Spitzer entered its *warm mission*, and photometric observations were limited to the 3.6 μm and 4.6 μm bandpasses of IRAC. Although many Spitzer exoplanet observations took place during the warm mission, data from the 3.6 μm and 4.6 μm bandpasses provide additional constraints on atmospheric models, since CH_4 , CO , and CO_2 all absorb strongly in these bandpasses. Unfortunately, because these are photometric bandpasses, the molecular features are not spectrally resolved, which can lead to some uncertainty in their interpretation.

Observations using HST/WFC3 in concert with HST/STIS have also proven fruitful.²⁹ STIS covers wavelengths from 1150 Å to 10300 Å, spanning the near ultraviolet (NUV) to NIR. Thus, STIS observations offer the opportunity to search for signs of Rayleigh scattering slopes or of atomic lines such as those of K I and Na I. In a pioneering study, [Sing et al. \(2016\)](#) compared the 0.3 μm to 5.0 μm spectra of 10 hot Jupiters spanning a large range of planetary temperatures, surface gravities, masses and radii, which in turn allowed examination of a broad range of planetary atmospheric parameters. Their analysis included data from HST/STIS (0.3 μm to 1.01 μm), HST/WFC3 (1.1 μm to 1.7 μm), and Spitzer IRAC (3.6 μm and 4.6 μm)—the broad spectral coverage allowed capture of features from the optical scattering slope to molecular absorption in the NIR. In addition to optical scattering slopes, they found prominent spectral absorption features from NaI, KI, and H_2O , but the strength—and even the presence—of the features varied between planets. They

²⁹Note that STIS was off-line from 2004 until HST servicing mission 4 in 2009.

found that comparison of the planetary radius measured in the optical and NIR regimes could reveal whether or not the planetary atmosphere was clear or cloudy. [Barstow et al. \(2017\)](#) performed atmospheric retrievals on the same sample of hot Jupiters analyzed by [Sing et al. \(2016\)](#). [Barstow et al. \(2017\)](#) found that retrievals for hot Jupiters with equilibrium temperatures between 1300 and 1700 K pointed to deeper, gray cloud layers, whereas hot Jupiters with cooler or hotter temperatures were best explained by higher altitude Rayleigh scattering. Recent work has shown that stellar activity can also produce larger transit depths in the optical regime that mimic scattering slopes, thus confounding our interpretation of transmission spectra and pointing to the importance of stellar activity monitoring (e.g., [Rackham et al., 2018, 2019](#)).

Soon after the [Sing et al. \(2016\)](#) and [Barstow et al. \(2017\)](#) studies, [Fu et al. \(2017\)](#) performed a statistical analysis of all published HST/WFC3 (1.1 μm to 1.65 μm) spatially scanned spectra available at the time for 34 planets ranging from hot Jupiters to hot Neptunes. They sought a correlation between the observed H₂O absorption feature and planetary parameters. They found a positive baseline correlation between water absorption expressed in scale heights and planet equilibrium temperature. [Fu et al. \(2017\)](#) proposed the correlation was due to decreasing cloud condensation (and thus more H₂O absorption) with increasing temperature.

Recently, [Gao et al. \(2020\)](#) used a grid of 1D giant planetary atmosphere models incorporating an aerosol microphysics model to determine the composition of aerosols across various temperature regimes. Their model grid spanned equilibrium temperatures T_{eq} from 700 to 2800 K, surface gravities of 4, 10, and 25 m s^{-1} , and

both solar and 10x solar metallicities. By comparing their model grid to transmission spectroscopy observations, they showed that silicates dominate the aerosol opacity for planets with $T_{\text{eq}} > 950$ K, while hydrocarbon aerosols dominate on planets with $T_{\text{eq}} < 950$ K.

A number of hot Jupiter transmission spectra display relatively large transit depths in the short wavelength ($< 0.5 \mu\text{m}$) regimes. Motivated by their analysis of the WASP-76b transmission spectrum (Fu et al., 2020), Lothringer et al. (2020) recently showed that metal opacities not commonly considered in planetary atmosphere models—for example, atoms and ions of Fe, Ti, Ni, Ca, Cr, Mn, and SiO—may explain these large transit depths. These metals are guaranteed to be present in conditions near chemical equilibrium. Due to such metal opacities, hot Jupiters with $T_{\text{eq}} \gtrsim 1000$ K exhibit NUV transit depths greater than those that can be explained by Rayleigh scattering alone. Furthermore, in the blue-optical regime, those hot Jupiters with $T_{\text{eq}} \gtrsim 2000$ K will have transit depths greater than those that can be explained by Rayleigh scattering, although for planets with $T_{\text{eq}} \lesssim 2000$ K Rayleigh scattering can dominate. Additionally, Allard et al. (2016, 2019) recently reported the importance of including properly broadened line wings for Na and K opacities when analyzing hot Jupiter spectra.

1.4 $R_{\text{pl}} < 4R_{\oplus}$ Planets

The work presented in Chapters 3 and 4 addresses follow-up of TESS-discovered exoplanets. The goal of the TESS mission is to find hundreds of planets smaller in

size than Neptune ($4R_{\oplus}$), orbiting host stars bright enough to facilitate follow-up spectroscopic radial velocity and atmospheric characterization observations (Ricker et al., 2015). Here, I briefly review our knowledge of $R_{\text{pl}} < 4R_{\oplus}$ planet occurrence rates—to include the *radius valley* found by analysis of Kepler data—as well as theory and observations concerning $R_{\text{pl}} < 4R_{\oplus}$ planet atmospheres. The radius valley provides the motivation for part of the analysis presented in Chapter 4.

1.4.1 Kepler Occurrence Rates and the Radius Valley

Analysis of data from NASA’s Kepler space telescope has taught us that the most common types of planets are $R_{\text{pl}} < 4R_{\oplus}$ super-Earths and sub-Neptunes (e.g., Dressing & Charbonneau, 2013, 2015; Fressin et al., 2013) that range in size between Earth ($1R_{\oplus}$) and Neptune ($4R_{\oplus}$). In addition, Kepler and K2 occurrence rate studies have revealed a *valley* (sometimes referred to as a *gap*) in the radius distribution between super-Earth and sub-Neptune-sized planets on $P < 100$ day orbits. The pioneering work of Fulton et al. (2017a) showed that the radius distribution for $R_{\text{pl}} < 4R_{\oplus}$ planets on short-period orbits cluster about values of $\sim 1.3R_{\oplus}$ (*super-Earths*) or $\sim 2.4R_{\oplus}$ (*sub-Neptunes*), with relatively few planets falling into the regime $1.5 - 2.0R_{\oplus}$ (Figure 1.8). Additional studies of Kepler and K2 planet occurrence rates verified the bimodal distribution of super-Earths and sub-Neptunes (Cloutier & Menou, 2020; Fulton & Petigura, 2018; Hardegree-Ullman et al., 2020; Martinez et al., 2019; Van Eylen et al., 2018). Most recently, Cloutier & Menou (2020) analyzed a sample of 275 confirmed Kepler planets and 53 confirmed K2 planets,

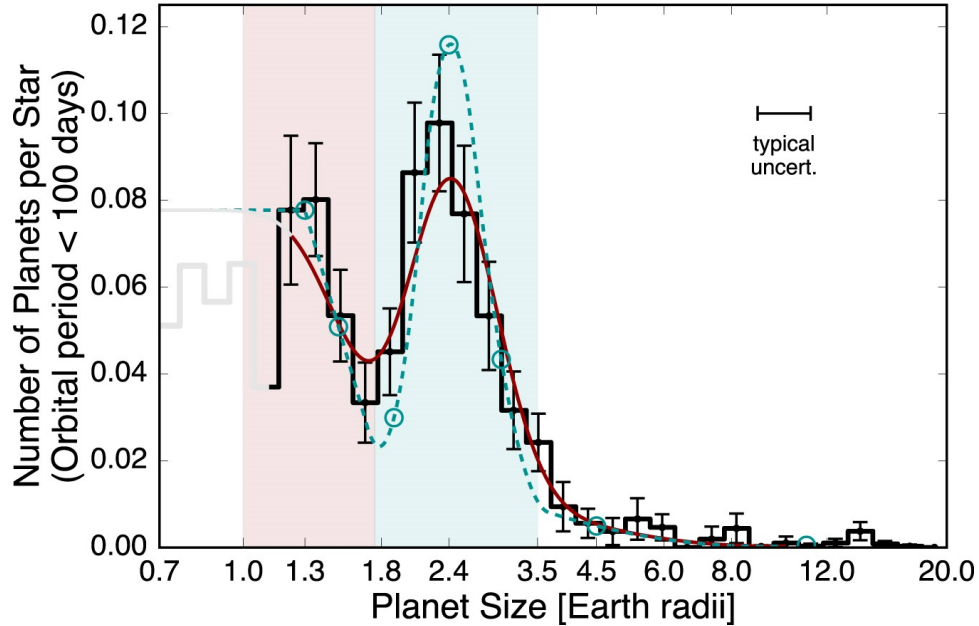


Figure 1.8: Radius valley in $R_{\text{pl}} < 4R_{\oplus}$ planets. Kepler occurrence rate studies show that the radius distribution for $R_{\text{pl}} < 4R_{\oplus}$ planets on short-period orbits cluster about values of $\sim 1.3R_{\oplus}$ (*super-Earths*, shaded in red) or $\sim 2.4R_{\oplus}$ (*sub-Neptunes*, shaded in cyan), with relatively few planets falling into the regime $1.5 - 2.0R_{\oplus}$. Figure from [Fulton et al. \(2017a\)](#).

all on $P < 100$ day orbits of mid-to-late K or M-dwarf host stars ($T_{\text{eff}} \leq 4700$ K), and confirmed the bimodal distribution in cool, low-mass host stars—the same stellar types that produce relatively larger transit depths and spectral features in transmission spectra.

Theories developed to explain the radius gap include mass loss by photoevaporation ([Jin & Mordasini, 2018](#); [Lopez & Fortney, 2014](#); [Lopez & Rice, 2018](#); [Owen & Wu, 2013, 2017](#)), core-powered mass loss ([Ginzburg et al., 2016, 2018](#); [Gupta & Schlichting, 2019, 2020](#)), impact erosion by planetesimals ([Schlichting et al., 2015](#); [Shuvalov, 2009](#); [Wyatt et al., 2020](#)), and distinct formation pathways for rocky and

non-rocky planets, with gas-poor formation explaining rocky planet origins (Lee & Chiang, 2016; Lee et al., 2014; Lopez & Rice, 2018). To date, observational tests of the theories do not reveal a conclusive origin for the radius gap. Atmospheric characterization of selected planets will provide important information such as metallicities and C/O ratios that will help us refine our theories of planet formation and evolution, and will also help us to pinpoint the origins of the radius valley.

1.4.2 Atmospheres of $R_{\text{pl}} < 4R_{\oplus}$ Planets – Theory and Observations

CoRoT-7b (Léger et al., 2009) and GJ1214b (Charbonneau et al., 2009) were the first transiting $R_{\text{pl}} < 4R_{\oplus}$ planets with measured masses and radii. CoRoT-7b is a $1.7R_{\oplus}$ planet orbiting a $0.83R_{\odot}$ G9V host star, while GJ1214b is a $2.85R_{\oplus}$ planet orbiting a $0.216R_{\odot}$ M4.5 host star.³⁰ Thus, GJ1214b’s transit depth (equation 1.1) is larger, and the prospects for observing its atmosphere greater, so a flurry of theoretical and observational studies related to measuring the planet’s transmission spectrum accompanied its discovery in 2009 (e.g., Bean et al., 2011, 2010; Berta et al., 2012; Désert et al., 2011; Miller-Ricci & Fortney, 2010).

Planets between the sizes of Earth ($1R_{\oplus}$) and Neptune ($4R_{\oplus}$) likely form via different mechanisms, and their atmospheres encode those formation mechanisms. In our own solar system, $R_{\text{pl}} \leq 1R_{\oplus}$ planets are rocky with high mean molecular weight atmospheres, while Neptune is an *Ice Giant* with a hydrogen and helium dominated atmosphere (e.g., Moses et al., 2020). Atmospheres of solar system terrestrial

³⁰Planetary system parameters are taken from the NASA Exoplanet Archive, accessed 2 December 2020.

planets formed via outgassing of volatiles from minerals (e.g., [Abe & Matsui, 1985](#); [Lange & Ahrens, 1982](#)). [Schaefer & Fegley \(2010\)](#) examined the chemical composition of terrestrial atmospheres formed from outgassing during planetary accretion and described their implications for rocky exoplanets. They determined that atmospheric composition would depend upon the source material for outgassing, and that 4 plausible atmospheric compositions³¹ were 1.) H₂O-rich (steam), 2.) H₂-rich with CO and H₂O, 3.) CO-rich with H₂, CO₂, and H₂O, and 4.) CO₂-rich with H₂O. Thus, measuring the chemical composition of a rocky exoplanet atmosphere would provide clues to that planet’s formation history.

The interior structure and atmospheric compositions of $R_{\text{pl}} < 4R_{\oplus}$ planets cannot be constrained by bulk density from mass and radius measurements alone ([Adams et al., 2008](#)). [Rogers & Seager \(2010a\)](#) introduced quaternary diagrams—shaped like three dimensional tetrahedons—which model a planet as composed of 4 components which are each expressed as mass fractions: a core, mantle, ice layer, and gas layer. [Rogers & Seager \(2010a\)](#) demonstrated their interior structure model on 4 planets, including CoRoT-7b, and showed that by using only the measured mass, radius, and stellar irradiation of a planet, they could constrain the range of mass fractions possible for each of the 4 components in their quaternary diagrams. Soon thereafter, [Rogers & Seager \(2010b\)](#) applied the same concepts to GJ1214b. They found that the GJ1214b low average density of $\rho_{\text{pl}} = 1870 \pm 400 \text{ kg m}^3$ implied that the planet has a large gas component. They considered three possible origins for

³¹The compositions list the primary chemical component, followed by the next most abundant gases in order of abundance.

the large gas layer—accretion from the protoplanetary disk, sublimation of ices, and outgassing from rocky material—and suggested spectral observations to distinguish between scenarios.

An earlier paper by [Miller-Ricci et al. \(2009\)](#) examined 3 plausible atmospheric compositions for the super-Earth Gl 581c ($M \sin i = 5M_{\oplus}$): a hydrogen-rich atmosphere accreted from the protoplanetary disk, an atmosphere depleted of hydrogen due to atmospheric escape, and a CO₂-rich and H-poor Venus-like atmosphere. They found that transmission spectra are the best method to distinguish between H-rich (low mean molecular weight μ) and H-poor atmospheres (high μ) due to the difference in scale height (equation 1.17) between such atmospheres.

Upon discovery of GJ1214b, [Miller-Ricci & Fortney \(2010\)](#) explored a range of atmospheres for the planet. They advocated that space-based follow-up observations would attain the precision to resolve spectral features in a hydrogen-rich atmosphere. They predicted that transmission spectra of hydrogen-rich atmospheres would be dominated by water and methane features. In contrast, they predicted that hydrogen-poor atmospheres would likely result in flat spectra due to the high mean molecular weight of such atmospheres. Although measurement of a flat spectrum would rule out a cloud-free hydrogen rich atmosphere, a flat spectrum could also result from a hydrogen-rich atmosphere with aerosols extending into the upper layers.

On the observational front, [Bean et al. \(2010\)](#) published the first GJ1214b transmission spectrum, which was produced from ground-based observations and spanned wavelengths from 780 to 1000 nm. The featureless spectrum ruled out

a cloud-free hydrogen-dominated atmosphere at 4.9σ -confidence. However, [Bean et al. \(2010\)](#) were unable to rule out a high mean molecular weight water vapor atmosphere. Several additional observational studies of GJ1214b were unable to decisively distinguish between either a hydrogen-dominated cloudy atmosphere or a high mean molecular weight atmosphere ([Bean et al., 2011](#); [Berta et al., 2012](#); [Désert et al., 2011](#); [Fraine et al., 2013](#)). Finally, [Kreidberg et al. \(2014a\)](#) used the HST/WFC3 G141 grism (1.1 to 1.7 μm) in spatial scan mode (see §1.3.3) to produce a featureless transmission spectrum with enough precision to detect any extant spectral features in a high mean molecular weight atmosphere. They produced this high signal-to-noise spectrum by combining observations of 12 transits. [Kreidberg et al. \(2014a\)](#) ruled out high mean molecular weight atmospheres composed of water, methane, carbon monoxide, nitrogen, or carbon dioxide to greater than $5\text{-}\sigma$ confidence, thus determining that GJ1214b’s atmosphere must contain aerosols.

In subsequent years, other astronomers have employed the HST/WFC3 G141 grism in spatial scan mode, sometimes combined with other space-based platforms, to produce transmission spectra for $R_{\text{pl}} < 4R_{\oplus}$ planets. [Knutson et al. \(2014\)](#) observed the Super-Earth HD 97658b ($R_{\text{pl}} = 2.4R_{\oplus}$, $R_{*} = 0.74R_{\odot}$, host star $T_{\text{eff}} = 5175$ K and spectral type K1), and ruled out a cloud-free solar metallicity atmosphere at the $10\text{-}\sigma$ level. [Tsiaras et al. \(2016\)](#) measured the transmission spectrum for the hot ($T_{\text{eq}} \sim 2000$ K) super-Earth 55 Cancri e ($R_{\text{pl}} = 1.91R_{\oplus}$, $R_{*} = 0.943R_{\odot}$, host star $T_{\text{eff}} = 5196$ K and spectral type G8V), and determined that the data were consistent with a hydrogen-rich atmosphere with $\text{C/O} = 1.1$. [de Wit et al. \(2018\)](#) observed TRAPPIST-1d, e, f, and g—the four TRAPPIST-1 planets within

or near the system’s habitable zone. Their analysis ruled out cloud-free, hydrogen-dominated atmospheres for TRAPPIST-1d, e, and f at confidence levels of 8, 6, and 4- σ , respectively. [Wakeford et al. \(2019\)](#) analyzed new HST/WFC3 data from an additional transit combined with previous data from [de Wit et al. \(2018\)](#) and were able to rule out a clear, solar H₂/He-dominated atmosphere on TRAPPIST-1g at greater than 3- σ confidence. [Benneke et al. \(2019\)](#) combined HST observations with Spitzer IRAC and K2 observations to detect water vapor and the likely presence of liquid and icy water clouds in the $2.6R_{\oplus}$ habitable-zone ($T_{\text{eq}} \sim 255$ K) planet K2-18b. The planet orbits a small, cool ($R_* = 0.45R_{\odot}$, $T_{\text{eff}} = 3457$ K, spectral type M3V) and bright host star, thus increasing the size of its spectral features. [Tsiaras et al. \(2019a,b\)](#) analyzed the same HST/WFC3 data and also reported finding water in the atmosphere of K2-18b, by making use of their publicly available WFC3 data reduction ([Tsiaras et al., 2018](#)) and atmospheric retrieval ([Waldmann et al., 2015](#)) codes. Recently, [Edwards et al. \(2021\)](#) reported a tentative water detection in the atmosphere of the $1.7R_{\oplus}$, rocky ($\rho_{\text{pl}} = 7.5$ g cm³), habitable zone ($T_{\text{eq}} \sim 235$ K) planet LHS-1140b.

The analysis of $R_{\text{pl}} < 4R_{\oplus}$ planet atmospheres is an evolving field of research. In Chapter 4, I look at the prospects for studying the atmospheres of these fascinating worlds using the higher resolution and broader spectral coverage of the James Webb Space Telescope.

Chapter 2: Supplemental Background Regarding TESS Predicted Planet Yield and Validation using Multi-Color Photometry

2.1 Overview

This Chapter presents supplemental background information to assist in understanding the analyses described in Chapters 3 and 4. The work in both Chapters 3 and 4 relies upon projections of the exoplanets that will be discovered by the Transiting Exoplanet Survey Satellite (TESS). In Section 2.2, I briefly describe various studies that predict the TESS planet yield, and I then quantify some key differences between the two planet yield predictions that I rely upon, those of [Sullivan et al. \(2015\)](#) and [Barclay et al. \(2018\)](#). In Chapter 3, I present a study to predict the ability of the Multi-color Simultaneous Camera for Studying Atmospheres of Transiting Planets (MuSCAT) instrument, as well as the MuSCAT2 instrument, to distinguish *bona fide* exoplanets from blended eclipsing binary (BEB) false positives (Figure 1.6). In Section 2.3, I show the difference between the TESS bandpass and the MuSCAT/MuSCAT2 bandpasses, and I provide insight into how observations using the multiple bandpasses of MuSCAT/MuSCAT2 can allow us to distinguish

false positives.

2.2 TESS Predicted Planet Yields

[Sullivan et al. \(2015\)](#) published the first comprehensive predictions of the planets and astrophysical false positives that TESS would detect. To conduct their analysis, they synthesized the stellar population of observed stars using the TRIdimensional model of the GALaxy, or TRILEGAL ([Girardi et al., 2012](#)). They applied Kepler planet occurrence rates from [Fressin et al. \(2013\)](#) for FGK stars and from [Dressing & Charbonneau \(2015\)](#) for $T_{\text{eff}} < 4000\text{K}$ stars. Finally, they determined whether a planet would be detected using models for the photometric performance and sky coverage of the TESS cameras. [Sullivan et al. \(2015\)](#) supplied a publicly available catalog of planetary system properties based upon their work.

Chapter 4, Sections 4.1 through 4.6, was published as [Louie et al. \(2018\)](#) and relied upon the [Sullivan et al. \(2015\)](#) TESS estimated planet yield. Since publication of [Louie et al. \(2018\)](#), additional teams have reevaluated the TESS estimated planet yield. [Bouma et al. \(2017\)](#) continued the work of [Sullivan et al. \(2015\)](#), using slightly modified versions of the [Sullivan et al. \(2015\)](#) simulation routines to examine six plausible options for a TESS Extended Mission. Notably, [Bouma et al. \(2017\)](#) reported a code error in calculation of dilution due to background stars used by [Sullivan et al. \(2015\)](#). After correcting this error, [Bouma et al. \(2017\)](#) predicted 30% fewer Earth-sized and super-Earth-sized planets than those found by [Sullivan et al. \(2015\)](#) during the TESS primary mission.

Most recently, [Ballard \(2019\)](#) reexamined the number and multiplicity of planets that TESS would find orbiting M-dwarf host stars. They predicted a 1.2-fold increase in the number of planets orbiting M-dwarfs, and they also predicted that TESS would find multiple planets in 20% of the M-dwarf systems.

[Barclay et al. \(2018\)](#) incorporated several improvements upon the [Sullivan et al. \(2015\)](#) simulations that enabled them to more closely replicate the TESS primary mission. They used the actual TESS Input Catalog (TIC) Candidate Target List (CTL, [Stassun et al., 2018](#)), version 6.1, rather than TRILEGAL, to provide the stellar population. The CTL contains 3.8 million stars that the TESS Target Selection Group has deemed most suitable for detection of small planet candidates. As discussed in Section 1.1.2, the TESS mission selected 200,000 target stars to be observed at 2-minute cadence. [Barclay et al. \(2018\)](#) used a realistic selection scheme based on the techniques applied by the TESS Target Selection Group to pick the CTL stars for simulated 2-minute observations. In contrast to other studies of the TESS planet yield ([Ballard, 2019](#); [Bouma et al., 2017](#); [Sullivan et al., 2015](#)), [Barclay et al. \(2018\)](#) limited the number of target stars observed at each ecliptic pole to 6000, which is the maximum possible with the actual flight hardware configuration. In addition, [Barclay et al. \(2018\)](#) limited full frame image (FFI) targets observed at 30-minute cadences to those in the CTL, whereas previous works had employed various cuts based upon stellar magnitudes. Like [Sullivan et al. \(2015\)](#) and [Bouma et al. \(2017\)](#), [Barclay et al. \(2018\)](#) employed Kepler planet occurrence rates from [Fressin et al. \(2013\)](#) and [Dressing & Charbonneau \(2015\)](#).

In Chapter 3, we base our analysis on the [Barclay et al. \(2018\)](#) simulated TESS

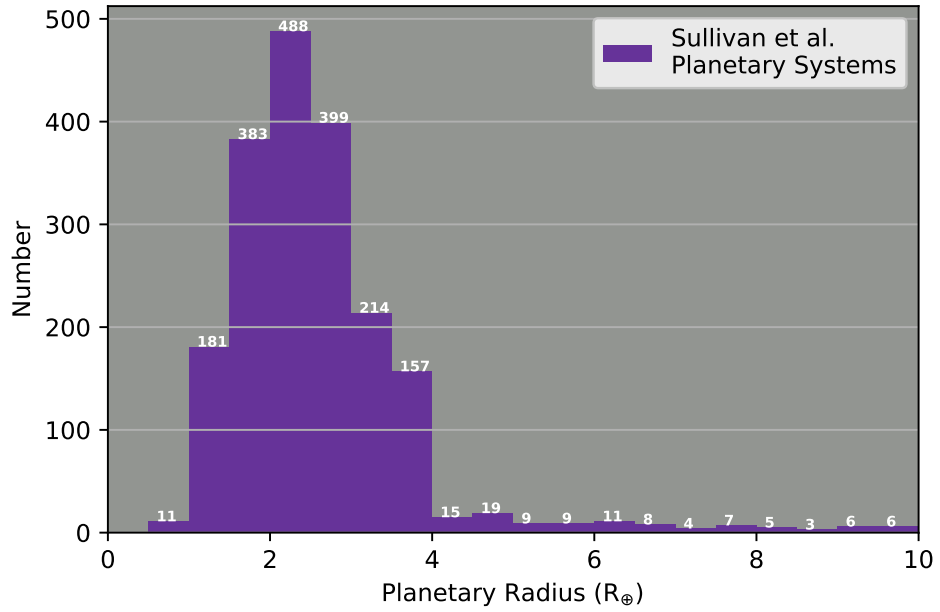
discoveries, since this recent work employs the most realistic scheme to predict the TESS primary mission exoplanet detections. Specifically, we used version 9 of the [Barclay et al. \(2018\)](#) TESS planet yield, which was posted on-line 18 July 2018.¹ Additionally, in Section 4.7, I apply our James Webb Space Telescope (JWST) simulation tool to predict the suitability of [Barclay et al. \(2018\)](#) predicted TESS exoplanet discoveries to atmospheric characterization using JWST.

In the remainder of this section, I produce histograms to illustrate key differences between the versions of the [Sullivan et al. \(2015\)](#) and [Barclay et al. \(2018\)](#) TESS planet catalogs relied upon for the analyses of Chapters 3 and 4. I begin with Figure 2.1, which compares the occurrence rate of TESS planets in various size bins. For the $R_{\text{pl}} \leq 4R_{\oplus}$ planets we look at in Chapters 3 and 4, [Sullivan et al. \(2015\)](#) detect greater numbers of planet in all bins with $R_{\text{pl}} < 3R_{\oplus}$. I refer the reader to [Barclay et al. \(2018\)](#) for a detailed discussion regarding differences between their occurrence rates and those of other studies ([Ballard, 2019](#); [Bouma et al., 2017](#); [Sullivan et al., 2015](#)).

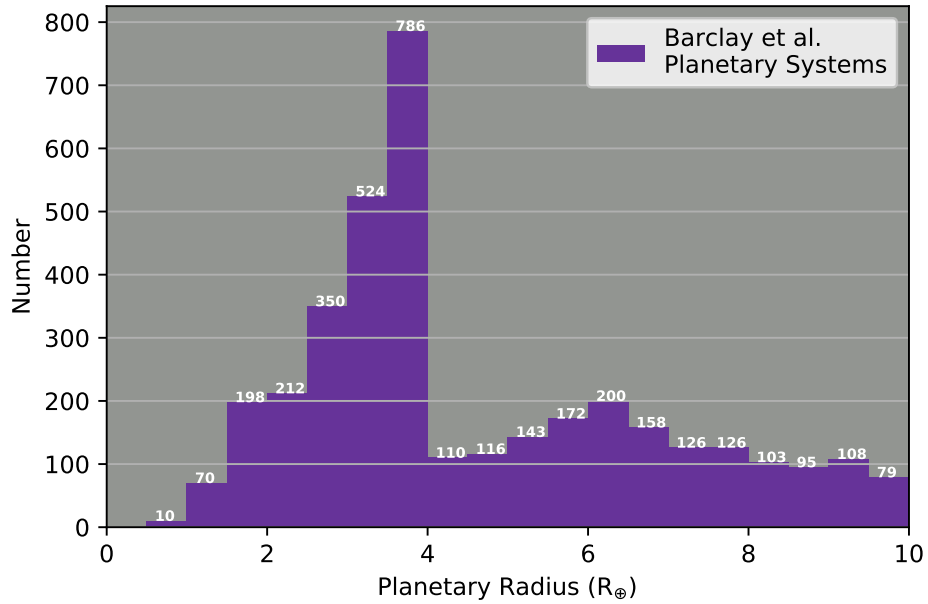
Figure 2.2 compares the J-band magnitude of all [Sullivan et al. \(2015\)](#) and [Barclay et al. \(2018\)](#) TESS discoveries, with various colors indicating the J-band magnitudes of $R_{\text{pl}} \leq 4R_{\oplus}$ and $R_{\text{pl}} \leq 2.5R_{\oplus}$ discoveries. For all bins with J-band magnitudes less than 12, [Barclay et al. \(2018\)](#) detect more planets per bin. Thus, [Barclay et al. \(2018\)](#) detect planets orbiting host stars with brighter J-band magnitudes.

Figure 2.3 illustrates the distribution of J-band magnitudes for $R_{\text{pl}} \leq 2.5R_{\oplus}$

¹https://figshare.com/articles/Planet_and_host_star_properties/6137672.

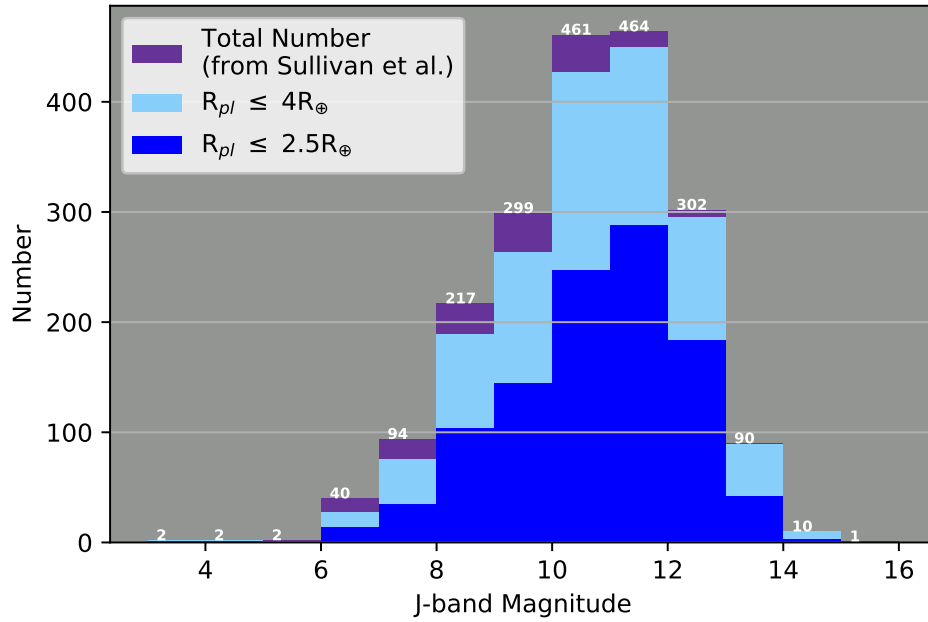


(a)

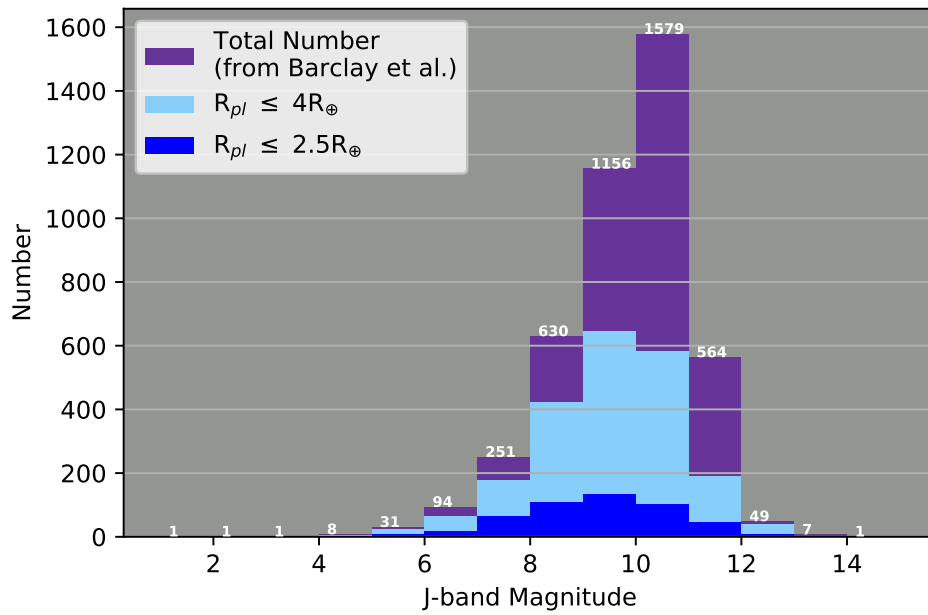


(b)

Figure 2.1: Histograms comparing the (a) Sullivan et al. (2015) and (b) Barclay et al. (2018) TESS planet yields. Notably, Sullivan et al. (2015) detect greater numbers of planet in all bins with $R_{pl} < 3R_{\oplus}$.



(a)



(b)

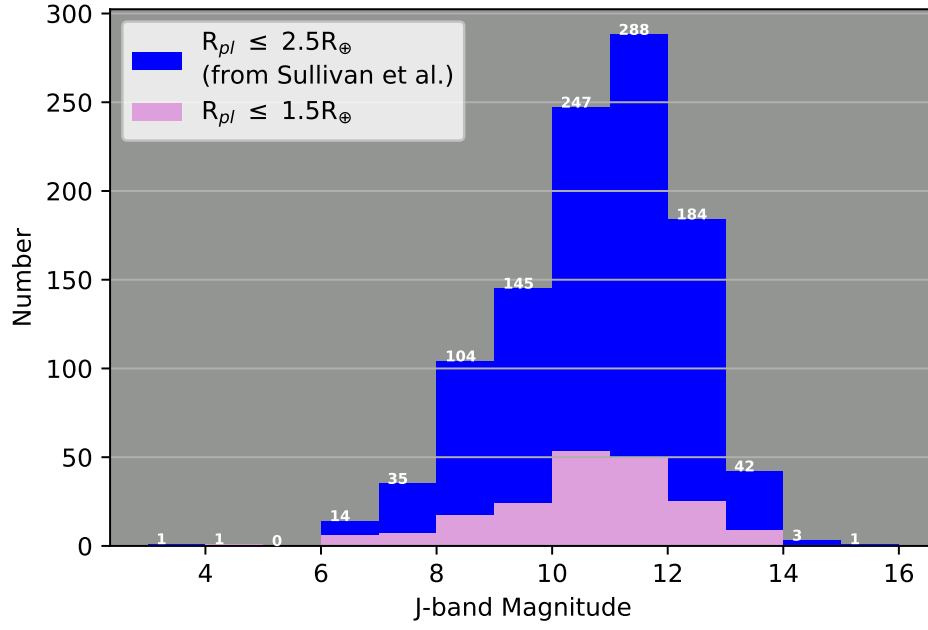
Figure 2.2: Histograms comparing the (a) Sullivan et al. (2015) and (b) Barclay et al. (2018) J-band magnitudes over various radius regimes. In general, Barclay et al. (2018) detect planets orbiting host stars with brighter J-band magnitudes.

planetary systems in the [Sullivan et al. \(2015\)](#) and [Barclay et al. \(2018\)](#) TESS primary mission predictions. Although [Sullivan et al. \(2015\)](#) detect larger numbers of planets in this radius regime, [Barclay et al. \(2018\)](#) report greater numbers of planets orbiting bright host stars (e.g., J-band magnitude ≤ 9).

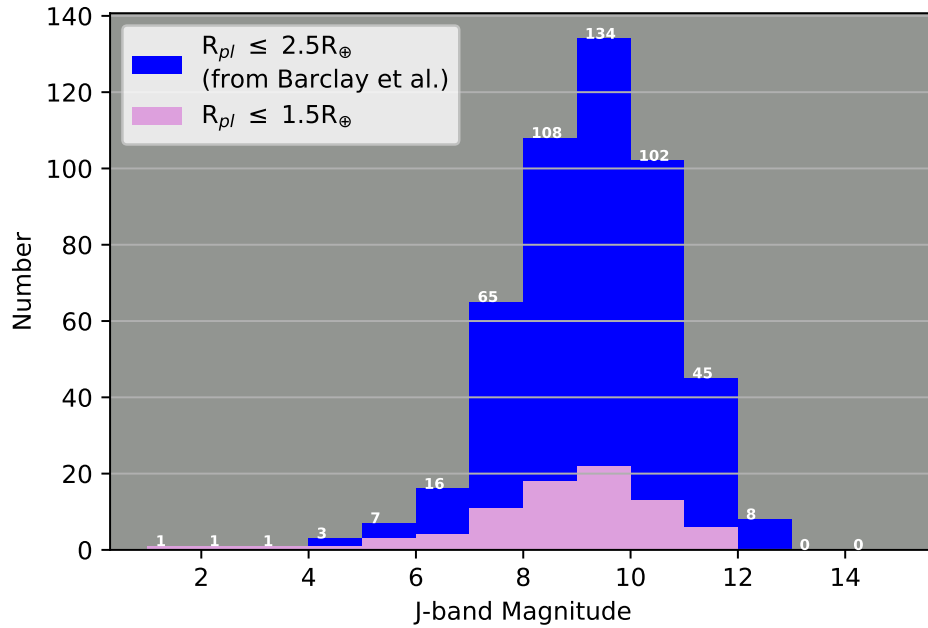
Figures 2.4 and 2.5 show the distribution of stellar temperatures for the [Sullivan et al. \(2015\)](#) and [Barclay et al. \(2018\)](#) TESS primary mission predictions. Figure 2.4 shows all planetary system projections, with colored overplots for planetary systems with $R_{\text{pl}} \leq 4R_{\oplus}$ and $R_{\text{pl}} \leq 2.5R_{\oplus}$ planet discoveries. By far, [Sullivan et al. \(2015\)](#) report a greater number of planets orbiting cool, low mass host stars. Both studies find the majority of $R_{\text{pl}} \leq 1.5R_{\oplus}$ planets orbiting cool, low mass host stars. [Barclay et al. \(2018\)](#) noted that the dearth of planets found orbiting K-dwarfs is a result of selecting fewer K-dwarfs as 2-minute cadence targets. See [Stassun et al. \(2018\)](#) for a comprehensive explanation of the source of the CTL “missing” K-dwarfs.

2.3 Distinguishing False Positives with Multi-Band Photometry

The MuSCAT/MuSCAT2 team members are part of the TESS Follow-up Observing Program, or TFOP, and take part in some of the earliest observations depicted in Figure 1.7. As mentioned in Section 1.1.3, TESS’ large pixel scale of 21 arcsec pixel⁻¹ increases the probability that BEB false positives will be detected, particularly in crowded fields of view. The combination of large pixel scale and crowded field makes it more likely that light from the targeted star will blend with that of a nearby eclipsing binary, separated spatially from the target star by only a

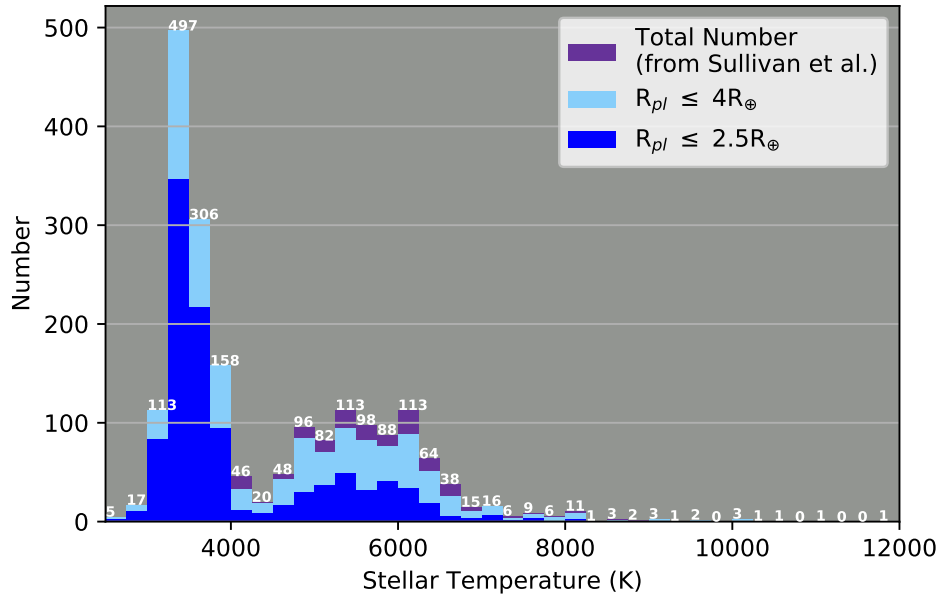


(a)

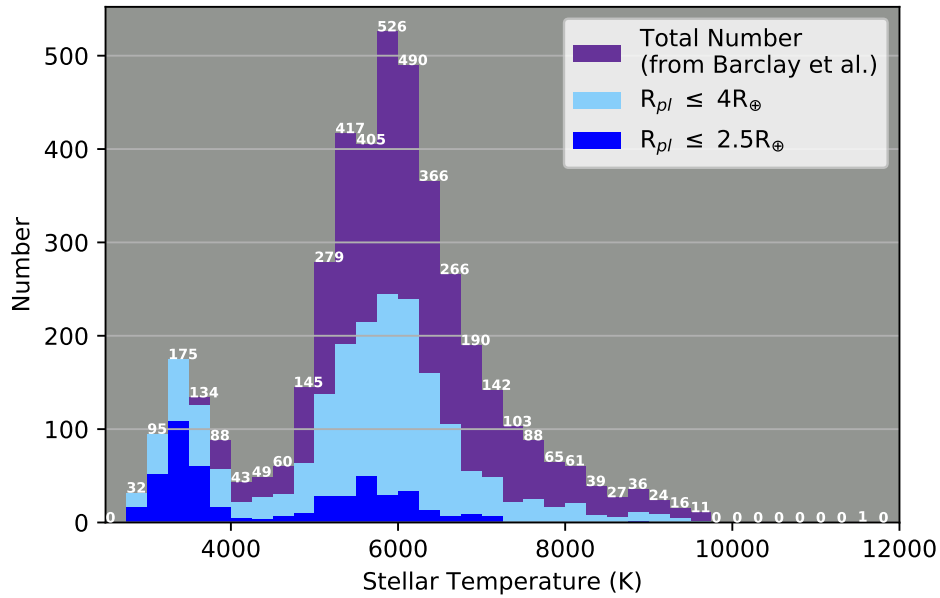


(b)

Figure 2.3: Histograms comparing the (a) Sullivan et al. (2015) and (b) Barclay et al. (2018) J-band magnitudes, showing values only for $R_{pl} \leq 2.5R_{\oplus}$ planets. Although Sullivan et al. (2015) detect larger numbers of planets in this radius regime, Barclay et al. (2018) report greater numbers of planets orbiting bright host stars (e.g., J-band magnitude ≤ 9).

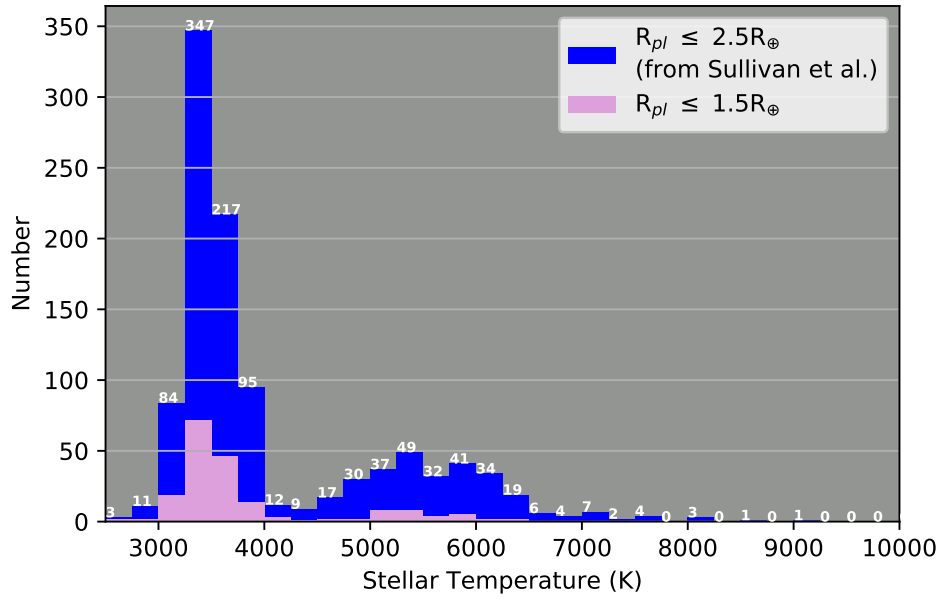


(a)

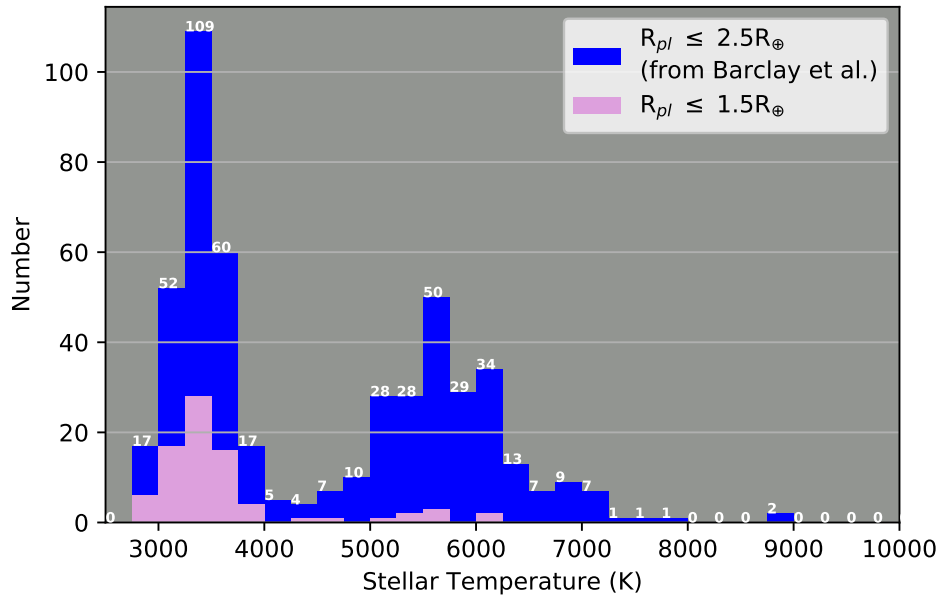


(b)

Figure 2.4: Histograms comparing the (a) Sullivan et al. (2015) and (b) Barclay et al. (2018) host star effective temperatures over various radius regimes. By far, Sullivan et al. (2015) report a greater number of planets orbiting cool, low mass host stars.



(a)



(b)

Figure 2.5: Histograms comparing the (a) Sullivan et al. (2015) and (b) Barclay et al. (2018) host star effective temperatures, showing values only for $R_{pl} \leq 2.5R_{\oplus}$ planets. Both studies find the majority of $R_{pl} \leq 1.5R_{\oplus}$ planets orbiting cool, low mass host stars.

small amount. In this short section, I present a comparison of the TESS and MuSCAT/MuSCAT2 bandpasses, and describe qualitatively how BEB false positives may be distinguished using multi-band simultaneous photometry.

Figure 2.6 compares the TESS bandpass to the MuSCAT2 g, r, i and z_s bandpasses. Note that MuSCAT has only the g, r, and z_s bandpasses. Figure 2.7 depicts blackbody curves at 3 temperatures, with the TESS and MuSCAT2 bandpasses overplotted near the bottom. The blackbody curves may be used to illustrate the concept behind distinguishing false positives using multi-band photometry.² Imagine that the blackbody curves represent stars at three different stellar temperatures, and that the 5000 K blackbody curve is our targeted star. Then, if that $T_{\text{eff}} = 5000$ K star hosts a transiting exoplanet, when the exoplanet transits, the entire stellar curve will dim by the same proportionate amount (R_{pl}^2/R_*^2) at each wavelength. In other words, the exoplanet transit will *not* be wavelength-dependent. However, assume instead that the light from the $T_{\text{eff}} = 5000$ K star is blended with the light from two stars of effective temperatures 4500 K and 3500 K, and assume that the cooler star periodically eclipses (or transits) the 4500 K star. In other words, assume we have a BEB. Thus, if we observe in any of the MuSCAT2 bandpasses, we are observing the integrated light of 3 stars across that bandpass. Whenever the 4500 K star is eclipsed by the cooler star, then only the light from the 4500 K blackbody curve will decrease by a proportional amount. The amount of light we detect (from 3 stars) during eclipse will decrease in each bandpass, and over time we would mea-

²Note that the actual PHOENIX stellar models we use in our analysis of Chapter 3 are much more complicated than blackbody curves, but the same concept applies.

sure something that appears like an exoplanet transit light curve. However, in this case the transit depth that we measure in each of MuSCAT2’s 4 bandpasses *will be* wavelength-dependent. This is because the blackbody curves for each star differ across wavelength—for example they peak at different wavelengths.

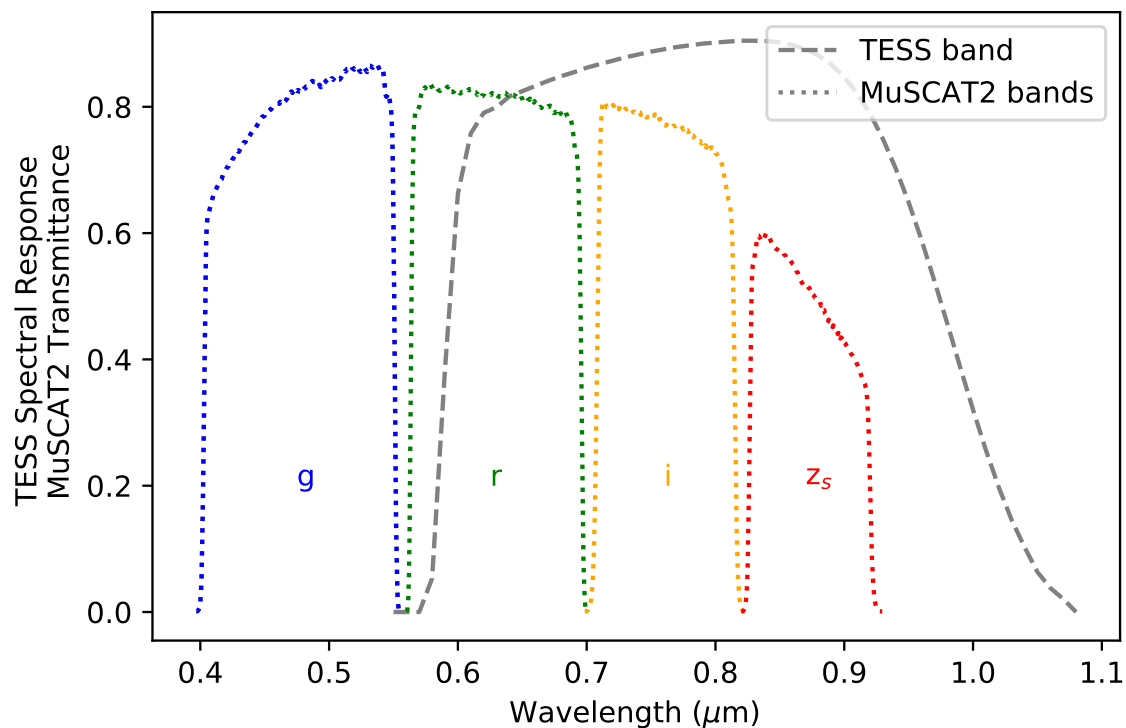


Figure 2.6: Comparison of the TESS Spectral Response curve from [Ricker et al. \(2014\)](#) to the [Narita et al. \(2019\)](#) MuSCAT2 Total Transmittance. While MuSCAT2 employs 4 bandpasses, the MuSCAT instrument only employs the g, r, and z_s bandpasses.

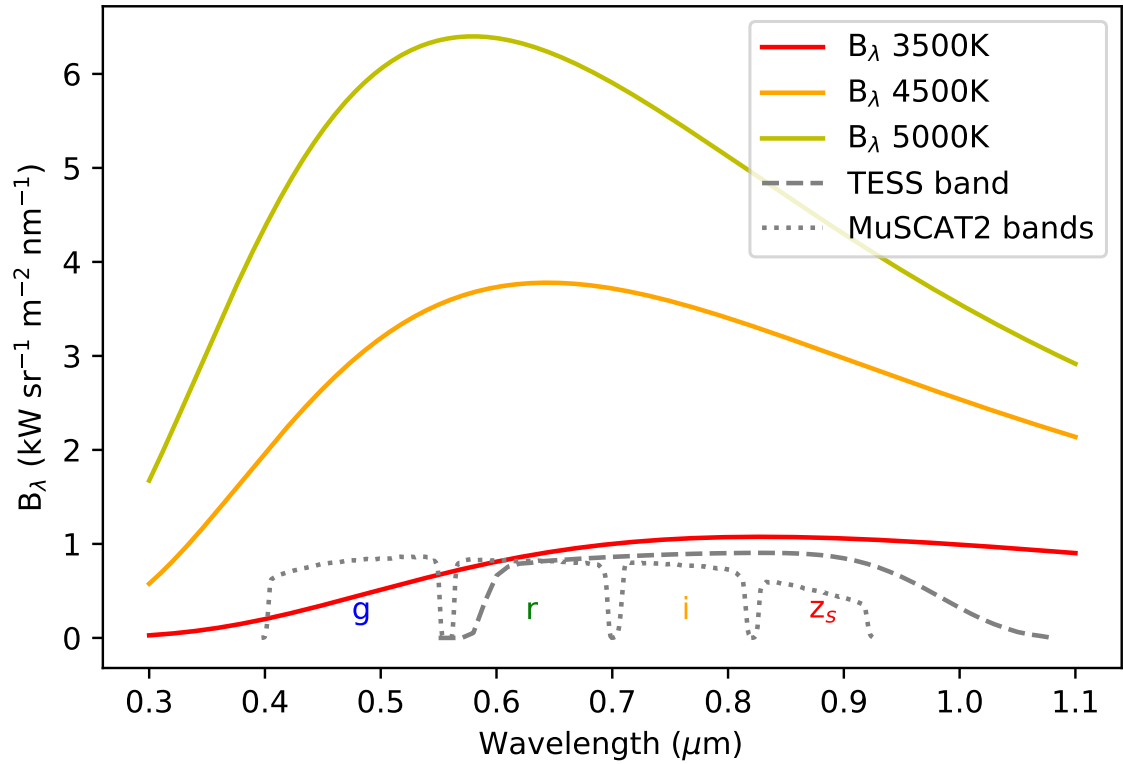


Figure 2.7: Here, we show the blackbody function plotted at three temperatures, overlaying the TESS and MuSCAT2 bandpasses from Figure 2.6. The blackbody curves can be used to approximate the number of photons received from a star at a given effective temperature. Higher values of radiated energy B_λ correspond to a larger number of photons received from a host star.

Chapter 3: Simulations Predicting the Ability of Multi-Color Simultaneous Photometry to Distinguish TESS Candidate Exoplanets from False Positives

3.1 Overview

The Transiting Exoplanet Survey Satellite (TESS) is currently concluding its 2-year primary science mission¹ searching 85% of the sky for transiting exoplanets. TESS has already discovered well over one thousand TESS objects of interest (TOIs), but these candidate exoplanets must be distinguished from astrophysical false positives using other instruments or techniques. The 3-band Multi-color Simultaneous Camera for Studying Atmospheres of Transiting Planets (MuSCAT), as well as the 4-band MuSCAT2, can be used to validate TESS discoveries. Transits of exoplanets are achromatic when observed in multiple bandpasses, while transit depths for false positives often vary with wavelength. We created software tools to simulate MuSCAT/MuSCAT2 TESS follow-up observations and reveal which planet candidates can be efficiently distinguished from blended eclipsing binary (BEB) false positives using these two instruments, and which must be validated using other tech-

¹Since publication of [Louie et al. \(2020\)](#), TESS has completed its primary science mission.

niques. We applied our software code to the Barclay et al. (2018) predicted TESS discoveries, as well as to TOIs downloaded from the ExoFOP-TESS website. We estimate that MuSCAT (MuSCAT2 values in parentheses) will be able to use its multi-color capabilities to distinguish BEB false positives for $\sim 17\%$ ($\sim 18\%$) of all TESS discoveries, and $\sim 13\%$ ($\sim 15\%$) of $R_{\text{pl}} < 4R_{\oplus}$ discoveries. Our TOI analysis shows that MuSCAT (MuSCAT2) can distinguish BEB false positives for $\sim 55\%$ ($\sim 52\%$) of TOIs with transit depths greater than 0.001, for $\sim 64\%$ ($\sim 61\%$) of TOIs with transit depths greater than 0.002, and for $\sim 70\%$ ($\sim 68\%$) of TOIs with transit depths greater than 0.003. Our work shows that MuSCAT and MuSCAT2 can validate hundreds of $R_{\text{pl}} < 4R_{\oplus}$ candidate exoplanets, thus supporting the TESS mission in achieving its Level 1 Science Requirement of measuring the masses of 50 exoplanets smaller in size than Neptune. Our software tools will assist scientists as they prioritize and optimize follow-up observations of TESS objects of interest.

3.2 Introduction

The Transiting Exoplanet Survey Satellite (TESS), which launched 18 April 2018, is projected to detect over one thousand transiting exoplanets smaller than Neptune (Barclay et al., 2018; Ricker et al., 2016; Sullivan et al., 2015). However, Sullivan et al. (2015) showed that TESS will also detect several thousand astrophysical false positives, produced by blended light from a target star and eclipsing binary stars in the foreground/background, or bound to the target star. The TESS Follow-Up Observing Program (TFOP)² will facilitate achievement of the TESS Level 1

²<https://tess.mit.edu/followup/>

Science Requirement to measure the masses of 50 exoplanets smaller in size than Neptune. The first step in the TFOP pipeline is to validate candidate exoplanets by distinguishing true exoplanets from astrophysical false positives.

Transiting exoplanets can be distinguished from astrophysical false positives by determining the wavelength/color-dependence of the amount of stellar light received—transiting exoplanets are largely achromatic when observed in different bandpasses (Alonso et al., 2004; Parviainen et al., 2019). Ground-based multiband photometry makes use of this color-dependence to distinguish true exoplanets from astrophysical false positives. The Multi-color Simultaneous Camera for Studying Atmospheres of Transiting Planets, or MuSCAT (Narita et al., 2015), a 3-color multiband photometer used on the National Astronomical Observatory of Japan (NAOJ) 1.88-m telescope at Okayama Astro-Complex (OAC), Japan, is one instrument the exoplanet community uses for TESS validation. The 4-color MuSCAT2 instrument (Narita et al., 2019) installed on the 1.52-m Carlos Sanchez Telescope at Teide Observatory in the Canary Islands also supports TESS validations with more than 200 dedicated observing nights per year.³

Sullivan et al. (2015) analyzed the types of false positives that TESS would detect when observing 200,000 preselected target stars at 2-minute cadences, and they found that TESS would discover 1103 ± 33 eclipsing binary (EB) systems which fall into the following three categories:⁴

1. Eclipsing binaries (EB): the target star is part of a binary system, and it is

³<http://vivaldi.ll.iac.es/OOCC/iac-managed-telescopes/telescopio-carlos-sanchez/muscat2/>

⁴Additional false positives would be discovered from full-frame image data, but Sullivan et al. (2015) only analyzed the 2-minute cadence data.

grazed by eclipses from its companion. For example, a solar type star may be grazed by eclipses from a late M dwarf companion.

2. Hierarchical EB (HEB): the target star is a triple or higher-order system, and one pair of stars eclipses. For example, if the target star is a solar type star, and another solar type star in the system is eclipsed by an M dwarf, the light from the target star will dilute the eclipse depth of the EB, producing a light curve similar to that of a planetary transit of the target star.
3. Blended EB (BEB): the target star blends with an EB in the foreground/background within the photometric aperture of the target star. This case is similar to an HEB, except that here the EB is not gravitationally bound to the target star. Note this may also be referred to as a nearby eclipsing binary (NEB).

[Sullivan et al. \(2015\)](#) examined the possibility of using TESS observation data to distinguish false positives through (1) ellipsoidal variations, (2) secondary eclipses, (3) lengthy ingress and egress durations, or (4) centroid motion of the image on the detector.⁵ They found that these methods provide clues to help distinguish EBs for 98.6% of the EBs and 93.0% of the HEBs. However, roughly one-quarter of the BEBs could not be distinguished from exoplanets using any of these methods, leaving ~ 150 of the false positives indistinguishable from actual exoplanets.

For those cases where TESS observation data cannot distinguish transiting exoplanets from false positives, we turn to ground-based multiband photometry. When a star is observed in a given photometric bandpass, both transiting exoplanets and

⁵See Section 1.1.4 for further details regarding these four situations.

eclipsing binary stars decrease the amount of light received as the planet transits, or as one star of a binary pair eclipses the other star. Transiting exoplanets block a portion of the host star’s light, and thus the decreases in host starlight received do not depend significantly on wavelength. False positives caused by blended light from target stars and eclipsing binaries also produce signals as one star eclipses its binary, but as long as the colors of the stars are significantly different, the signal is much more wavelength dependent (see, e.g., [Colón et al., 2012](#)). This wavelength dependence would be evident by comparing the amount of light received in MuSCAT’s three bandpasses (or in MuSCAT2’s four bandpasses), which collect light over different wavelengths. Notably, the sensitivity of the instrument to a given signal will depend on the physical parameters (e.g. radius, temperature, etc.) of the star(s) and planet being observed. These physical parameters will vary tremendously between TESS planet candidates.

Our goal is to simulate MuSCAT and MuSCAT2 follow-up observations to reveal which planet candidates can be efficiently distinguished from BEB false positives using these instruments. This understanding will allow TFOP working group members to better prioritize and optimize follow-up validations of TESS detections. We also examine our results to determine any common characteristics between those planet candidates that can be validated using MuSCAT and MuSCAT2. In addition, we provide a software tool to assist in planning MuSCAT and MuSCAT2 follow-up observations. The code reads in a list of parameters for several TESS discoveries (e.g. a list of TESS objects of interest (TOIs) released to the community on the

Exoplanet Follow-up Observing Program for TESS (ExoFOP-TESS) website⁶), and predicts the probability that each discovery can be successfully distinguished from BEB false positives using MuSCAT and/or MuSCAT2.

This work presents the results of a computationally simple analysis that can be easily applied to a large sample of TESS candidate exoplanets. Recently, [Parviainen et al. \(2019\)](#) showed that multi-color transit photometry can be used to determine the true radius ratio of an exoplanet candidate to its host star, when the light from the host star blends with unresolved light sources in the photometric aperture. [Parviainen et al. \(2019\)](#)'s work is complementary to our current study since their analysis methods can be applied to any exoplanet candidate after actual observations are taken with MuSCAT or MuSCAT2.

This chapter is organized as follows. In Section 3.3, we describe the simulated TESS exoplanet discoveries and the false positives we use in our analysis, and we explain the design and validation of our MuSCAT and MuSCAT2 simulation tools. In Section 3.4, we present our findings. We summarize in Section 3.5.

3.3 Methods

True exoplanet transits are largely achromatic, but we expect false positives produced by blended eclipsing binary stars (BEBs) to produce different transit depths in the MuSCAT and MuSCAT2 bandpasses. To predict MuSCAT and MuSCAT2 performance, we compare the transit depths we would obtain by observing a large sample of true exoplanets to the transit depths we would obtain in the MuS-

⁶<https://exofop.ipac.caltech.edu/tess/>

CAT and MuSCAT2 bandpasses by observing those same systems as BEB false positives. We then determine the extent to which MuSCAT and MuSCAT2 can discriminate between true exoplanet and BEB transit depths. We use the [Barclay et al. \(2018\)](#) predicted TESS exoplanet discoveries (Section 3.3.1) for our candidate exoplanet sample. In section 3.3.2, we describe those aspects of the MuSCAT and MuSCAT2 instruments incorporated into our simulation tools. We also describe our noise model. We validated our simulation tools by comparing results produced by the simulations to those from observations of actual transiting exoplanets, incorporating a random factor to account for variations in quantities such as atmospheric transmittance and mirror reflectance (Section 3.3.3). We calculate MuSCAT and MuSCAT2 transit depths for BEB false positives as explained in Section 3.3.4, and we determine the extent to which MuSCAT and MuSCAT2 can discriminate these BEBs using the criterion presented in Section 3.3.5. Finally, we applied our tools to TESS objects of interest (TOIs), as posted to the ExoFOP-TESS website. Figure 3.1 shows a block diagram of our simulation routine.

3.3.1 Predicted TESS Exoplanet Discoveries

[Barclay et al. \(2018\)](#) used Monte Carlo methods to predict the properties of the exoplanets that TESS is likely to discover, and published a machine-readable file containing the properties of their 4,373 predicted planetary systems.⁷ [Barclay et al. \(2018\)](#) used stars in the TESS Input Catalog (TIC) Candidate Target List (CTL) ([Stassun et al., 2019](#)), employing Monte Carlo techniques to assign planets to the

⁷<https://iopscience.iop.org/article/10.3847/1538-4365/aae3e9/meta#apjsaae3e9t2>

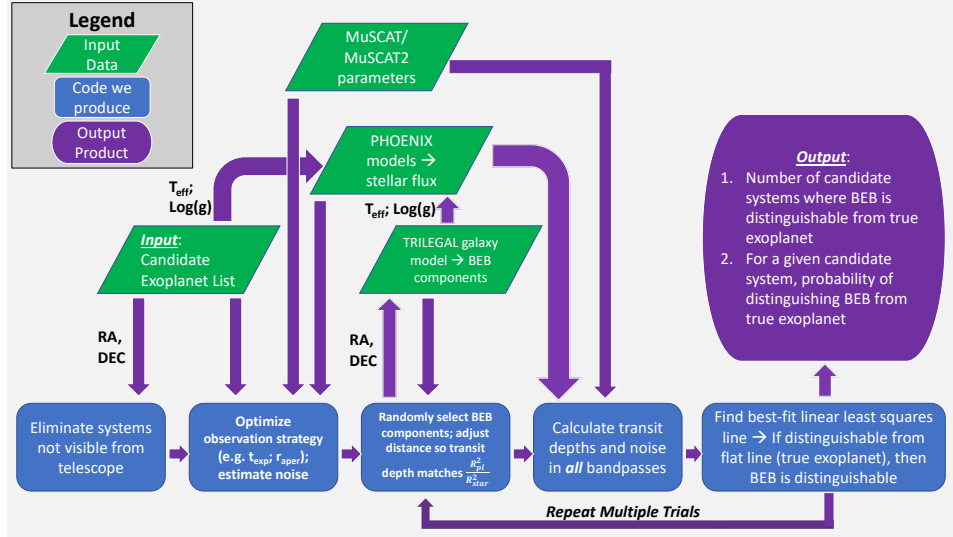


Figure 3.1: Block diagram outlining the major components of our MuSCAT and MuSCAT2 simulation tools.

stars and determine how many of the planets TESS would detect. They adopted Kepler planet occurrence rates from [Fressin et al. \(2013\)](#) for AFGK stars, and from [Dressing & Charbonneau \(2015\)](#) for M stars. The predicted planet yield includes discoveries orbiting both pre-selected target stars viewed at 2-minute cadence, as well as stars viewed in full-frame images at 30-minute cadence.

Our simulations use the parameters in the [Barclay et al. \(2018\)](#) machine-readable file as inputs. For example, we determine whether a given system is observable from either Okayama Astro-Complex (OAC) or Teide Observatory using the system’s right ascension and declination. To calculate stellar flux emanating from the system, we use reported values of stellar effective temperature and $\log(g)$ (calculated from radius and mass) to select an appropriate PHOENIX stellar model, and we then use reported TESS-band magnitude to scale the PHOENIX model. We

calculate transit depth using the radii of the planet and star. Note that we ignore limb darkening in the transit depth calculation, but we deal with a large range of transit depths across our planetary candidates, and the effects of limb darkening are relatively small compared to other aspects of our simulation.

3.3.2 MuSCAT and MuSCAT2 Simulation Tools

Our simulation tools incorporate several components. First, we use PHOENIX stellar spectra to estimate the light received across each bandpass for a given star. In addition, we include important details regarding MuSCAT⁸ (Narita et al., 2015) and MuSCAT2⁹ (Narita et al., 2019) into our simulations, such as geographic location, telescope aperture, and throughput. We also make assumptions about observational selections such as exposure times and telescope defocusing based upon experience. In this section, we describe each aspect of our code in detail, working from the targeted star to the instrument array in our description.

PHOENIX/BT-NextGen and PHOENIX/BT-Settl stellar emission spectrum grids (Allard et al., 2012) provide stellar flux across the wavelength regimes of both the MuSCAT and MuSCAT2 instruments. We employ PHOENIX stellar models for the target star, as well as the primary and secondary components of BEBs. Our simulation routine selects the stellar model with effective temperature and $\log(g)$ values closest to those of the particular star(s) in the system we are modeling. We employ solar metallicity spectra. Louie et al. (2018) provide further details about

⁸<http://espro.mtk.nao.ac.jp/MuSCAT/observing.html>

⁹<http://vivaldi.ll.iac.es/00CC/iac-managed-telescopes/telescopio-carlos-sanchez/muscat2/>

the stellar models employed.

The stellar flux ($\text{ergs sec}^{-1} \text{ cm}^{-2} \mu\text{m}^{-1}$) received at Earth is calculated by scaling the PHOENIX stellar model to the star’s TESS-band magnitude. We then convert vacuum wavelengths to wavelengths in air as prescribed by [Morton \(1991\)](#). For each band, MuSCAT throughput¹⁰—which includes reflectances and transmittances of the dichroic mirrors, broadband anti-reflection coating on the CCD windows, filters, and quantum efficiencies of the CCDs—is provided in increments of 10 nanometers. MuSCAT2 throughput is provided in increments of 0.5 nanometers. Before applying the throughput to the PHOENIX stellar model, we smooth the stellar model with a Gaussian to produce a spectrum with resolution matching that of the throughput. As we split the PHOENIX model light into the three bandpasses of MuSCAT, or the four bandpasses of MuSCAT2, we also apply factors for atmospheric transmittance, as well as throughput of mirrors M1 and M2 on the telescopes, as reported by [Narita et al. \(2015, 2019\)](#). Next, we multiply by the telescope area to produce an output flux across each bandpass in $\text{ergs sec}^{-1} \mu\text{m}^{-1}$. Finally, we convert this to a photon flux across each bandpass (photons sec^{-1}) by dividing by the energy per photon $h\nu$, where h is Planck’s constant and ν is the frequency of the photon, and then numerically integrating with respect to wavelength across each bandpass.

We use the right ascension and declination of the target star to determine whether the system can be observed using MuSCAT or MuSCAT2. The OAC 188-cm telescope is located at a latitude of $34^\circ 34' 37.47''$ North. MuSCAT is unable to

¹⁰http://esppro.mtk.nao.ac.jp/MuSCAT/TM_MuSCAT.dat

observe at declinations greater than 75 degrees. We calculate the fraction of TESS discoveries visible from OAC by assuming that we wish to view through an airmass of 2 or less, which equates to 60 degrees from zenith. For simplicity, we assume that we view all targeted systems as they cross the meridian, so that only the declination angle enters into our calculation. Thus, TESS discoveries with declination angles between -25.42 degrees South and +75 degrees North should be visible during some portion of the calendar year.

We perform a similar calculation for MuSCAT2. The Carlos Sanchez Telescope is located at latitude 28° 18' 01.8" North and has physical limits of +64.55° North and -36° South. Assuming an airmass limit of 2 and that all targeted systems are observed as they cross the meridian, we determine that TESS discoveries with declination angles between -31.70 degrees South and +64.55 degrees North should be visible using MuSCAT2.

Noise associated with our observations originates from multiple sources. In our simulations, we model photon noise from the target star, BEB component stars (false positives only), and sky background, as well as scintillation noise, read noise, and comparison star noise.

We calculate photon noise for the target star and BEB component stars using

$$N_{\text{star}} = \sqrt{F_{\text{star}} t_{\text{exp}}}, \quad (3.1)$$

where F_{star} is the photon flux (photons sec^{-1}) received in a given bandpass from the

star, and t_{exp} is the exposure time in seconds.

We estimate MuSCAT sky background by using the noise values reported for a moonless night by [Narita et al. \(2015\)](#) during MuSCAT first light observations. Specifically, we use 19.9 mag arcsec⁻², 19.5 mag arcsec⁻², and 18.7 mag arcsec⁻² for the g'_2 , r'_2 , and z'_{s2} bands, respectively. We then apply the MuSCAT pixel scale, a Sloan filter conversion tool,¹¹ and the bandpass effective wavelengths and widths reported by [Bessell \(2005\)](#) to convert mag arcsec⁻² in the MuSCAT bandpasses to an electron noise count per square pixel, n_{sky} , which varies with the exposure time duration. Sky background noise for a given exposure depends upon the photometric aperture on the CCD over which the photons are spread. We calculate sky background noise for an exposure using (e.g., [Chromey, 2010](#))

$$N_{\text{sky}} = \sqrt{n_{\text{sky}} \pi r_{\text{aper}}^2}, \quad (3.2)$$

where r_{aper} is the radius of the photometric aperture in pixels.

We calculate sky background for MuSCAT2 using the same methods, but for MuSCAT2 we use the noise values reported for a moonless night by [Narita et al. \(2019\)](#), which are 20.4 mag arcsec⁻², 19.8 mag arcsec⁻², 19.0 mag arcsec⁻², and 18.2 mag arcsec⁻² for g , r , i , and z_s bands, respectively.

We calculate scintillation noise using the method described by [Young \(1967\)](#) and by [Dravins et al. \(1998\)](#), which is given by

¹¹<https://www.gemini.edu/sciops/instruments/midir-resources/imaging-calibrations/fluxmagnitude-conversion>

$$N_{\text{scin}} = 0.064D^{-2/3}(\sec Z)^{7/4}e^{-h/h_o}t_{\text{exp}}^{-1/2}F_{\text{star}}t_{\text{exp}}, \quad (3.3)$$

where D is the diameter of the primary telescope mirror in cm, Z is the local zenith angle of the target star, h is the elevation of the telescope above sea level (372 meters at Okayama Astro-Complex, Japan, and 2,387 meters at Teide Observatory in the Canary Islands), and $h_o = 8000$ meters is a constant. We use the zenith angle calculated as the target star crosses the meridian.

Read noise varies with MuSCAT bandpass and also depends upon whether fast readout time (0.58 sec) or slow readout time (10 sec) is selected.¹² For this study, we assume all observations are conducted using a fast readout time, which results in MuSCAT read noise per square pixel n_{read} of 11, 12, and 12 electrons for the g'_2 , r'_2 , and z'_{s2} bands, respectively. Similarly, MuSCAT2 read noise per square pixel for fast readout times are 12.35, 11.51, 13.13, and 12.56 electrons for the g , r , i , and z_s bands, respectively. Like sky background noise, read noise for a given exposure depends upon the photometric aperture. We calculate read noise for an exposure using

$$N_{\text{read}} = \sqrt{n_{\text{read}}\pi r_{\text{aper}}^2}. \quad (3.4)$$

Observational experience has shown that bright comparison stars are not al-

¹²<http://espro.mtk.nao.ac.jp/MuSCAT/observing.html>

ways available within the MuSCAT/MuSCAT2 fields of view,¹³ so that comparison stars are a non-negligible noise source.¹⁴ However, the actual comparison stars that will be available for any given candidate exoplanet observation are difficult to predict in advance.

We incorporate comparison star noise into our results by scaling comparison star noise (N_{comp}) recorded during past observations of WASP-12 (Narita et al., 2015, 2019) to the Barclay et al. (2018) and TOI systems. Although our computations using WASP-12 are likely to vary from the true comparison star noise for any given stellar system, we note that our analysis applied to all systems as a whole provides a reasonable estimate of the effects of comparison star noise on our results. This is because the V-band magnitude of WASP-12 is 11.57, and the median V-band magnitude of all Barclay et al. (2018) TESS predicted exoplanets is 11.69. Thus, the brightness of WASP-12 roughly corresponds to the median brightness of the Barclay et al. (2018) exoplanet systems. For stars that are dimmer than WASP-12, we will likely find more bright comparison stars available for relative photometry, such that comparison star noise will have a lesser effect on the results. However, for stars that are brighter than WASP-12, we will likely find fewer bright comparison stars available, so that comparison star noise will have a greater effect on results.

Finally, we determine the overall effect of these noise sources on our measurement of transit depth in each bandpass. To do so, we estimate the noise from all

¹³The MuSCAT field of view is 6.1×6.1 arcmin,² while that of MuSCAT2 is 7.4×7.4 arcmin.²

¹⁴We analyzed the sensitivity of our results to comparison star noise by calculating results both with and without this noise source. For MuSCAT (MuSCAT2 values in parentheses), we estimate that including comparison star noise decreases the number of candidate exoplanets that can be distinguished from BEB false positives by $\sim 3\%$ ($\sim 2\%$) for all candidate exoplanets, and by $\sim 2\%$ ($\sim 1\%$) for $R_{\text{pl}} < 4R_{\oplus}$ candidate exoplanets.

sources for a single mid-transit exposure. We add the stellar photon, sky background, scintillation, and read noise in quadrature, and then divide by total number of photons received from all stars (targeted star and BEB component stars, if applicable) in one exposure to calculate σ_1 , the error associated with the aforementioned noise sources. We then add $\sigma_{\text{comp}} = 1/\sqrt{N_{\text{comp}}}$ to σ_1 in quadrature to compute our total estimated error, σ_{total} .

Our total noise calculation depends upon exposure times. During actual observations of bright stars, stellar flux is defocused across a larger number of pixels to allow for longer exposure times while still remaining within the linear response regime of the CCD pixels. Defocusing stellar light also mitigates adverse effects on observations such as scintillation, changing atmospheric conditions, telescope tracking errors and flat-fielding errors (Southworth et al., 2009).

Our simulation tool includes an algorithm to optimize telescope defocusing and exposure time for observations of a given system. We limit exposure times in each band to values between 5 and 60 seconds, and we limit the radius used for telescope defocusing, r_{aper} , to values between 3 and 21 pixels for MuSCAT, and to values between 2 and 18 pixels for MuSCAT2. Our choice of minimum defocusing aperture is motivated by the typical seeing conditions, which are 1.5" at Okayama Astro-Complex, Japan, and 0.8" at Teide Observatory in the Canary Islands. The maximum aperture radius corresponds to $\sim 15''$, above which the stellar point spread function becomes asymmetric so that further defocusing is no longer effective.

The defocusing algorithm selects the combination of exposure time and r_{aper}

that maintains CCD response in the linear regime¹⁵ while producing the highest signal-to-noise (S/N) across an entire planetary transit. We calculate S/N using

$$S/N_{\text{transit}} = \text{Transit Depth} \times \frac{\sqrt{m_{\text{exposure}}}}{\sigma_1}. \quad (3.5)$$

Here, m_{exposure} is the number of exposures recorded during the transit, calculated by dividing the transit duration by the exposure cadence. The exposure cadence is equal to the exposure time plus the dead time per exposure, which accounts for the time required to save data into a proper FITS format and add header information to the FITS file. Based upon observational experience, we assume a constant 4 sec dead time for each exposure.

3.3.3 Comparison of Simulation Results to Observations

We compared our output MuSCAT/MuSCAT2 simulation results to actual data from [Fukui et al. \(2016\)](#)'s MuSCAT observations of HAT-P-14b, as well as [Narita et al. \(2019\)](#)'s MuSCAT2 observations of WASP-12b. Initially, our calculations for both target star photons collected and for total noise exceeded those measured during actual observations. However, we modified our simulation routines to incorporate random factors to account for the largest sources of the differences between our calculated results and observed results, which we deemed to be due to fluctuations in atmospheric transmittance and degradation of mirror reflectance.

We note that our initial simulation output results would lead to better photometric

¹⁵The MuSCAT linearity range is <50,000 ADU for <1% non-linearity, while that for MuSCAT2 is <62,000 ADU for <1% non-linearity.

precision, which in turn would bias our results to indicate better ability to distinguish BEB false positives than what would likely be encountered during actual observations. Thus, application of the random factors is designed to maintain the conservative nature of our results. In this section, we describe the development of the uniform distributions from which we draw our random factors, and how the random factors are applied in our code.

For each bandpass of each instrument (MuSCAT or MuSCAT2), we derive a uniform distribution between some minimum value and 1.0 to account for both variations in atmospheric transmittance and degradation of mirror reflectivity. A value of 1.0 on these distributions represents photometric sky conditions soon after mirror recoating and maintenance. Conversely, a value near the minimum on these distributions represents poor atmospheric transmittance, with mirror reflectivity degraded by the maximum amount that we consider.

During a long-term monitoring campaign, [Fukui et al. \(2019\)](#) recorded the night-to-night variations in relative transmittance of the sky for all bands of both MuSCAT and MuSCAT2. We use the recorded values as typical variations in atmospheric transmittance for each site. The data recorded by [Fukui et al. \(2019\)](#) show correlation between bandpasses. For example, if atmospheric transmittance was near 1.0, then that was true of all bandpasses. On the other hand, if the transmittance was near the minimum or near some mid-range value, then that was true of all bandpasses as well.

Telescope mirror reflectance has been shown to degrade due to chemical reactions and physical effects (e.g., [Abril-Abril et al., 2016](#); [Holzlöhner et al., 2018](#);

Okita et al., 2019). Mirror recoating and cleaning can offset this degradation, but overall reflectivity has been shown to vary by over 10 percent in the course of a year (Abril-Abril et al., 2016). In our simulations, we assume that reflectivity will degrade by as much as 15%.

We create each uniform distribution by taking the variations in atmospheric transmittance found by Fukui et al. (2019), and decreasing the minimum values by 0.15 to account for reflectivity degradation. For example, Fukui et al. (2019) found that MuSCAT r-band atmospheric transmittance varies between 0.65 to 1.0. Decreasing the minimum value on this distribution by 0.15 to account for mirror degradation, we use a uniform distribution from 0.50 to 1.0 for MuSCAT r-band. Similarly, Fukui et al. (2019) found that MuSCAT2 r-band atmospheric transmittance varies between 0.76 and 1.0. Decreasing the minimum value on this distribution by 0.15 to account for mirror degradation, we use a uniform distribution from 0.61 to 1.0 for MuSCAT2 r-band.

For each trial of our simulation for a given instrument (MuSCAT or MuSCAT2), we draw a random number on a uniform distribution from 0 to 1, $n_{r,0-1}$. We draw a unique random number for each Barclay et al. (2018) or TOI system. Then, for each bandpass of the instrument, we calculate a random factor using

$$f_{r,\text{band}} = v_{\text{min},\text{band}} + n_{r,0-1} \times (v_{\text{max},\text{band}} - v_{\text{min},\text{band}}), \quad (3.6)$$

where $f_{r,\text{band}}$ is the random factor derived for a given bandpass, and $v_{\text{min},\text{band}}$ and $v_{\text{max},\text{band}}$ are the minimum and maximum values of the uniform distributions cre-

ated for the corresponding bandpass. Equation 3.6 allows us to model the observed correlation across bandpasses. For each bandpass and for each stellar system, we multiply the corresponding random factor, $f_{r,\text{band}}$, by the number of stellar photons calculated to be collected by the MuSCAT or MuSCAT2 instrument in that bandpass.

We can apply *ad hoc* factors¹⁶ to ensure that our calculations for target star photons collected at the telescope exactly match those of the Fukui et al. (2016) MuSCAT observations of HAT-P-14b and the Narita et al. (2019) MuSCAT2 observations of WASP-12b. The *ad hoc* factors that we select for each instrument all lie within the random uniform distributions developed for the bandpasses of MuSCAT and MuSCAT2. By applying these *ad hoc* factors, our noise calculations for HAT-P-14b also match those of Fukui et al. (2016) to within 3% for every band. For MuSCAT2, our noise calculations match those of Narita et al. (2019) to 7%, 6%, 3%, and <1% for the g , r , i , and z_s bands. This shows that application of random factors drawn from the uniform distributions that we developed are more likely to produce realistic results.

3.3.4 Blended Eclipsing Binary False Positives

We construct false positives for all simulated TESS discoveries in the Barclay et al. (2018) machine-readable file such that the transit depths for both the false positive and the transiting exoplanet are the same in the TESS bandpass. During

¹⁶We call these factors *ad hoc* because they are chosen by design, rather than randomly. However, we select the *ad hoc* factors from the same uniform distributions developed for our random factors.

the actual TESS mission, some *candidate* exoplanets are true exoplanets, while some are false positives that mimic the signal of a transiting exoplanet. Here, we use the [Barclay et al. \(2018\)](#) simulated TESS discoveries as a representative sample of the types of signals that TESS may discover. After creating the false positives, we determine whether MuSCAT and MuSCAT2 can distinguish varying transit depths between bandpasses, as described in Section [3.3.5](#).

To create BEB false positives, we begin by calculating the transit depth for a true exoplanet using the relationship

$$\frac{\Delta F}{F} = \frac{R_{\text{pl}}^2}{R_{\text{star}}^2}, \quad (3.7)$$

where ΔF refers to the difference between out-of-transit and mid-transit flux, while R_{pl} and R_{star} refer to the radii of the planet and of the target star, respectively. By calculating the exoplanet transit depth using equation [3.7](#), we inherently assume that the planet emits no flux of its own.

We pick the primary and secondary components of the BEBs from data files of simulated stars downloaded from the TRIdimensional modeL of thE GALaxy, or TRILEGAL ([Girardi et al., 2012](#)). We downloaded selections of TRILEGAL stars¹⁷ at Galactic coordinates with Longitudes of 0, 30, 60, 90, 120, 150, and 180 degrees, and at Latitudes of 0, 30, 60, and 90 degrees. We chose solid angles ranging from 0.0001 deg² to 1 deg², depending upon proximity to the Galactic center. In every case, the data files we downloaded for each Galactic coordinate pair contained

¹⁷<http://stev.oapd.inaf.it/cgi-bin/trilegal>

selections of over 10,000 stars. We assume symmetry in the Galactic coordinates, and then choose BEB components from the TRILEGAL data file corresponding to Galactic coordinates closest to those of the target star under consideration. The TRILEGAL data files include important parameters for the stars, such as masses, $\log(g)$, effective temperatures, distances, and TESS-band apparent magnitudes.

We choose the primary BEB component such that the star lies on the main sequence, and so that its apparent magnitude is greater than that of the target star apparent magnitude (i.e. the primary BEB component is fainter than the target star). We randomly pick the primary BEB component from the appropriate TRILEGAL data file, making our selection from stars with maximum and minimum TESS-band apparent magnitudes between the values of

$$m_{\text{BEB,pri,max}} = m_{\text{star}} - 2.5 \log \left(\frac{R_{\text{pl}}^2}{R_{\text{star}}^2} \right), \quad (3.8)$$

and

$$m_{\text{BEB,pri,min}} = m_{\text{star}} - 0.5 \log \left(\frac{R_{\text{pl}}^2}{R_{\text{star}}^2} \right), \quad (3.9)$$

where $m_{\text{BEB,pri,max}}$ and $m_{\text{BEB,pri,min}}$ are our maximum and minimum TESS-band apparent magnitude limits for the BEB primary component, and m_{star} is the target star TESS-band apparent magnitude. Here, the maximum apparent magnitude limit is chosen such that the ratio of the primary component's flux to that of the target star is equal to the transit depth calculated using equation 3.7. We could expect a primary component magnitude near this value if the primary component

star is totally eclipsed during transit (i.e. if primary and secondary components are the same size). Our apparent magnitude selection limits are designed to give us a wide selection of choices for BEB primary components from the TRILEGAL file. The number of choices actually available will depend upon the transit depth in the system under consideration. For most systems, the magnitude cuts provide hundreds of choices for primary BEB component star with masses $\sim 1M_{\odot}$ or less. Even the systems with the largest transit depths (~ 0.1) provide ~ 100 choices for the BEB primary component star.

Following the method of [Grekle-McKeon & Deming \(2019\)](#), we next select the *desired* mass of the secondary component by randomly selecting a mass on a uniform distribution between $0.1M_{\odot}$ to the mass of the primary BEB component. We then pick a star from the TRILEGAL catalog that matches this desired secondary component mass. We note that other authors have used different distributions for the secondary component masses (e.g., [Morton et al., 2016](#)). However, the precise mass function for BEB components is uncertain, and the uniform distribution used here provides a reasonable estimate that is suitable for our purposes.

After the primary and secondary components to the BEB are selected, we calculate the transit depth caused by the BEB system using

$$\frac{\Delta F}{F} = \frac{F_{\text{OOT}} - F_{\text{MT}}}{F_{\text{OOT}}}, \quad (3.10)$$

where F_{OOT} is the out-of-transit flux and F_{MT} is the mid-transit flux. We calculate out-of-transit flux by summing the total flux from the target star and two BEB com-

ponent stars. We calculate mid-transit flux by summing total flux from the target star and BEB secondary star, but we decrease the amount of flux from the BEB primary component star by the factor $R_{\text{BEB,sec}}^2/R_{\text{BEB,pri}}^2$. Note that our method assumes all BEBs are observed edge-on. We adjust the distance to the BEB such that the transit depths calculated using equations 3.7 and 3.10 (in the TESS bandpass) match to within machine accuracy. The adjusted distance is close to that of the original TRILEGAL distance, thus preserving the integrity of the TRILEGAL sample. We then calculate the TESS-band magnitudes of the primary and secondary BEB components corresponding to the newly calculated distance of the BEB, and apply our simulation tools as described in section 3.3.2 to determine the noise produced in the MuSCAT or MuSCAT2 bandpasses for each BEB component star, in addition to that produced by the target star. We compute transit depths in all MuSCAT and MuSCAT2 bandpasses by applying equation 3.10 to our estimated flux (Section 3.3.2) for each bandpass.

3.3.5 Distinguishing BEBs with MuSCAT/MuSCAT2

We use a simple computational model to determine whether MuSCAT/MuSCAT2 can discriminate between a true exoplanet and a BEB false positive. We expect the transit depth for a BEB false positive to vary approximately linearly with wavelength, such that the transit depths in MuSCAT’s 3 bandpasses—or in MuSCAT2’s 4 bandpasses—can be reasonably fit with a straight line. The MuSCAT/MuSCAT2 simulation tools (Section 3.3.2) applied to BEBs (Section 3.3.4) produce estimated

transit depths and noise values, σ_{total} , for each MuSCAT bandpass. For each system, we use the estimated transit depths and noise values to find the best-fit linear least squares line, and then we determine whether that line can be distinguished from a flat line. We would expect the best-fit line to be flat for a true exoplanet if the presence of a planetary atmosphere is neglected. Thus, a non-zero slope in the best-fit line should indicate that the transit depths are those of a BEB false positive.

Mathematically, we find that MuSCAT or MuSCAT2 can discriminate a BEB if

$$|\text{slope}| - 3 \times |\text{slope}_{\text{err}}| > 0, \quad (3.11)$$

where slope is the slope of the line determined by the least squares fit, and $\text{slope}_{\text{err}}$ is the error in that slope. We multiply the slope error by 3 to ensure that the slope of the best-fit line can be clearly distinguished from a flat line.

3.4 Results and Discussion

We applied our MuSCAT and MuSCAT2 simulation tools to the [Barclay et al. \(2018\)](#) predicted TESS planet yield to determine the characteristics of those planetary systems where the two instruments can best distinguish between true exoplanets and BEB false positives (Section 3.4.1). Next, we applied our simulation tools to TESS Objects of Interest (TOIs) posted to the Exoplanet Follow-up Observing Program for TESS (ExoFOP-TESS) website¹⁸ to predict the probabilities

¹⁸<https://exofop.ipac.caltech.edu/tess/> accessed on 16 August 2019

that recent TOIs can be distinguished from BEB false positives using MuSCAT and MuSCAT2 (Section 3.4.2). As discussed in section 3.3.4, our simulation randomly generates BEBs each time the routine is applied to a group of planetary systems, and then adjusts the distance to those BEBs so that the transit depth of each BEB false positive matches that of a true transiting exoplanet in the TESS bandpass. The ability of a given instrument to actually distinguish a false positive for a given system will depend upon the characteristics of the BEB in the system, which is something we will not know *a priori*. In order to account for natural variation in BEB component characteristics and attain statistically robust results, for both the Barclay et al. (2018) planetary systems and the TOIs we report the results attained over 20 trials. We conducted 20 trials to ensure that our reported results do not vary by more than 1% throughout our computed 99% confidence regions (Ross, 2014). As described in section 3.3.5, the criterion we use to determine whether or not MuSCAT or MuSCAT2 can distinguish a true exoplanet from a false positive relies upon determining the best-fit line to the transit depths. For MuSCAT, we found the best-fit line using all bandpasses. For MuSCAT2, we found the best-fit line using the g , r , and z_s bands, since these correspond to the three bandpasses of MuSCAT. Determining the best-fit line using three bandpasses allows more direct comparison of the MuSCAT and MuSCAT2 results.

Figure 3.2 illustrates the criterion that we use to determine whether MuSCAT and MuSCAT2 can distinguish BEB false positives. We show two example cases: one where MuSCAT can distinguish the BEB (Figures 3.2a and 3.2b), and one where it cannot (Figures 3.2c and 3.2d). The system shown in parts (a) and (b) has a transit

depth of ~ 0.00287 in the TESS bandpass, a transit duration of 2.594 hours, and a J-band magnitude of 10.42. The target star radius is $0.517R_{\odot}$. If the transit depth were produced by a true exoplanet, that planet would have a radius of $3.031R_{\oplus}$. We created a BEB by adding a primary component star of mass $0.978M_{\odot}$, and a secondary component star of mass $0.254M_{\odot}$. The system in parts (c) and (d) of the figure has a transit depth of ~ 0.0127 in the TESS bandpass, a transit duration of 4.944 hours, and a J-band magnitude of 10.65. The target star radius is $1.2R_{\odot}$. If the transit depth were produced by a true exoplanet, that planet would have a radius of $4.682R_{\oplus}$. We created a BEB by adding a primary component star of mass $0.439M_{\odot}$, and a secondary component star of mass $0.424M_{\odot}$.

3.4.1 MuSCAT/MuSCAT2 Ability to Distinguish BEBs

We report the ability of MuSCAT and MuSCAT2 to distinguish BEBs for the [Barclay et al. \(2018\)](#) systems in Tables 3.1 and 3.2, respectively. Overall, we find that MuSCAT is able to discriminate BEBs for $\sim 17\%$ of the 2,575 [Barclay et al. \(2018\)](#) systems observable from the Okayama Astro-Complex (OAC), while MuSCAT2 is able to discriminate BEBs for $\sim 18\%$ of the 2,485 systems observable from Teide Observatory. Of the systems visible from OAC, 1,306 have transit depths corresponding to planets with radii less than $4R_{\oplus}$, and MuSCAT would be able to discriminate $\sim 13\%$ of these systems. For MuSCAT2, 1,212 systems have transit depths corresponding to planets with radii less than $4R_{\oplus}$, and MuSCAT2 would be able to distinguish $\sim 15\%$ of these systems.

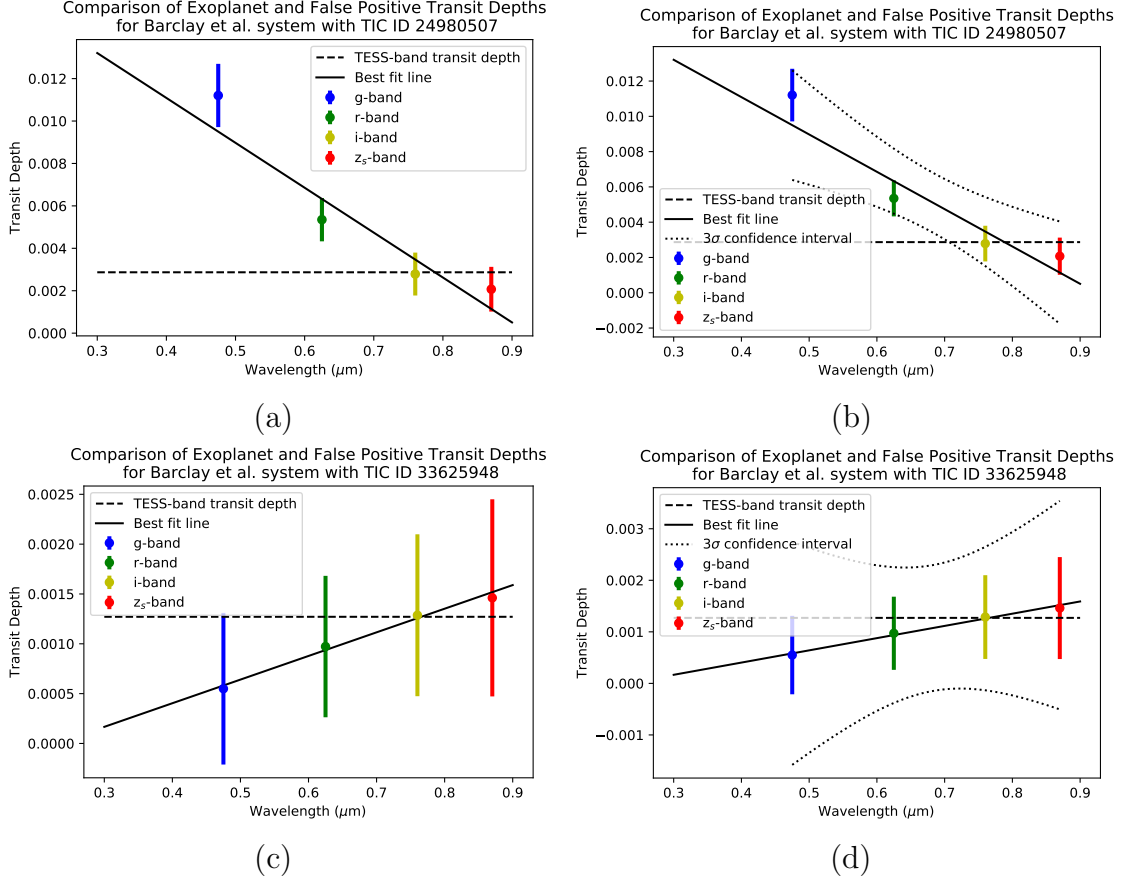


Figure 3.2: Two examples showing estimated transit depth in MuSCAT2’s 4 band-passes for a BEB, as well as the least squares best-fit line to those transit depths. For comparison, the TESS-band transit depths for a true exoplanet are also shown. In panels (b) and (d), we also plot the 3σ hyperbolic confidence bands (Liu et al., 2008) for the best-fit line to help illustrate the criterion we use to determine whether MuSCAT2 can discriminate between a BEB false positive and a true exoplanet. If MuSCAT2 *cannot* distinguish the BEB, then the line for the TESS-band transit depth falls within the hyperbolic confidence band. (Note that our criterion in equation 3.11 is actually much simpler than the hyperbolic confidence bands, which we use here for illustrative purposes only.) In panels (a) and (b), the magnitude of the slope of the best fit line exceeds the 3σ slope error magnitude (equation 3.11), so we determine that MuSCAT2 *can* discriminate the BEB. In panels (c) and (d), MuSCAT2 is *unable* to discriminate the BEB. See text for further details regarding characteristics of these two systems.

	Total	Year 1 Ecliptic South	Year 2 Ecliptic North
Barclay et al. Candidate Exoplanets	4,373	2,196	2,177
Observable from Okayama Astro-Complex ⁱⁱ	2,575 (59%)	539 (25%)	2,036 (94%)
MuSCAT Can Distinguish ⁱⁱⁱ (Total)	426 ± 10 (17%)	98 ± 6 (18%)	329 ± 9 (16%)
MuSCAT Can Distinguish ^{iv} ($R_{\text{pl}} < 4.0R_{\oplus}$)	173 ± 7 (13%)	39 ± 3 (16%)	134 ± 7 (13%)

NOTES:

ⁱWe report the mean number of planets distinguishable over 20 trials, as well as the 99% confidence intervals (Ross, 2014). Each mean is rounded to the nearest whole number of systems, while each confidence interval is rounded up to an integer value.

ⁱⁱWe assume the system is observable if it is visible through 2 airmasses or less at some point during the calendar year. See section 3.3.2 for details. Percentages in parentheses refer to percent of total Barclay et al. candidate exoplanets in first row.

ⁱⁱⁱWe report the mean number MuSCAT can distinguish, plus or minus the 99% confidence intervals over 20 trials. The number in parentheses is the percentage of the total observable (second row) that MuSCAT can distinguish.

^{iv}The number in parentheses is the percentage of observable $R_{\text{pl}} < 4.0R_{\oplus}$ candidate planets (1,306 total) that MuSCAT can distinguish. Note that 243 $R_{\text{pl}} < 4.0R_{\oplus}$ candidates are observable during year 1, and 1,063 candidates are observable during year 2.

Table 3.1: Predicted number of Barclay et al. (2018) systems where MuSCAT can distinguish *bona fide* exoplanets from BEB false positivesⁱ

	Total	Year 1 Ecliptic South	Year 2 Ecliptic North
Barclay et al. Candidate Exoplanets	4,373	2,196	2,177
Observable from Teide Observatory ⁱⁱ	2,485 (57%)	721 (33%)	1,764 (81%)
MuSCAT2 Can Distinguish ⁱⁱⁱ (Total)	456 ± 12 (18%)	142 ± 7 (20%)	314 ± 11 (18%)
MuSCAT2 Can Distinguish ^{iv} ($R_{\text{pl}} < 4.0R_{\oplus}$)	180 ± 8 (15%)	59 ± 5 (18%)	121 ± 6 (14%)

NOTES:

ⁱWe report the mean number of planets distinguishable over 20 trials, as well as the 99% confidence intervals (Ross, 2014). Each mean is rounded to the nearest whole number of systems, while each confidence interval is rounded up to an integer value.

ⁱⁱWe assume the system is observable if it is visible through 2 airmasses or less at some point during the calendar year. See section 3.3.2 for details. Percentages in parentheses refer to percent of total Barclay et al. candidate exoplanets in first row.

ⁱⁱⁱWe report the mean number MuSCAT2 can distinguish, plus or minus the 99% confidence intervals over 20 trials. The number in parentheses is the percentage of the total observable (second row) that MuSCAT2 can distinguish.

^{iv}The number in parentheses is the percentage of observable $R_{\text{pl}} < 4.0R_{\oplus}$ candidate planets (1,212 total) that MuSCAT2 can distinguish. Note that 321 $R_{\text{pl}} < 4.0R_{\oplus}$ candidates are observable during year 1, and 891 candidates are observable during year 2.

Table 3.2: Predicted number of Barclay et al. (2018) systems where MuSCAT2 can distinguish *bona fide* exoplanets from BEB false positivesⁱ

Figures 3.3 and 3.4 show a series of histograms comparing the total number of systems observable from OAC and Teide Observatory to those that would be distinguishable as BEB false positives. Surprisingly, the fraction of systems distinguishable does *not* appear to rise with planetary radius. However, the fraction of distinguishable systems *does* rise with increasing transit depth and with decreasing stellar radius. Indeed, Figures 3.3 and 3.4 indicate that transit depth is the most important indicator of whether or not MuSCAT and MuSCAT2 can distinguish a true exoplanet from a BEB false positive. In addition, panel (d) in both figures illustrates that MuSCAT and MuSCAT2 are very powerful in discriminating BEBs for the smallest host stars (mid-to-late M dwarfs).

We examine transit depth further in Figures 3.5 and 3.6. Here, for each Barclay et al. (2018) system, we plot transit depth versus planetary radius, stellar effective temperature, stellar radius, and TESS-band magnitude. The points correspond to each Barclay et al. system, and are color coded to correspond to the percentage of trials for which that system could be discriminated as a BEB false positive. For example, dark red color coding indicates that a given system could not be distinguished for any trial as a BEB false positive. Conversely, dark blue color coding indicates that a given system could be distinguished as a BEB false positive for 100% of the trials. In general, the figures confirm that transit depth is the most important characteristic in determining whether MuSCAT or MuSCAT2 can distinguish between true exoplanets and false positives. Both instruments are quite effective in distinguishing BEBs for systems with transit depths of 0.003 or greater.

Finally, we note some of the limitations of this study. First, our analysis as-

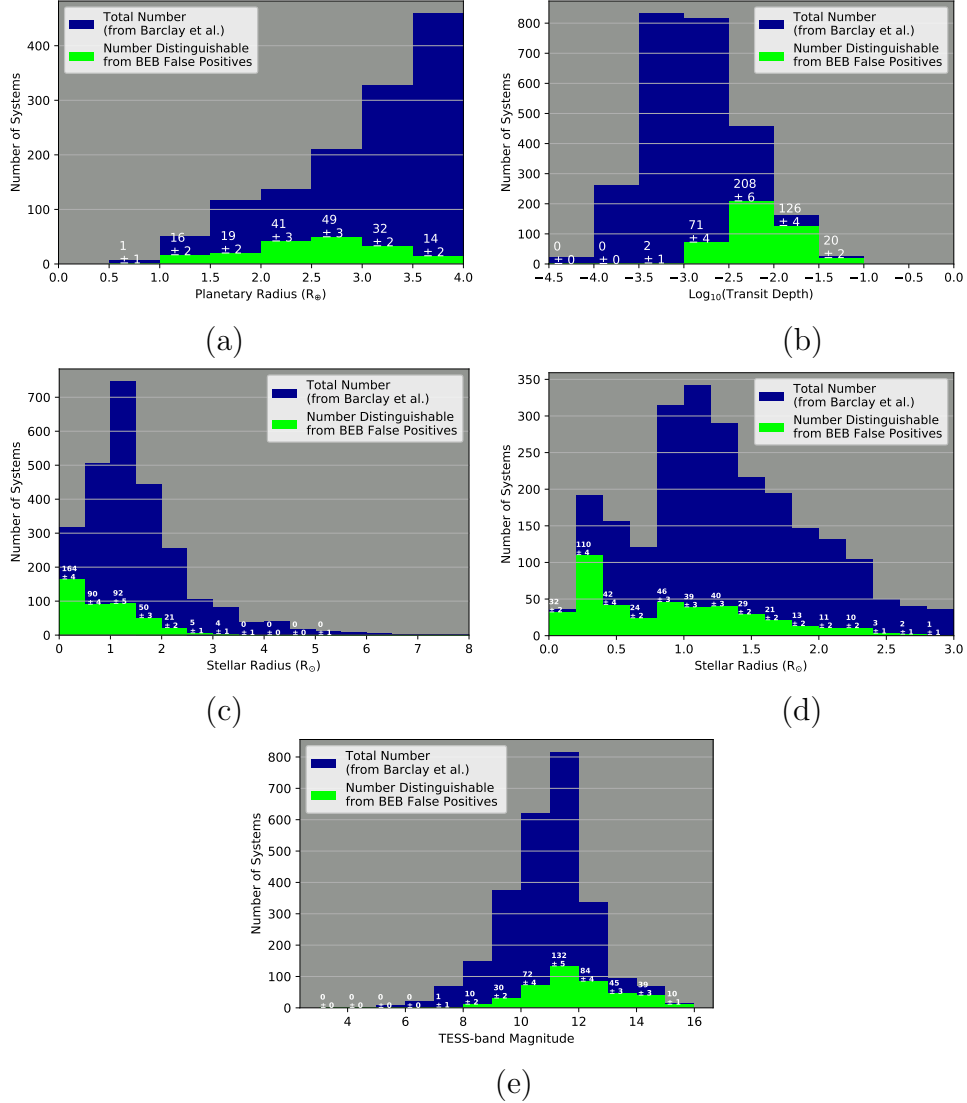


Figure 3.3: Histograms comparing the total number of Barclay et al. (2018) systems visible from Okayama Astro-Complex (2,575 systems) to those that would be distinguishable as BEB false positives using MuSCAT. We plot the number of systems distinguishable over 20 trials versus (a) planetary radius, (b) transit depth, (c) and (d) stellar radius, and (e) TESS-band magnitude. We print the average number of distinguishable systems over 20 trials above each bin. Note that both panels (c) and (d) show the number of systems versus stellar radius, but panel (d) shows this information on a refined grid only for $R_{\text{star}} \leq 3R_{\odot}$. The fraction of systems distinguishable does *not* appear to rise with planetary radius. However, the fraction of distinguishable systems *does* rise with increasing transit depth and with decreasing stellar radius. The large fraction of systems distinguishable at higher values of TESS magnitude is due to the fact that transit depths in general are larger for dimmer TESS detections. For example, the median transit depth for systems visible from Okayama Astro-Complex that have TESS magnitude greater than 13 is 0.00879, while the median transit depth for systems brighter than TESS magnitude 13 is 0.00112.

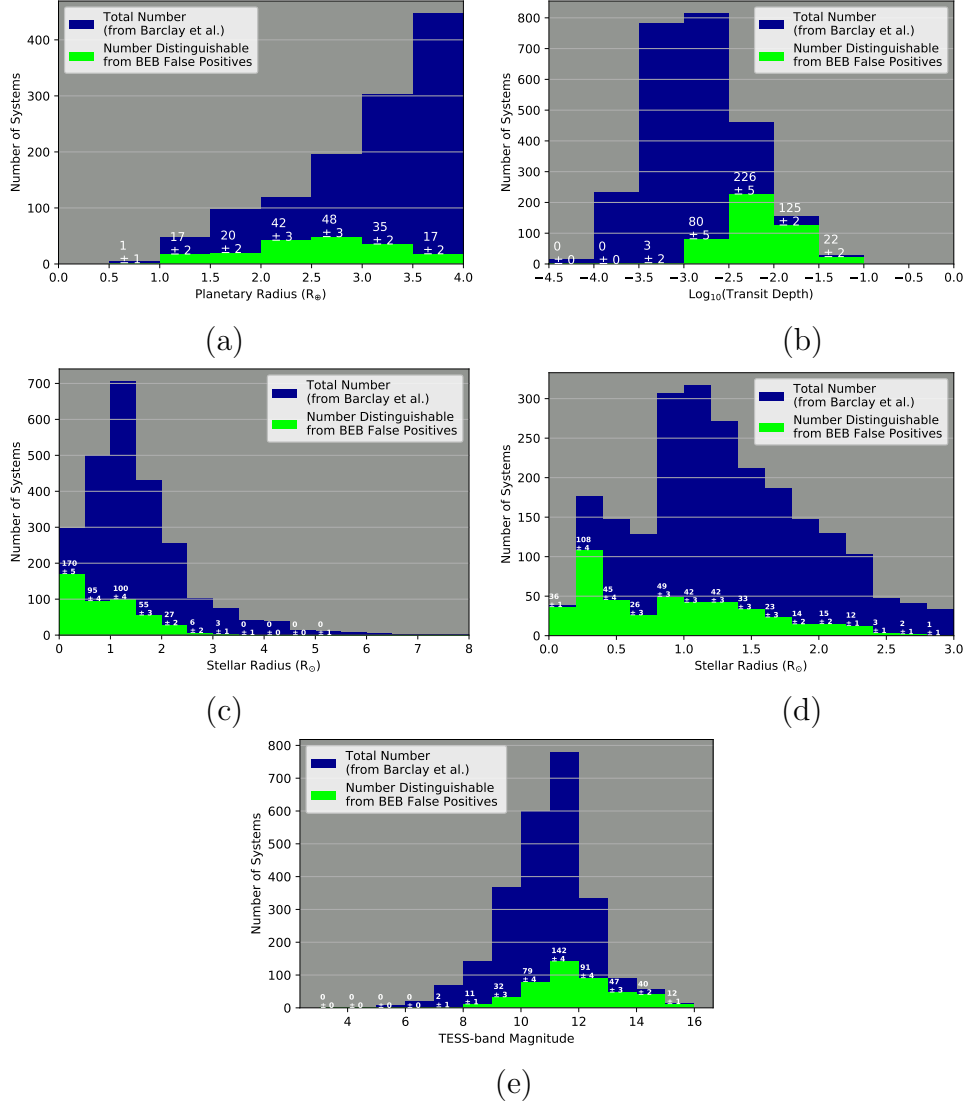


Figure 3.4: Same as Figure 3.3, but for MuSCAT2. Histograms comparing the total number of Barclay et al. (2018) systems visible from Teide Observatory (2,485 systems) to those that would be distinguishable as BEB false positives using MuSCAT2. We plot the number of systems distinguishable over 20 trials versus (a) planetary radius, (b) transit depth, (c) and (d) stellar radius, and (e) TESS-band magnitude. We print the average number of distinguishable systems over 20 trials above each bin. Note that both panels (c) and (d) show the number of systems versus stellar radius, but panel (d) shows this information on a refined grid only for $R_{\text{star}} \leq 3R_{\odot}$. As with MuSCAT, the fraction of systems distinguishable does *not* appear to rise with planetary radius. However, the fraction of distinguishable systems *does* rise with increasing transit depth and with decreasing stellar radius. The large fraction of systems distinguishable at higher values of TESS magnitude is due to the fact that transit depths in general are larger for dimmer TESS detections. For example, the median transit depth for systems visible from Teide Observatory that have TESS magnitude greater than 13 is 0.00989, while the median transit depth for systems brighter than TESS magnitude 13 is 0.00118.

sumes that we defocus the MuSCAT and MuSCAT2 instruments during observations (Section 3.3.2), and that light from the targeted star and the BEB component stars blends together. However, if the instruments are not defocused during observations, and if the target star and BEB are sufficiently spatially separated, then the target star and BEB can be observed separately so that the nature of the TOI is much more easily determined. For this reason, our estimates for the number of planetary candidates that MuSCAT and MuSCAT2 can discriminate should be considered as conservative minimal estimates to the number of TOIs that the two instruments can actually validate. In addition, we note that this study does not take into account observational factors such as weather or scheduling. Although the capabilities of MuSCAT and MuSCAT2 appear to be similar, in reality MuSCAT2 is likely to validate many more candidates than MuSCAT. The MuSCAT2 developers group has 162 guaranteed nights per year on MuSCAT2,¹⁹ and much of that time will be devoted to TESS follow-up. In addition, useful observing time at Teide Observatory reaches up to 78% in the summer (Varela et al., 2002).

3.4.2 Application to TESS Objects of Interest

We applied our MuSCAT and MuSCAT2 simulation tools to TESS Objects of Interest (TOIs) posted to the Exoplanet Follow-up Observing Program for TESS (ExoFOP-TESS) website,²⁰ to predict the probabilities that recent TOIs can be distinguished from BEB false positives using MuSCAT and MuSCAT2. At the time

¹⁹<http://vivaldi.ll.iac.es/OOCC/iac-managed-telescopes/telescopio-carlos-sanchez/muscat2/>

²⁰<https://exofop.ipac.caltech.edu/tess/>

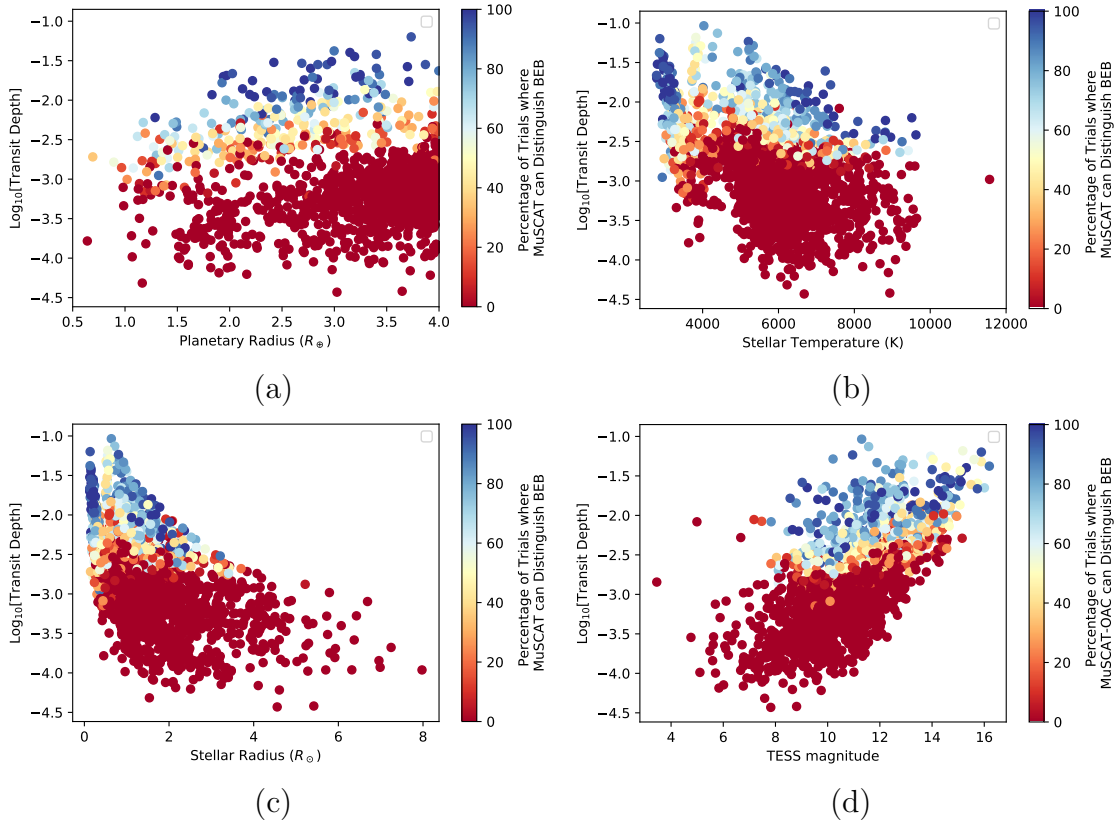


Figure 3.5: Plots showing the percentage of trials where MuSCAT can distinguish BEB false positives from true exoplanets for the 2,575 [Barclay et al. \(2018\)](#) systems visible from Okayama Astro-Complex. Each point represents one Barclay et al. system, with the color coding indicating the percentage of trials for which that system could be distinguished as a BEB false positive. We plot transit depth versus (a) planetary radius, (b) stellar effective temperature, (c) stellar radius, and (d) TESS-band magnitude. MuSCAT is quite effective at distinguishing BEBs for systems with transit depths of 0.003 or greater. For bright TESS magnitudes, MuSCAT CCD pixels saturate even with defocusing to 15 arcsec (Section 3.3.2), and therefore we report that MuSCAT is unable to distinguish BEBs in these bright systems.

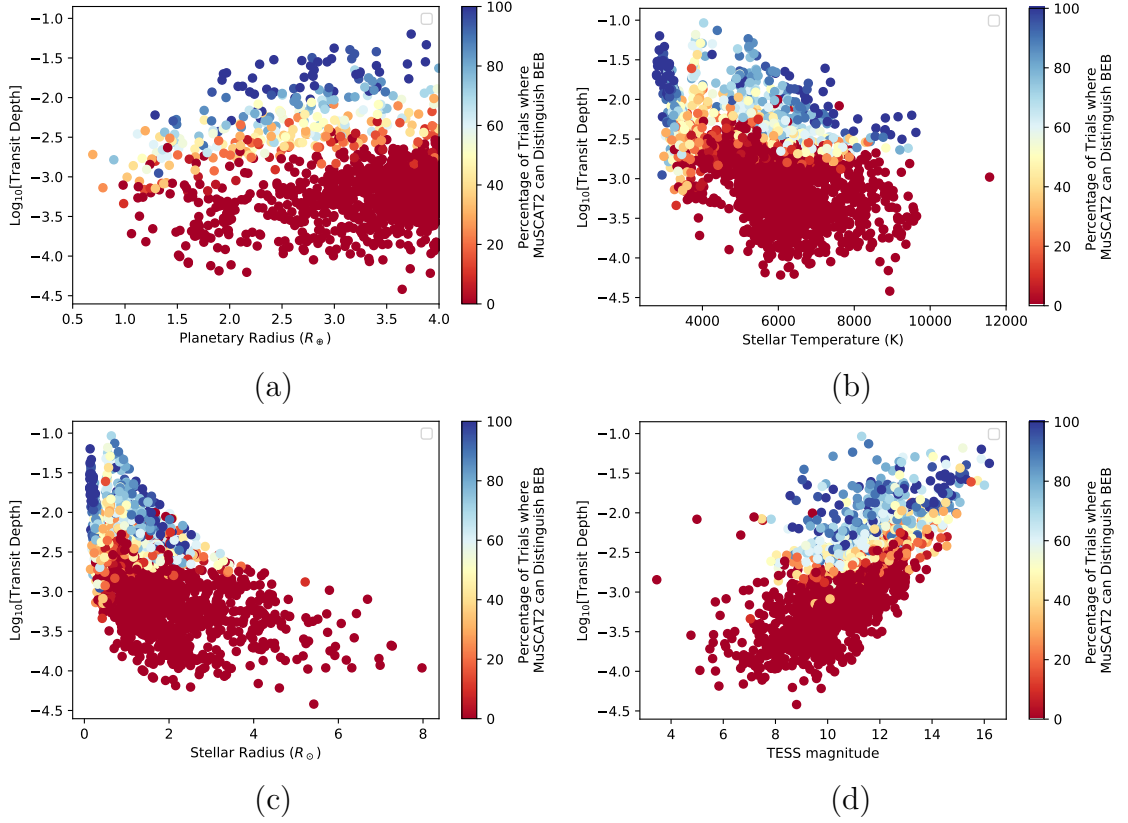


Figure 3.6: Plots showing the percentage of trials where MuSCAT2 can distinguish BEB false positives from true exoplanets for the 2,485 [Barclay et al. \(2018\)](#) systems visible from Teide Observatory. Each point represents one Barclay et al. system, with the color coding indicating the percentage of trials for which that system could be distinguished as a BEB false positive. We plot transit depth versus (a) planetary radius, (b) stellar effective temperature, (c) stellar radius, and (d) TESS-band magnitude. MuSCAT2 is quite effective at distinguishing BEBs for systems with transit depths of 0.003 or greater. For bright TESS magnitudes, MuSCAT2 CCD pixels saturate even with defocusing to 15 arcsec (Section 3.3.2), and therefore we report that MuSCAT2 is unable to distinguish BEBs in these bright systems.

ExoFOP-TESS was accessed, 995 TOIs had been uploaded to the database, spanning TESS observation sectors 1 through 12. Since all sectors were in the Ecliptic South, we found that only 334 systems would be observable from OAC (407 systems from Teide Observatory) at some time during the year through an airmass of 2 or less. Of the observable TOIs, the simulation tool could not be applied to 76 systems visible with MuSCAT (92 systems for MuSCAT2) because the database lacked parameters required by our routine. For example, some systems lacked values for stellar effective temperature or $\log(g)$, which are required to select a stellar model. Other systems lacked estimated values for planetary radius, which we use to calculate transit depth. Below, we discuss the results of applying our routine to the 258 systems visible from OAC (315 systems from Teide Observatory), for which all required parameters were available.

In applying our simulation routine to the TOIs, we confirmed that MuSCAT and MuSCAT2's ability to distinguish BEB false positives depends largely upon transit depth. We show this in Figure 3.7, where for MuSCAT2 we plot transit depth versus planetary radius, stellar temperature, stellar radius, and TESS magnitude, respectively, indicating with a color bar the percentage of trials where MuSCAT2 can distinguish the BEBs from true exoplanets. The plots indicate that MuSCAT2 is quite effective at distinguishing BEBs for systems with transit depths of 0.003 or greater. In addition, for the TOIs that we analyzed, MuSCAT2 is able to distinguish BEBs at slightly smaller transit depths for smaller planetary radii, smaller stellar effective temperatures and radii, and smaller TESS magnitudes (i.e., brighter systems).

Transit Depth (TD)	Number Distinguishable	Total Number of TOIs ⁱ	Percentage (%)
TD > 0.001	135 ± 5	259	52
TD > 0.002	133 ± 5	217	61
TD > 0.003	128 ± 4	187	68

NOTE:

ⁱIn this column, we report the total number of systems at the indicated transit depth, out of the 315 TOIs from TESS' Southern Ecliptic survey that are observable using MuSCAT2, for which all required parameters were available.

Table 3.3: Predicted number of TOI systems where MuSCAT2 can distinguish true exoplanets from BEB false positives (20 trials)

Transit Depth (TD)	Number Distinguishable	Total Number of TOIs ⁱ	Percentage (%)
TD > 0.001	115 ± 5	210	55
TD > 0.002	114 ± 5	179	64
TD > 0.003	108 ± 5	153	70

NOTE:

ⁱIn this column, we report the total number of systems at the indicated transit depth, out of the 258 TOIs from TESS' Southern Ecliptic survey that are observable using MuSCAT, for which all required parameters were available.

Table 3.4: Predicted number of TOI systems where MuSCAT can distinguish true exoplanets from BEB false positives (20 trials)

In Tables 3.3 and 3.4, we show our predictions for the number of TOIs distinguishable by MuSCAT2 and MuSCAT at transit depths greater than 0.001, 0.002, and 0.003, respectively. The values reported confirm that both instruments are quite effective at distinguishing BEBs for systems with transit depths of 0.003 or greater, but they also show that the two instruments are quite effective for even smaller transit depths. For example, they can discriminate over half of the systems with transit depths of 0.001 or greater.

Although not depicted here, our analysis for MuSCAT gives similar results to

those shown in Figure 3.7. In addition, for MuSCAT, the median transit depth for those systems that are distinguishable *less than* 50% of the time is 0.00122, while that for systems that are *never* distinguishable is 0.000886. For MuSCAT2, the median transit depth for those systems that are distinguishable *less than* 50% of the time is 0.00131, while that for systems that are *never* distinguishable is 0.000941.

We can use our simulation tools to predict the probability that a given system can be distinguished as either a true exoplanet or a false positive. Overall, for MuSCAT we found that 16 systems ($\sim 6\%$) could be distinguished 100% of the time (all 20 trials). For MuSCAT2, 17 systems ($\sim 5\%$) could be distinguished 100% of the time. Table 3.5 lists the 17 TOIs always distinguished by MuSCAT2 in order of increasing stellar temperature. For MuSCAT, thirty-five systems ($\sim 14\%$) were distinguishable at least 90% of the time, while 42 systems ($\sim 13\%$) were distinguishable $\geq 90\%$ of the time with MuSCAT2. For both instruments, approximately half of the systems (135 systems out of 258 for MuSCAT and 158 systems out of 315 for MuSCAT2) could be distinguished $\geq 50\%$ of the time. Eighty-one systems ($\sim 31\%$) could *never* be distinguished by MuSCAT, and 107 systems ($\sim 34\%$) could never be distinguished by MuSCAT2.

When we average the results over all 20 trials for each instrument, we find that MuSCAT can distinguish true exoplanets from BEBs for 115 (45%) ± 5 of all TOIs, while MuSCAT2 can do so for 135 (43%) ± 5 of all TOIs. For $R_{\text{pl}} < 4R_{\oplus}$ candidates, MuSCAT can distinguish true exoplanets from BEBs for 13 (18%) ± 2 of the 71 TOIs for which we have sufficient parameters to run our simulation tools, while MuSCAT2 can do so for 16 (18%) ± 2 of the 90 TOIs for which we have

sufficient parameters.

In July 2019, TESS began searching for transiting exoplanets in the Northern Ecliptic Hemisphere, which is composed of observation sectors 14 through 26. MuSCAT and MuSCAT2 will be able to observe most of the TOIs discovered in these sectors. Our results indicate that MuSCAT and MuSCAT2 will make significant contributions to the TESS Level 1 Science Requirement of measuring the masses of 50 exoplanets smaller in size than Neptune.

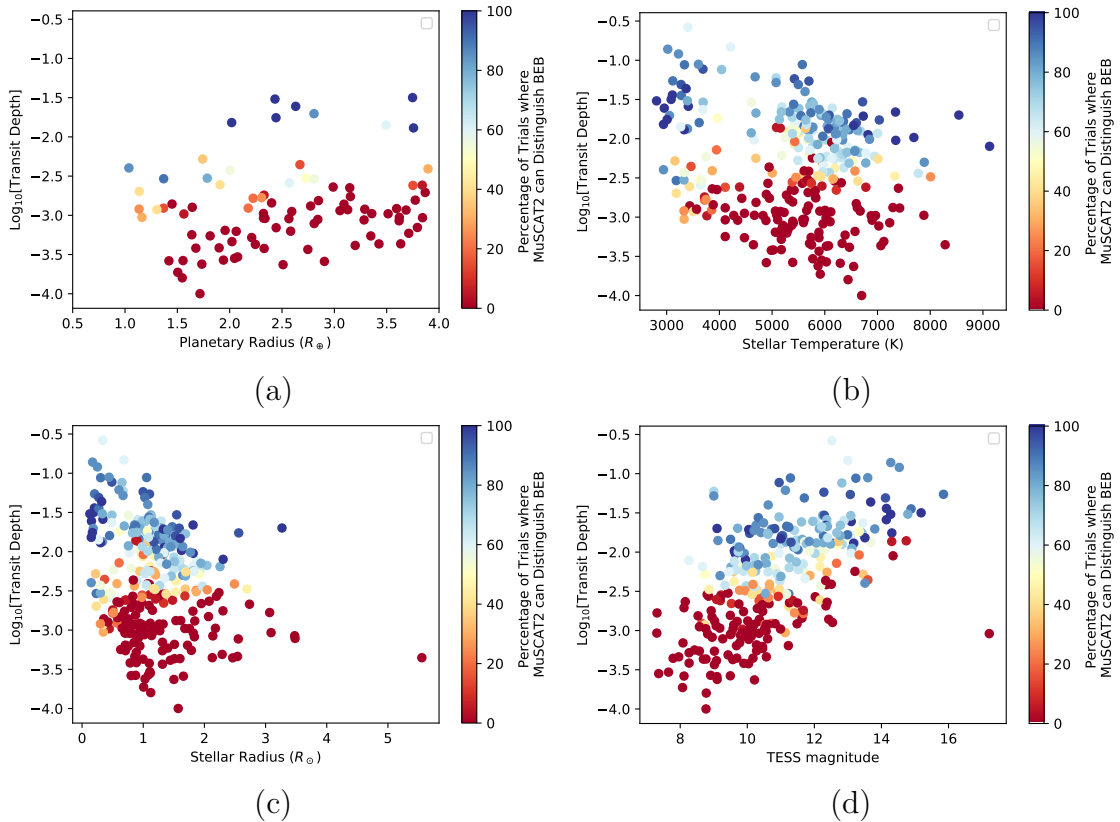


Figure 3.7: Plots showing the percentage of trials where MuSCAT2 can distinguish BEB false positives from true exoplanets for 315 TESS Objects of Interest (TOIs) visible from Teide Observatory. TOIs were downloaded from ExoFOP-TESS on 16 August 2019. MuSCAT2 is quite effective at distinguishing BEBs for systems with transit depths of 0.003 or greater. For the TOIs that we analyzed, the plots indicate that MuSCAT2 is able to distinguish BEBs at slightly smaller transit depths for smaller planetary radii (a), smaller stellar effective temperatures (b) and radii (c), and smaller TESS magnitudes (i.e., brighter systems) (d).

TOI ⁱ	T _{eff} (K)	R _{star} (R _☉)	T _{pl} (K)	R _{pl} (R _⊕)	TESS magnitude	Transit Depth
227.01	2,808	0.128	187	2.43	14.3	0.0302
736.01	2,940	0.150	302	2.02	13.5	0.0151
278.01	2,955	0.154	781	2.63	13.1	0.0244
549.01	3,009	0.169	680	2.44	14.3	0.0174
543.01	3,085	0.193	714	3.75	15.2	0.0315
516.01	3,109	0.202	581	4.18	14.2	0.0358
497.01	3,333	0.302	492	3.76	13.2	0.0130
643.01	3,369	0.320	339	7.28	13.7	0.0432
538.01	3,411	0.341	632	5.98	14.1	0.0259
1050.01	6,548	1.60	1,619	21.3	11.0	0.0148
951.01	6,730	1.33	1,554	20.2	10.0	0.0193
471.01	6,820	1.34	1,426	15.5	9.78	0.0112
577.01	7,341	1.81	1,917	29.3	12.3	0.0217
508.01	7,346	1.82	1,722	19.3	9.64	0.00946
625.01	7,690	1.63	1,919	18.1	9.61	0.0103
433.01	8,543	3.27	3,578	50.4 ⁱⁱ	9.10	0.0199
627.01	9,126	2.31	3,157	22.5	9.95	0.00794

NOTES:

ⁱListed in order of increasing stellar effective temperature

ⁱⁱAlthough listed as a TOI, the calculated radius of this candidate exoplanet is larger than that of any known exoplanet, and thus the system is likely an eclipsing binary.

Table 3.5: TOIs for which MuSCAT2 Can Distinguish BEBs from True Exoplanets in 100% of Trials

3.5 Summary and Conclusion

MuSCAT and MuSCAT2 can validate hundreds of $R_{\text{pl}} < 4R_{\oplus}$ candidate exoplanets, thus supporting the TESS team in achieving its Level 1 Science Requirement of measuring the masses of 50 exoplanets smaller in size than Neptune. Specifically, we draw the following conclusions.

1. Transit depth is the most important characteristic in determining whether or not MuSCAT and MuSCAT2 can distinguish between true exoplanets and BEB false positives. The two instruments are most effective at distinguishing

BEBs for systems with transit depths of 0.003 or greater.

2. We estimate that MuSCAT can distinguish BEB false positives for $\sim 17\%$ of all TESS discoveries, and $\sim 13\%$ of $R_{\text{pl}} < 4R_{\oplus}$ discoveries.
3. We predict MuSCAT2 will be able to distinguish BEB false positives for $\sim 18\%$ of all TESS discoveries, and $\sim 15\%$ of $R_{\text{pl}} < 4R_{\oplus}$ discoveries.
4. In analyzing actual TESS objects of interest (TOIs) from the Southern Ecliptic Hemisphere, we predict that MuSCAT can distinguish true exoplanets from BEBs for $115 (45\%) \pm 5$ of all observable TOIs, and for $13 (18\%) \pm 2$ of $R_{\text{pl}} < 4R_{\oplus}$ observable planet candidates.
5. In analyzing TOIs from the Southern Ecliptic Hemisphere, we predict that MuSCAT2 can distinguish true exoplanets from BEBs for $135 (43\%) \pm 5$ of all observable TOIs, and for $16 (18\%) \pm 2$ of $R_{\text{pl}} < 4R_{\oplus}$ observable planet candidates.
6. In analyzing TOIs from the Southern Ecliptic Hemisphere, we estimate that MuSCAT can distinguish true exoplanets from BEBs for $115 (55\%) \pm 5$ TOIs with transit depths greater than 0.001, for $114 (64\%) \pm 5$ TOIs with transit depths greater than 0.002, and for $108 (70\%) \pm 5$ TOIs with transit depths greater than 0.003.
7. In analyzing TOIs from the Southern Ecliptic Hemisphere, we estimate that MuSCAT2 can distinguish true exoplanets from BEBs for $135 (52\%) \pm 5$ TOIs with transit depths greater than 0.001, for $133 (61\%) \pm 5$ TOIs with transit

depths greater than 0.002, and for 128 (68%) ± 4 TOIs with transit depths greater than 0.003.

Our software tools will assist TFOP working group members as they prioritize and optimize follow-up observations of TESS objects of interest.

Chapter 4: Simulated JWST/NIRISS Transit Spectroscopy of Anticipated TESS Planets Compared to Select Discoveries from Space-Based and Ground-Based Surveys

4.1 Overview

The Transiting Exoplanet Survey Satellite (TESS) will embark in 2018 on a 2-year wide-field survey mission,¹ discovering over a thousand terrestrial, super-Earth and sub-Neptune-sized exoplanets ($R_{\text{pl}} \leq 4R_{\oplus}$) potentially suitable for follow-up observations using the James Webb Space Telescope (JWST). This work aims to understand the suitability of anticipated TESS planet discoveries for atmospheric characterization by JWST's Near InfraRed Imager and Slitless Spectrograph (NIRISS) by employing a simulation tool to estimate the signal-to-noise (S/N) achievable in transmission spectroscopy. We applied this tool to Monte Carlo predictions of the TESS expected planet yield and then compared the S/N for anticipated TESS discoveries to our estimates of S/N for 18 known exoplanets. We analyzed the sensitivity of our results to planetary composition, cloud cover, and presence of an observational

¹Since publication of [Louie et al. \(2018\)](#), TESS launched on 18 April 2018, and also completed its primary science mission in July 2020.

noise floor. We find that several hundred anticipated TESS discoveries with radii $1.5R_{\oplus} < R_{\text{pl}} \leq 2.5R_{\oplus}$ will produce S/N higher than currently known exoplanets in this radius regime, such as K2-3b or K2-3c. In the terrestrial planet regime, we find that only a few anticipated TESS discoveries will result in higher S/N than currently known exoplanets, such as the TRAPPIST-1 planets, GJ1132b, and LHS1140b. However, we emphasize that this outcome is based upon Kepler-derived occurrence rates, and that co-planar compact multi-planet systems (e.g., TRAPPIST-1) may be under-represented in the predicted TESS planet yield. Finally, we apply our calculations to estimate the required magnitude of a JWST follow-up program devoted to mapping the transition region between hydrogen-dominated and high molecular weight atmospheres. We find that a modest observing program of between 60 to 100 hours of charged JWST time can define the nature of that transition (e.g., step function versus a power law).

4.2 Introduction

The approaching launch of the James Webb Space Telescope (JWST), coupled with the 2018 launch of the Transiting Exoplanet Survey Satellite (TESS), heralds a new era in exoplanet science, with TESS projected to detect over one thousand transiting exoplanets smaller than Neptune ([Ricker et al., 2014](#)), and JWST offering unprecedented spectroscopic capabilities through which we can examine exoplanetary atmospheres ([Beichman et al., 2014](#); [Gardner et al., 2006](#); [Greene et al., 2016](#)).

One goal of exploring exoplanet atmospheres is to identify biosignatures, thus

firmly establishing whether life exists on planets orbiting other stars (Seager & Deming, 2010). Further, because water is necessary for life on Earth, we expect life will develop on planets able to maintain liquid water, and atmospheric water vapor can be used as a proxy for liquid surface water (Seager, 2013). Rather than focusing on true Earth analogs, Charbonneau & Deming (2007) describe the advantages offered through atmospheric characterization of super-Earths orbiting in the habitable zone (HZ) of nearby M-dwarfs.

Sullivan et al. (2015) used Monte Carlo simulations to predict that TESS will detect approximately 1,700 transiting planets orbiting pre-selected target stars during its 2-year wide-field survey of the northern and southern ecliptic hemispheres. The simulations employ Kepler-derived planet occurrence rates, as well as photometric performance models for the TESS cameras. Notably, Sullivan et al. (2015) found that about one-third of the TESS-discovered transiting exoplanets will have radii less than twice that of the Earth's, and three-quarters of these $R_{\text{pl}} < 2R_{\oplus}$ planets will orbit M-dwarfs. Slightly fewer than 10 percent of the $R_{\text{pl}} < 2R_{\oplus}$ planets will orbit near or within their host star's habitable zone. Exoplanets found by TESS will orbit stars 10-100 times brighter than those found during Kepler's primary mission, thus facilitating follow-up characterization of their atmospheres (Ricker et al., 2014).

Although TESS is poised to discover a multitude of M-dwarf-transiting sub-Neptune-sized and smaller exoplanets, other missions and ground-based projects have already discovered many favorable transiting planets. NASA's Kepler spacecraft was repurposed to fulfill the K2 mission, which includes observation of tran-

siting exoplanets orbiting bright, low-mass stars (Howell et al., 2014). Furthermore, ground-based surveys such as MEarth (Irwin et al., 2009, 2015; Nutzman & Charbonneau, 2008) and TRAPPIST (Jehin et al., 2011) have recently announced exciting exoplanet discoveries, such as that of GJ1132 (Berta-Thompson et al., 2015), the seven terrestrial-sized TRAPPIST-1 planets (Gillon et al., 2016, 2017), and the habitable zone super-Earth LHS-1140b (Dittmann et al., 2017b).

The targeted planets for JWST atmospheric characterization studies must be chosen wisely to maximize the amount of scientific knowledge attained for a given amount of JWST observation time (Batalha & Line, 2017; Howe et al., 2017). During its 2-year primary mission, TESS will discover exoplanets continually, and the first discoveries will not necessarily be those most conducive to follow-up atmospheric characterization.

One motivation of this work is to determine which TESS discoveries will produce the highest signal-to-noise (S/N) in transmission spectroscopy using the JWST Near-Infrared Imager and Slitless Spectrograph (NIRISS) operating in Single Object Slitless Spectroscopy (SOSS) mode. To attain this goal, we simulate NIRISS instrument performance during observations of the anticipated TESS exoplanet discoveries, limiting our predictions to planets with $R_{\text{pl}} < 4R_{\oplus}$. We then compare our results for the TESS planets to similar predictions for selected exoplanets already discovered via space-based or ground-based surveys. This comparison allows us to predict the highest priority TESS discoveries for immediate confirmation and follow-up observation. Furthermore, the TESS discoveries we examine lie within that regime where planets transition from rocky planets surrounded by high molecular

weight atmospheres, to icy sub-Neptunes enveloped in hydrogen-dominated atmospheres (Fulton et al., 2017b). Thus, an additional motivation of our work is to predict the magnitude of the observational program required to map this transition region.

Numerous past studies have estimated JWST’s capabilities during exoplanet atmosphere characterization (Barstow et al., 2015, 2016; Batalha & Line, 2017; Beichman et al., 2014; Belu et al., 2011; Clampin, 2011; Crouzet et al., 2017; Deming et al., 2009; Greene et al., 2016; Howe et al., 2017; Mollière et al., 2017), and NIRISS has emerged as the workhorse instrument for transit spectroscopy (e.g., Stevenson et al., 2016). Greene et al. (2016) modeled archetypal hot Jupiter, warm Neptune, warm sub-Neptune, and cool super-Earth exoplanets observed using several JWST instruments during both transit and secondary eclipse. One of their conclusions was that NIRISS transit spectra alone can often constrain the major molecular constituents of clear solar atmospheres, although additional wavelength coverage may be required in certain cases. Howe et al. (2017) and Batalha & Line (2017) used information content analysis—often used in studies of solar system atmospheres—to explore optimization of multiple JWST instruments and modes during observations of exoplanet atmospheres in transmission. In their examination of 11 transiting hot Jupiters, Howe et al. (2017) found that within the constraints of their model, NIRISS consistently provides the most information content for a given integration time. Batalha & Line (2017) studied an $R_{\text{pl}} = 1.39R_{\text{Jupiter}}$ planet of various temperatures, C/O ratios, and metallicities, orbiting WASP-62. They found that a single observation with NIRISS SOSS always provides the spectra with the highest

information content and tightest constraints. Additionally, when combining two modes, the highest information content spectra with tightest constraints are found by combining NIRISS SOSS with NIRSpec G395 M/H.

Here, we build upon these previous studies by predicting the properties of the population of TESS discoveries with $R_{\text{pl}} \leq 4R_{\oplus}$ that will be most conducive to NIRISS follow-up transit spectroscopy observations, and we then apply our findings to estimate the scope of a JWST follow-up program to map the transition region between hydrogen-dominated and high molecular weight atmospheres.

[Crouzet et al. \(2017\)](#) also predicted the capabilities of NIRISS, as well as of SOPHIE and SPIRou, in a follow-up program of the [Sullivan et al. \(2015\)](#) anticipated TESS discoveries. Our work differs from theirs in that we investigate only NIRISS observations, but we attempt to do so as realistically as possible. We include the sensitivity of our results to factors such as clouds, planetary composition, observational overhead, and systematic noise. Our instrument simulator also more closely emulates actual NIRISS observations for all of the planets considered, and we employ theoretical transmission spectra (rather than an atmospheric annulus) to estimate the signal produced by the planetary atmosphere during transit. In addition, to improve the reliability of our results, we analyze 50 Monte Carlo realizations of the TESS primary mission. Prior to JWST follow-up observations of TESS-discovered exoplanets, further characterization of TESS planet masses using the radial velocity technique with instruments such as SOPHIE or SPIRou will be required. In particular, the SPIRou near-infrared spectrometer will be important in characterizing the masses of small planets such as those examined in this work.

Thus, our results are complementary to those of [Crouzet et al. \(2017\)](#) in defining a JWST follow-up strategy for TESS-discovered exoplanet observations.

Recently, [Crossfield & Kreidberg \(2017\)](#) examined characteristics of six well-studied warm Neptunes, or short period planets of size $2R_{\oplus} < R_{\text{pl}} < 6R_{\oplus}$. They found that the amplitude of a given planet’s spectral transmission features correlates with either the planet equilibrium temperature, or with the bulk mass fraction of H/He in the planetary atmosphere. [Crossfield & Kreidberg \(2017\)](#) applied their findings to the [Sullivan et al. \(2015\)](#) anticipated TESS discoveries within the same radius regime, estimating the observation time required to distinguish features in planetary spectra using NIRISS. They show that the number of warm Neptune TESS planets amenable to atmospheric characterization may decrease by up to a factor of eight if transmission amplitude decreases linearly with the bulk mass fraction of H/He. The work of [Crossfield & Kreidberg \(2017\)](#) serves to identify trends in features of TESS planet discoveries that can be used to select the best planets for atmospheric characterization follow-up studies.

This paper is organized as follows. In Section 4.3, we describe pertinent exoplanet system properties for both the anticipated TESS discoveries and the existing exoplanets; we discuss our use of stellar and transmission spectra; and we describe the function of our NIRISS simulation tool. In Section 4.4, we present our findings, quantifying the sensitivity of our results to such factors as planetary composition, observational overhead, planetary cloud cover, and existence of systematic noise. We use our estimated S/N to produce simulated spectra for three existing exoplanets. In Section 4.5, we apply our findings to estimate the scope of a JWST follow-up

program devoted to mapping the transition region between high molecular weight and hydrogen-dominated atmospheres. We summarize in Section 4.6.

4.3 Methods

We require three major components to successfully predict NIRISS signal-to-noise. First, we require system parameters for the planetary systems that we wish to observe. Below, we describe our use of anticipated TESS discoveries in Section 4.3.1, and our use of planets already discovered in space-based and ground-based surveys in Section 4.3.2. The second major component is model spectra for both the star and the planetary atmosphere, which we describe in Section 4.3.3. Finally, we require a simulator that models NIRISS operational performance, which we present in Section 4.3.4.

4.3.1 Predicted Properties of TESS Discoveries

Sullivan et al. (2015) used Monte Carlo simulations to predict the properties of the planets that TESS is likely to detect, and published a catalog of 1,984 planets representing the planet yield from a single Monte Carlo realization of the TESS primary mission. The published catalog only includes planets detected from preselected target star observations rather than full frame image data. The target star detections make up all of the expected TESS detections for $R_{\text{pl}} < 2R_{\oplus}$, and $\sim 30\%$ of the detections for $2R_{\oplus} < R_{\text{pl}} < 4R_{\oplus}$. Sullivan et al. (2015) adopted Kepler planet occurrence rates from Fressin et al. (2013) for FGK stars, and from Dressing

& Charbonneau (2015) for stars with $T_{\text{eff}} < 4000$ K.

The Sullivan et al. (2015) TESS simulated planet catalog contains properties of the planetary systems, which we use as inputs to the NIRISS simulator. Parameters include stellar temperature and radius, distance and J-band magnitude, and planetary radius and insolation. We assume all planets are on circular orbits with an impact parameter of 0.5 during transit. From the catalog properties, we can calculate other required quantities, such as transit duration (T_{14}) and orbital semi-major axis. Importantly, the simulated TESS planet catalog does not contain planetary mass, which is required to calculate the scale height of the atmosphere for the planets, and thus is important in estimating the transmission spectroscopy signal.

To calculate the mass of the TESS planets, we explored using a variety of empirical mass-radius relationships (Chen & Kipping, 2017; Weiss & Marcy, 2014; Wolfgang et al., 2016), and ultimately adopted the Chen & Kipping (2017) model. Chen & Kipping (2017) examine 316 objects with well-constrained masses and radii to develop their relationship. In fitting their empirical data, they employ a broken power-law spanning four regimes which they describe as Terran, Neptunian, Jovian, and Stellar worlds. Unlike other approaches, in their analysis Chen & Kipping (2017) treat the transition points between regimes as free parameters. Their final result is a probabilistic model with credible intervals of values for the transition points, power-law indices in each regime, and radius dispersion in each regime.

In our application of the Chen & Kipping (2017) broken power-law model to TESS planets with $R_{\text{pl}} < 4R_{\oplus}$, we employ only the portion of the model valid for

Terran and Neptunian worlds, which is given by

$$M_{\text{pl}} = 0.9718R_{\text{pl}}^{3.58} \quad (4.1)$$

for $R_{\text{pl}} < 1.23R_{\oplus}$, and

$$M_{\text{pl}} = 1.436R_{\text{pl}}^{1.70} \quad (4.2)$$

for $1.23R_{\oplus} \leq R_{\text{pl}} < 14.26R_{\oplus}$, where mass and radii are given in units of M_{\oplus} and R_{\oplus} , respectively. We apply only the basic model and do not vary the parameters within the credible interval.

In reality, the planets that TESS discovers will not fall squarely upon the [Chen & Kipping \(2017\)](#) mass-radius relationship, but will exhibit some variation depending upon planetary composition, which in turn will affect the signal-to-noise (S/N) we compute in this project. To determine the sensitivity of alternative planetary compositions on our results, we show in Section 4.4 the S/N attained for planets composed of pure iron (Fe), perovskite (MgSiO_3), and ice (H_2O). In Figure 4.1, we compare the [Chen & Kipping \(2017\)](#) mass-radius relationship to the theoretical mass-radius relationships found in [Seager et al. \(2007\)](#) for planets of homogeneous compositions. All models are applied to the [Sullivan et al. \(2015\)](#) predicted TESS exoplanet discoveries.

The [Sullivan et al. \(2015\)](#) catalog of TESS discoveries represents only one possible realization of the TESS primary mission. To improve statistical confidence in our results, we also applied our NIRISS simulator to Monte Carlo simulations for 50 trials of the TESS primary mission, provided by [Bouma et al. \(2017\)](#). [Bouma](#)

et al. (2017) used the same techniques as Sullivan et al. (2015) in determining the planet yield for each trial of the TESS primary mission.²

4.3.2 Selection of Known Exoplanets for Comparison

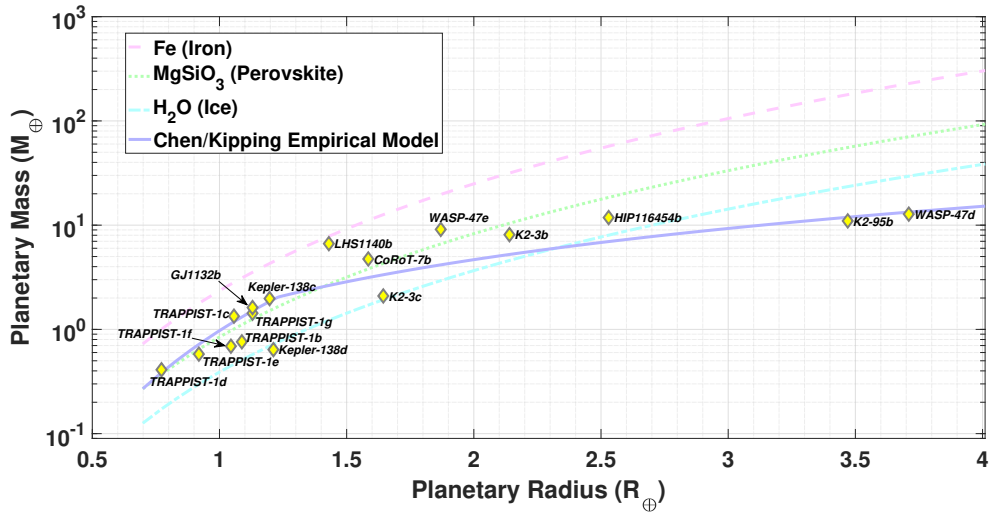
We examined the NASA Exoplanet Archive³ (Akeson et al., 2013) and the literature seeking Neptune-sized or smaller ($R_{\text{pl}} \leq 4R_{\oplus}$) confirmed exoplanet discoveries likely to produce strong signals in transmission if observed by NIRISS. For example, with all other factors the same, an exoplanet with a larger planet-to-star radius ratio will produce a larger transmission spectrum signal. In addition, a planet with a smaller density will have an atmosphere with a larger scale height, which will also produce a higher signal. In searching the archive, we sought planets with masses estimated through observations that are orbiting host stars smaller than the Sun. Tables 4.1 and 4.2 list the exoplanets and their parameters used in this study. In Sections 4.3.2.1 and 4.3.2.2 we discuss further details concerning our choice of these exoplanets for examination.

4.3.2.1 Space-Based Exoplanet Discoveries

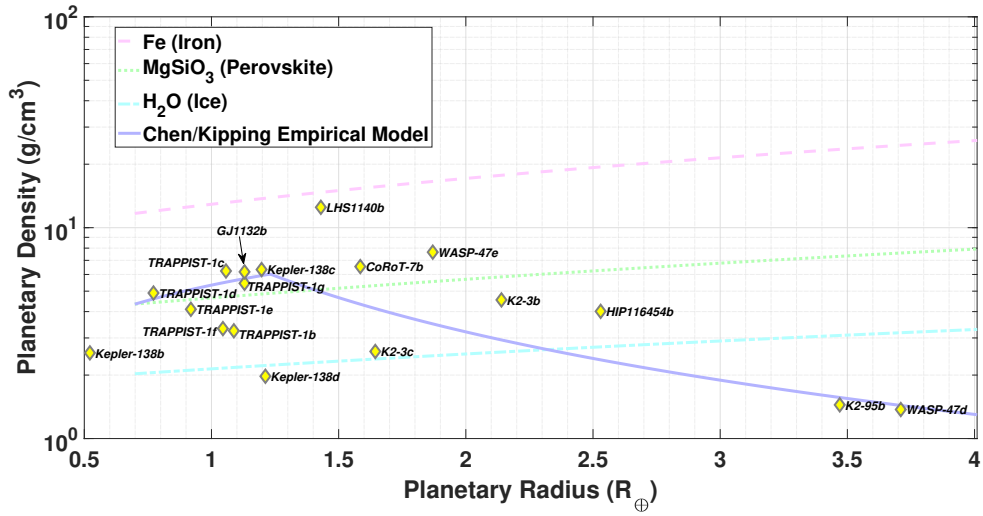
We primarily examine space-based discoveries from the K2 mission (Howell et al., 2014). However, we also look at one discovery from the CONvection, ROTation and planetary Transits (CoRoT) minisatellite mission (Baglin et al., 2006), as well as one multiplanetary system discovered during Kepler’s primary mission (Borucki

²Fifty trials of TESS primary mission from Bouma et al. (2017) may be found at <http://scholar.princeton.edu/jwinn/extended-mission-simulations>.

³<http://exoplanetarchive.ipac.caltech.edu>



(a)



(b)

Figure 4.1: Comparison of the empirical [Chen & Kipping \(2017\)](#) mass-radius relationship (equations 4.1 and 4.2) to the theoretical models of [Seager et al. \(2007\)](#). In (a) we show the masses calculated for each model applied to the [Sullivan et al. \(2015\)](#) predicted TESS exoplanet discoveries. In (b) we show the resulting exoplanet densities. Masses and densities of space-based and ground-based discoveries analyzed in this project are plotted for comparison.

et al., 2009).

In October 2009, Léger et al. (2009) announced CoRoT-7b, heralding the discovery as the first super-Earth with a measured radius. The planet serves as an interesting point of comparison to TESS discoveries, since it orbits a G9V host star that is hotter than most of the best anticipated TESS discoveries.

Kepler discovered thousands of exoplanet candidates, but only some of these planets have estimated masses. A search of the NASA Exoplanet Archive⁴ reveals that Kepler-138 is the only M-dwarf hosting planets with estimated masses and with radii less than $1.5R_{\oplus}$. We consider this system to determine how the S/N compares to the TESS discoveries.

The K2 mission differs from and is complementary to TESS in that the target fields are located along the ecliptic plane, a field that is not observed during the TESS primary mission. In this study, we first compare the anticipated TESS-discovered exoplanets to those K2-discoveries with M dwarf host stars. In particular, we look at two planets from the K2-3 system, as well as K2-95b. We did not look at K2-3d due to uncertainties in its mass estimate. We add to this list HIP-116454b, a $2.53R_{\oplus}$ planet orbiting a bright K-dwarf which was K2's first exoplanet discovery. The planet serves as an interesting point of comparison because its brightness is near the NIRISS J-band limiting magnitude, and the host star is somewhat hotter than the best-anticipated TESS discoveries. We also examine Neptune-sized WASP-47d and the super-Earth WASP-47e, which orbit a G9V host star with an estimated radius slightly larger than our Sun's. Because these latter three planets

⁴Accessed 3 May 2017

Exoplanet	J	Distance	Stellar Radius R_* (R_\odot)	Stellar Temperature (K)	Planet Radius R_{pl} (R_\oplus)	Planet Mass M_{pl} (M_\oplus)	Planet Temperature ^a (K)	Semi- major Axis (AU)	Impact Parameter b
CoRoT-7b ^b	10.301	153.7	0.820	5259	1.585	4.73	1756	0.017016	0.713
HIP-116454b ^c	8.60	55.2	0.716	5089	2.53	11.82	690	0.0906	0.65
K2-3b ^d	9.421	42	0.561	3896	2.14	8.1	463	0.0769	0.54
K2-3c ^e	9.421	42	0.561	3896	1.644	2.1	344	0.1405	0.31
K2-95b ^f	13.312	172	0.402	3471	3.47	10.99	415	0.0653	0.32
Kepler-138b ^g	10.293	66.5	0.442	3841	0.522	0.066	444	0.077	0.53
Kepler-138c	10.293	66.5	0.442	3841	1.197	1.970	409	0.0906	0.922
Kepler-138d	10.293	66.5	0.442	3841	1.212	0.640	344	0.12781	0.767
WASP-47d ^h	10.613	200	1.18	5475	3.71	12.75	986	0.0846	0.18
WASP-47e	10.613	200	1.18	5475	1.87	9.11	2221	0.01667	0.17

NOTES:

^aEquilibrium temperatures are calculated assuming zero albedo and uniform redistribution of heat.

^bCoRoT-7b system parameters from Léger et al. (2009), Barros et al. (2014), and Haywood et al. (2014).

^cHIP-116454b system parameters from Vanderburg et al. (2015).

^dK2-3b system parameters from Sinukoff et al. (2016) and Dai et al. (2016).

^eK2-3c system parameters from Sinukoff et al. (2016) and Almenara et al. (2015).

^fK2-95b system parameters from Obermeier et al. (2016) and Mann et al. (2017). Obermeier et al. (2016) estimated the planetary mass using an empirical mass-radius relationship.

^gKepler-138a, b, and c system parameters from Muirhead et al. (2012), Jontof-Hutter et al. (2015), and Souto et al. (2017).

^hWASP-47d and e system parameters from Becker et al. (2015) and Sinukoff et al. (2017).

Table 4.1: Space-based exoplanet discoveries used for comparison

orbit host stars that are hotter, and thus larger, than many TESS discoveries, we expect the transit depths to be smaller, and thus the S/N to be lower, than most TESS discoveries.

4.3.2.2 Exoplanets Discovered by Ground-Based Surveys

The ground-based discoveries examined in this work were found in either the MEarth survey or the TRAnsiting Planets and Planetesimals Small Telescope (TRAPPIST) survey.

The MEarth-North and MEarth-South transit surveys were designed to search for super-Earths orbiting mid-to-late M dwarfs with radii less than $0.33R_\odot$ that

are located within 33 parsecs of the Earth (Irwin et al., 2009, 2015; Nutzman & Charbonneau, 2008). Here, we examine two MEarth-South discoveries: GJ1132b and LHS1140b.

Berta-Thompson et al. (2015) announced the discovery of GJ1132b in November 2015. Since that time, further studies conducted using ground-based facilities and the Spitzer Space Telescope have allowed further refinement of system parameters such as stellar and planetary radii (Dittmann et al., 2016). The water atmosphere we examine in this work is one plausible atmospheric composition for GJ1132b. In addition, Dittmann et al. (2017b) recently reported observations of LHS1140b, a nearby $1.4R_{\oplus}$ super-Earth orbiting its M dwarf host star within the habitable zone. The authors note that if this super-Earth had an extended magma-ocean phase, then water may have remained in the mantle until the star reached its current luminosity, thus allowing the presence of water in its atmosphere.

One goal of the TRAPPIST survey is to monitor a select sample of ultra-cool dwarf stars for planetary transits (Jehin et al., 2011). Gillon et al. (2016, 2017) determined that TRAPPIST-1 hosts at least seven Earth-sized planets that are likely to be tidally synchronized. de Wit et al. (2016) analyzed the combined transmission spectrum of TRAPPIST-1 b and c, determining that the featureless spectrum ruled out a cloud-free hydrogen-dominated spectrum on the two planets. However, heavier atmospheres, such as the water atmosphere studied here, remain plausible. Although here we examine the signal produced by water lines in a water atmosphere, we note that the actual atmospheric composition of the TRAPPIST-1 planets depends upon several factors, such as X-Ray and EUV fluxes, which are

areas of active research (Bourrier et al., 2017; O’Malley-James & Kaltenegger, 2017; Wheatley et al., 2017).

Multiple recent studies (Quarles et al., 2017b; Wang et al., 2017) have estimated the masses of the TRAPPIST-1 planets in order to further constrain the planetary compositions. In this work, we use the planetary masses inferred by Quarles et al. (2017b) using N-body dynamical simulations that determine planetary parameters stable over millions of years.

The masses of the TRAPPIST-1 planets and of LHS-1140b are not well constrained. Since the density of the planet used in simulations impacts the scale height and thus the predicted S/N, uncertain mass estimates may lead to incorrect conclusions. Thus, for comparison, we also calculate S/N for the TRAPPIST-1 planets and LHS-1140b by assuming an *Earthlike* composition. We use the semi-empirical mass-radius relationship developed by Zeng et al. (2016), assuming a core mass fraction of 0.3, the same as that for Earth and Venus. Since the relationship does not apply to planets with masses less than $1M_{\oplus}$, for TRAPPIST-1d and TRAPPIST-1e, we simply assume the density is the same as that of Earth’s. Table 4.3 shows the masses and densities we used for these alternative calculations.

4.3.3 Spectra

The models we use for stellar and transmission spectra allow us to estimate both the signal and the noise that we detect from a given planetary system. With stellar model spectra, we determine the number of photons output by a host star

Exoplanet	J	Distance	Stellar Radius R_* (R_\odot)	Stellar Temperature (K)	Planet Radius R_{pl} (R_\oplus)	Planet Mass M_{pl} (M_\oplus)	Planet Temperature ^a (K)	Semi- major Axis (AU)	Impact Parameter b
GJ1132b ^b	9.245	12.04	0.2105	3270	1.13	1.62	579	0.01619	0.38
LHS-1140b ^c	9.612	12.47	0.186	3131	1.43	6.65	230	0.0875	0.155
TRAPPIST-1b ^d	11.4	12.1	0.117	2559	1.088	0.76	400	0.01111	0.126
TRAPPIST-1c	11.4	12.1	0.117	2559	1.057	1.34	342	0.01522	0.161
TRAPPIST-1d	11.4	12.1	0.117	2559	0.722	0.41	288	0.02144	0.170
TRAPPIST-1e	11.4	12.1	0.117	2559	0.919	0.58	251	0.02818	0.120
TRAPPIST-1f	11.4	12.1	0.117	2559	1.045	0.69	219	0.03707	0.382
TRAPPIST-1g	11.4	12.1	0.117	2559	1.130	1.43	199	0.04510	0.421

NOTES:

^aEquilibrium temperatures are calculated assuming zero albedo and uniform redistribution of heat.

^bGJ1132b system parameters from [Berta-Thompson et al. \(2015\)](#) and [Dittmann et al. \(2017a\)](#).

^cLHS-1140b system parameters from [Dittmann et al. \(2017b\)](#).

^dTRAPPIST-1 system parameters from [Gillon et al. \(2017\)](#) and [Quarles et al. \(2017a\)](#).

Table 4.2: Ground-based exoplanet discoveries used for comparison

Exoplanet	Planet Mass, M_{pl} (M_\oplus)	Planet Density (g cm^{-3})
LHS-1140b	3.73	7.03
TRAPPIST-1b	1.36	5.81
TRAPPIST-1c	1.22	5.69
TRAPPIST-1d	0.38	5.51
TRAPPIST-1e	0.78	5.51
TRAPPIST-1f	1.17	5.65
TRAPPIST-1g	1.56	5.96

Table 4.3: Masses for select exoplanets assuming an Earthlike composition

at each wavelength across the NIRISS bandpass. The photons received from the host star make up the major source of noise in our simulations. Our transmission spectroscopy code provides the wavelength-dependent fraction of the stellar area that is blocked by an exoplanet during transit, which constitutes the signal in our simulations. In Sections 4.3.3.1 and 4.3.3.2, we describe these important inputs to our NIRISS simulator.

4.3.3.1 Stellar Spectra

PHOENIX/BT-NextGen and PHOENIX/BT-Settl stellar emission spectrum grids (Allard et al., 2012) provide stellar flux across the NIRISS bandpass at a resolution of ~ 2 Angstroms. We employ solar metallicity spectra, which include the effects of absorption from molecules such as water vapor (Barber et al., 2006) in the stellar atmosphere. The host stars of our target systems range in effective temperature from 2,090 K to 14,655 K. We employ BT-Settl models for host stars with effective temperatures less than 2,600 K,⁵ and BT-NextGen models for those systems with higher effective temperatures. BT-NextGen models span stellar temperature values from 2,600 K to 70,000 K, and $\log(g)$ values from -0.5 to 6.0 . Stellar models are provided in $\log(g)$ increments of 0.5 , and in temperature increments of 100 K up to a stellar temperature of 7,000 K, then in temperature increments of 200 K up to a temperature of 12,000 K, and thereafter in temperature increments of 500 K. Our simulation routine selects the stellar model with effective temperature and

⁵In all of our calculations, only 43 systems adopt BT-Settl stellar models. For the published Sullivan et al. (2015) planetary systems, only one has a host star of temperature less than 2,600 K, and for the 50 Monte Carlo realizations of the TESS primary mission, only 42 stellar systems (out of 124,173) have host stars with effective temperatures less than 2,600 K.

$\log(g)$ values closest to the particular planetary system we wish to observe.

4.3.3.2 Planetary Atmospheres and Transmission Spectra

The TESS planet catalog discussed in Section 4.3.1 includes planetary radii, but the radii do not vary with wavelength, and the Sullivan et al. (2015) simulations make no assumptions regarding planetary atmospheres. For the known planets discussed in Section 4.3.2, we can make some assumptions regarding likely planetary atmospheres based upon observations and estimated bulk densities. Recent research has identified the radius regime from $1.5R_{\oplus}$ to $2R_{\oplus}$ as the transition region from rocky, terrestrial planets with high molecular weight atmospheres to sub-Neptune planets enveloped in hydrogen-dominated atmospheres (Elkins-Tanton & Seager, 2008; Fulton et al., 2017b; Kempton, 2011; Marcy et al., 2014; Miller-Ricci et al., 2009; Rogers, 2015).

Clear Atmospheres—For the purposes of our calculations, we assume that *all* planets with $R_{\text{pl}} \leq 1.5R_{\oplus}$ are enveloped in a clear, isothermal water atmosphere (mean molecular weight $\mu = 18$), and we assume that *all* planets with $1.5R_{\oplus} < R_{\text{pl}} \leq 4R_{\oplus}$ are surrounded by a clear, isothermal hydrogen-dominated atmosphere ($\mu = 2.39$). We use an isothermal atmosphere because we do not have sufficient information to justify a more complex structure, and also because transit spectra are not directly sensitive to the source function in the exoplanetary atmosphere. For each planet, we calculate the equilibrium temperature assuming zero albedo and uniform redistribution of heat. These temperatures are reported for known

exoplanets in Tables 4.1 and 4.2. In reality, some planets in the transition region will likely have heavy atmospheres, some will likely have lighter atmospheres, and some will be rocky cores stripped of an atmosphere. By assuming a single atmospheric composition within the two radii regimes, we can better determine the contributions of other planetary parameters on resultant S/N.

For most planetary compositions, the spectrum of water vapor will dominate the NIRISS spectral region. We estimate the signal produced by water lines in the isothermal planetary atmospheres by employing a version of a spectral transmittance code presented previously in Deming et al. (2013). Here, we modify the code to cover the NIRISS bandpass. Our code uses a slant-path geometry, assuming a 200-layer atmosphere in hydrostatic equilibrium, with pressures in the layers equally spaced in log from 1 to 10^7 dynes cm^{-2} . The hydrogen-dominated atmospheres include continuous opacity due to collision-induced absorption of H_2 (Borysow, 2002; Zheng & Borysow, 1995). For the water atmospheres, we place a solid surface at 1 bar (10^6 dynes cm^{-2}). We calculate water opacity using water lines (Barber et al., 2006) downloaded from the Exomol Database⁶ (Tennyson & Yurchenko, 2012). Our code scales the strengths of the lines at the isothermal temperature of the planet, and then bins the scaled strengths of the water lines into bins of width 0.01 cm^{-1} , much smaller than the NIRISS resolution (Deming & Sheppard, 2017). We convolve the high-resolution transmission spectrum output by our code to the resolution of the NIRISS instrument prior to employing the output spectrum in our NIRISS

⁶<http://www.exomol.com/data/data-types/linelist/H2O/1H2-160/BT2/>, accessed 29 Jan 2017

simulator.

We previously validated the code as described in [Deming et al. \(2013\)](#). In addition, our code is in close agreement with output results from [Line et al. \(2013a\)](#), as shown in their Figure 5. In this work, we further compare our code to the output results of Exo-Transmit ([Kempton et al., 2017](#)), as shown in Figure 4.2 for a super-Earth ($R_{\text{pl}} = 1.28R_{\oplus}$) at equilibrium temperature 788 K with a clear water atmosphere. The system parameters of the chosen super-Earth correspond to mean values of system parameters for the published [Sullivan et al. \(2015\)](#) TESS planets in the radius regime $R_{\text{pl}} \leq 1.5R_{\oplus}$. Exo-Transmit produces transmission spectra at a fixed spectral resolution $R = 1000$. Our code produces a high-resolution spectrum with millions of lines across the NIRISS bandpass at sub-Doppler resolution ($R > 300,000$ across the NIRISS bandpass), which we then convolve with a Gaussian to produce the $R = 1000$ spectrum illustrated in Figure 4.2. The Exo-Transmit spectrum retains more structure since the spectrum is produced at a native resolution $R = 1000$, whereas our high-resolution code is smoothed to the same resolution. The average values across the two spectra are in close agreement.

Cloud Effects—Our spectral transmittance code allows placement of an opaque cloud layer at a pressure level of our choice. In this work, we examine the effects of clouds by placing an opaque cloud deck at a pressure of 10 mbar for planets with both water and hydrogen-dominated atmospheres.

Use of Transmittance Code with Planetary Systems—When applying our spectral transmittance code to the known exoplanets, we apply the code to each planet individually, using the system parameters reported in Tables 4.1, 4.2, and 4.3. How-

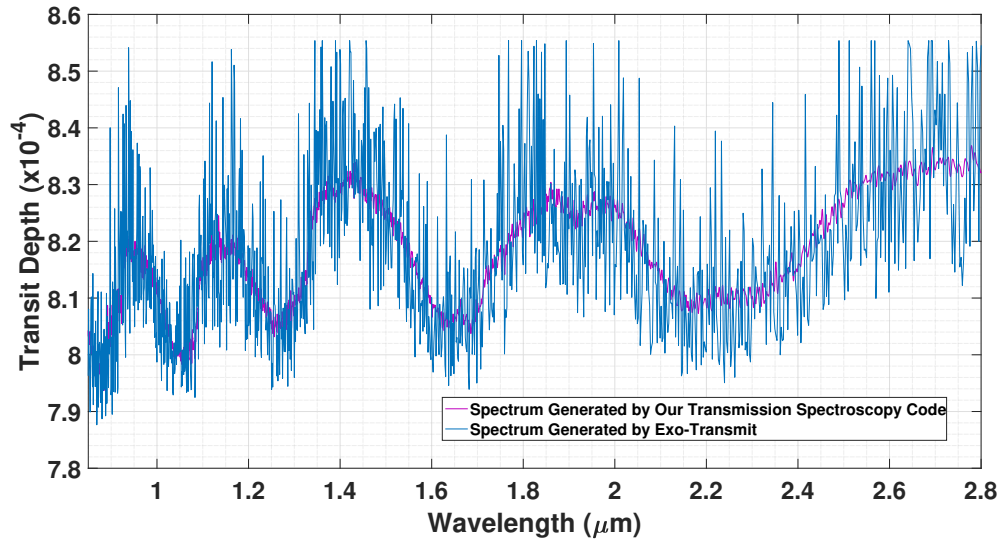


Figure 4.2: Comparison of our transmission spectroscopy code to Exo-Transmit (Kempton et al., 2017) for a super-Earth ($R_{\text{pl}} = 1.28R_{\oplus}$) at equilibrium temperature 788 K with a clear water atmosphere. The system parameters of the chosen super-Earth correspond to mean values of system parameters for the published Sullivan et al. (2015) TESS planets in the radius regime $R_{\text{pl}} \leq 1.5R_{\oplus}$. Both spectra have resolving powers of 1000 but differ in details due to binning (see text).

ever, when applying the code to the [Sullivan et al. \(2015\)](#) anticipated TESS planets and to the 50 Monte Carlo realizations of the TESS primary mission data, it is computationally expedient to scale the transmission spectra to planetary systems with mean values of stellar radius and planetary radius, mass, and temperature for the [Sullivan et al. \(2015\)](#) anticipated TESS planets within each radius regime. The remainder of this subsection outlines the method we employ in scaling the transmission spectrum of each TESS planet to one of the two reference planets.

Our code outputs a transmission spectrum equivalent to the transit depth of each reference planet. In general,

$$\text{Transit Depth} = \frac{\text{Area}_{\text{pl}}}{\text{Area}_{\star}} = \frac{(R_{\text{pl}} + h)^2}{R_{\star}^2}, \quad (4.3)$$

where R_{pl} is the radius of the solid surface of the planet, h is the wavelength-dependent thickness of the atmosphere, and R_{\star} is the stellar radius. Expanding equation 4.3 and ignoring small terms, we find

$$\text{Transit Depth} \approx \frac{R_{\text{pl}}^2}{R_{\star}^2} + \frac{2R_{\text{pl}}h}{R_{\star}^2}. \quad (4.4)$$

The second term in equation 4.4 is the wavelength-dependent term that must be scaled to each planetary system. We note that since h represents the thickness of the atmosphere, it must be proportional to the atmospheric scale height H , which is found from

$$H = \frac{kT_{\text{pl}}}{\mu m_H g} = \frac{kT_{\text{pl}} R_{\text{pl}}^2}{\mu m_H G M_{\text{pl}}}, \quad (4.5)$$

where k is Boltzmann’s constant, T_{pl} is the equilibrium temperature of the planet, m_H is the mass of the hydrogen atom, and $g = \frac{GM_{\text{pl}}}{R_{\text{pl}}^2}$ is the acceleration due to gravity on the planet, where G is the universal gravitational constant and M_{pl} is the mass of the planet. Denoting the second term in equation 4.4 with the variable S , substituting equation 4.5 for $H \propto h$, and dropping various constants, we find

$$S = \frac{2R_{\text{pl}}h}{R_*^2} \propto \frac{T_{\text{pl}}R_{\text{pl}}^3}{M_{\text{pl}}R_*^2} \propto \frac{T_{\text{pl}}}{\rho_{\text{pl}}R_*^2}, \quad (4.6)$$

where ρ_{pl} is the density of the planet.

We use equation 4.6 to scale the atmosphere of any TESS planet in one of the two radius regimes to the appropriate reference planet. Specifically, using the subscript T to refer to the TESS planetary system, and the subscript “ref” to refer to the reference planetary system, we have

$$S_T = S_{\text{ref}} \times \frac{T_{\text{pl},T}}{T_{\text{pl,ref}}} \times \frac{\rho_{\text{pl,ref}}}{\rho_{\text{pl},T}} \times \frac{R_{*,\text{ref}}^2}{R_{*,T}^2}, \quad (4.7)$$

where S_T is the wavelength-dependent transmission spectrum for the TESS system, scaled to the reference transmission spectrum S_{ref} for the regime of interest.

4.3.4 Description of NIRISS Simulator

In this work, our simulator predicts the S/N attainable by NIRISS, operating in SOSS mode, during 10-hour observation programs of the [Sullivan et al. \(2015\)](#) anticipated TESS discoveries, predicted TESS discoveries from 50 Monte Carlo re-

alizations of the TESS primary mission, and the known exoplanets listed in Tables 4.1 and 4.2. We chose 10 hours per target to represent the order of magnitude observation time, t_{obs} , required to complete a statistical survey project of multiple exoplanets. Except as noted during our description of observational overhead, our simulations equally apportion the observation time to periods in and out of transit. We do not take into account minor effects such as stellar limb darkening, and we assume that the entire cross sectional area of the planet blocks the star throughout the transit. For comparison, we also examine the S/N attainable in more intensive 100-hour observation programs of the potentially habitable TESS planets—those with $R_{\text{pl}} \leq 1.5R_{\oplus}$ and cool or temperate equilibrium temperature.⁷

We have developed our NIRISS simulator in consultation with the NIRISS instrument team, and we have incorporated the latest NIRISS design values into our simulator to the extent possible.⁸ In this section, we describe in detail the method we use to model NIRISS observations. We close the section by briefly explaining how we explore the effects of observational overhead and the presence of systematic noise on our S/N results.

4.3.4.1 Predicting JWST/NIRISS S/N

The NIRISS SOSS mode offers three readout modes covering wavelengths from 0.6 to 2.8 microns (Doyon et al., 2012). Here, we estimate NIRISS S/N only for Or-

⁷In planning actual observation programs, visibility of the targeted planetary systems and potential contamination by partly overlapping spectra from nearby stars must be considered: http://maestria.astro.umontreal.ca/niriss/SOSS_cont/SOSScontam.php. These topics are beyond the scope of this work.

⁸http://jwst.astro.umontreal.ca/?page_id=51

der 1 spectra produced in *nominal* (256 x 2048 pixel subarray) and *bright* (96 x 2048 pixel subarray) modes, spanning wavelengths from 0.8 to 2.8 microns.⁹ The *bright* mode read time (2.213 sec) is faster than that of *nominal* mode (5.491 sec), thus allowing observation of brighter targets before saturating the subarray pixels. A weak cylindrical lens at the entrance to the NIRISS cross-dispersed grism spreads light across approximately 23 pixels in the spatial direction, also enabling observation of brighter objects before reaching pixel saturation.

Given a targeted planetary system for NIRISS observations, our simulation begins by selecting the appropriate PHOENIX stellar model, which provides output stellar flux in $\text{ergs sec}^{-1} \text{cm}^{-2} \text{\AA}^{-1}$. We convolve the stellar spectrum with a Gaussian corresponding to the NIRISS optics resolution (~ 1.6 pixels FWHM), and then convert the model flux output at the star to a photon flux arriving at the JWST observatory by scaling the stellar model to the J-Band magnitude of the star, multiplying by the area of JWST (25.3 m^2), and then dividing by the energy per photon $h\nu$, where h is Planck’s constant and ν is the frequency of the photon. We calculate the signal produced by the planetary atmosphere by determining the wavelength-dependent portion of the stellar photons that are blocked by the atmospheric annulus during transit (equation 4.3).

To determine the signal and noise detected by NIRISS, we must account for instrument throughput and dispersion. The NIRISS design team has provided an estimate of throughput across the NIRISS bandpass at a resolution of 1 nm. The estimate includes detector quantum efficiency and transmission through all opti-

⁹The blue cut-off in *bright* mode is 0.9 microns due to the smaller size of the subarray.

cal elements of the JWST observatory, NIRISS instrument, and GR700XD grism. We apply the wavelength-dependent throughput to the stellar model and to the wavelength-dependent signal produced by the atmosphere during transit. The dispersion of 0.974 nm/pixel allows us to determine the wavelength range of each NIRISS subarray column in the dispersion direction. Knowing the wavelength (and frequency) range covered by each column in the dispersion direction, we can then determine the photon flux spread across the spatial direction both in and out of transit. Our simulation also incorporates noise due to zodiacal light (Kelsall et al., 1998) and JWST telescope thermal background (Swinyard et al., 2004), but these effects are negligible in practice for the observation of the bright transiting planet host stars. Read noise and dark currents are also regarded as negligible for well-exposed integrations.

Before calculating the signal and noise produced during an observation program, we must first determine the efficiency of the observation. The on-sky efficiency achievable with NIRISS depends upon the brightness of the targeted stellar system. The integration time of a given observation is determined by the number of *reads*, also known as n_{groups} , performed before resetting the well (Batalha et al., 2017b; Beichman et al., 2014). The time to reset the well is equal to the time to perform one read, which we denote as t_{frame} . We calculate integration time¹⁰ with

$$t_{\text{int}} = t_{\text{frame}} \times (n_{\text{groups}} - 1), \quad (4.8)$$

¹⁰http://maestria.astro.umontreal.ca/niriss/simu1D/SOSS_Simulator_Guide.pdf

and on-sky efficiency using

$$\eta = \frac{n_{\text{groups}} - 1}{n_{\text{groups}} + 1}. \quad (4.9)$$

Our simulation calculates and employs the maximum on-sky efficiency possible without saturating any pixels. We do this by calculating the maximum number of n_{groups} we can use without any pixels accumulating greater than the full well capacity of 72,000 electrons.¹¹ In performing this calculation, we make use of the fact that when the photon flux is spread across the pixels in the spatial direction, 7% of the photons fall in the peak pixel. In calculating efficiency, we consider only correlated double sampling, where flux is calculated by subtracting the last read from the first read. The NIRISS design also allows a superbias subtraction method to calculate flux when observing brighter objects, but this mode has more uncertainty in its noise properties, and we do not consider it in this work.

In calculating n_{groups} , our simulator first assumes that we are observing in *nominal* mode. If the required value of n_{groups} is less than 2, which is the minimum value of n_{groups} required when using correlated double sampling, then we recalculate n_{groups} using *bright* mode instead. For some stellar systems, pixels will saturate even in *bright* mode. For the [Sullivan et al. \(2015\)](#) planets, the plot of our output results shows those systems which were observed using *bright* mode, and we also indicate those systems where some pixels saturate. When analyzing the 50 trials of

¹¹We used full well capacity in our calculations since that is the value used by the NIRISS 1D SOSS simulator. Going to full well capacity could result in systematic effects ([Wilkins et al., 2014](#)). Thus, we examined using 55,000 electrons rather than full well capacity and found that on-sky efficiency and therefore S/N changes minimally in most cases. The greatest change in S/N of $\sim 20\%$ occurs for systems that are viewed at $n_{\text{groups}} = 3$ ($\eta = 0.5$) for 72,000 electrons and then $n_{\text{groups}} = 2$ ($\eta = 0.33$) for 55,000 electrons. The conclusions of this work are unaltered by changing the electron level used for saturation.

TESS data, we present our results as a 2-dimensional histogram in $S/N-R_{\oplus}$ space. In presenting these results, we ignore those systems where pixel saturation occurs in *bright* mode.¹² For those systems that are dim, the highest value of n_{groups} our simulator employs is 88 (Beichman et al., 2014). After the optimum number of n_{groups} has been calculated, our simulator determines the on-sky efficiency using equation 4.9.

Knowing the efficiency, the observation time, and the photon flux from the star falling across the pixels, the stellar shot noise is determined by using

$$N_{\text{shot}} = \sqrt{\eta t_{\text{obs}} F_*}, \quad (4.10)$$

where N_{shot} represents the photon shot noise and F_* is the photon flux falling across the pixels. Photon shot noise is the primary source of noise for the S/N values we report in Section 4.4.

A similar calculation is possible for the signal. Knowing the number of stellar photons blocked by the atmospheric annulus across the NIRISS bandpass, we can calculate the signal produced by the water lines in the atmosphere from

$$S_{\text{atm}} = \eta \frac{t_{\text{obs}}}{2} F_{\text{atm}}, \quad (4.11)$$

where S_{atm} represents the signal produced by the atmosphere and F_{atm} is that portion of the stellar flux blocked by the atmospheric annulus.

¹²If the systems where pixel saturation occurs are included, our results support the same conclusions.

The S/N varies greatly across the NIRISS bandpass, which is to be expected since the strength of water lines and the brightness of the host star differ with wavelength. In this work, after calculating the wavelength-dependent values of N_{shot} and S_{atm} across the columns of the NIRISS subarray, we next calculate the *integrated* S/N for the detection of the atmosphere across the NIRISS bandpass. In Figure 4.3, we illustrate graphically our calculation of the signal (equation 4.11) in each column across the subarray, as well as the integrated S/N, which is what we report on our Figures in Section 4.4.

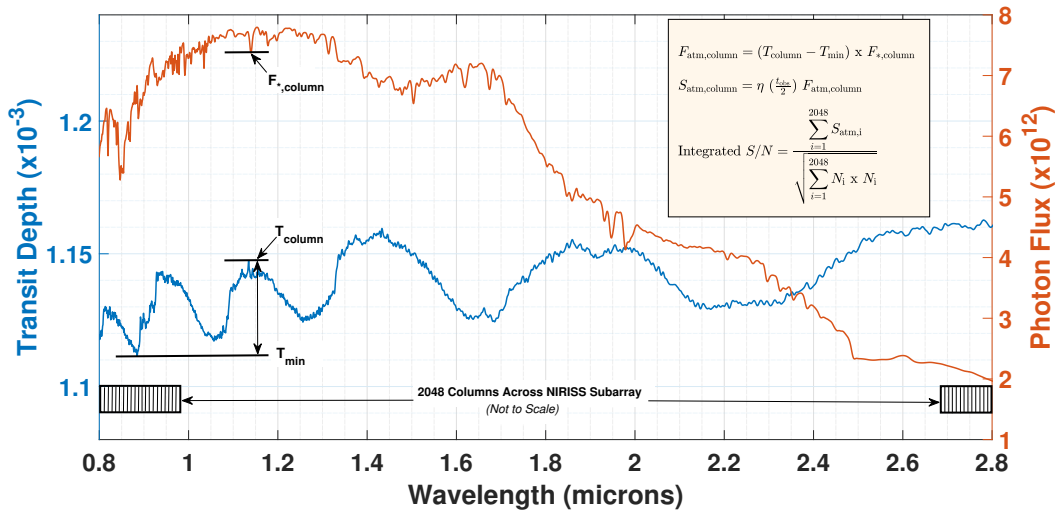


Figure 4.3: Graphical illustration showing our calculation of signal (equation 4.11) in each column of the NIRISS subarray, as well as the integrated S/N across the NIRISS bandpass. The left vertical axis (blue curve) shows the transit depth, while the right vertical axis (orange curve) shows photon flux. In calculating integrated S/N, N_i is the noise both in and out of transit due to stellar photons, zodiacal light, and JWST telescope background.

We validated our NIRISS simulation code by comparing it to the 1D SOSS

simulator developed by the NIRISS instrument design team.¹³ For all planetary systems where we compared the two codes, our results differed from those of the 1D SOSS simulator by 8 to 11%. In Figure 4.4, we depict the out-of-transit stellar photons collected per column on the NIRISS subarray as estimated by both our simulator and that of the NIRISS instrument team for a 100-hour observation program of GJ1132. In this case, our photon count per pixel exceeds that found by the NIRISS 1D SOSS simulator by $\sim 11\%$.

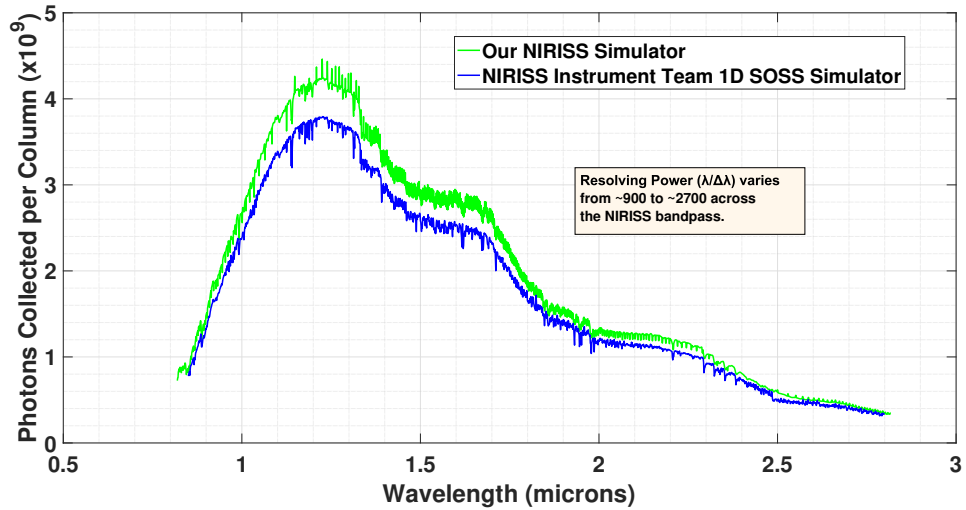


Figure 4.4: Comparison of the out-of-transit photon count per column of our NIRISS simulator to that of the NIRISS 1D SOSS simulator produced by the instrument design team. Here, we compare photon counts for 72 transit observations of GJ1132b. In this case, our photon count per column exceeds that found by the NIRISS 1D SOSS simulator by $\sim 11\%$. For all planetary systems where we compared the two codes, our results differed from those of the 1D SOSS simulator by 8 to 11%.

¹³<http://maestria.astro.umontreal.ca/niriss/simu1D/simu1D.php>

4.3.4.2 Observational Overhead

Observational overhead accounts for the fact that during actual JWST observations, not all of the telescope time devoted to a program will be used for science. Rather, some of the time will be used to slew the observatory or set up the instrument. In general, the clock time for a JWST observation is given by¹⁴

$$t_{\text{clock}} = (t_{\text{slew}} + t_{\text{science}} + t_{\text{instrument}}) \times 1.16 + t_{\text{scheduling}}. \quad (4.12)$$

Here, $t_{\text{slew}} = 30$ min is the time to slew the telescope;¹⁵ t_{science} is the observation time, both in and out of transit; $t_{\text{instrument}} = 17.1$ min is an instrument overhead time;¹⁶ and $t_{\text{scheduling}} = 60$ min is the additional JWST time required when scheduling an observation with a start time more precise than 24 hours, certainly the case with exoplanet transits. The factor of 1.16 is observatory overhead that takes into account losses due to calibrations and dead time of JWST. We note that equation 4.12 is the current expression used to estimate clock time, but the expression is likely to change when JWST is operational.

To determine the effects of observational overhead, we modify equations 4.10 and 4.11 so that we calculate N_{shot} and S_{atm} using the number of transits, n_{trans} ,

¹⁴<https://jwst-docs.stsci.edu/display/JPPOM/Overhead+Duration+Components>

¹⁵The time to slew JWST varies depending upon the slew distance in arcseconds: <https://jwst-docs.stsci.edu/display/JPPOM/Slew+Times>. The longest slew time reported, for 180 degrees, is ~ 1 hour, so we use half of this time for all TESS systems.

¹⁶Instrument overhead time includes target acquisition (10 minutes) and filter wheel movements. Further details can be found at: <https://jwst-docs.stsci.edu/display/JPPOM/NIRISS+Overheads>.

and transit duration (T_{14}), t_{trans} , as

$$N_{\text{shot}} = \sqrt{2 \eta n_{\text{trans}} t_{\text{trans}} F_*}, \quad (4.13)$$

and

$$S_{\text{atm}} = \eta n_{\text{trans}} t_{\text{trans}} F_{\text{atm}}. \quad (4.14)$$

Then, we calculate n_{trans} using

$$n_{\text{trans}} = \frac{t_{\text{obs}}}{(2t_{\text{trans}} + 47.1) \times 1.16 + 60}, \quad (4.15)$$

where times are in minutes. As before, we use $t_{\text{obs}} = 10 \text{ hrs} = 600 \text{ min}$. Note that equations 4.13 and 4.14 could be used in place of equations 4.10 and 4.11 in the simple observation program described previously, where we apportion equal amounts of time in and out of transit, but in that case, the number of transits would be calculated using the simple relationship $n_{\text{trans}} = t_{\text{obs}}/(2t_{\text{trans}})$.

4.3.4.3 Systematic Noise per Transit Observation

In Section 4.4, we examine the effects of the systematic noise per transit observation on TESS discoveries, and then go on to show the spectra that may be anticipated for NIRISS observation programs of the known exoplanet K2-3c, both with and without considering this systematic noise. A relatively low residual systematic noise level is anticipated for JWST observations, since with existing instruments we have already achieved residual noise levels of ~ 25 ppm with Hubble (Kreidberg

et al., 2014a) and ~ 30 ppm using Spitzer (Demory et al., 2016). Here we adopt the noise floor used by Greene et al. (2016) of 20 ppm for one planetary transit. We note that the exact nature of the systematic noise will not be known until JWST commissioning. However, we expect that any residual noise will be due to systematic effects that can be represented by an equivalent sine wave because instrumental noise is commonly bandwidth-filtered. For the observation programs we examine, multiple transits will be observed, with the state of the instrument different for each telescope pointing, and where the equivalent sine wave representing systematic effects is most likely observed at a different phase during each observation. Thus, we assume the systematic noise will decrease as the square root of the number of independent measurements, or transits.

To determine the effects of systematic noise on the integrated S/N across the entire NIRISS bandpass for the Sullivan et al. (2015) anticipated TESS planets, we apply the systematic noise to each resolution element (i.e., 2 columns). However, in presenting spectra for K2-3c, we bin the S/N into 64 bins across the NIRISS bandpass. Binning increases S/N above that of the individual NIRISS resolution elements, but reduces resolving power across the bandpass. For 64 bins, resolving power ranges from almost 30 at the blue cut-off to about 95 at the red cut-off. For the spectrum where systematic noise has been incorporated, the noise in each of the 64 bins is calculated with

$$N_{\text{bin,total}} = \sqrt{N_{\text{bin,shot}}^2 + \left(\frac{20 \times 10^{-6}}{\sqrt{n_{\text{trans}}}} \times F_{\text{bin,*}} \right)^2}, \quad (4.16)$$

where the second term inside the square root on the right-hand side of the equation represents the adjustment made due to systematic noise.

4.4 Results and Discussion

In this section, we present our analysis of attainable NIRISS S/N in 10-hour observation programs of the [Sullivan et al. \(2015\)](#) predicted TESS planets, as well as our analysis of 50 Monte Carlo realizations of TESS primary mission data, with comparisons to expected S/N for known exoplanets. For comparison, we also examine the S/N attainable in more intensive 100-hour observation programs of the potentially habitable [Sullivan et al. \(2015\)](#) predicted TESS planets—those with $R_{\text{pl}} \leq 1.5R_{\oplus}$ and cool or temperate equilibrium temperatures. First we show our results for the [Sullivan et al. \(2015\)](#) planets where mass is calculated using the [Chen & Kipping \(2017\)](#) mass model. We then explore the effects of planetary composition, observational overhead, and existence of planetary clouds on these results. We next show our results from analyzing 50 Monte Carlo realizations of TESS primary mission data. We conclude the section by presenting our analysis of the effects of systematic noise on our predicted S/N for the TESS anticipated discoveries. Additionally, based upon our estimates of NIRISS S/N, we create sample spectra for the known exoplanet K2-3c, illustrating the effects of adding systematic noise to a simulated spectrum.

4.4.1 S/N for Anticipated TESS Discoveries

We present our predicted NIRISS S/N for the anticipated TESS discoveries published by [Sullivan et al. \(2015\)](#) in Figure 4.5, overplotting our predictions of S/N for existing exoplanet discoveries from space-based and ground-based surveys. We then present predicted S/N for more thorough 100-hour observation programs of potentially habitable TESS discoveries in Figure 4.6. Our results show that TESS is likely to discover many super-Earths and sub-Neptunes ($1.5R_{\oplus} < R_{\text{pl}} \leq 4R_{\oplus}$) that are more amenable to atmospheric characterization than anything we have yet discovered. However, our results also show that for small exoplanets ($R_{\text{pl}} \leq 1.5R_{\oplus}$) we expect very few TESS discoveries will be better for atmospheric characterization than already-discovered exoplanets. We emphasize that this outcome is based upon Kepler-derived occurrence rates, and that co-planar compact multi-planet systems (e.g., TRAPPIST-1) may be under-represented in the predicted TESS planet yield.

Closer examination of the small anticipated TESS planets with the highest anticipated S/N reveals the properties of the TESS discoveries likely to be most conducive to follow-on atmospheric characterization studies. Two small planets achieved NIRISS S/N higher than TRAPPIST-1b without saturating any of the NIRISS pixels, and three cold or temperate planets with radii $\sim 1.4R_{\oplus}$ have a higher S/N than LHS1140b. Table 4.4 shows that these planetary systems with high S/N values have system parameters comparable to those of GJ1132b, LHS1140b, and the TRAPPIST-1 planets, so it is not surprising that NIRISS is able to attain a high S/N. The planets orbit nearby low radii ultra-cool or M dwarf host stars, which

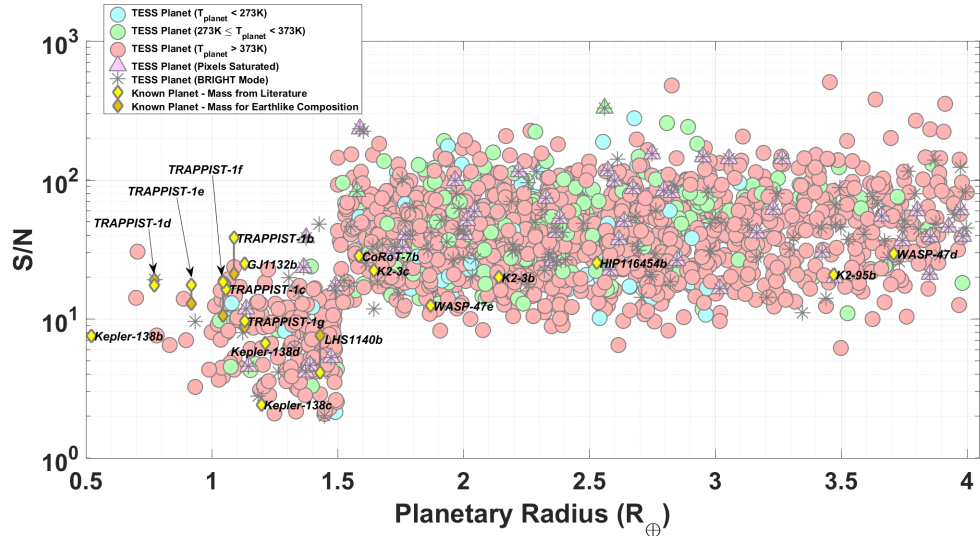


Figure 4.5: Integrated Signal-to-Noise (S/N) we predict for NIRISS detection of the atmosphere of anticipated TESS planets in 10-hour observation programs of all planets. We also show integrated S/N for known exoplanets discovered from space-based and ground-based surveys. Our results show that TESS is likely to find many planets with promising properties in the radius regime $1.5R_{\oplus} < R_{\text{pl}} < 4R_{\oplus}$. In particular, the planets found in the radius regime $1.5R_{\oplus} < R_{\text{pl}} < 2R_{\oplus}$ will help to define the parameter space where planetary atmospheres transition from hydrogen-dominated to high molecular weights. However, TESS is unlikely to discover many terrestrial-sized planets more amenable to atmospheric characterization than those that have already been discovered. We emphasize that the outcome for terrestrial-sized planets is based upon Kepler-derived occurrence rates, and that co-planar compact multi-planet systems (e.g., TRAPPIST-1) may be under-represented in the predicted TESS planet yield. The apparent step function at $1.5R_{\oplus}$ results from assuming all planets with $R_{\text{pl}} \leq 1.5R_{\oplus}$ have water atmospheres, and all planets with $1.5R_{\oplus} < R_{\text{pl}} < 4R_{\oplus}$ have hydrogen-dominated atmospheres (Section 4.3.3.2).

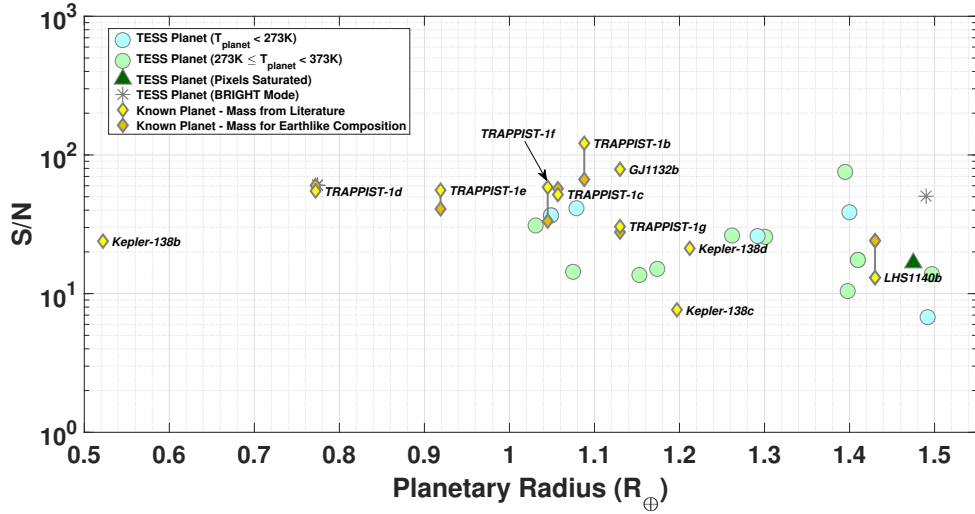


Figure 4.6: Integrated Signal-to-Noise (S/N) we predict for NIRISS detection of the atmosphere in 100-hour observation programs of potentially habitable anticipated TESS discoveries—planets with $R_{\text{pl}} \leq 1.5R_{\oplus}$ and cool or temperate equilibrium temperatures. We compare resulting S/N to that of known discoveries from space-based and ground-based surveys.

appear relatively bright when observed in the J-band. In addition, from Table 4.4 we see that the estimated radial velocity semi-amplitude for these planets is $\sim 3 \text{ m s}^{-1}$ or greater for all except the smallest planet. Thus, we anticipate that current or forthcoming radial velocity instruments should be able to estimate the masses of these promising TESS discoveries.

Two prominent features in Figure 4.5 lead us to examine the following questions. First, why are there so many cold and temperate super-Earth and sub-Neptune planets with S/N comparable to or better than that for hot planets with similar planetary radii? Does this make sense, given the fact that we would expect the scale height of the planetary atmosphere, and thus the signal, to increase with an increase in the temperature of the planet’s atmosphere? Second, the S/N appears

TESS	J	V	Distance	Stellar	Stellar	Planet	Planet	Radial	NIRISS
Catalog				Radius	Temperature	Radius	Temperature	Velocity	S/N
Number	(mag)	(mag)	(pc)	R_*	(K)	R_{pl}	(K)	Semi-	
				(R_{\odot})		(R_{\oplus})		Amplitude	
								(m s^{-1})	
922	11.3	16.2	13.2	0.116	2730	1.39	290	6.65	23.8
1308	7.97	11.6	8.71	0.249	3370	1.49	289	2.90	16.0
1622	11.4	15.3	26.9	0.172	3230	0.71	693	0.76	30.6
1745	10.4	14.0	25.1	0.224	3340	1.09	904	2.97	23.6
1919	12.2	16.8	22.4	0.119	2840	1.40	236	5.08	12.2

NOTE:

Planetary systems parameters, including the estimate of radial velocity semi-amplitude, are taken from [Sullivan et al. \(2015\)](#). NIRISS signal-to-noise is calculated in this work.

Table 4.4: Terrestrial-Sized Anticipated TESS Planets with High NIRISS S/N

relatively flat in the radius regime $1.5R_{\oplus} < R_{\text{pl}} \leq 4R_{\oplus}$. But according to equation 4.6, the signal produced by the atmosphere should increase as density decreases, and Figure 4.1 shows that density decreases with planetary radius across this regime. Why doesn't the S/N have a positive slope on this plot?

The considerable number of cold and temperate super-Earths and sub-Neptunes with relatively high S/N is explained by realizing that the signal depends not only on the temperature of the planet's atmosphere, but also on the planet's density and the cross sectional area of the star, as can be seen by examining equations 4.5 and 4.6. In Figure 4.7, we plot a dimensionless ratio of planet temperature, density, and stellar cross-sectional area (the "signal") versus planet temperature. The colorbar on the plot indicates stellar temperature. We see that many of the cold and temperate planets predicted by [Sullivan et al. \(2015\)](#) have system parameters that produce a high value of the dimensionless ratio, which accounts for the considerable number of cold and temperate planets with relatively high S/N values in Figure 4.5. In particular, the highest values of the dimensionless ratio are produced by those

planets orbiting the coolest host stars, which also have the smallest cross-sectional areas.

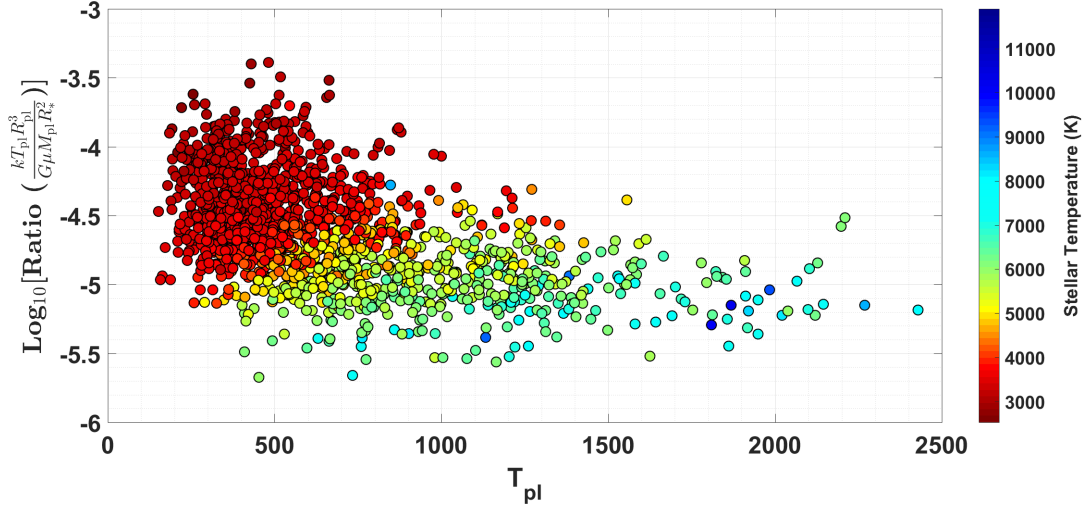


Figure 4.7: Examination of cold and temperate planets suitable for atmospheric characterization. The signal produced by the planetary atmosphere varies directly with the planet’s temperature, and inversely with the planetary density and stellar cross-sectional area. We create a dimensionless ratio of these factors by multiplying by $\frac{k}{\mu G}$, where k is Boltzmann’s constant, G is Newton’s gravitational constant, and μ is the molecular weight in kg of the hydrogen-dominated atmosphere. We then plot this dimensionless ratio versus planetary temperature for those planets with $1.5R_{\oplus} < R_{pl} \leq 4R_{\oplus}$. We see that many of the cold and temperate planets predicted by Sullivan et al. (2015) have system parameters that produce a high value of the dimensionless ratio, which accounts for the considerable number of cold and temperate planets with relatively high S/N values in Figure 4.5. In particular, the highest values of the dimensionless ratio are produced by those planets orbiting the coolest host stars, which also have the smallest cross-sectional areas.

The apparent flatness of the S/N in the radius regime $1.5R_{\oplus} < R_{pl} \leq 4R_{\oplus}$ of Figure 4.5 results from a combination of the type of preselected target stars chosen for the TESS survey and the planet occurrence rates employed for those target stars in the Sullivan et al. (2015) simulations. For multiple planets orbiting the same host star, we expect S/N to increase with planetary radius. However, the TESS planets

of various radii orbit different host stars, and other factors will also influence S/N. Nevertheless, we would expect that if we plot S/N versus R_{pl} for a large sample of TESS host stars of the same stellar type, the best-fit line should have a positive slope. We illustrate this in Figure 4.8 by showing S/N versus planetary radius, with the symbols color-coded by stellar temperature. By referring to each color (i.e., each stellar type) separately, we detect a trend towards a positive slope across the sub-Neptune radius regime. To aid in visualization, we also plot best-fit lines for host stars of three different stellar temperatures. However, we emphasize that we are only looking qualitatively for a positive trend. Although the host stars have the same stellar temperatures, the planetary systems vary in stellar radii, distance from Earth (affecting brightness and thus on-sky efficiency η), and planetary equilibrium temperature, all of which will influence the attainable S/N. For the best-fit lines, we used 18 planetary systems to compute the best-fit line for 3300K, 22 planetary systems to compute the best-fit line for 3500K, and 25 planetary systems (with $5470\text{K} \leq T_{\text{eff}} \leq 5530\text{K}$) to compute the best-fit line for 5500K. For each of the three stellar temperatures examined, we use the same PHOENIX stellar model spectra for all host stars.

4.4.2 Sensitivity to Planetary Composition

We turn now to an examination of the sensitivity of our results shown in Figure 4.5 to various factors, beginning with planetary composition. For each TESS planet, Figure 4.9 shows the S/N attained for three homogeneous compositions,

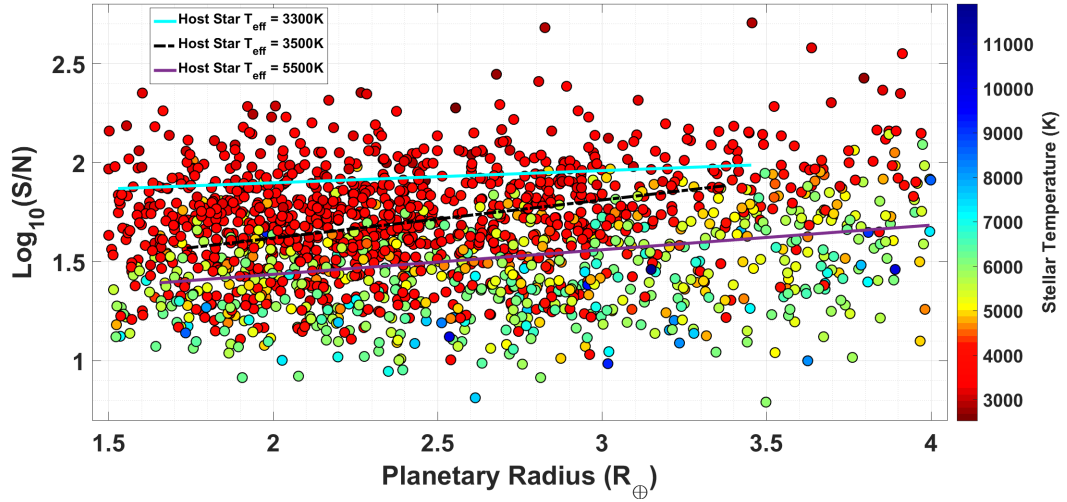


Figure 4.8: For a given host star, the signal produced by the planetary atmosphere during transit increases with planetary radius. However, this increase in S/N with planetary radius is hidden in Figure 4.5 since all of the TESS systems are shown on a single Figure. In addition, the stellar types observed vary with planetary radius due to a combination of the preselected target stars chosen for the TESS mission and the planet occurrence rates employed for those target stars in the Sullivan et al. (2015) simulations. Here, we plot S/N versus planetary radius with the color of the symbols indicating stellar temperature. By referring to each color (i.e., each stellar type) in this Figure separately, we detect a trend towards a positive slope across the sub-Neptune radius regime. To aid in visualization, we also plot best-fit lines for host stars of three different stellar temperatures. From top to bottom, the three lines are for host star temperatures of 3300K, 3500K, and 5500K. Each line spans planetary radii values between the lowest and highest planetary radii values used in fitting the line.

where we calculated masses using theoretical models (Seager et al., 2007), and we compare to the S/N predicted for the Chen & Kipping (2017) empirical mass model. For comparison, we overplot our predictions of S/N attainable for currently known exoplanets.

In the radius regime examined, the NIRISS S/N attained for a given TESS planet with an ice composition is 6 to 7 times higher than that attained for an iron composition. The S/N values for the perovskite composition and Chen/Kipping mass model lie between the values for ice and iron. The wide variation of S/N for TESS planets of different compositions emphasizes the importance of constraining planetary masses prior to conducting JWST observations (Batalha et al., 2017a).

Low density is one factor contributing to a relatively high S/N. Referring to Figure 4.1, we see that the relatively low estimated densities of the TRAPPIST-1 planets contribute to their high S/N. In fact, the S/N for most of the TRAPPIST-1 planets falls when density is estimated using an Earth-like composition. Interestingly, although the current density estimate of LHS-1142b lies near that of a dense, pure iron planet, its S/N rivals that of similarly-sized TESS planets with masses calculated using the Chen/Kipping empirical relationship. In fact, the S/N for LHS-1142b rises when we estimate its mass using an Earth-like composition. Thus, as the masses of these planets are further constrained, we would expect our predictions of S/N to change.

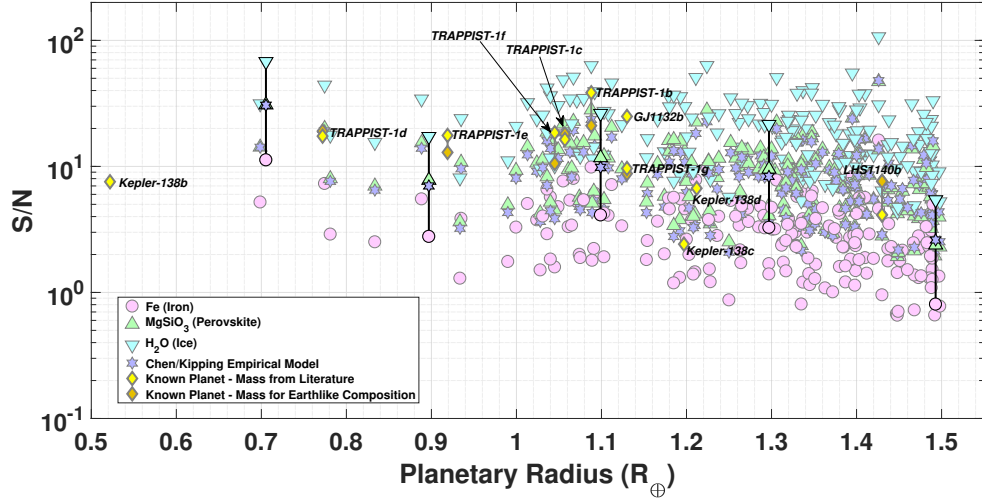


Figure 4.9: Integrated Signal-to-Noise (S/N) we predict for NIRISS detection of the atmosphere in 10-hour observation programs of anticipated TESS planets for four different compositions. We calculated masses for the three homogeneously composed planets using the theoretical relationships of Seager et al. (2007), and we compared this to the S/N attainable with masses calculated using the Chen & Kipping (2017) empirical relationship. We overplot our predictions of S/N for known exoplanets, where we used the masses reported in Tables 4.1, 4.2, and 4.3. For the Sullivan et al. (2015) anticipated TESS planets, our predicted NIRISS S/N for an ice composition is 6 to 7 times higher than that for a dense iron composition. To better visualize the impact of various compositions on a single planet, we chose five anticipated TESS planets and outlined the four symbols (one for each composition) in black, joining the symbols with a black line.

4.4.3 Observational Overhead Effects

The S/N estimates presented thus far assume 10-hour observation programs, with equal amounts of time in and out of transit. Figure 4.10 shows that when observational overhead is considered in 10-hour observation programs, we will have a 7 to 9 percent decrease in predicted S/N for the TESS anticipated discoveries, with the coolest host stars suffering the largest impacts. Planetary systems with short transit durations suffer greater effects from the *constant time periods per visit* required to set up the JWST observatory or the NIRISS instrument. The reason for this impact is that planetary systems with short transit durations must be revisited more often in order to accumulate a given amount of scientific observation time. Thus, a greater amount of the total requested telescope time is devoted to non-scientific activities. Note that the apparent decrease in the number of cool host stars with planetary radius in Figure 4.10 is due to a combination of a selection bias for M dwarfs in the preselected TESS target stars, the planet occurrence rates used in the Sullivan et al. (2015) simulations, and increased TESS sensitivity to shorter period exoplanets.

4.4.4 Cloud Effects

The presence of clouds in planetary atmospheres decreases S/N by effectively blocking transmission of stellar radiation above some pressure level, allowing us to detect spectral features due to molecular absorption only in regions of the atmosphere above the level where clouds condense. As shown in Figure 4.11, we estimate

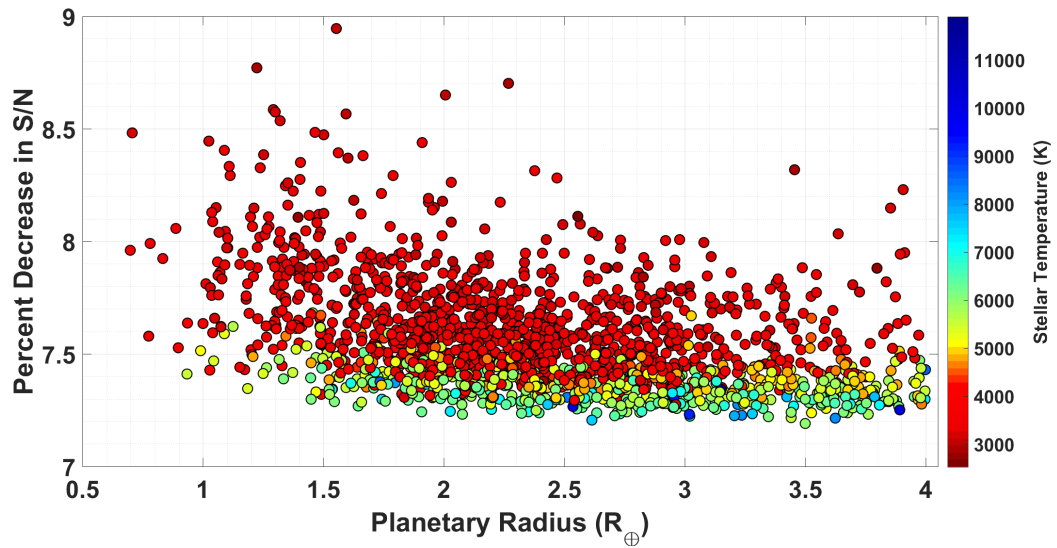


Figure 4.10: Our predictions of the percent decrease in Signal-to-Noise (S/N) when considering observational overhead for 10-hour observation programs. In general, the coolest stars suffer the highest percent decrease in S/N. This is because the transit duration is generally shorter for cooler—and thus smaller—stars, where the orbital semi-major axis is shorter. The decrease in the number of cool host stars with planetary radius results from a combination of a selection bias for M dwarfs in the preselected TESS target stars, the planet occurrence rates used in the [Sullivan et al. \(2015\)](#) simulations, and increased TESS sensitivity to shorter period exoplanets.

the effects of clouds on S/N by placing an opaque cloud deck at 10 mbar. For small planets with water atmospheres ($R_{\text{pl}} \leq 1.5R_{\oplus}$), the S/N for clear atmospheres shown in Figure 4.5 is about 1.5 times higher than that found for cloudy atmospheres. For larger planets with hydrogen-dominated atmospheres ($1.5R_{\oplus} < R_{\text{pl}} \leq 4R_{\oplus}$), we find that S/N for clear atmospheres is about 5.5 times greater than that for cloudy atmospheres.

During actual observations, the percentage of cloud cover as well as the pressure level where clouds condense will vary depending upon the observed exoplanet. In Section 4.5, we explore this statistical variation in cloud effects by applying random fluctuations to the number of atmospheric scale heights through which water absorption can be detected.

4.4.5 Analysis Of 50 Trials of TESS Primary Mission

The catalog of anticipated TESS discoveries published by Sullivan et al. (2015) represents only one possible outcome for the planet yield from the TESS primary mission. To achieve a more statistically robust prediction of the suitability of TESS primary mission discoveries to atmospheric characterization, we examined data from 50 Monte Carlo realizations of the TESS primary mission. We present our results as Figure 4.12, a 2-dimensional histogram in S/N- R_{pl} space. We place thirty bins logarithmically from 10^0 to 10^3 along the S/N axis, and every $0.1R_{\oplus}$ along the R_{pl} axis. The number of planets found in a given bin is an average of the number predicted over all 50 trials of the TESS primary mission, and represents the expected

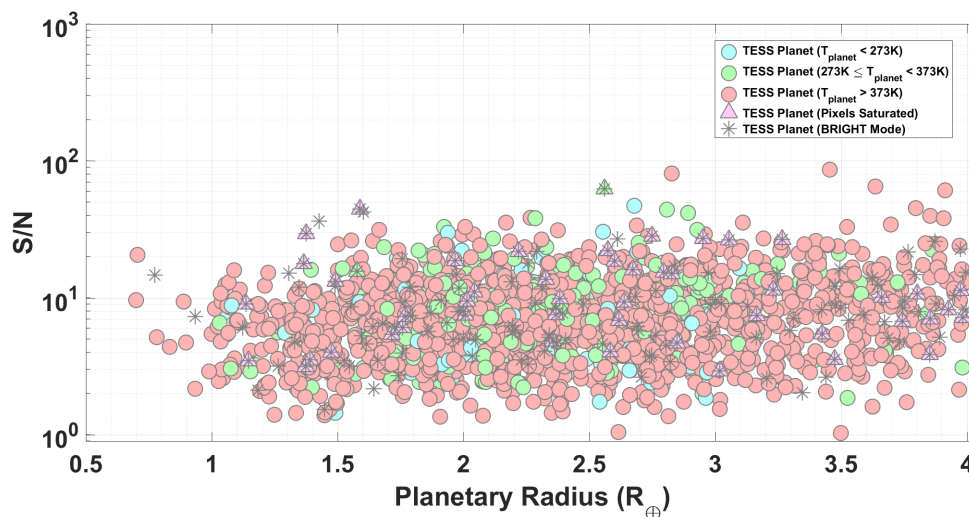


Figure 4.11: Our predictions showing the anticipated Signal-to-Noise (S/N) achievable in 10-hour observation programs of planets with cloud decks placed at a pressure of 10 mbar. When compared to our results in Figure 4.5, cloudy atmospheres will reduce S/N values for small planets with water atmospheres ($R_{\text{pl}} \leq 1.5R_{\oplus}$) by about 1.5 times, and for larger planets with hydrogen-dominated atmospheres ($1.5 < R_{\text{pl}} \leq 4R_{\oplus}$) by about 5.5 times.

number of planets we will discover in that regime. As in Figure 4.5, we overplot our predictions of S/N for existing discoveries from space-based and ground-based surveys. Figure 4.12 supports our conclusions from Figure 4.5. While TESS will discover very few terrestrial-sized planets more amenable to atmospheric characterization than those that have already been discovered, TESS *is* likely to find many planets with promising properties in the radius regime $1.5R_{\oplus} < R_{\text{pl}} \leq 4R_{\oplus}$. However, we reiterate that this outcome is based upon Kepler-derived occurrence rates, and that co-planar compact multi-planet systems (e.g., TRAPPIST-1) may be under-represented in the predicted TESS planet yield.

Numerical integration of various regions of Figure 4.12 provides some quantitative insight into our conclusions. For example, if we integrate the region with $R_{\text{pl}} < R_{\text{GJ1132b}}$ and $S/N > S/N_{\text{GJ1132b}}$, we find that TESS is likely to discover only 1.84 planets in this regime over its 2-year primary mission. Similarly, TESS is likely to discover only about 6.18 cold or temperate planets ($T < 373\text{K}$) with radii less than and S/N higher than LHS1140b with an Earthlike density. In the radius regime $1.5R_{\oplus} < R_{\text{pl}} \leq 2R_{\oplus}$, TESS will discover about 245 planets over its primary mission with S/N greater than that of K2-3c. Similarly, in the radius regime $2R_{\oplus} < R_{\text{pl}} \leq 2.5R_{\oplus}$, we predict TESS will discover about 391 planets with S/N greater than that of K2-3b. Thus, TESS is likely to discover many promising super-Earth and sub-Neptune-sized exoplanet targets.

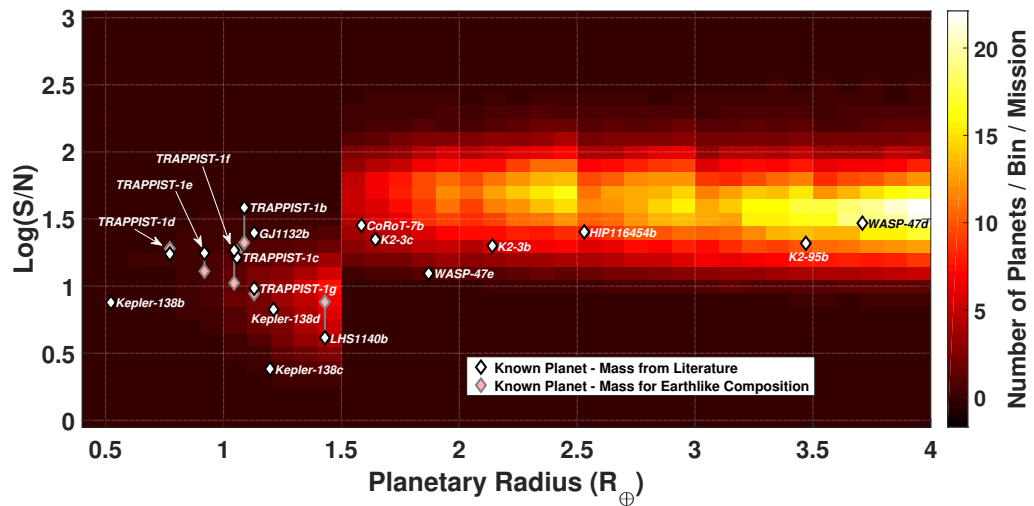


Figure 4.12: Two-dimensional histogram showing the Signal-to-Noise (S/N) we predict for 10-hour observation programs based upon analysis of 50 Monte Carlo realizations of the TESS primary mission. Thirty bins are logarithmically spaced from 10^0 to 10^3 along the S/N axis, and bins are spaced every $0.1R_{\oplus}$ along the R_{pl} axis. For comparison, we overplot our results for existing discoveries from space-based and ground-based surveys.

4.4.6 Sensitivity to Systematic Noise

We present our estimates of NIRISS S/N sensitivity to systematic noise for the anticipated TESS discoveries in Figure 4.13. For 10-hour observation programs, we find that systematic noise will cause S/N to decrease by up to $\sim 20\%$ (i.e., S/N is ~ 0.8 times that without systematic noise), with the hottest host stars suffering the greatest effects. One reason that the hottest stars are affected most is that the TESS discoveries with the hottest host stars also generally have the longest orbital periods and the longest transit durations, so that fewer visits are required to accumulate 10 hours of observation time. Since the systematic noise decreases with the square root of the number of observed transits, the hottest host stars are thus affected more. Brighter host stars also generally suffer greater effects.

Importantly, we note that the spectral scale at which we apply the systematic noise is critical. In our results for the 1,984 Sullivan et al. (2015) TESS planets, we applied the systematic noise to the resolution elements (i.e., two columns) across the NIRISS bandpass. If instead the systematic noise is applied to larger bins (e.g., 32 columns) across the NIRISS bandpass, the effects of the systematic noise are magnified. In Figure 4.14, we show the results of applying systematic noise to the known exoplanet K2-3c. As described in Section 4.3.4.3, we apply the systematic noise to each of the 64 bins in our spectra. For K2-3c, we also tried applying the systematic noise to each NIRISS resolution element (i.e., two columns) instead, and we found that in that case the effects of the systematic noise on each of the 64 bins was negligible.

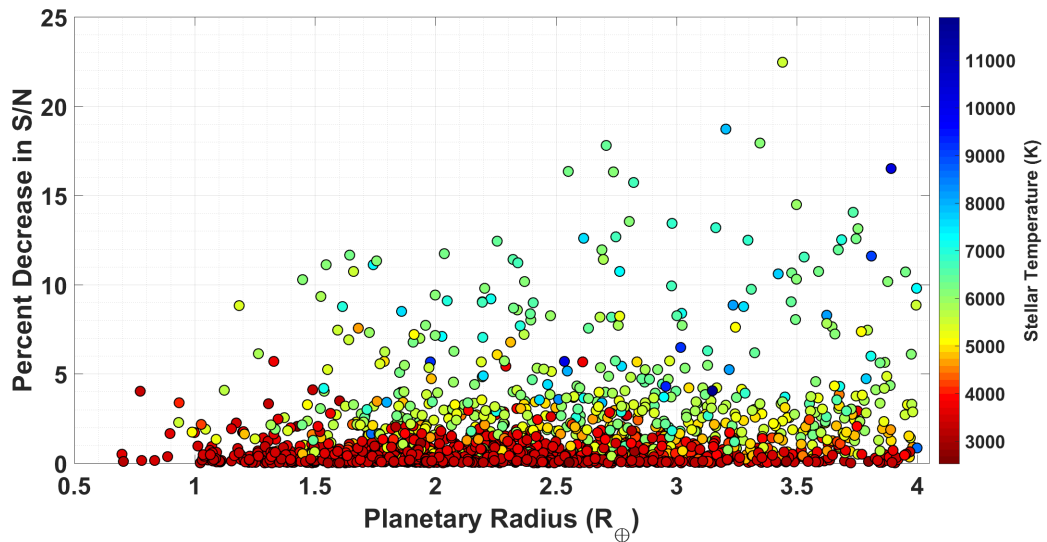


Figure 4.13: Our predictions of the percent decrease in Signal-to-Noise (S/N) when a 20 ppm residual noise level—decreasing with the square root of the number of transits—is incorporated into 10-hour observation programs. The decrease in S/N is not uniform across all Sullivan et al. (2015) anticipated TESS discoveries, but varies with planetary system properties, reaching up to $\sim 20\%$ for some systems. In 10-hour observation programs, the hottest host stars are affected the most by systematic noise. This is partially because the orbital period and transit duration of TESS discoveries are longest for the hottest host stars, so that fewer visits are required to complete a given observation program. In addition, the brightest host stars suffer the greatest effects.

We use estimated S/N for a 10-hour observation program of K2-3c, which we assume has a hydrogen-dominated atmosphere, to develop the predicted transmission spectra of Figure 4.14. In the S/N presented in previous sections, photon noise constitutes the major noise source. In our predicted spectral plot for K2-3c, we show two spectra: one where photon noise dominates, and one with systematic noise incorporated in addition to all other sources of noise. Although the addition of systematic noise does affect the output spectra in Figure 4.14, the variation of transit depth with wavelength—as caused by water lines in an atmosphere—will still be detectable in a 10-hour observation program.

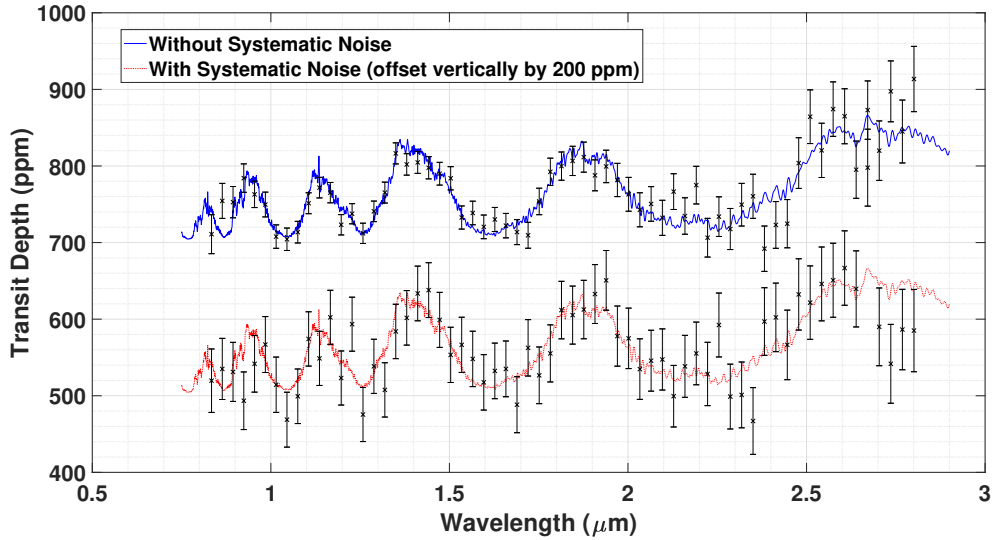


Figure 4.14: Predicted transit spectra resulting from a 10-hour observation program of the known exoplanet K2-3c, assuming a hydrogen-dominated atmosphere. Spectra for the planet are shown both with and without systematic noise. The systematic noise is set at 20 ppm for one transit, but decreases as the square root of the number of transits. Although systematic noise will affect the quality of the observed spectrum, the variation of transit depth with wavelength should be detectable.

4.5 JWST Follow-Up Observation Program

We have shown in Sections 4.4.1 and 4.4.5 that TESS will discover many promising exoplanet targets for atmospheric characterization in the radius regime $1.5R_{\oplus} < R_{\text{pl}} < 2R_{\oplus}$. Recent work has shown that planetary atmospheres are likely to transition from hydrogen-dominated atmospheres to high molecular weight atmospheres within this radius regime (Fulton et al., 2017b; Rogers, 2015). Here, we use our results from Section 4.4 to estimate the scope of a JWST follow-up observation program of TESS discoveries that would enable us to map the transition from low to high mean molecular weight atmospheres.

We have run 100,000 trials of a synthetic observing program that seeks to map the nature of the transition from low to high molecular weight atmospheres. For each trial, we compare our synthetic observations to two possible functions that describe the transition in water vapor absorption going from exo-Neptunes to the domain of rocky planets at small radii. Since our simulations use a step function in atmospheric composition with the discontinuity at $1.5R_{\oplus}$, that step function is our first possible transition function. We compare it to a function wherein the water absorption measured in equivalent scale heights (see below) is assumed to be a linear function of the log of planetary radius, similar to the power law described by Kreidberg et al. (2014a). For each trial observing program, we calculate the Bayesian Information Criterion for the step function, and the power law after fitting to the data. Since our synthetic data are based on the step function, a sufficiently intense JWST transit spectroscopy program should produce a BIC value exceeding

(by > 10) the BIC value for the best fitting power law.

Our trials seek to incorporate realistic observing conditions as much as possible. The primary limitation will be due to the presence of clouds on the exoplanets. For hot Jupiters, clouds reduce the magnitude of the water absorption from ~ 5 scale heights in a clear atmosphere to much less. In their statistical study, [Iyer et al. \(2016\)](#) found an average of 1.8 scale heights of absorption in hot Jupiters, and [Fu et al. \(2017\)](#) found 1.4 scale heights with a larger sample. We therefore scale our calculated spectra and S/N ratios to the equivalent of N scale heights for each planet, and we vary N by adding random fluctuations to mimic the cosmic variation in cloud occurrence. (This assumes that the cloud properties of small planets are statistically similar to the hot Jupiters, but inadequate statistics for small planets allow no alternative.) We adopt a log-normal distribution for N , using the average value (1.4) and dispersion ($\sigma = 0.13$ in \log_{10}), from [Fu et al. \(2017\)](#). For each trial, we choose 2 to 15 planets orbiting stars brighter than $J=10$, picking an equal number randomly from both ranges in radii ($< 1.5R_{\oplus}$ and $\geq 1.5R_{\oplus}$). We observe one transit of each planet, we include JWST's charged overhead per visit to each transit based on equation [4.12](#), and we convert our scaled synthetic spectra and signal-to-noise ratios to an equivalent number of scale heights, under the assumption that every planet has a mean molecular weight of 2.3 (i.e., a H-He atmosphere). This scaling is not physical, but conveniently serves to illustrate the transition between the H-He and water vapor atmospheres.

We fit our transition functions to the number of equivalent scale heights of absorption as a function of planetary radius. The number of equivalent scale heights

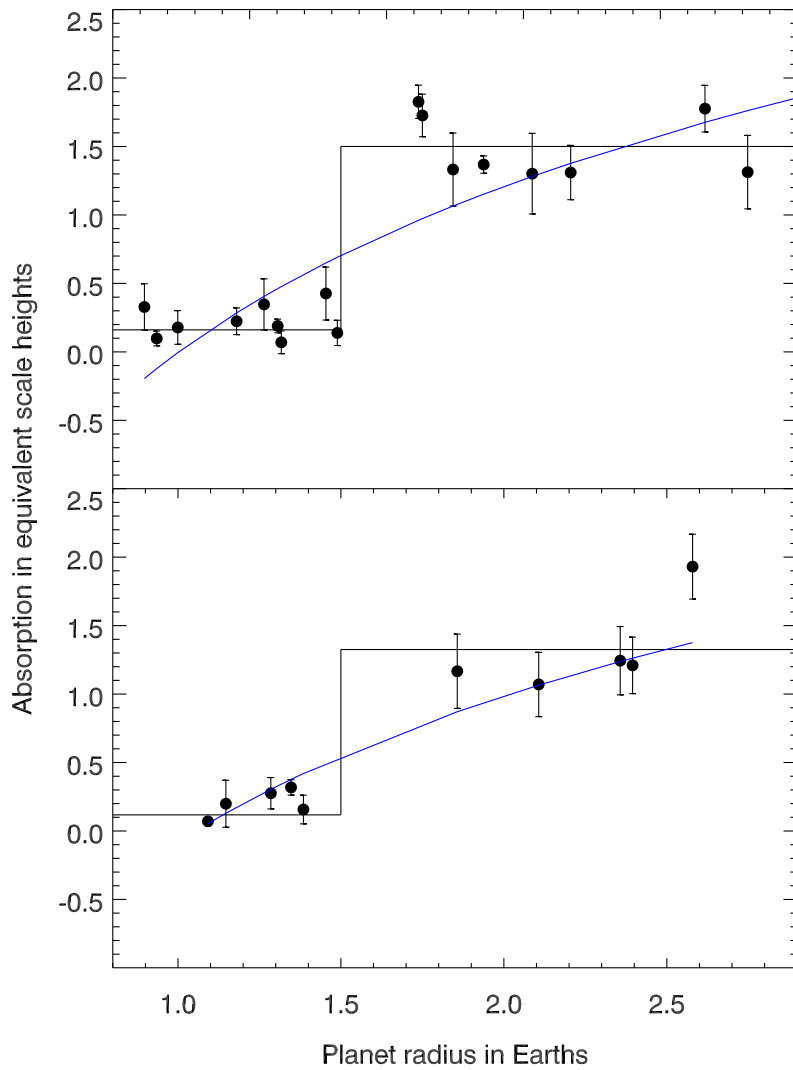


Figure 4.15: Examples of results from two of our trial synthetic JWST observing programs using NIRISS. The abscissa is planet radius, and the ordinate is the equivalent number of scale heights of absorption, scaled to a mean molecular weight of 2.3. Since the small planets have water vapor atmospheres, their equivalent scale height values are small, reflecting the high molecular weight of their atmospheres. The top panel observes 18 planets in 117 hours of charged JWST time, at one transit per planet. It easily discriminates the step function from the poorly-fitting power law (blue line), with a BIC difference of 180. The lower panel shows results from a 66-hour observing program, wherein the power law (blue line) is a better fit (BIC smaller by 15) than the step function, in spite of the fact that these synthetic data were drawn from a distribution using the step function.

effectively measures the composition of the atmosphere, because the high molecular weight atmospheres will produce smaller signals. Our simulated observing program interprets those small signals as fewer equivalent scale heights. This simple method follows [Miller-Ricci et al. \(2009\)](#), and is a conservative (worst-case) procedure because more sophisticated analysis methods (e.g., retrievals for all planets as per [Line et al. 2013b](#)) would have greater ability to clarify the nature of the transition function.

Figure 4.15 shows two example trials from our simulation. The top panel shows a 117-hour observing program that obtains spectra of 9 planets in each radius regime (18 planets total), and it easily discriminates the step function from the power law. However, the lower panel shows a 66-hour observing program (10 total planets) that would conclude in favor of the power law, in spite of the fact that the synthetic data are derived from the step function. That occurs because two of the rocky planets have very small observed errors, and by chance the power law that connects them extends reasonably well to the larger planets. Since the planets with the smallest errors dominate χ^2 (and hence the BIC), the result in this case would erroneously conclude in favor of a power law relation between planet radius and atmospheric mean molecular weight.

Considering the totality of our 100,000 trials, we find good news, and bad news, both illustrated in Figure 4.16. The good news is that the TESS planets will enable even modest observing programs (between 60 and 100 hours of charged time) to define the physical nature of the transition between low and high molecular weight atmospheres. Specifically, the cumulative distribution of ΔBIC values for

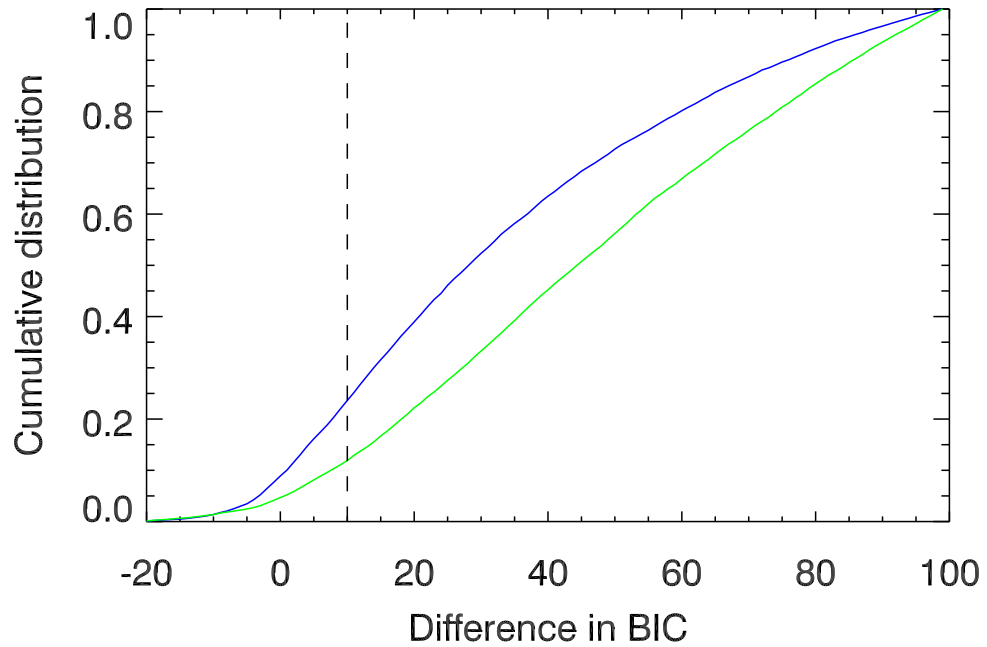


Figure 4.16: Cumulative distribution of the difference in Bayesian Information Criteria for best fit step functions and the power law, wherein a difference greater than 10 (vertical dashed line) strongly favors the step function. The blue line shows the distribution for observing programs between 60 and 100 hours of charged JWST time, and the green line is for programs between 100 and 140 hours.

the 60-100 hour observing programs exceeds 10 (strongly supporting the step function) 76% of the time, and 100-140 hour observing programs have ΔBIC exceeding 10 for 88% of the trials. The bad news is that even the largest programs fall short of the levels of certainty that are desired for such an important problem (we would prefer 95% or greater). However, inspection of the failed cases (as in the lower panel of Figure 4.15) indicates how to achieve greater certainty. Observing programs often fail when a relatively few planets are observed to high signal-to-noise, and they dominate the BIC values, but the random nature of cloud coverage biases the best fitting function. Specifically, a cloudy atmosphere on a small planet combined with a clear atmosphere on a larger planet, can be mis-interpreted as a trend in mean molecular weight. Other caveats are that the transition from low- to high-molecular-weight atmospheres may be more complex than either of our simple models, and the nature and occurrence of clouds may differ from the statistical behavior that we have inferred based on current observations. Nevertheless, based on our simple assumptions, we conclude that good observing program design (uniformity in observed signal-to-noise from planet to planet), combined with analysis methods that break degeneracies between water abundance and cloud coverage, can potentially enable JWST observing programs of 60 to 100 hours to define the nature of the transition in atmospheric properties going from Neptunes to rocky super-Earths.

4.6 Summary and Conclusion

We have analyzed the anticipated TESS discoveries published by [Sullivan et al. \(2015\)](#), as well as 50 Monte Carlo realizations of the TESS primary mission produced by [Bouma et al. \(2017\)](#), to predict the NIRISS S/N likely to be achieved in transmission spectroscopy of the TESS planets. In order to predict the TESS discoveries with the best prospects for atmospheric characterization, we compared our results to predictions of S/N for 18 already known exoplanets. In calculating S/N, we modeled all $R_{\text{pl}} \leq 1.5R_{\oplus}$ planets with cloud-free pure water atmospheres, and all $1.5R_{\oplus} < R_{\text{pl}} < 4R_{\oplus}$ planets with clear hydrogen-dominated atmospheres. We investigated the effects of planetary composition, cloud cover, and systematic noise on our results. We found:

1. TESS will find hundreds of super-Earths and sub-Neptunes ($1.5R_{\oplus} < R_{\text{pl}} \leq 4R_{\oplus}$) capable of producing higher S/N than already known exoplanets. In particular, TESS is likely to produce ~ 245 planets within the radius regime ($1.5R_{\oplus} < R_{\text{pl}} \leq 2R_{\oplus}$) with S/N higher than that of K2-3c, and ~ 391 planets within the radius regime ($2R_{\oplus} < R_{\text{pl}} \leq 2.5R_{\oplus}$) with S/N higher than that of K2-3b.
2. TESS will find very few terrestrial-sized planets ($R_{\text{pl}} \leq 1.5R_{\oplus}$) with NIRISS S/N better than that of already-known exoplanets such as the TRAPPIST-1 planets, GJ1132b, or LHS1140b. However, we note that the [Sullivan et al. \(2015\)](#) and [Bouma et al. \(2017\)](#) anticipated TESS discoveries are based upon

the Kepler planet occurrence rates reported by [Fressin et al. \(2013\)](#) and [Dressing & Charbonneau \(2015\)](#), and that co-planar compact multi-planet systems orbiting ultra-cool dwarf stars (e.g., TRAPPIST-1) may be under-represented. Such systems may boost the number of TESS-discovered rocky planets producing high NIRISS S/N in transmission spectroscopy.

3. Our analysis of planetary composition shows that attainable S/N is sensitive to planet density. NIRISS S/N for an ice composition is 6 to 7 times higher than that for a dense iron composition. Thus, we emphasize the importance of constraining planet mass prior to conducting JWST follow-up observations for a given planet.
4. The presence of an opaque cloud deck at 10 mbar will decrease attainable S/N by about 5.5 times for planets with hydrogen-dominated atmospheres. Longer observation programs will be required to constrain molecular abundances in planets with clouds. In addition, [Greene et al. \(2016\)](#) showed that 1-11 spectra, requiring multiple JWST instruments, may be necessary to fully constrain cloudy atmospheres.
5. Residual systematic noise will decrease attainable S/N in 10-hour observation programs by up to $\sim 20\%$, with hotter and brighter host stars suffering the most effects. We assume the systematic noise will decrease with the square root of the number of observed transits, so effects will be minimized in programs that observe more transits within a given total duration. We applied the systematic noise to each resolution element (i.e., 2 columns) when examining its effects on

the TESS planets.

6. We applied our NIRISS S/N calculations to estimate the required magnitude of a JWST follow-up program devoted to mapping the transition region between high molecular weight and hydrogen-dominated atmospheres. We conclude that the TESS planets will allow relatively modest observing programs (60 to 100 hours of charged JWST time) to define the nature of that transition (e.g., step function versus a power law). However, it will be necessary to design the observing program to have good uniformity in S/N, so that the results are not biased by a few planets with high S/N and unusual atmospheric conditions (e.g., cloud coverage).

4.7 Addendum

The results presented through Section 4.6 are based upon application of our NIRISS simulation routines to the [Sullivan et al. \(2015\)](#) TESS estimated planet yield, and have been published in [Louie et al. \(2018\)](#). Since that time, two papers have been published that warrant further discussion. As described in Chapter 2, [Barclay et al. \(2018\)](#) released a revised TESS planet yield based upon target stars in the actual TESS Input Catalog (TIC, [Stassun et al., 2018](#)). In addition, [Kempton et al. \(2018\)](#) developed a simple-to-compute analytic metric that can be applied to quickly filter those TESS discoveries most amenable to atmospheric characterization, which in turn identifies those planets to prioritize for rapid radial velocity follow-up. In this short section, I compare our results of NIRISS S/N for the predicted [Barclay](#)

et al. (2018) TESS planet yield to those of the Sullivan et al. (2015) projected planet yield. In addition, I downloaded the 80 available TESS confirmed transiting exoplanet discoveries from the Exoplanet Archive,¹⁷ and compare our calculations of NIRISS S/N to the Kempton et al. (2018) Transmission Spectroscopy Metric (TSM) for these planets.

4.7.1 NIRISS S/N for Barclay et al. (2018) TESS Planet Yield

Figure 4.17 presents our predicted NIRISS S/N for the projected Barclay et al. (2018) TESS planet yield, with predictions of S/N for previously known exoplanets (same as in Figure 4.5) overplotted for comparison. Comparing Figures 4.5 and 4.17 qualitatively, we can readily see that more of the Barclay et al. (2018) planetary systems must be observed in *bright* mode, and indeed more of those observations would exceed the saturation level of the NIRISS pixels. In addition, the number of planets appear sparser in the radii regimes $R_{\text{pl}} < 1.5R_{\oplus}$, as well as $1.5R_{\oplus} \leq R_{\text{pl}} < 2.5R_{\oplus}$ of Figure 4.17. The sparse appearance of planets in these radii regimes is not surprising, since Barclay et al. (2018) reported fewer planet discoveries in these regimes than Sullivan et al. (2015). See Figure 2.1.

Table 4.5 quantifies the trends seen by comparing Figures 4.5 and 4.17. Sullivan et al. (2015) report detecting 2.4 times the number of $R_{\text{pl}} < 1.5R_{\oplus}$ planets as Barclay et al. (2018), yet fewer of them must be observed in *bright* mode, and only 8 systems (4%) would result in pixel saturation, whereas 12 of the Barclay et al. (2018) systems (15%) would cause saturation. Similarly, Sullivan et al. (2015)

¹⁷<https://exoplanetarchive.ipac.caltech.edu/>, accessed 23 November 2020.

report detecting 2.1 times the number of $1.5R_{\oplus} \leq R_{\text{pl}} < 2.5R_{\oplus}$ planets as [Barclay et al. \(2018\)](#), yet fewer planets must be observed in *bright* mode and fewer systems would cause pixel saturation. For the $2.5R_{\oplus} \leq R_{\text{pl}} < 4.0R_{\oplus}$ radius regime, [Barclay et al. \(2018\)](#) would detect more systems, and again the percentage of systems that must be observed in *bright* mode and the percentage of systems resulting in pixel saturation are higher than for the [Sullivan et al. \(2015\)](#) systems. Examining the results from Table 4.5, it is also clear that the total number of $R_{\text{pl}} < 1.5R_{\oplus}$ planets differ: [Sullivan et al. \(2015\)](#) found 1833, while [Barclay et al. \(2018\)](#) reported 2150.

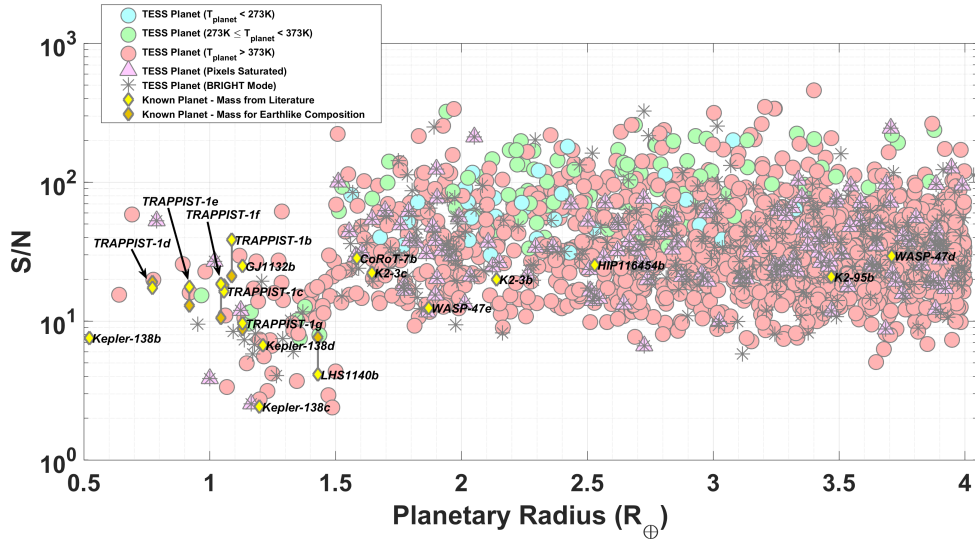


Figure 4.17: Same as Figure 4.5, but applied to the [Barclay et al. \(2018\)](#) predicted TESS discoveries. Compared to Figure 4.5, we see that more of the [Barclay et al. \(2018\)](#) planetary systems must be observed in *bright* mode, and indeed more of those observations would exceed the saturation level of the NIRISS pixels. In addition, the number of planets appear sparser in the radii regimes $R_{\text{pl}} < 1.5R_{\oplus}$, as well as $1.5R_{\oplus} \leq R_{\text{pl}} < 2.5R_{\oplus}$. While Figure 4.5 shows only 2 planets with NIRISS S/N greater than that of GJ1132b (without pixel saturation), 8 [Barclay et al. \(2018\)](#) planets meet those criteria.

As described in Chapter 2, [Barclay et al. \(2018\)](#) used the TIC Candidate

Planet Size		Sullivan	et al.	Systems	Barclay	et al.	Systems
		Number	J (mag) min	J (mag) max	Number	J (mag) min	J (mag) max
$R_{\text{pl}} < 1.5R_{\oplus}$	Total	192	4.961	13.57	80	1.791	11.8
	Bright	19 (10%)	4.961	8.210	24 (30%)	1.791	8.084
	Saturated	8 (4%)	4.961	7.238	12 (15%)	1.791	7.005
$1.5R_{\oplus} \leq R_{\text{pl}} < 2.5R_{\oplus}$	Total	871	3.862	15.23	410	4.348	12.756
	Bright	61 (7%)	3.862	8.349	96 (23%)	4.348	8.299
	Saturated	14 (1.6%)	3.862	7.326	33 (8%)	4.348	7.297
$2.5R_{\oplus} \leq R_{\text{pl}} < 4.0R_{\oplus}$	Total	770	3.397	14.49	1660	4.179	13.29
	Bright	77 (10%)	3.397	8.31	263 (16%)	4.179	8.41
	Saturated	27 (3.5%)	3.397	7.321	95 (6%)	4.179	7.36

NOTE:

Columns 3 and 6 show the number of planetary systems meeting various criteria. *Bright* refers to systems that must be observed in NIRISS Bright Mode, as described in Section 4.3.4. *Saturated* refers to those systems where the saturation level of 72000 electrons per pixel is exceeded during observations. The percentages in parentheses represent the percentage of systems in a given radius regime that meet the applied criterion. For example, 19 of 192, or 10%, of $R_{\text{pl}} < 1.5R_{\oplus}$ must be observed in *bright* mode.

Table 4.5: NIRISS Atmospheric Characterization Predictions for Sullivan et al. (2015) and Barclay et al. (2018) TESS Planet Yields—Comparison of Bright Mode and Saturation

Target List (CTL) as their stellar population. However, Barclay et al. (2018) noted that a particular problem in developing stellar catalogs based upon photometric colors is distinguishing between dwarf main sequence stars and subgiants. Gaia data release 2 (Gaia Collaboration et al., 2018, 2016) has been used to update stellar parameters (e.g., radii) in more recent versions of the TIC, but these updates were not incorporated into version 6.1 used to produce the Barclay et al. (2018) catalog. I manually examined the properties of Barclay et al. (2018) systems where the planetary radii were less than $1.5R_{\oplus}$. I excluded 7 systems from Figure 4.17 that appear to be subgiant stars, since the J-band magnitudes are too bright for the reported stellar radii. Table 4.6 lists the excluded systems. As a point of comparison, the closest M-dwarf star to Earth at 4.24 light years, Proxima Centauri, has a J-band magnitude of 5.357 and stellar temperature $T_{\text{eff}} \approx 3042$ K.

Barclay System	J (mag)	R_* (R_\odot)	$T_{*,\text{eff}}$ (K)	R_{pl} (R_\oplus)	T_{pl} (K)	NIRISS S/N
1023	5.486	0.266	3155	1.079	336	34.5
1024	5.486	0.266	3155	1.408	280	31.8
1025	5.486	0.266	3155	1.300	424	43.3
1927	3.501	0.377	3671	1.127	870	111.2
2018	2.962	0.703	3925	1.062	546	27.1
2123	4.953	0.422	3308	0.987	474	31.0
3651	1.791	0.300	3330	1.238	383	159.6

NOTE:

If observed using NIRISS, all systems in this Table would require use of *bright* mode, and all observations would result in pixel saturation.

Table 4.6: Probable Subgiant Stars in Barclay et al. (2018) $R_{\text{pl}} \leq 1.5R_\oplus$ TESS Planet Yield

The number of Barclay et al. (2018) systems that would require NIRISS observations in *bright* mode, and the number of systems that would saturate NIRISS pixels, is not surprising in light of the Chapter 2 comparisons between the Sullivan et al. (2015) and Barclay et al. (2018) simulated systems. Although Sullivan et al. (2015) detect larger numbers of $R_{\text{pl}} \leq 2.5R_\oplus$ planets, Barclay et al. (2018) report greater numbers of planets orbiting bright host stars (e.g., J-band magnitude ≤ 9) in this radius regime. See Figures 2.2 and 2.3.

The most encouraging difference between Figures 4.5 and 4.17 is the number of $R_{\text{pl}} < 1.5R_\oplus$ planets amenable to atmospheric characterization. While only two Sullivan et al. (2015) simulated planets attain NIRISS S/N greater than that of GJ1132b (without pixel saturation), 8 Barclay et al. (2018) planets meet those criteria. In Table 4.7, I list those 8 planets, as well as the temperate $R_{\text{pl}} < 1.5R_\oplus$ Barclay et al. (2018) planet with the highest NIRISS S/N.¹⁸ In addition, I note

¹⁸Two Barclay et al. (2018) planets are excluded from the Table since observations with NIRISS would result in pixel saturation. Two Sullivan et al. (2015) planets with NIRISS S/N greater than that of GJ1132b in the same radius regime would also result in pixel saturation.

Barclay System	J (mag)	R_* (R_\odot)	$T_{*,\text{eff}}$ (K)	R_{pl} (R_\oplus)	T_{pl} (K)	NIRISS S/N
2766	9.234	0.152	2947	1.287	684	61.4
3112	10.417	0.145	2985	0.692	641	58.6
606	9.754	0.230	3178	1.474	691	29.7
916	10.842	0.174	3027	1.119	731	29.6
212	8.299	0.231	3371	1.273	599	27.3
137	11.148	0.125	2763	1.185	413	26.9
166	9.236	0.202	3296	1.494	423	26.8
2203	8.896	0.202	3107	0.893	409	25.7
4255	9.169	0.237	3257	0.967	360	15.3

NOTE:

Here, we report the eight $R_{\text{pl}} \leq 1.5R_\oplus$ Barclay et al. (2018) planets that would attain the highest S/N if observed with NIRISS SOSS. Additionally, we report the temperate planet that would attain the highest NIRISS S/N during observations.

Table 4.7: Barclay et al. (2018) $R_{\text{pl}} \leq 1.5R_\oplus$ Simulated TESS Planets with Highest NIRISS S/N

that analysis of data from 50 trials of the TESS primary mission resulted in ~ 1.84 planets with $R_{\text{pl}} < R_{\text{GJ1132b}}$ and $\text{S/N} > \text{S/N}_{\text{GJ1132b}}$. In Table 4.7, 4 planets meet those same criteria. Thus, I conclude that although Barclay et al. (2018) report about 40% the number of $R_{\text{pl}} < 1.5R_\oplus$ planets compared to Sullivan et al. (2015), the planets reported make more suitable atmospheric characterization targets.

4.7.2 NIRISS S/N and Transmission Spectroscopy Metric for TESS

Confirmed Planets

Kempton et al. (2018) developed the Transmission Spectroscopy Metric (TSM) as a simple-to-compute analytic metric that could be applied to TESS discoveries to prioritize them for radial velocity (RV) follow-up observations. As mentioned in Chapter 1, planet mass determination via RV follow-up is critical prior to conducting

atmospheric characterization observations (Batalha et al., 2017a, 2019). The TSM can be applied to predict planet suitability for transmission spectroscopy not only for JWST follow-up observations, but also for future observatories such as ground-based Extremely Large Telescopes (ELTs) and the Atmospheric Remote-Sensing Infrared Exoplanet Large-survey (ARIEL, Tinetti et al., 2016).¹⁹

The Transmission Spectroscopy Metric (TSM) is calculated using (Kempton et al., 2018)

$$\text{TSM} = (\text{Scale Factor}) \times \frac{R_{\text{pl}}^3 T_{\text{pl}}}{M_{\text{pl}} R_*^2} 10^{-m_J/5}, \quad (4.17)$$

where m_J is J-band magnitude. The *Scale Factor* is a value defined in Kempton et al. (2018) Table 1 and is designed to give one-to-one scaling between the TSM and the meticulously calculated NIRISS S/N values of (Louie et al., 2018) for $m_J > 9$ host stars. The *Scale Factor* also absorbs unit conversion factors, allowing radii and planetary mass to be expressed in Earth and Solar units. Since the TSM was developed to correlate with the (Louie et al., 2018) NIRISS S/N, we would expect TSM and NIRISS S/N values for the TESS confirmed planets (CPs) to be approximately equal for those systems with $m_J > 9$ host stars.

Figure 4.18 shows predicted NIRISS S/N for TESS CPs. Numbers next to the data points correspond to the TESS CP in their order of listing within the Exoplanet Archive. Two of the $R_{\text{pl}} \leq 1.5R_{\oplus}$ TESS CPs have NIRISS S/N greater than that of GJ1132b, and they are LHS 3844b (CP #35)²⁰ and TOI-504b (CP

¹⁹<https://arielmision.space/>

²⁰I note that Kreidberg et al. (2019) reported Spitzer phase curve observations of LHS 3844b

Planet Name	CP Number	J (mag)	R_* (R_\odot)	$T_{*,\text{eff}}$ (K)	R_{pl} (R_\oplus)	T_{pl} (K)	NIRISS S/N	TSM	n_{groups}^a
TOI-270d	64	9.099	0.38	3386	2.13	340	170	207	4
LP 791-18c	37	11.599	0.17	2960	2.31	370	164	163	42
L 98-59d ^b	33	7.933	0.31	3412	1.57	409	159	233	3
HD 39091c ^{b,c}	80	4.869	1.1	6037	2.042	1170	118	229	2
HD 63433b ^{b,c}	22	5.624	0.91	5640	2.15	968	109	208	2
TOI-1130b	43	9.055	0.69	4250	3.65	810	104	126	4
HD 63433c ^{b,c}	23	5.624	0.91	5640	2.67	679	102	194	2
TOI-270c	63	9.099	0.38	3386	2.42	424	101	123	4
LHS 3844b	35	10.046	0.19	3036	1.303	805	38.0	40.6	10
TOI-540b	67	9.755	0.19	3216	0.903	611	36.7	39.7	8

NOTES:

^a Observational efficiency may be calculated using equation 4.9.

^b System must be observed using NIRISS *bright* mode.

^c Observation will saturate NIRISS pixels.

Table 4.8: TESS Confirmed Planets with Highest Estimated NIRISS S/N

et al. (2018) TSM values for TESS CPs. The NIRISS S/N values are color-coded according to the J-band magnitude of the system. The TSM value corresponding to a given CP is found by tracing a vertical line at the appropriate value of R_{pl} from the NIRISS S/N symbol to the TSM symbol above it. As expected, the TSM values for the dimmest systems (highest J-band magnitudes), or deepest blue colors, coincide most closely with the estimated NIRISS S/N. For brighter systems (lower J-band magnitudes), or redder colors, a larger gap appears between the TSM and estimated NIRISS S/N.

As Kempton et al. (2018) discussed, the Louie et al. (2018) NIRISS S/N estimates take into account the on-sky efficiency (equation 4.9), while the TSM does not. Thus, if desired, the TSM could be corrected by adjusting for the duty cycle. By visually examining the output results for the TESS CPs, I found that although the difference between NIRISS S/N and TSM correlates generally with J-band magnitude, the correlation is not exact. The value of n_{groups} may be a better predictor

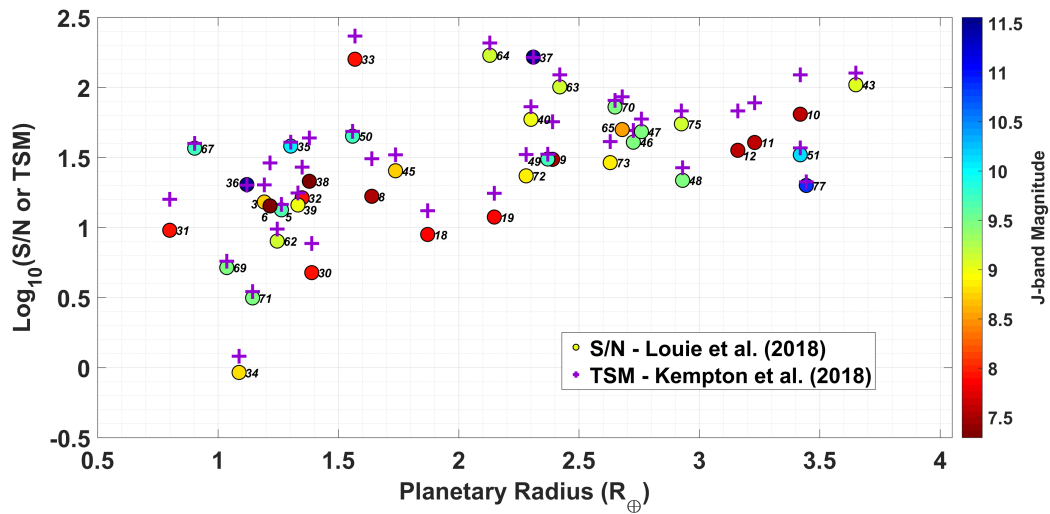


Figure 4.19: Here, we compare the results of our NIRISS S/N to the (Kempton et al., 2018) Transmission Spectroscopy Metric (TSM) for the TESS confirmed planets (CPs) shown in Figure 4.18. The NIRISS S/N values are color-coded according to the J-band magnitude of the system. The TSM value corresponding to a given CP is found by tracing a vertical line at the appropriate value of R_{p1} from the NIRISS S/N symbol to the TSM symbol above it. As expected, the TSM values for the dimmest systems (highest J-band magnitudes), or deepest blue colors, coincide most closely with the estimated NIRISS S/N.

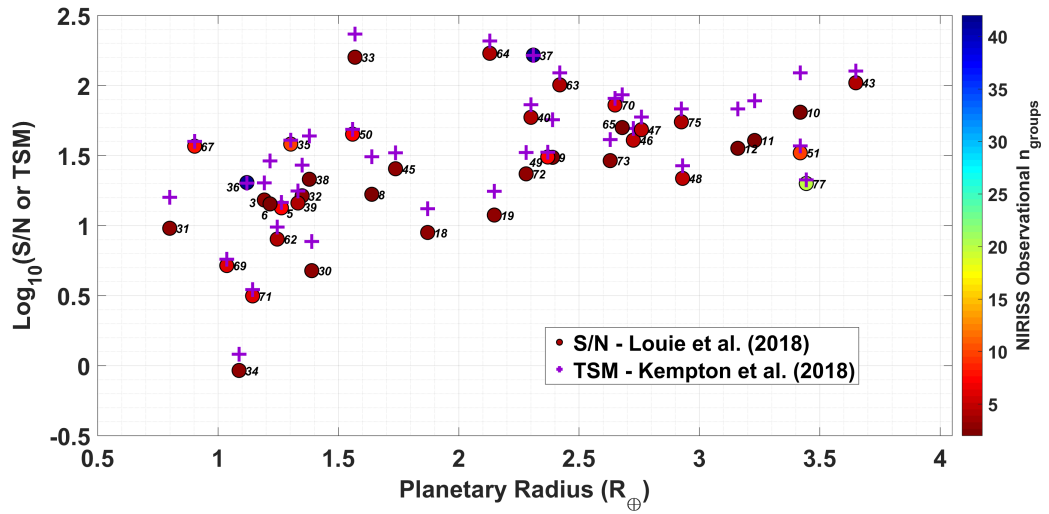


Figure 4.20: Here, we compare the results of our NIRISS S/N to the (Kempton et al., 2018) Transmission Spectroscopy Metric (TSM) for the TESS confirmed planets shown in Figure 4.18. The colorbar corresponds to n_{groups} required for NIRISS observations. In general, NIRISS S/N and TSM agree to within 10% for $n_{\text{groups}} > 6$ (on-sky efficiency $\eta \geq 0.714$). If $n_{\text{groups}} = 2$ (on-sky efficiency $\eta = 0.333$), TSM ranges from 1.7 to 2 times the value of estimated NIRISS S/N.

of whether or not the NIRISS S/N and TSM values will agree. Figure 4.20 shows a comparison between NIRISS S/N and TSM, but with a colorbar corresponding to n_{groups} . In general, NIRISS S/N and TSM agree to within 10% for $n_{\text{groups}} > 6$ (on-sky efficiency $\eta \geq 0.714$). If $n_{\text{groups}} = 2$ (on-sky efficiency $\eta = 0.333$), TSM ranges from 1.7 to 2 times the value of estimated NIRISS S/N. The TESS CPs for which estimated NIRISS S/N and TSM correspond most closely are LP 791-18b (CP #36; NIRISS S/N = 20.20; TSM = 20.02) and LP 791-18c (CP #37; NIRISS S/N = 164.0; TSM = 163.1), which are two planets residing in the same system, straddling the so-called *Fulton gap* (Figure 1.8), orbiting a $T_{\text{eff}} = 2960\text{K}$, J-magnitude 11.559 host star. The system would require $n_{\text{groups}} = 42$ (on-sky efficiency $\eta = 0.953$) to observe. [Kempton et al. \(2018\)](#) designed the TSM to apply not just to JWST, but to other observatories such as the ELTs. Thus, the differences between estimated NIRISS S/N and the TSM point to the importance of considering the facilities that will be used for atmospheric characterization when evaluating a TESS candidate exoplanet for follow-up mass determination.

4.7.3 Summary and Additional Conclusions

In this addendum, I have used the predicted NIRISS S/N to compare the suitability of the [Sullivan et al. \(2015\)](#) and [Barclay et al. \(2018\)](#) TESS simulated planetary systems for atmospheric characterization. In addition, I have estimated the NIRISS S/N for TESS confirmed planets (CPs) listed on the NASA Exoplanet Archive, and have compared that estimated S/N to the ([Kempton et al., 2018](#)) TSM.

I make the following conclusions:

1. Although [Barclay et al. \(2018\)](#) report about 40% the number of $R_{\text{pl}} < 1.5R_{\oplus}$ planets compared to [Sullivan et al. \(2015\)](#), the planets reported make more suitable atmospheric characterization targets.
2. Our estimated NIRISS S/N for TESS CPs is consistent with expectations from our analysis of the [Barclay et al. \(2018\)](#) projected TESS discoveries.
3. The [Kempton et al. \(2018\)](#) Transmission Spectroscopy Metric (TSM) is a valuable metric to prioritize TESS discoveries for follow-up mass determination, followed by atmospheric characterization. However, in prioritizing TESS targets, consideration should also be given to limitations of the instruments that will be used in the near-term for atmospheric characterization. In particular, efficiency of JWST/NIRISS observations will be reduced for bright exoplanet host stars.

Chapter 5: Transmission Spectroscopy of the Hot Jupiter KELT-7b

5.1 Overview

We present and analyze the composite 0.3 - 5.0 μm transmission spectrum of the hot Jupiter KELT-7b. The planet was observed with HST STIS and WFC3 as part of the Panchromatic Comparative Exoplanet Treasury (PanCET) program, and we combine those data with TESS Sector 19 and previously reported Spitzer IRAC observations. We present the HST STIS transmission spectrum for the first time. We examine the atmospheric properties of KELT-7b using the isothermal equilibrium chemistry PLATON retrieval code with the *dynesty* nested sampling package, and find our transmission spectrum is consistent with a subsolar C/O = $0.35^{+0.21}_{-0.19}$, high metallicity $\log \frac{Z}{Z_{\odot}} = 1.44^{+1.04}_{-0.88}$ atmosphere with high altitude clouds condensing at a pressure level $\log \frac{P_{\text{cloud}}}{\text{Pascals}} = 1.94^{+1.20}_{-0.78}$. By comparing the Bayesian evidence for models with and without various opacity sources, we found strong evidence for H₂O opacity, corresponding to a 3.6- σ detection in frequentist terms. By analyzing the STIS spectrum only, we found moderate evidence for K opacity, corresponding to a 3- σ detection. The planets's subsolar C/O ratio combined with supersolar metallicity are in agreement with predictions for disk-driven planet migration. Furthermore, KELT-7b's retrieved supersolar metallicity agrees well with the [Thorngren & Fortney \(2019\)](#)

predicted value of $21.08 \times$ solar, with an uncertainty of 7.00.

5.2 Introduction

[Bieryla et al. \(2015\)](#) reported the discovery and confirmation of KELT-7b, a hot Jupiter orbiting the bright ($V = 8.54$), rapidly rotating F-type star HD 33643. The planet was detected via the Kilodegree Extremely Little Telescope (KELT) transit survey ([Pepper et al., 2007](#)), which was specifically designed to detect planets orbiting bright ($8 < V < 10$) host stars (§1.1.1).

[Bieryla et al. \(2015\)](#) completed multiple observations to confirm the planetary nature of KELT-7b. They observed 10 full or partial transits in multiple bandpasses from ground-based facilities, and also collected 64 high-resolution ($R = 44,000$) spectra using the Tillinghast Reflector Echelle Spectrograph (TRES) at Mt. Hopkins, Arizona for both confirmation and radial velocity (RV) analyses. Using the transit observations and RVs as inputs, and relying upon Yonsei-Yale stellar evolutionary models ([Demarque et al., 2004](#)), [Bieryla et al. \(2015\)](#) derived the KELT-7 system parameters with the EXOFAST ([Eastman et al., 2013](#)) modeling package by performing a global fit of stellar and planetary properties. We use the [Bieryla et al. \(2015\)](#) system parameters in our analysis of this Chapter, and list those parameters in Table 5.1.

Because KELT-7 is a rapidly rotating ($\sim 73 \pm 0.5 \text{ km s}^{-1}$) star, the spin-orbit alignment of KELT-7b may be estimated by making use of the Rossiter-McLaughlin (RM) effect ([McLaughlin, 1924](#); [Rossiter, 1924](#)). [Bieryla et al. \(2015\)](#) found a spin-

Parameter	Units	Value
Stellar Parameters		
R_*	Radius (R_\odot)	$1.732^{+0.043}_{-0.045}$
M_*	Mass (M_\odot)	$1.535^{+0.066}_{-0.054}$
$\log g_*$	Surface Gravity (cgs)	4.149 ± 0.019
$T_{*,eff}$	Effective Temperature (K)	6789^{+50}_{-49}
Planetary Parameters:		
R_{pl}	Radius (R_\oplus)	$1.533^{+0.046}_{-0.047}$
M_{pl}	Mass (M_\oplus)	1.28 ± 0.18
ρ_{pl}	Density (g cm^{-3})	$0.442^{+0.079}_{-0.068}$
$T_{pl,eq}$	Equilibrium Temperature (K)	2048 ± 27
Primary Transit Parameters:		
T_o	Mid-Transit Time (BJD_{TDB})	$2456355.229809 \pm 0.000198$
P	Period (days)	2.7347749 ± 0.0000039
R_{pl}/R_*	Planet Radius (R_*)	$0.09097^{+0.00065}_{-0.00064}$
a_{pl}/R_*	Semi-major Axis (R_*)	$5.49^{+0.12}_{-0.11}$
i	Inclination (degrees)	$83.76^{+0.38}_{-0.37}$

NOTE:

All parameters from [Bieryla et al. \(2015\)](#).

Table 5.1: System Parameters for KELT-7b

orbit alignment of $\lambda = 9.7^\circ \pm 5.2^\circ$, where λ is angle between the angular momentum vector of the planetary orbit and the angular momentum vector of stellar rotation as viewed on-sky ([Ohta et al., 2005](#)). [Zhou et al. \(2016\)](#) applied Doppler tomography to the [Bieryla et al. \(2015\)](#) TRES spectra to recompute KELT-7b’s spin-orbit alignment as $\lambda = 2.7^\circ \pm 0.6^\circ$. [Zhou et al. \(2016\)](#) found no evidence that KELT-7’s rotation rate had been modified via star-planet tidal interactions, suggesting that the spin-orbit alignment is primordial. The spin-orbit alignment has implications for planet formation, which we discuss further in Section 5.7.

[Pluriel et al. \(2020\)](#) also characterized the atmosphere of KELT-7b. They analyzed Hubble Space Telescope (HST) Wide Field Camera 3 (WFC3) data for KELT-7b in both transmission and emission. For their transmission analysis, they

added transit depths from the Transiting Exoplanet Survey Satellite (TESS) and Spitzer’s Infrared Array Camera (IRAC, see [Garhart et al., 2020](#)). Their spectral retrievals showed that KELT-7b’s transmission spectrum is consistent with a cloud-free atmosphere containing H₂O and H⁻ opacities. We expand upon the [Pluriel et al. \(2020\)](#) analysis by examining HST Space Telescope Imaging Spectrograph (STIS) data, which comprises transit depths in the optical regime, for the first time. In Section [5.7](#), we compare the results of our analysis with those of [Pluriel et al. \(2020\)](#).

In this Chapter, we produce and analyze the 0.3 - 5.0 μm transmission spectrum for the hot Jupiter KELT-7b based upon observations ([§5.3](#)) from HST WFC3 and STIS, TESS, and Spitzer IRAC. We explain our data analysis procedures in Section [5.4](#) and our derivation of white light curves for WFC3 and STIS in Section [5.5](#). In Section [5.6](#), we explain our techniques to produce the HST WFC3 and STIS transmission spectra, and we present our composite transmission spectrum for all observations. In Section [5.7](#), we analyze this spectrum using the PLATON retrieval code (see [§1.2.3](#), as well as [Zhang et al., 2019, 2020](#)), compare our results with previous work, and discuss our findings within the larger context of planet formation. We summarize in Section [5.8](#), and discuss future work in Section [5.9](#).

5.3 Observations

The Panchromatic Comparative Exoplanet Treasury (PanCET) program is an HST General Observer (GO) Cycle 24 large program, led by principal investi-

gators (PIs) Professor David Sing and Dr. Mercedes López-Morales (Program ID 14767). The program was designed to observe planets ranging in size from super-Earths to Jupiter, across the entire spectral range of HST from ultraviolet (UV) to near infrared (NIR), with the goal of comparing the characteristics of planetary atmospheres, thus gaining insights into the underlying physical processes.

As part of the PanCET program, we observed three primary transits of KELT-7b, one on 28 February 2017 using the STIS G430L grating (0.29 to 0.57 μm), one on 25 August 2017 with the STIS G750L grating (0.52 to 1.0 μm), and one on 18 October 2017 using the WFC3 G141 grism (1.1 to 1.7 μm). In order to gather enough baseline out-of-transit (OOT) flux, we observed 5 orbits during each visit. We measured baseline OOT flux during 3 orbits and mid-transit flux during 2 orbits.

Our WFC3 visit began by using the F139M filter to take an undispersed image of the star, which was later used for wavelength calibration. WFC3 G141 grism observations took advantage of spatial scanning mode (see §1.3.3) to increase the signal-to-noise (S/N) of each exposure. We used round-trip scanning mode with 22 sec exposures, adopting a scanning rate of 0.9 arcsec sec⁻¹. We adopted NSAMP=4, allowing 4 non-destructive reads per exposure, and employed SPARS10 readout mode.¹ In total, we collected 93 science exposures using forward scan, and 93 in reverse scan mode. To reduce overhead, our observations were recorded on the 256×256 subarray.

Our STIS visit made use of successful strategies and instrument set-ups from

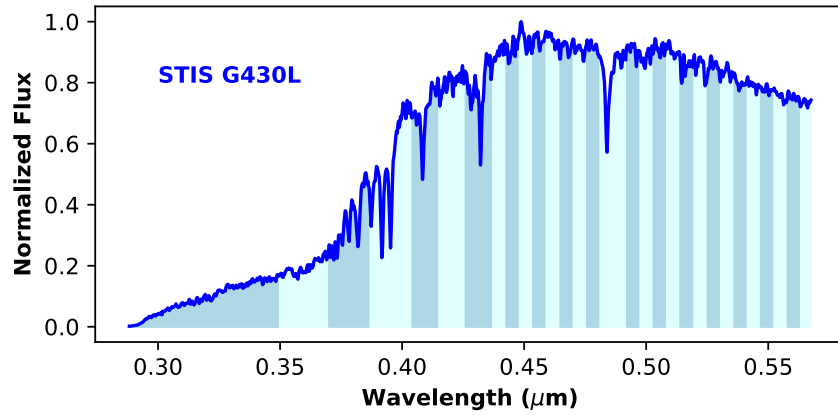
¹See the WFC3 Instrument Handbook at <https://www.stsci.edu/hst/instrumentation/wfc3> for further details.

past programs to maximize photometric precision. We utilized the 52×2 arcsec slit (widest available) to minimize slit losses and telescope breathing. We reduced overhead by reading out only the 1024×128 subarray upon which the STIS spectrum falls. To prepare the STIS array for science observations, we took a short 1 sec exposure at the beginning of each orbit, which was later discarded in our analyses. The purpose of this exposure was to eliminate a systematic effect observed in past programs (e.g., [Evans et al., 2013](#); [Nikolov et al., 2015, 2014](#); [Sing et al., 2015](#)), whereby the first STIS exposure of any given orbit produces a lower number of counts on the array. To increase the duty cycle, no changes were made to the instrument settings during the visit, and a single wavelength calibration (*wavecal*) exposure of the target was taken using the 52×0.2 arcsec slit following all transit observations. Flat fielding and tungsten lamp wavelength exposures were taken after transit observations as well, during Earth occultation of the last orbit.

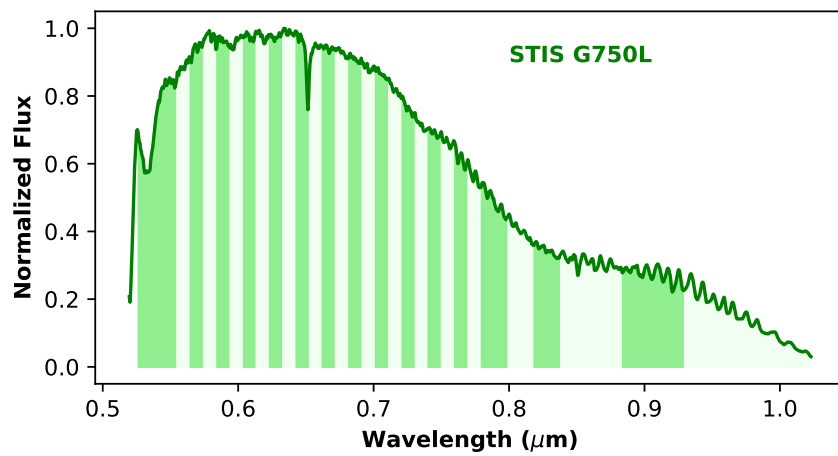
For STIS observations, we collected a total of 96 science exposures with the G430L grating, and 120 science exposures using the G750L grating. For all STIS exposures, the detector gain was set to 4. Exposure times of 116 sec and 88 sec were used for the G430L and G750L gratings, respectively.

Figure [5.1](#) shows example spectra from our STIS and WFC3 observations, with the alternating light and dark bands illustrating the wavelength bins used in our spectral analyses.

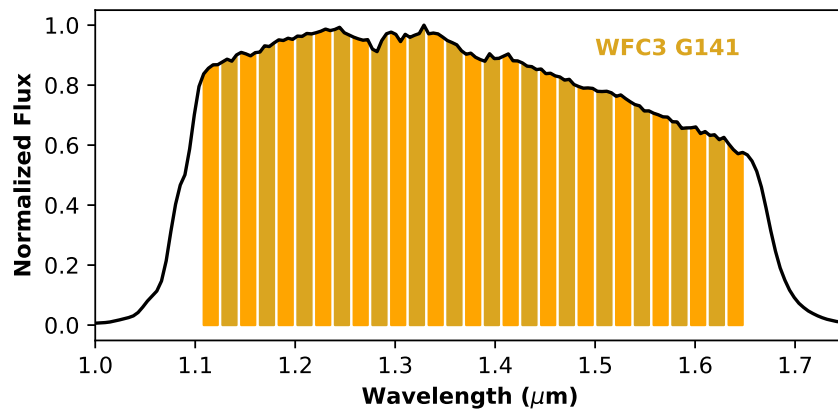
TESS observed KELT-7b at 2-min cadence between 28 November and 23 December 2019 during its Primary Mission survey of Sector 19 in the Northern Ecliptic Hemisphere. We analyze the TESS light curves to compute a transit depth in the



(a)



(b)



(c)

Figure 5.1: Example spectra from our observations using the HST STIS (a) G430L and (b) G750L gratings, as well as (c) WFC3 G141 grism. For each spectrum, alternating light and dark bands show the wavelength bins we adopted in our spectral data analyses.

TESS bandpass that we include in our transmission spectrum.

We complement our HST and TESS observations by adding Spitzer transit depths reported by [Garhart et al. \(2020\)](#) for the Infrared Array Camera (IRAC) 3.6 and 4.5 μm bandpasses.

5.4 Data Analysis

5.4.1 WFC3 Data Analysis

We follow the [Deming et al. \(2013\)](#) methods in our WFC3 data analysis, relying upon the [Wilkins et al. \(2014\)](#) procedures for wavelength calibration. We highlight key aspects of these methods and procedures in this section. We refer the reader to [Deming et al. \(2013\)](#) for extensive discussion of the analysis techniques.

We employed the KELT-7b **.ima.fits* files—hereafter referred to as IMA files—downloaded from the Mikulski Archive for Space Science (MAST) in our analysis of the spatially scanned spectra. When using round-trip scanning mode, the forward and reverse scans are recorded in separate IMA files. We analyzed the data for all forward and reverse scan directions separately—93 IMA files for the forward direction, and 93 for the reverse—producing transmission spectra for each direction, and then we combined the forward and reverse transmission spectra into our final WFC3 G141 transmission spectrum.

Our analysis begins by producing a WFC3 spectral data frame such as that shown in [Figure 5.2](#). During spatial scan mode, the electron accumulation levels are measured via a series of non-destructive reads of the detector throughout the

exposure, and these electron accumulation levels are recorded in extensions to the IMA data file. We followed the method described in the Appendix to [Deming et al. \(2013\)](#), which makes use of the difference between two successive non-destructive reads to find the spectrum over a limited range of rows. We then apply a top-hat function to that limited spectrum to zero out rows not containing the target star, which eliminates background flux levels except those close to the target star. By looking at the difference between each pair of non-destructive reads in turn, we gradually build up the spectral data frame for one IMA file. We next correct obviously hot pixels by applying filters to each row in two passes. In the first pass, we compare the value of a given pixel to the value of a 7-point median filter applied across the row for that pixel, setting obviously hot pixels (those where the difference between the pixel value and its median is > 2000 electron counts) equal to the median value. In the second pass, we look at the value of a given pixel across time. We compare its value for a given exposure (a given IMA file) to the value of a 7-point median filter calculated across all IMA files (comparing forward scan files to forward scan only, and reverse scan files to reverse scan only). If the pixel value differs from its median across time (across IMA files) by more than 4σ , then the value of that pixel is replaced by its median.

After constructing our initial spectral data frame, we apply wavelength and flat-field calibrations. Wavelength calibration uses a mathematical formula—dependent upon the centroid position of the target star nondispersed image² upon the subarray—to determine the wavelength of light falling upon a given pixel along the x-direction

²We downloaded the **.flt.fits* file with the target star nondispersed image from MAST.

of the first order spectrum. The WFC3 G141 grism wavelength calibration formula was originally developed by [Kuntschner et al. \(2009\)](#). However, [Wilkins et al. \(2014\)](#) applied empirically developed correction factors that modified some of the original coefficients in the mathematical formula by up to 10%. The empirically derived correction factors ensure that the stellar hydrogen lines for Paschen Beta ($1.282 \mu\text{m}$) and Brackett-12 ($1.646 \mu\text{m}$) appear at the correct wavelengths in the observed stellar spectrum. We apply the [Wilkins et al. \(2014\)](#) empirically modified wavelength calibration in our analysis, and we also check to ensure that the Paschen Beta hydrogen line is at the expected wavelength value.

We next apply a wavelength-dependent flat field calibration, which is a function of where the stellar spectrum falls upon the subarray. Following this calibration, we perform additional steps—again in two passes—to check for discrepant pixels across time (across IMA files) in our spectral data frame. In the first pass, for a given row, we perform a linear fit of the value of a given pixel across time (across IMA files) to the sum of all pixels in that row across time. If the value of a pixel in a given IMA file differs by more than 8σ from the linear fit, then we replace the value of that pixel with the value of the linear fit. In the second pass, we perform a linear regression analysis, and replace any pixels differing by greater than 4σ from the fit. In practice, the number of pixels replaced by our 4σ fit was miniscule, less than 2 pixels per spectral data frame ($\sim 10^{-3}$ %). Following these corrections, we perform a final 5-point median filter check across rows in each IMA file to eliminate any remaining discrepant pixels. During this check, we replace any pixel differing from its median value by greater than 8σ with its median.

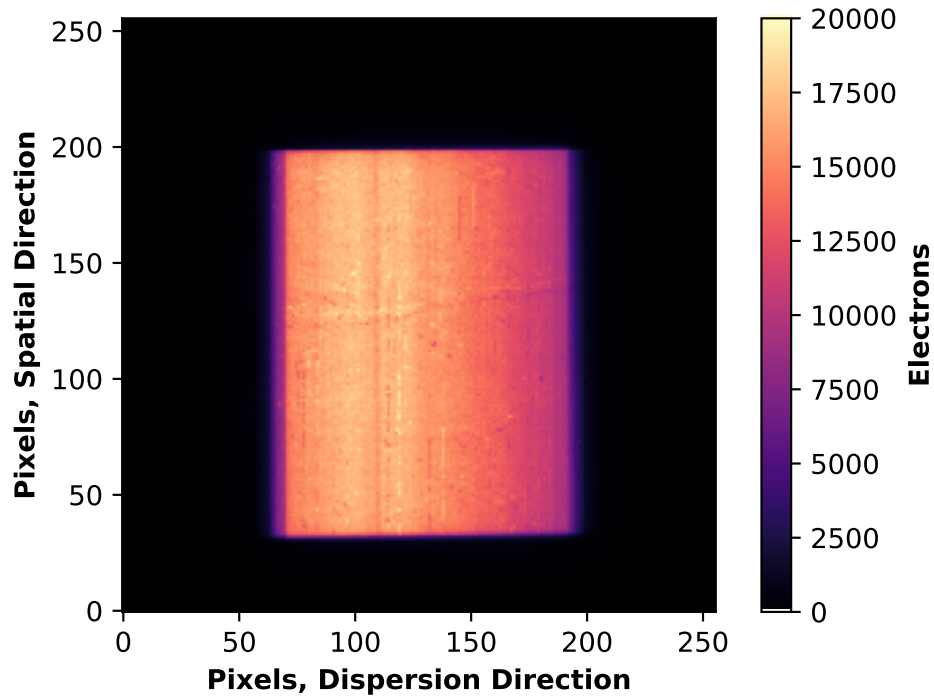


Figure 5.2: Example spatial scan image of KELT-7 upon the 256×256 WFC3 subarray following flat-fielding and background subtraction. The scan height spans 168 pixels.

As a final step in our initial calibration, we subtract any residual background from our spectral data frame. We find the background flux level by computing the median value of those pixels outside of our spectral data frame. Figure 5.2 shows a spatially scanned image of KELT-7b upon the 256×256 WFC3 subarray following flat-fielding, background subtraction, and smoothing of discrepant pixels.

For each 2-dimensional (2D) spatially scanned image and each IMA file, we create a 1-dimensional (1D) stellar spectrum, such as that depicted in Figure 5.1c, by summing each column of the 2D image. These 1D stellar spectra provide the starting point to produce both our white light curve (§5.5.1) and our transmission

spectrum (§5.6.1).

5.4.2 STIS Data Analysis

Our STIS data analysis includes procedures similar to those used for our WFC3 analysis, but is simpler since movement of the spectrum upon the detector is minimized, and our analysis begins with precalibrated data files. We employed the KELT-7b **.flt.fits* files—hereafter referred to as FLT files—downloaded from MAST in our analysis of G430L and G750L spectra. STIS science data recorded in FLT files are preprocessed for bias subtraction, dark subtraction, flat-fielding, and linearity correction using the Space Telescope Science Institute (STScI) *calstis*³ calibration pipeline.

One FLT data file is produced for each orbit, with individual spectra for each orbit saved as FITS file extensions. We analyzed 93 G430L spectra and 120 G750L spectra. Example spectra—as read from the FITS file extensions—are depicted upon the 1024×128 STIS subarray in Figure 5.3. The green box surrounding the spectrum shows the pixel range that we used in our analysis.

After loading our spectral images, we correct discrepant pixels using methods similar to those employed for our WFC3 analysis. We correct the pixels in two passes, where for each pass we compare pixels only within a given orbit. First, we check for extreme values by comparing a given pixel value on the array to a 7-point median filter value calculated for that same pixel across exposures for a given orbit.

³See the STIS Data Handbook at https://www.stsci.edu/files/live/sites/www/files/home/hst/instrumentation/stis/documentation/_documents/stis_dhb.pdf for further details.

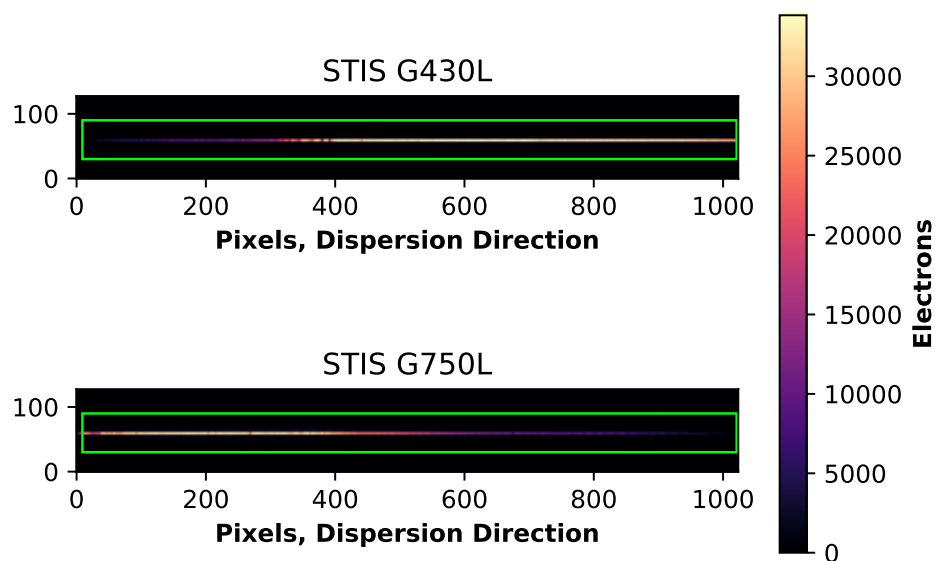


Figure 5.3: Example images of STIS G430L and G750L spectra upon the 1024×128 subarray. The green box, which spans 1014 pixels in the dispersion direction and 30 pixels in the spatial (vertical) direction, shows the pixel range that we used in our analysis.

This first pass corrects any pixels differing from the median by more than 20%, if the absolute difference from the median is greater than 80 electron counts. Any such discrepant pixel value is replaced by its median value. In the second pass, we replace any pixel by its median value if the pixel value differs from its 7-point median value (across orbital exposures) by greater than 4σ .

Next, we create 1D spectra, like those shown in Figure 5.1a and b, by summing along the columns of each spectral image. This summation provides the flux level associated with each column in the dispersion, or x, direction. We calculate the associated wavelength for each column by reading the reference x-direction pixel and reference wavelength from the FLT file, and then applying the dispersion in the $\pm x$ direction. The reference wavelength for the G430L grism is 4300 Å, while that for the G750L grism is 7751 Å. The dispersion for the G430L grating is 2.73 Å/pixel, and that for the G750L grating is 4.92 Å/pixel. As with our WFC3 analysis, we perform our spectral data analysis (§5.6.2) based upon the 1D spectra.

5.4.3 TESS Data Analysis

We downloaded the KELT-7b transit light curve file from MAST, and analyzed the 9 observed Sector 19 transits to compute the transit depth and uncertainty in the TESS bandpass. We first extracted the 9 transits from the complete 2-min cadence TESS light curve for Sector 19, and then we normalized each transit with its median out-of-transit flux. For each of the 9 transits, we generated theoretical transit curves using the methods of Mandel & Agol (2002), employing the Bieryla et al. (2015)

Telescope	Wavelength (μm)	Bandwidth (μm)	Transit Depth (ppm)	Uncertainty (ppm)
TESS ^a	0.7865	0.4	7920	175
Spitzer ^b	3.6	0.8	7925	62
Spitzer	4.5	1.0	8092	36

NOTES:

^a We analyzed TESS Sector 19 observations of KELT-7b to calculate TESS transit depth and errors. See Section 5.4.3.

^b Spitzer IRAC transit depths and errors from Garhart et al. (2020).

Table 5.2: KELT-7b TESS and Spitzer Transit Depths and Uncertainties

values for Period P , inclination i , and semi-major axis a/R_* , as well as the Claret (2017) quadratic limb darkening coefficients for the TESS bandpass. With these parameters fixed, we varied the planet-to-star radius ratio R_{pl}/R_* to determine the best fit curve for each transit, which we define as the curve resulting in the lowest root mean square deviation between the TESS and theoretical transit curves. Our transit depth for a given TESS transit curve is then computed using the best fit curve planet-to-star radius ratio as $(R_{\text{pl}}/R_*)^2$. Figure 5.4 shows our fits, transit depths, and root mean square errors for each curve. We then combined the 9 transit depths and errors derived from each light curve according to the methods described by textbooks such as Chromey (2010) and Wall & Jenkins (2012) for combining multiple independent estimates for a given variable. We report our values for TESS transit depth and uncertainty in Table 5.2.

5.5 White Light Transit Curves

We produce white light transit curves for both HST WFC3 (§5.5.1) and STIS (§5.5.2). The term *white light* refers to the total amount of light received across

KELT-7b Transits, TESS Sector 19

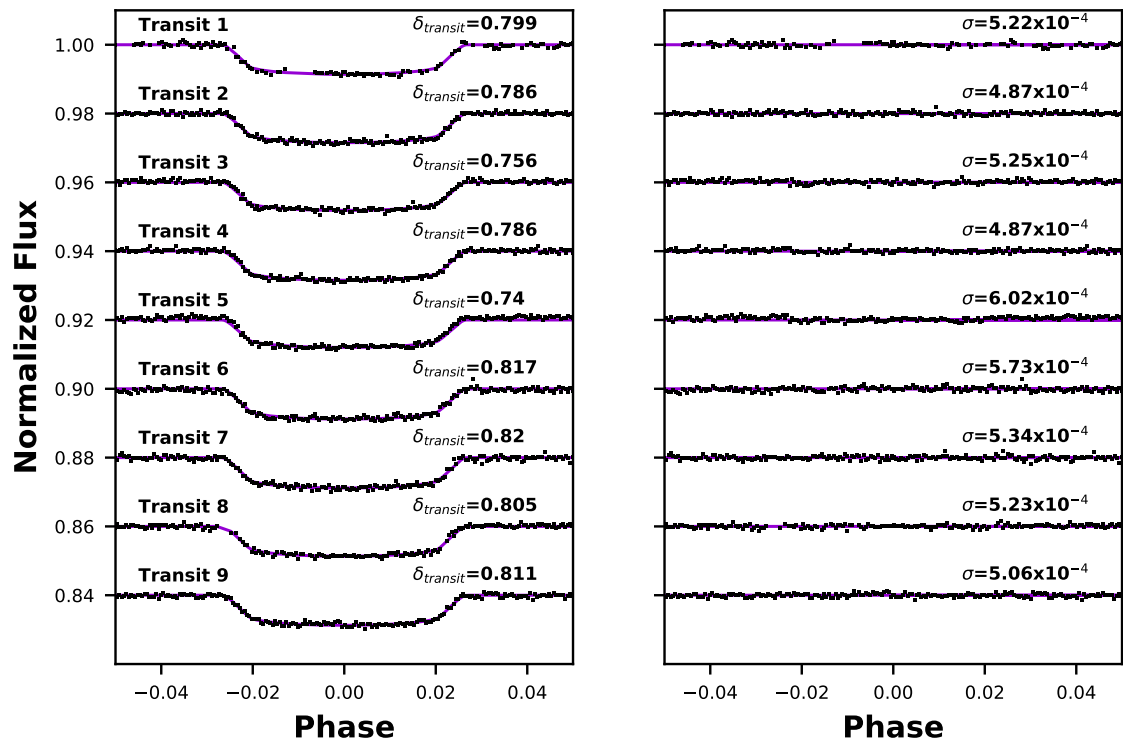


Figure 5.4: KELT-7b transits observed by TESS in Sector 19. We estimate transit depths and uncertainties for the nine observed transits, and include our combined estimate for transit depth and uncertainty on our composite transmission spectrum (Figure 5.13).

all wavelengths for a given instrument. We produce white light transit curves by summing the flux received in all spectral channels across a given subarray. White light curves typically require correction for systematic effects. Sections 5.5.1 and 5.5.2 present the white light curves for WFC3 and STIS, respectively, and describe those corrections applied to create the curves.

5.5.1 WFC3 White Light Transit Curves

We create the data points for our raw white light transit curve by simply integrating our 1D stellar spectra across wavelength. The result is the total amount of flux—represented by electrons recorded on the WFC3 subarray—received throughout the time period of our observations. We typically plot the white light curve as the flux level versus orbital phase, with the phase of mid-transit equal to zero.

Past HST WFC3 transit observations have shown a systematic effect whereby the amount of electrons recorded on the subarray throughout a given orbit gradually increases across time. Deming et al. (2013) dubbed this systematic effect the *hook*, since the “T” shape is reminiscent of a fishhook. The hook effect is typically most severe during the first orbit, as the telescope settles into its new pointing position and the instrument begins to collect data. Figure 5.5 shows our normalized raw white light curve for both forward and reverse scan directions, where the hook is clearly visible. Following standard practice for HST WFC3 transit observations (e.g., Evans et al., 2016; Haynes et al., 2015), we eliminate all data points collected during the first orbit from our white light curve transit fit, as well as from our

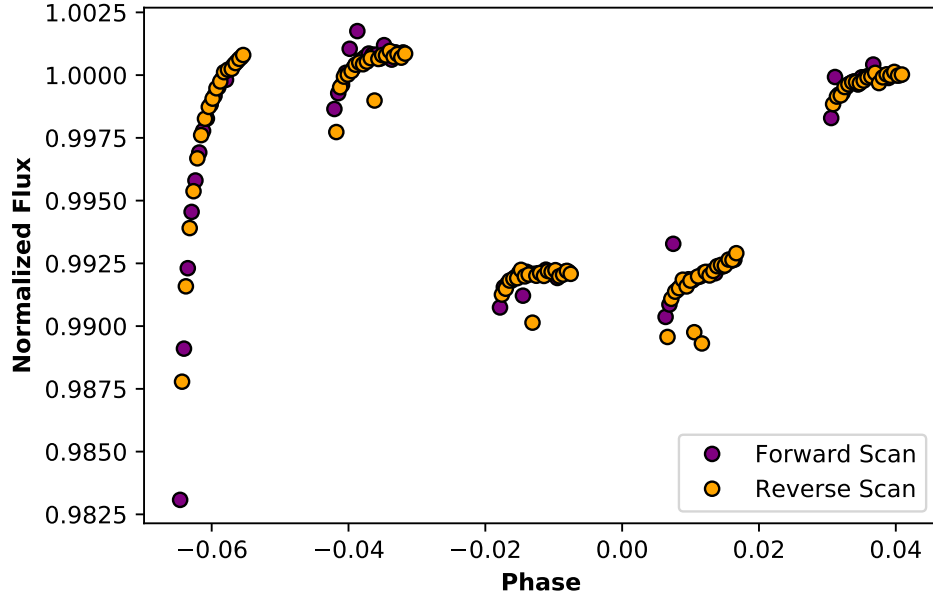


Figure 5.5: Normalized uncorrected white light curve for WFC3 forward and reverse scan directions. Systematic effects are most evident for data collected during the first orbit.

spectral analysis (§5.6.1).

We correct the hook in the white light curve by dividing the data points from each orbit by a *pattern* representing the systematic effects. The *pattern* is created by averaging the normalized flux for each data point in the out-of-transit (second and fifth) orbits (see, e.g., Berta et al., 2012). Figure 5.6 shows the WFC3 white light curve corrected using the *pattern*.

To fit the white light transit, we generated theoretical transit curves using the methods of Mandel & Agol (2002), employing quadratic limb darkening coefficients (Claret & Bloemen, 2011). We utilize the orbital parameters (Period P , inclination i , and semi-major axis a/R_*) reported by Bieryla et al. (2015) in the discovery paper. With these parameters fixed, we vary the planet-to-star radius ratio (R_{pl}/R_*) and

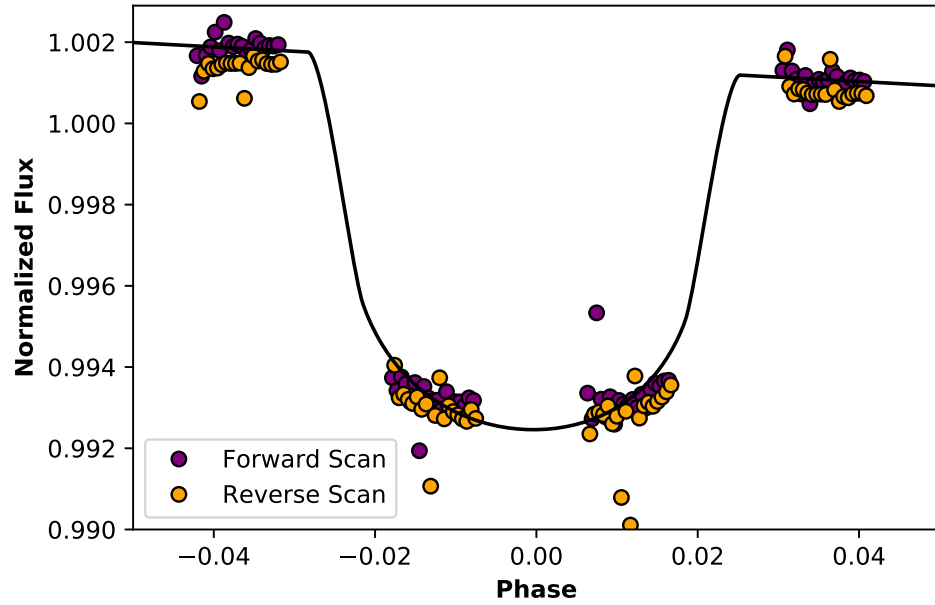


Figure 5.6: Corrected normalized white light curve for WFC3 forward and reverse scan directions. Here, orbit 1 has been omitted.

the time of mid-transit (to account for imprecision in the ephemeris) to determine the best fit curve, which is shown in Figure 5.6.

5.5.2 STIS White Light Transit Curves

We create the data points for the STIS raw white light transit curve by summing the total amount of flux received across columns for each spectral image (Figure 5.3). We then normalize the raw white light curve by the median value of the out-of-transit data points (Figure 5.7). As with our WFC3 analysis, we correct the systematic effects in the STIS raw white light curve by dividing the data points from each orbit by a *pattern*, which is created by averaging the normalized flux for each

data point in the out-of-transit orbits.⁴ We present our STIS corrected, normalized white light curves in Figure 5.8. The fits to the white light curves are computed using the same procedures as those for WFC3.

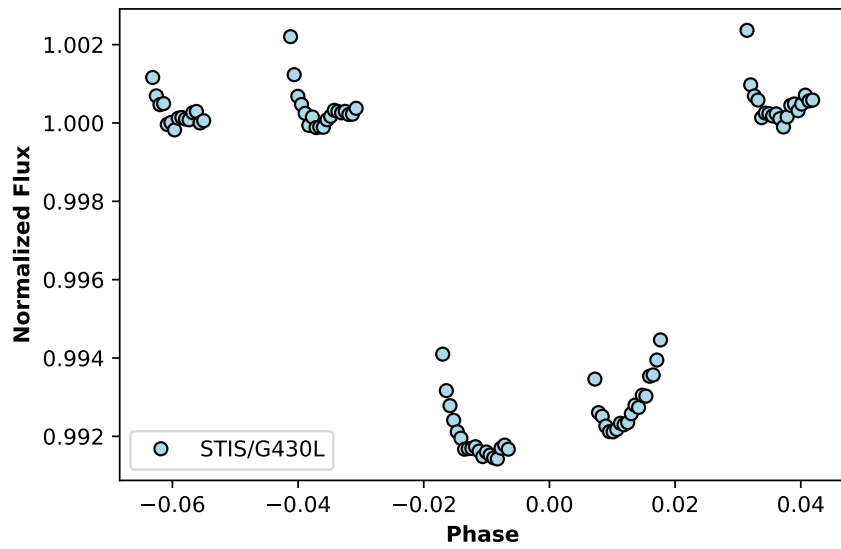
A few STIS data points could not be corrected using the *pattern*, and they are not shown in Figure 5.8. For the G430L grating, we omitted the first exposure of each orbit from our data analysis, which is a common practice (e.g., [Alam et al., 2020](#)). In addition, we eliminated orbit 1 from our analysis, although it is shown in Figure 5.8. For the G750L grating, orbit 2 suffered from an overall decrease in the amount of flux as compared to orbits 1 and 5 (the other out-of-transit orbits), so we eliminated all exposures from the second orbit from our data analysis.

5.6 Transmission Spectrum

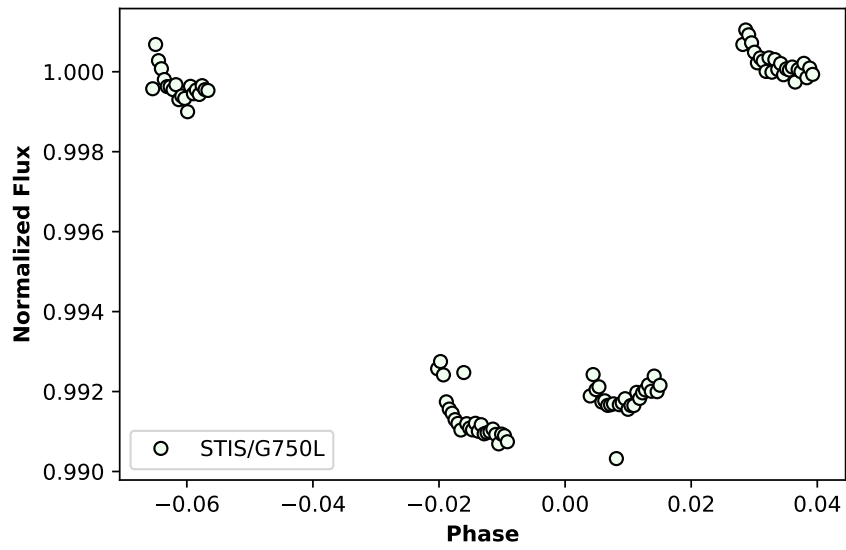
5.6.1 WFC3 Transmission Spectrum

Our WFC3 transmission spectrum is formed from wavelength and time-dependent residuals between shifted template model spectra and each 1D stellar spectrum (§5.4.1). As reported by [Deming et al. \(2013\)](#), the 1D stellar spectra we produce are offset with respect to wavelength—in the case of KELT-7b, they are offset by up to ± 0.2 pixels. We follow [Deming et al. \(2013\)](#) and use a shift routine to compare each 1D stellar spectrum to a series of template spectra that are shifted in 0.001 pixel (or wavelength) increments. The template spectra are created by averaging the values

⁴Note that we developed a separate pattern for each visit. In this case, we developed one pattern for the G430L grating using orbits 2 and 5, and one for the G750L grating using orbits 1 and 5.

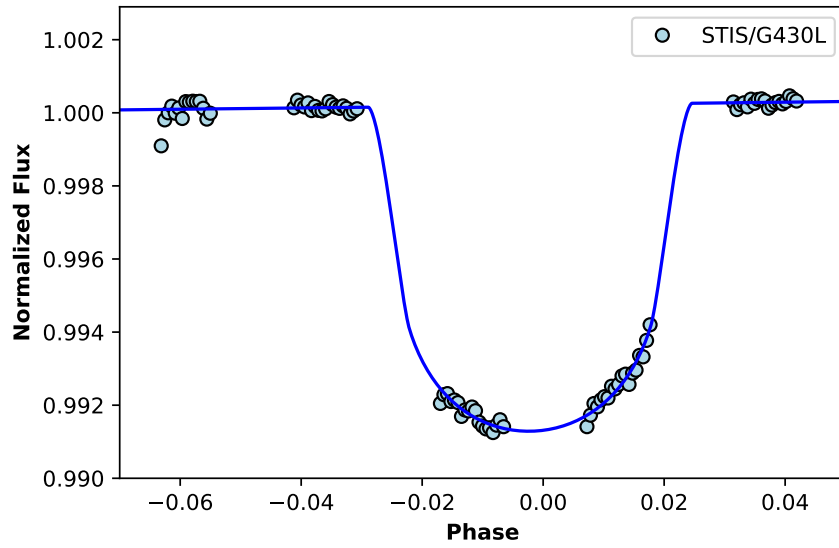


(a)

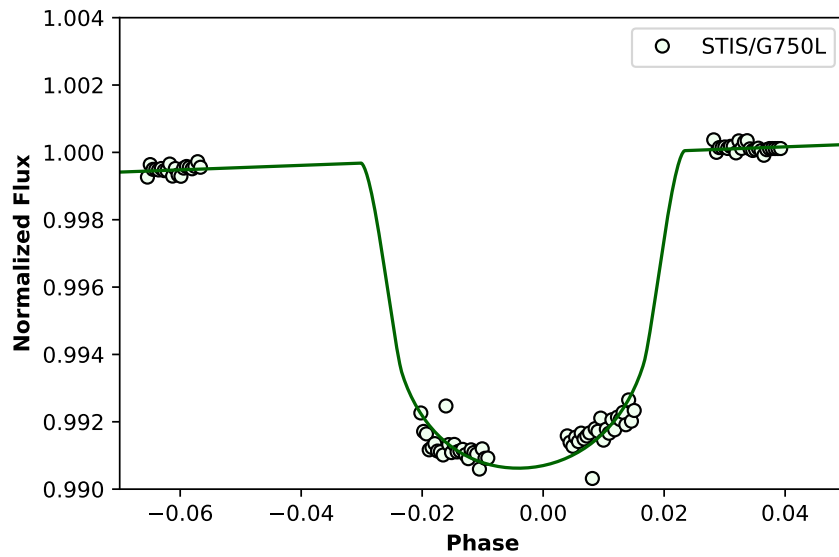


(b)

Figure 5.7: Normalized uncorrected white light curves for STIS (a) G430L and (b) G750L gratings. The G750L grating recorded an uncharacteristically low level of flux for orbit 2, so we omitted it from our data analysis and it is not shown here.



(a)



(b)

Figure 5.8: Corrected normalized white light curves for STIS (a) G430L and (b) G750L gratings. The G750L grating recorded an uncharacteristically low level of flux for orbit 2, so we omitted it from our data analysis and it is not shown here.

of the columns for all out-of-transit spectra for either the forward or reverse scan direction, depending upon which data we are analyzing. The shape of all template spectra are the same—their only difference is the pixel/wavelength shift. We determine which template spectrum (which shift) provides the best fit to each 1D stellar spectrum by finding the best fit linear model to the data, where the best fit model is found by minimizing the standard deviation of the residuals between the model and the data. The linear model essentially stretches the template in intensity.

As explained by [Deming et al. \(2013\)](#), for each stellar spectrum throughout our transit, the residuals between our best fit model spectrum and our data (the stellar spectrum) hold the information that we seek to form our transmission spectrum. The residuals are functions of both time (different IMA files, or orbital phases) and wavelength. For each wavelength of the residual, we perform a linear regression analysis to determine the extent to which the residual across time (throughout the transit) depends upon a scaled version of the white light transit curve, a series of ordinal time steps ([Deming et al. \(2013\)](#)'s *ordinal baseline*), and an array constructed of a series of *shapes* for each orbit. Each of the orbital *shapes* is created by normalizing the flux in a given orbit by the average flux for that orbit. The coefficient to the scaled white light transit curve returned by the fit is the differential transit depth, and when added to the white light curve transit depth it gives us the transit depth for a given wavelength. These wavelength-dependent transit depths are binned across 4 columns to produce our transmission spectrum for either the forward or reverse direction.

[Deming et al. \(2013\)](#) explain in detail two methods used to compute errors on

the differential transit depths: one that makes use of residuals, and one applying a prayer-bead analysis (Gillon et al., 2007). In practice, we use the method relying upon residuals since the estimated errors are higher and thus more conservative. We briefly review that method here. Residuals for the differential transit curves are computed by subtracting the best-fit differential transit from the data points for each differential transit. The scatter of the transit curve, σ_1 , is computed by finding the standard deviation of these residuals. Next, we successively calculate values of σ_N , where N is the number of transit points we consider, from 1 up to half the number of transit points in our curve. Deming et al. (2013) present the relationship $\log \sigma_N = \log \sigma_1 - 0.5 \log N$, which allows us to compute the associated error for N points in the differential transit curve. We use this relationship to compute $\sigma_{N_{\text{in}}}$ and $\sigma_{N_{\text{out}}}$, the errors on the number of points in-transit and out-of-transit. We then add these errors in quadrature to compute our estimated error for a given differential transit depth.

Finally, we produce the combined spectrum by combining the forward and reverse scan transit depths and their errors in each bin according to the methods described by textbooks such as Chromey (2010) and Wall & Jenkins (2012) for combining multiple independent estimates for a given variable. We present our transmission spectrum for HST WFC3 in Figure 5.9, with transit depths and their uncertainties reported in Table 5.3.

Wavelength (μm)	Transit Depth (ppm)	Uncertainty (ppm)
1.116	7928	47
1.134	8073	41
1.153	7962	43
1.172	7969	44
1.191	8051	41
1.209	8113	39
1.228	8090	37
1.247	8044	41
1.266	8085	43
1.284	8062	46
1.303	8095	46
1.322	8137	51
1.341	8083	42
1.359	8079	37
1.378	8038	39
1.397	8052	41
1.416	8146	45
1.434	8095	44
1.453	8073	43
1.472	8088	42
1.491	8019	40
1.509	7890	42
1.528	8002	43
1.547	8028	46
1.566	7997	52
1.584	7859	53
1.603	7838	54
1.622	7848	51
1.641	7879	48

Table 5.3: KELT-7b WFC3 G141 Grism Transit Depths and Uncertainties

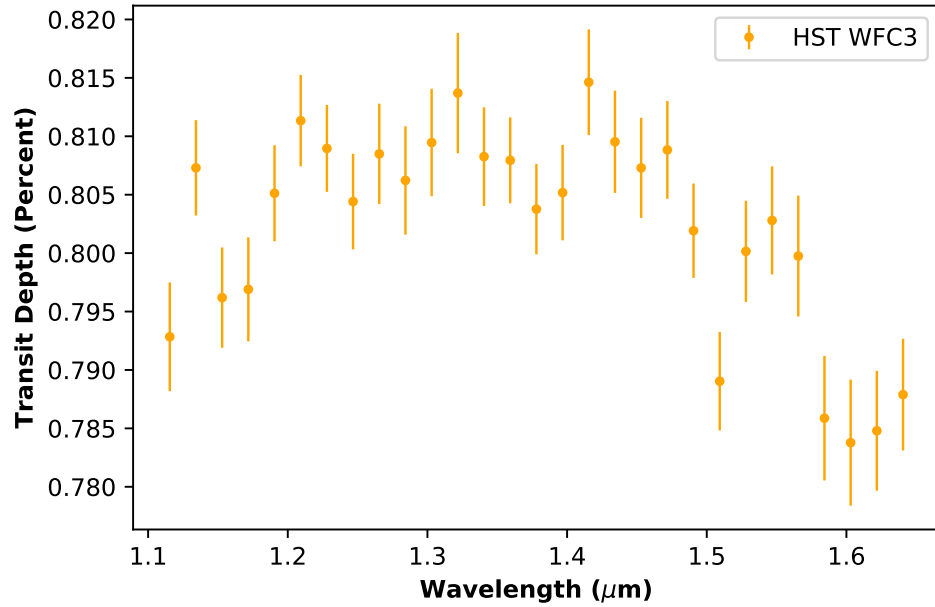


Figure 5.9: HST WFC3 transmission spectrum produced by our analysis.

5.6.2 STIS Transmission Spectrum

Our STIS spectral analysis begins by examining the 1D spectra (§5.4.2). As with the WFC3 analysis (§5.6.1), we find that the STIS 1D spectra are slightly offset with respect to wavelength upon the subarray, and thus we begin by determining the *shift* required to align the spectra. Our procedure is much like that described in Section 5.6.1 for WFC3, except that the initial template spectrum is created by averaging the columns for *all* 1D spectra in our data set. We then create a set of 800 template spectra that are shifted by up to ± 4 pixels, in 0.01 pixels increments, along the dispersion direction, or x-axis (see Figure 5.3). We perform a linear fit between each of our 1D spectra and the set of template spectra. For a given 1D spectrum, the template spectrum producing the smallest root mean square deviation

between that 1D spectrum and linear model fit reveals the x-axis pixel shift for that 1D spectrum. We apply our shift routine twice to the STIS 1D spectra, each time shifting the 1D spectra by the prescribed number of pixels and recording the total pixel shift applied.

After the 1D spectra are shifted, we next examine the transit light curves for the STIS wavelength bins depicted in Figure 5.1 and listed in Tables 5.4 and 5.5. The bin widths are designed to achieve similar fluxes in each spectroscopic channel and also to isolate stellar absorption lines. We produce spectroscopic data points for a given bin, or channel, by summing the columns of the 1D spectra corresponding to that bin. We correct for wavelength-independent systematic trends by dividing the spectroscopic data points for each orbit in a given channel by the same *pattern* derived to correct the STIS raw white light curve. We then perform a linear regression to jointly fit a systematics model and a Mandel & Agol (2002) analytic transit light curve to the spectroscopic data points in a given channel. Our systematics detrending model includes corrections for the HST orbital phase, time, and the tilt, shape, and shift of the spectra upon the detector subarray. We computed the Mandel & Agol (2002) analytic transit light curve using the orbital parameters (Period P , inclination i , planet-to-star radius ratio R_{pl}/R_* , and semi-major axis a/R_*) from Bieryla et al. (2015), and the four parameter non-linear limb darkening coefficients derived with the Magic et al. (2015) 3D theoretical models. We compute the transit depth in a given spectroscopic channel from the correlation coefficient to the analytic transit curve.

Since the transit depth is essentially the difference between our out-of-transit

flux and in-transit flux, the error on that depth is the quadrature sum of the out-of-transit and in-transit errors. We assume that the error on each spectroscopic transit data point is equal to the root mean square deviation, σ , between our spectroscopic transit curve and the regression analysis fit. The transit error is then given by $\sqrt{\sigma^2/n_{\text{out}} + \sigma^2/n_{\text{in}}}$, where n_{out} and n_{in} refer to the number of out-of-transit and in-transit spectroscopic data points, respectively. The values of our transit errors are 1-2 \times those of the photon errors in each spectroscopic channel.

We show our spectroscopic transit curves and residuals for the G430L and G750L gratings in Figures 5.10 and 5.11. The data points have been corrected for systematics, and the best fit transit curves are overplotted with solid lines. We present our HST STIS transmission spectrum in Figure 5.12, with TESS-band transit depth and uncertainty overplotted for comparison. We list STIS transit depths and their uncertainties in Tables 5.4 and 5.5.

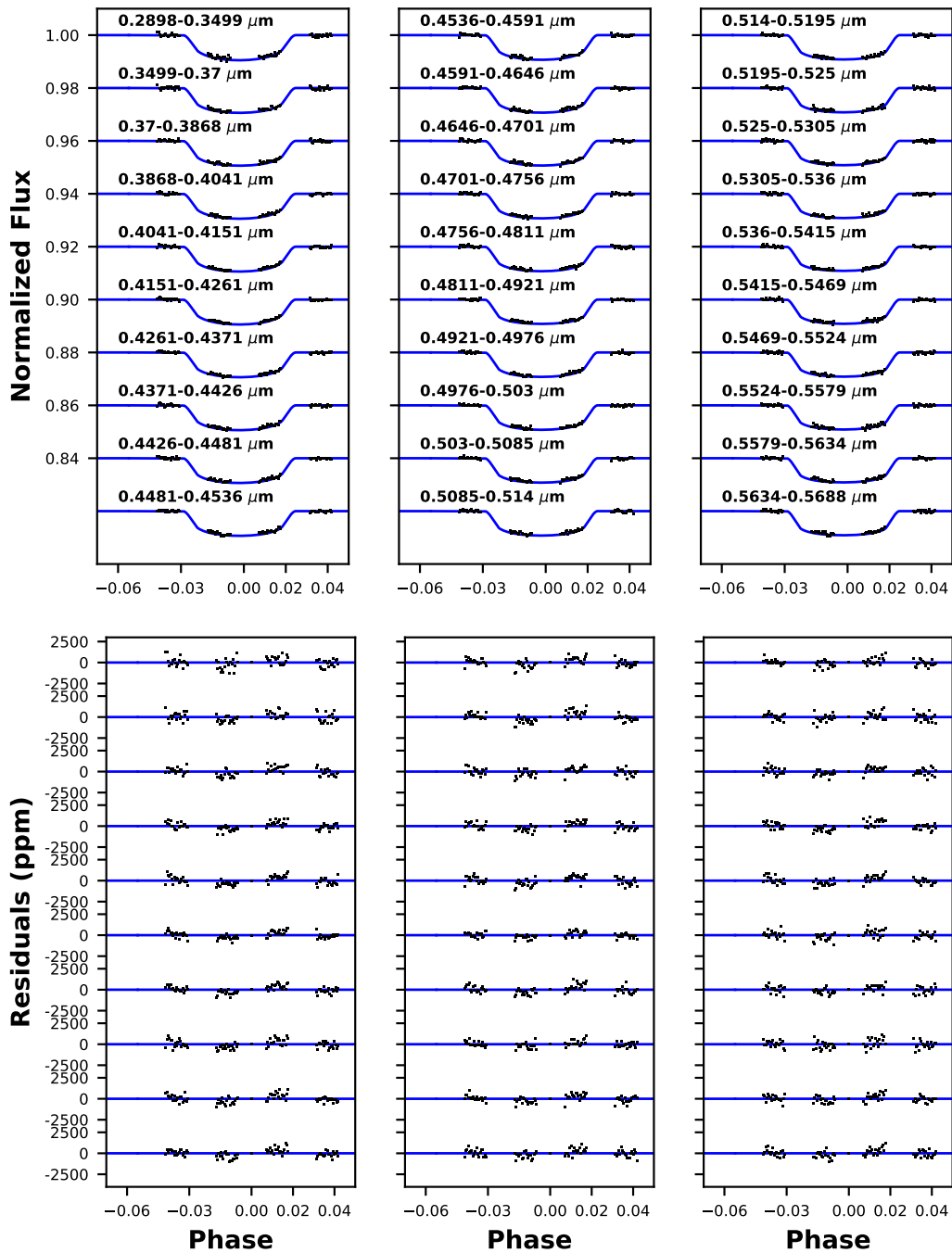


Figure 5.10: Spectroscopic light curves for STIS G430L data. Data were corrected for systematics as described in Section 5.6.2, and the best fit transit curve is overplotted in blue. Note that orbit 1 and the first exposure of each orbit were omitted from our data analysis and are not shown.

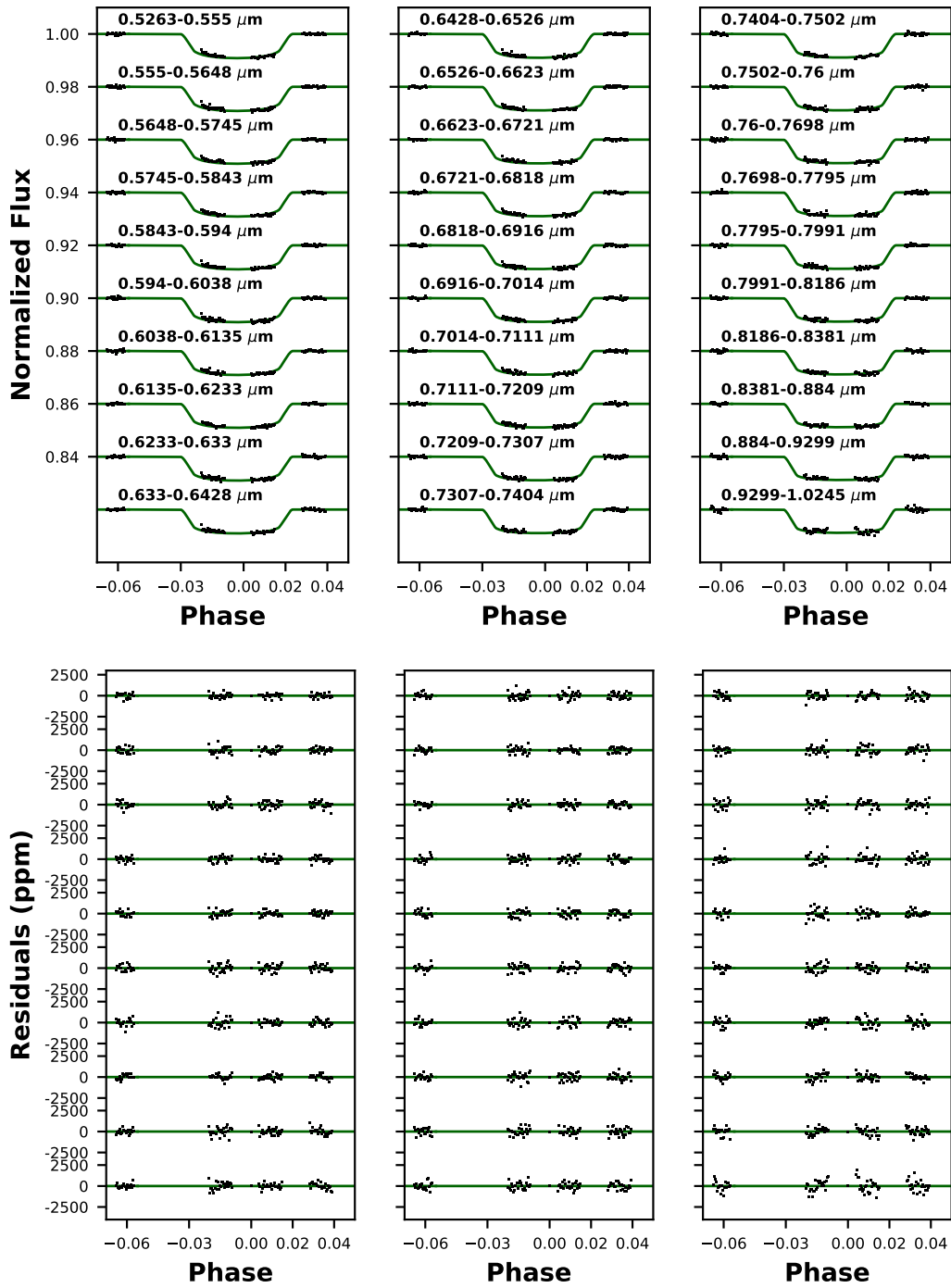


Figure 5.11: Spectroscopic light curves for STIS G750L data. Data were corrected for systematics as described in Section 5.6.2, and the best fit transit curve is overplotted in dark green. Note that orbit 2 was omitted from our data analysis and is not shown.

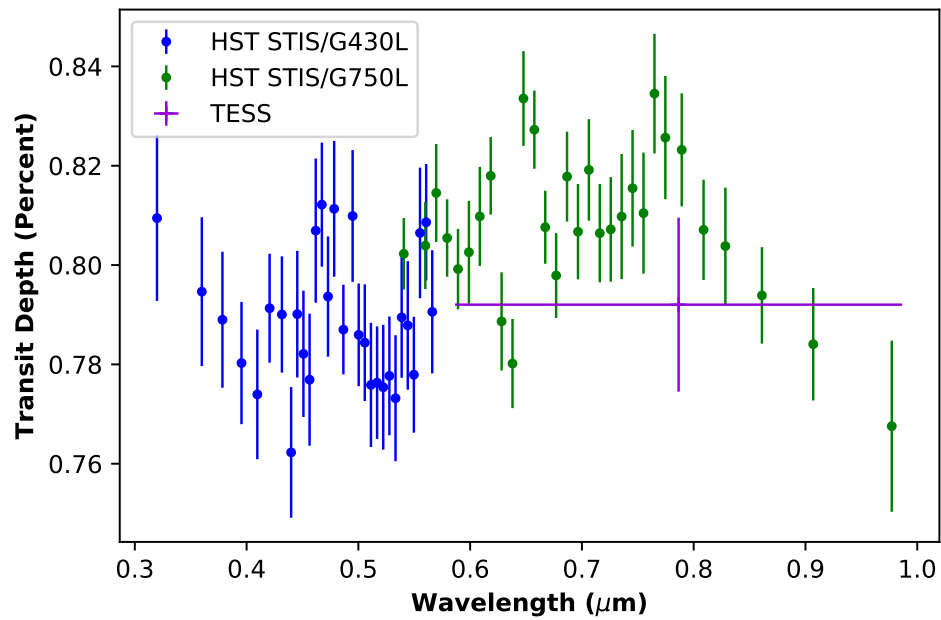


Figure 5.12: HST STIS transmission spectrum produced by our analysis. We overplot our derived value of the TESS-band transit depth. The width of the TESS data point indicates the width of the TESS bandpass.

Wavelength Bin (μm)	Transit Depth (ppm)	Uncertainty (ppm)
[0.2898, 0.3499]	8095	167
[0.3499, 0.3700]	7946	150
[0.3700, 0.3868]	7890	137
[0.3868, 0.4041]	7803	123
[0.4041, 0.4151]	7740	130
[0.4151, 0.4261]	7913	110
[0.4261, 0.4371]	7901	117
[0.4371, 0.4426]	7623	132
[0.4426, 0.4481]	7901	127
[0.4481, 0.4536]	7821	127
[0.4536, 0.4591]	7769	133
[0.4591, 0.4646]	8069	145
[0.4646, 0.4701]	8122	125
[0.4701, 0.4756]	7937	121
[0.4756, 0.4811]	8113	137
[0.4811, 0.4921]	7870	90
[0.4921, 0.4976]	8099	133
[0.4976, 0.5030]	7860	103
[0.5030, 0.5085]	7844	117
[0.5085, 0.5140]	7759	125
[0.5140, 0.5195]	7763	113
[0.5195, 0.5250]	7754	126
[0.5250, 0.5305]	7777	120
[0.5305, 0.5360]	7732	127
[0.5360, 0.5415]	7895	122
[0.5415, 0.5469]	7879	129
[0.5469, 0.5524]	7779	117
[0.5524, 0.5579]	8065	131
[0.5579, 0.5634]	8086	117
[0.5634, 0.5688]	7906	124

Table 5.4: KELT-7b STIS G430L Grating Transit Depths and Uncertainties

Wavelength Bin (μm)	Transit Depth (ppm)	Uncertainty (ppm)
[0.5263, 0.5550]	8023	72
[0.5550, 0.5648]	8039	88
[0.5648, 0.5745]	8145	99
[0.5745, 0.5843]	8054	78
[0.5843, 0.5940]	7992	81
[0.5940, 0.6038]	8026	103
[0.6038, 0.6135]	8098	100
[0.6135, 0.6233]	8180	78
[0.6233, 0.6330]	7887	99
[0.6330, 0.6428]	7802	90
[0.6428, 0.6526]	8335	95
[0.6526, 0.6623]	8273	79
[0.6623, 0.6721]	8076	74
[0.6721, 0.6818]	7979	85
[0.6818, 0.6916]	8178	90
[0.6916, 0.7014]	8067	96
[0.7014, 0.7111]	8192	102
[0.7111, 0.7209]	8064	99
[0.7209, 0.7307]	8072	105
[0.7307, 0.7404]	8098	126
[0.7404, 0.7502]	8155	117
[0.7502, 0.7600]	8105	122
[0.7600, 0.7698]	8345	121
[0.7698, 0.7795]	8257	124
[0.7795, 0.7991]	8232	114
[0.7991, 0.8186]	8071	101
[0.8186, 0.8381]	8038	118
[0.8381, 0.8840]	7939	97
[0.8840, 0.9299]	7841	113
[0.9299, 1.0245]	7676	172

Table 5.5: KELT-7b STIS G750L Grating Transit Depths and Uncertainties

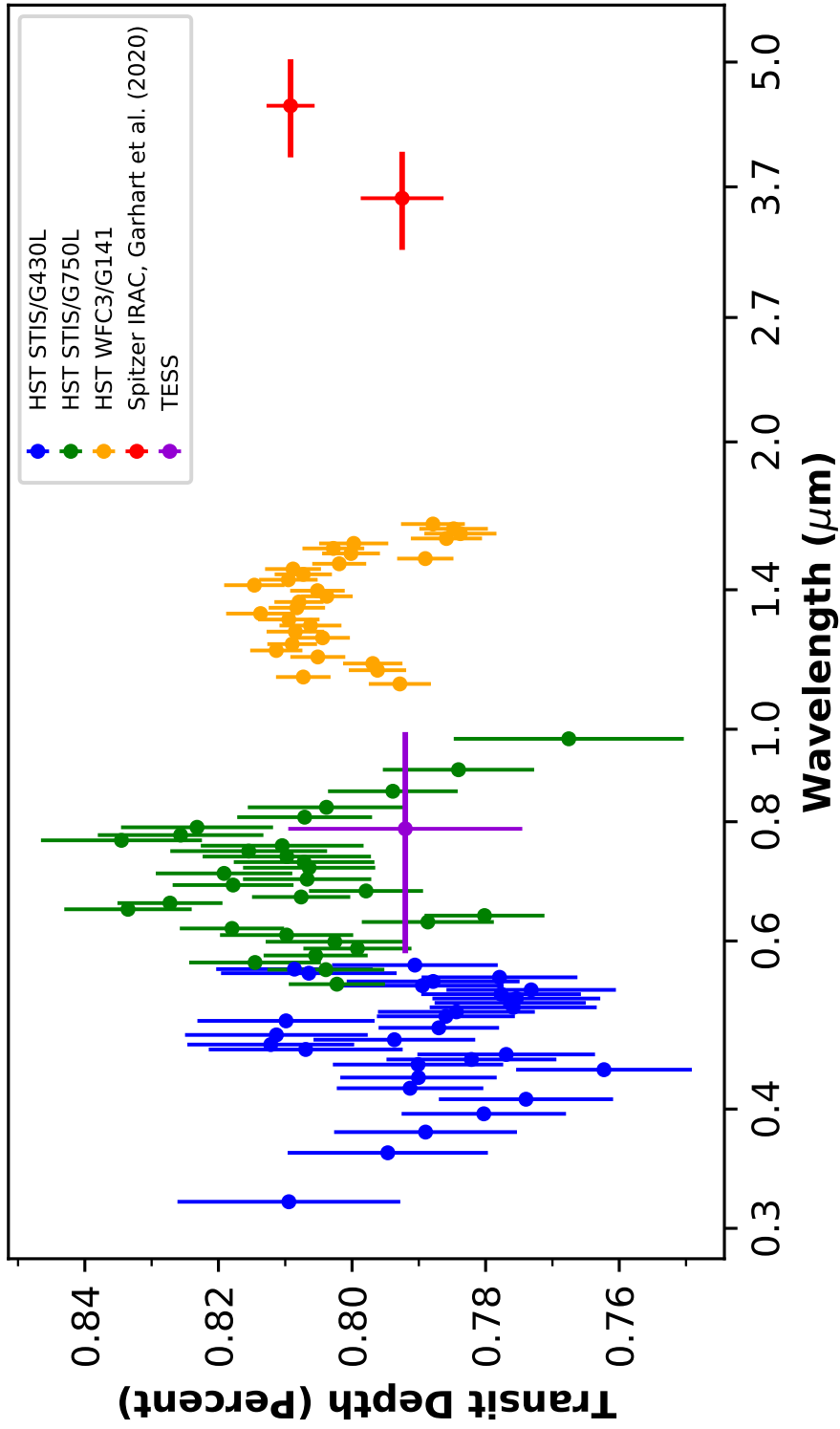


Figure 5.13: Our composite transmission spectrum. The transit depths reported for HST STIS and WFC3, as well as for TESS, are derived in this study. Spitzer transit depths are from [Garhart et al. \(2020\)](#). Horizontal widths of the TESS and Spitzer points indicate the widths of the respective bandpasses.

5.7 Results and Discussion

After producing our transmission spectrum, we next examine what this spectrum reveals about KELT-7b’s atmospheric properties. In this section, we employ the isothermal equilibrium chemistry PLATON retrieval code, version 5.1 (§1.2.3, Zhang et al., 2019, 2020) to explore KELT-7b’s transmission spectrum (§5.7.1). We then discuss our retrieval results in Section 5.7.2, compare our results to those reported by Pluriel et al. (2020) in Section 5.7.3, and briefly assess the implications of KELT-7b’s chemistry on its planet formation pathway in Section 5.7.4.

5.7.1 KELT-7b Atmospheric Retrievals

PLATON is a fast, easy-to-use, open source retrieval code that employs isothermal, equilibrium chemistry parametric models to explore the prior parameter space (§1.2.3). We chose to use PLATON in our analysis for several reasons. First, the code is well-documented, with a dedicated paper and website, and it is publicly available. We found that only the publicly available Tau-REx3 code (Al-Refaie et al., 2019),⁵ recently updated from a previous version (Waldmann et al., 2015), has a similar level of documentation. Second, PLATON retrievals can be performed on the order of a few hours or less using a laptop computer, allowing rapid exploration of parameter space to quickly determine those parameters which may be of most importance in explaining a transmission spectrum. In contrast, a typical retrieval takes days to weeks on a standard desktop computer (Zhang et al., 2019). However,

⁵https://github.com/ucl-exoplanets/TauREx3_public

we note that benchmark tests of the improved Tau-REx3 code demonstrate that it rivals PLATON in speed (Al-Refaie et al., 2019). Third, the PLATON transmission spectrum forward model is based upon Exo-Transmit (Kempton et al., 2017), which was developed by a University of Maryland (UMD) professor, and UMD Astronomy Department members have developed in-house expertise in using the code. Finally, PLATON has been used with success in multiple other PanCET analyses (e.g., Alam et al., 2020; Chachan et al., 2019; Fu et al., 2020; Sheppard et al., 2021).

One key difference between exoplanet retrieval codes used to analyze transmission spectra deals with the scheme used to retrieve atmospheric chemical composition. PLATON allows the user to specify two parameters to determine chemical composition: metallicity and C/O ratio (Zhang et al., 2019). Metallicity is expressed as the abundance of metals⁶ with respect to hydrogen [M/H], and is specified in PLATON as a multiple of the solar value (Asplund et al., 2009). Some retrieval codes employ free chemistry retrieval schemes, whereby each chemical species is retrieved based upon spectral features (e.g., ATMO, see Evans et al., 2017; Wakeford et al., 2017). Free retrieval codes then allow computation of C/O directly based upon abundances of carbon and oxygen bearing species such as CO, CO₂, H₂O, or CH₄. See Madhusudhan (2018) for a recent review with further details concerning retrieval codes that have been employed in published works.

We incorporated many of the options available in the updated PLATON version 5.1 retrieval code (§1.2.3). Because we expect metal opacities to be important in the optical regime observed by STIS, we downloaded the updated line profiles

⁶In Astronomy, the term *metal* refers to all elements heavier than helium.

Parameter	Symbol	Distribution	Range/Width ^a	Default Value
Planet Radius	R_{pl}	Uniform	1.38 - 1.68 R_{J}^b	1.53 R_{J}
Limb Temperature	T	Uniform	1024 - 3072K ^c	2048K ^d
Carbon-to-Oxygen Ratio	C/O	Uniform	0.05 - 2.0	0.53 ^e
Metallicity	Z	Log-uniform	0.1 - 1000 Z_{\odot}	1 Z_{\odot}
Planet Mass	M_{pl}	Gaussian	0.18 M_{J}	1.28 M_{J}
Stellar Radius	R_{*}	Gaussian	0.045 R_{\odot}	1.73 R_{\odot}
Cloudtop Pressure	P_{cloud}	Log-uniform	10 ⁻¹ - 10 ⁶ Pa	10 ⁴ Pa

NOTES:

^a Range for uniform or log-uniform; width is standard deviation of a Gaussian.

^b Range from 0.9 to 1.1 times the default value.

^c Range from 0.5 to 1.5 times the default value.

^d Equilibrium temperature from [Bieryla et al. \(2015\)](#).

^e Solar C/O.

Table 5.6: Prior Parameter Distribution for Fiducial Model

produced for K ([Allard et al., 2016](#)) and Na ([Allard et al., 2019](#)), which more accurately estimate the far wings of the lines for these atoms. We also incorporate H⁻ opacity ([John, 1988](#)) into our fiducial model, since this opacity source has been shown to be important for highly irradiated giant planets like KELT-7b ([Parmentier et al., 2018](#)). We use the *dynesty* nested sampling package ([Speagle, 2020](#)) to sample the model parameter space and estimate posterior distributions and evidences. Nested sampling offers several advantages compared to Markov Chain Monte Carlo (MCMC) Bayesian samplers. An important advantage relevant to this work is that nested sampling generates Bayesian evidence, $\ln \mathcal{Z}$, in addition to the posterior distribution ([Speagle, 2020](#)). The Bayesian evidence allows comparison of two models by computing the *odds ratio*, \mathcal{O} , between a pair of atmospheric models. In addition, nested sampling possesses well-motivated stopping criteria.

We define our fiducial model as one where we fit for the parameters listed

in Table 5.6, with prior distributions and default values as indicated. In addition, we fix the Rayleigh scattering slope at 4 for our fiducial model. Our choice of distribution for each prior parameter is driven by the degree of prior knowledge concerning a given parameter. In general, we choose Gaussian distributions for parameters where we have a high degree of confidence in the prior distribution, while we choose uninformative uniform or log-uniform prior distributions for parameters where we possess less prior knowledge. Specifically, the mass of the planet is well-constrained by radial velocity analyses, so we specify a Gaussian prior with a width equivalent to the $1\text{-}\sigma$ uncertainty in that prior value. We follow this same logic and use a Gaussian prior for stellar radius, since it is also well constrained by prior observations. The default value and width for both of these parameters are taken from the Bieryla et al. (2015) discovery paper (Table 5.1). We also use the planet radius from Bieryla et al. (2015) as the default value. However, since planet radius is closely related to the wavelength-dependent transit depth—our data—we choose a noninformative uniform prior. The range of planet radius values yields a range of transit depths from 0.67% to 1%, when computed using equation 1.1 with the default value of stellar radius. Transit depths for all data points of Figure 5.13 clearly fall within this range of values, thus demonstrating that our choice of prior values for planet radius should not constrict our retrieval solution. Our priors for C/O ratio and metallicity span the full range of values supported by PLATON. PLATON supports cloud levels between 10^{-4} and 10^8 . However, we find that in all of our models, the credible interval for clouds is well-contained within the regime from 10^{-1} and 10^6 . Our range of cloud-top pressures contains those pressure levels

where atmospheric modelers predict that clouds will form (e.g., [Robinson & Catling, 2014](#)). In addition to the prior parameter distributions listed in [Table 5.6](#), we fix the stellar temperature at the [Bieryla et al. \(2015\)](#) value, since stellar temperature has little impact on the transmission spectrum, and since the published value will always be better than any value derived from a retrieval based upon a transmission spectrum ([Zhang et al., 2019](#)).

PLATON’s rapid computation speed allowed us to quickly explore a few variations upon the fiducial model. The *odds ratio*, or *Bayes factor*, defined as the ratio of evidences between two models, allows us to statistically determine whether a given model is preferred over an alternative ([Trotta, 2008](#)). In general, the model with the higher value of Bayesian evidence is preferred. We use the Jeffrey’s scale from [Trotta \(2008\)](#) to interpret the degree of preference for one model over another. We examined adding a uniform fit to the scattering slope, as well as a uniform fit to the WFC3 data point offsets.⁷ Our prior parameter distributions for scattering slope and WFC3 offset are listed in [Table 5.7](#), and we compare our results from the 3 retrievals in [Table 5.8](#). The best-fit models for all 3 retrievals are depicted alongside our data in [Figure 5.14](#).

When we compare the fiducial model to the two more complicated models (i.e., the models with 8 fitting parameters rather than 7), Jeffreys’ scale indicates there is inconclusive evidence to prefer either of the two more complicated models over the fiducial model. [Trotta \(2008\)](#) explains that Bayesian model comparison provides a formal method to apply *Occam’s razor*—the simplest model compatible with the

⁷PLATON currently supports offsets only with WFC3 data.

Parameter	Symbol or Abbreviation	Distribution	Range ^a	Default Value
Scattering Slope	s	Uniform	4 - 9	4 ^b
WFC3 Offset	WO	Uniform	-500 - 500 ppm	0 ppm

NOTES:

^a Range of values explored.

^b The default value of 4 corresponds to Rayleigh scattering.

Table 5.7: Prior Parameter Distributions - Scattering Slope and WFC3 Offset

Model	$\log_{10} Z^a$	Z^b	C/O ^c	$\log_{10} P_{\text{cloud}}^d$	$\ln \mathcal{Z}^e$	\mathcal{O}^f	Interpretation ^g
Fiducial (F)	$1.44^{+1.04}_{-0.88}$	3.63 - 302	$0.35^{+0.21}_{-0.19}$	$1.94^{+1.20}_{-0.78}$	588.4	Reference	Basis Model
F + s	$1.63^{+0.68}_{-0.66}$	9.33 - 204	$0.32^{+0.22}_{-0.18}$	$1.52^{+0.75}_{-0.68}$	588.3	1.1	Inconclusive
F + WO	$1.71^{+0.89}_{-1.03}$	4.79 - 398	$0.36^{+0.23}_{-0.20}$	$2.04^{+2.10}_{-1.01}$	588.5	0.9	Inconclusive

NOTES:

^a Median log metallicity with 16% and 84% quantiles, in units of log solar metallicity.

^b 68% credible interval for metallicity, in units of solar metallicity.

^c Median C/O ratio with 16% and 84% quantiles.

^d Median log pressure level for base of cloud deck in Pascals, with 16% and 84% quantiles.

^e Natural logarithm of Bayesian evidence \mathcal{Z} computed by *dynesty* nested sampling package.

^f Here, the odds ratio \mathcal{O} is the ratio of the Bayesian evidence of the fiducial model to that of the other models.

^g Interpretation using Jeffreys' scale from [Trotta \(2008\)](#).

Table 5.8: Comparison of Fiducial and More Complicated Model Retrievals

available evidence should be preferred. Thus, we use our fiducial model in our next analysis, where we explore the importance of various atomic and molecular species in our retrieval.

Figure 5.15 depicts a corner plot showing the results from a PLATON retrieval using our fiducial model. Histograms along the diagonal of the corner plot indicate median values and 68% credible intervals for each of our retrieved parameters. Our results indicate that our transmission spectrum is consistent with a subsolar C/O ratio (median 0.35), supersolar metallicity (median $27.5 \times$ solar) atmosphere. The

median value for the base of the cloud deck is at 87 Pascals, indicating high altitude clouds. The 68% credible interval for the base of the cloud deck ranges between 14 - 1380 Pa, or between 0.14 mbar and 13.8 mbar. We note a degeneracy between cloud pressure levels and metallicity. Higher metallicities correlate with clouds at higher pressures, and vice versa. This degeneracy makes sense, since both high metallicities and high altitude (low pressure) clouds produce the same effect of muting spectral features. Values of stellar radius, planet mass, and planet radius are close to their prior values. As expected, the retrieved limb temperature of 1093 K (68% credible interval 904 K to 1282 K) is less than the planet's equilibrium temperature. We discuss the results of this PLATON retrieval further in Section 5.7.2.

Next, we compute the odds ratio between the fiducial model and a series of models lacking various opacity sources to determine whether models with those opacity sources are preferred or not. If the fiducial model has a higher Bayesian evidence than the model without a given opacity source, then that opacity source is important to the model. Jeffrey's scale indicates the degree to which the opacity source is preferred. As described earlier in this section, we expect H^- opacity to be important for highly irradiated giant planets like KELT-7b (Parmentier et al., 2018). We expect atomic and molecular opacities from H_2O , K, Na, CO, and CO_2 to be important across the 0.3 - 5.0 μm wavelength regime examined in this study. We thus examine the significance of these opacity sources. Table 5.9 lists the results of our analysis. Of the opacity sources examined, we find that only H_2O opacity is strongly favored in our analysis. We note that the odds ratio found for H_2O opacity is equivalent to a $\sim 3.6\text{-}\sigma$ detection in frequentist terms (Trotta, 2008).

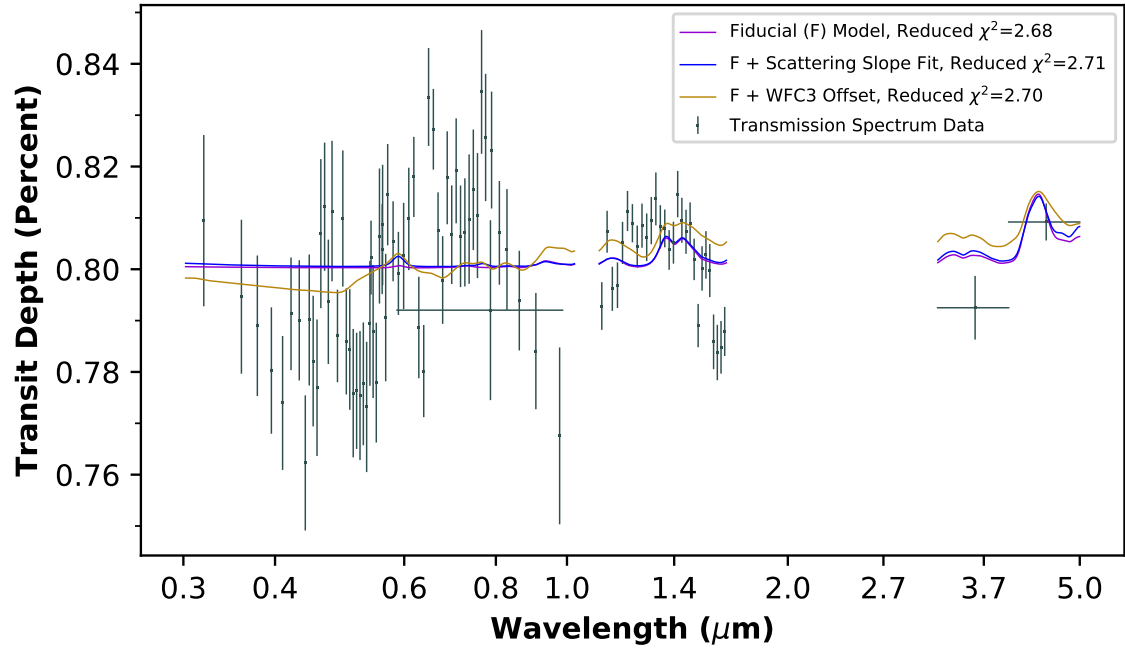


Figure 5.14: Best fit models corresponding to PLATON retrieval of fiducial model, as well as fiducial model with fits for either scattering slope or WFC3 offset. In each case, PLATON retrieves a subsolar C/O ratio, supersolar metallicity, cloudy atmosphere (see Table 5.8). For each model, the reduced chi-squared χ^2_{ν} is greater than 1, indicating that the fit has not fully captured the data. However, the fit allowing WFC3 offset in particular allows the model to capture some of the variation in the optical regime. Note that the models are not shown between data sets.

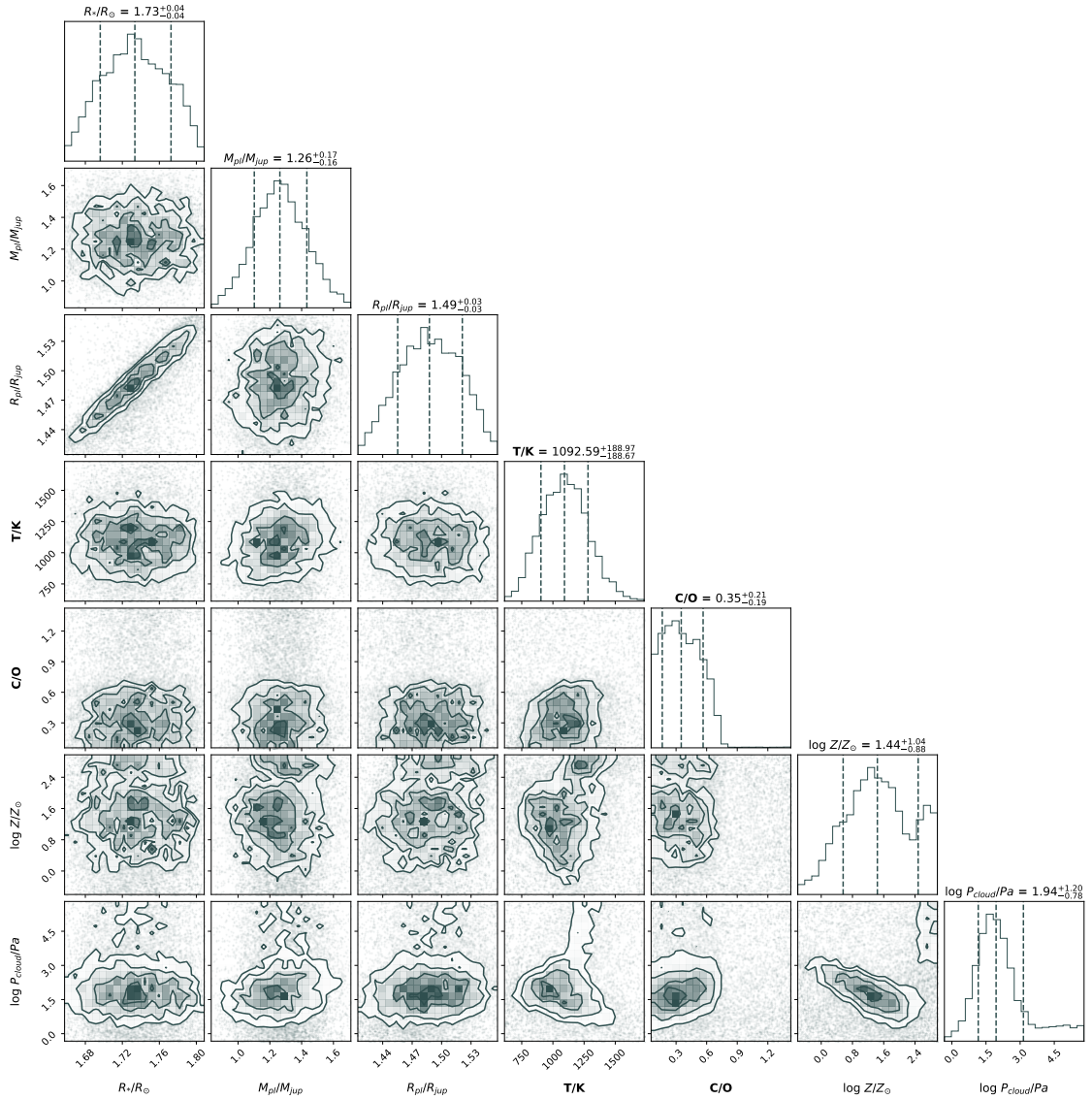


Figure 5.15: Corner plot depicting the results of our PLATON retrieval for the fiducial model, and using the prior distribution listed in Table 5.6. Histograms along the diagonal of the corner plot indicate median values and 68% credible intervals for each of our retrieved parameters. Our results are consistent with a subsolar C/O ratio, supersolar metallicity atmosphere with clouds forming at low pressure.

Model	$\ln \mathcal{Z}^a$	\mathcal{O}^b	Interpretation ^c
Fiducial (F)	588.4	Reference	Basis Model
F Without H ⁻	588.5	0.9	Inconclusive
F Without H ₂ O	581.5	992	Strong evidence
F Without K	588.4	1	Inconclusive
F Without Na	588.4	1	Inconclusive
F Without CO	588.3	1.1	Inconclusive
F Without CO ₂	587.5	2.46	Inconclusive

NOTES:

^a Natural logarithm of Bayesian evidence \mathcal{Z} computed by *dynesty* nested sampling package.

^b Here, the odds ratio \mathcal{O} is the ratio of the Bayesian evidence of the model including all opacity sources (the Basis Model) to the model without various opacity sources. A high odds ratio indicates that the model with that opacity source is preferred.

^c Interpretation using Jeffreys' scale from [Trotta \(2008\)](#).

Table 5.9: Detection of Various Atomic and Molecular Species

Model	Instrument	$\ln \mathcal{Z}^a$	\mathcal{O}^b	Interpretation ^c
Fiducial (F)	STIS G430L, G750L	351.2	Reference	Basis Model
F Without K	STIS G430L, G750L	348.1	22	Moderate evidence
F Without Na	STIS G430L, G750L	351.9	0.5	Inconclusive
Fiducial (F)	WFC3 G141	140.3	Reference	Basis Model
F Without H ₂ O	WFC3 G141	134.5	330	Strong evidence

NOTES:

^a Natural logarithm of Bayesian evidence \mathcal{Z} computed by *dynesty* nested sampling package.

^b Here, the odds ratio \mathcal{O} is the ratio of the Bayesian evidence of the model including all opacity sources (the Basis Model) to the model without various opacity sources. A high odds ratio indicates that the model with that opacity source is preferred.

^c Interpretation using Jeffreys' scale from [Trotta \(2008\)](#).

Table 5.10: Examination of STIS and WFC3 Data for Various Species

The composite spectrum examined thus far combines data from two STIS gratings, WFC3, TESS, and Spitzer IRAC. Observations were taken at different times when the planetary system may have been in a different state. For example, stellar activity, spots, and faculae have been shown to affect transmission spectra (e.g., [Rackham et al., 2018, 2019](#)), and those effects will differ as the stellar activity level changes over time. Variations in the state of the instrument, as well as in data analysis procedures applied between data sets, can alter the white light transit fit between data sets, which may in turn lead to offsets between data sets (e.g., [Diamond-Lowe et al., 2014; Stevenson et al., 2014](#)).

To overcome the inherent shortcomings from combining data sets, we examined the importance of various opacity sources by performing PLATON retrievals on STIS data only as well as WFC3 data only. For the STIS only data, we examined Na and K opacity, since those opacity sources are predicted in the optical regime ([Seager & Sasselov, 2000](#)). For the WFC3 data only, we examined H₂O opacity, since it has been shown to be an important opacity source in the WFC3 bandpass (see §1.3.3). The results of our analysis are shown in Table 5.10. Our most important finding is that analysis of STIS data provides moderate evidence supporting detection of K opacity. The odds ratio found for K opacity is equivalent to a 3.0- σ detection in frequentist terms ([Trotta, 2008](#)).

5.7.2 Discussion of Retrieval Results

The PLATON fiducial model retrieval applied to the KELT-7b 0.3 - 5.0 μm transmission spectrum reveals a subsolar C/O ratio, supersolar metallicity atmosphere with high altitude clouds. Retrievals of slightly more complicated models, which include fits for either scattering slope or WFC3 offsets, indicate the same general characteristics for KELT-7b’s atmosphere. Qualitatively examining our composite transmission spectrum in Figure 5.13, we note higher transit depths—and thus higher opacities—coincident with the well-known 1.4 μm H₂O-band (§1.3.3). We also note higher transit depths and thus higher opacities near the K I resonance doublet at 0.77 μm and the Na I resonance doublet at 0.59 μm (Seager & Sasselov, 2000). At blue-optical wavelengths, the downward slope from $\sim 0.3 \mu\text{m}$ to $0.4 \mu\text{m}$ is consistent with Rayleigh scattering as well as opacity from atomic metals and ions (see §1.3.3, Lothringer et al., 2020).

The best fit model from the fiducial retrieval fails to capture the rich variation in transit depths displayed by the KELT-7b transmission spectrum. Rather, the model flattens the spectrum by imposing some combination of high altitude clouds and metallicity to mute the features. The only model that displayed some of the variation due to Na and K opacities was that of the fiducial model with a WFC3 offset. Despite these limitations, by examining various opacity sources, we were able to show that the KELT-7b composite transmission spectrum is consistent with detection of H₂O at the 3.6- σ level, and that the STIS-only transmission spectrum is consistent with detection of K at the 3- σ level. In this section, we will highlight

some of the limitations of the PLATON retrievals conducted thus far, and how we will overcome these limitations in our future work (§5.9). The topics addressed include instrumental offsets, the possibility of inhomogeneous clouds, free chemistry retrievals, and forward models with enhanced metal opacities.

We briefly discussed the potential for offsets between data sets in Section 5.7.1. One reason that the PLATON fiducial retrieval mutes the features of the transmission spectrum (i.e, through some combination of high metallicity and high-altitude clouds) is that the code is unable to account for variation in transit depths between data sets. Rather, the code flattens the spectrum, thus returning a best fit model that is an average between the high and low transit depth features. If the data sets are offset, however, including free parameters for offsets of all instruments may improve results, allowing a retrieval solution that better matches the data. This hypothesis is supported by our limited analysis of WFC3 offsets. Only our models allowing for WFC3 offsets returned best fit models that clearly showed some of the expected optical bandpass spectral features, such as those for Na and K.⁸ Sheppard et al. (2021) recently published a more complicated retrieval analysis for HAT-P-41b, where they found that their best fit model included offsets for 3 data sets—those from STIS G430L, STIS G750L, and WFC3. Examination of offsets between STIS data sets in particular may allow better understanding of the KELT-7b transmission spectrum. For example, the STIS G430L transmission spectrum appears to have several inexplicably low data points between 0.5 and 0.6 μm . If

⁸Note, however, that models allowing WFC3 offsets as free parameters in general showed only limited increases in $\ln \mathcal{Z}$, and χ^2_ν values for best fit models showed little to no improvement.

the entire STIS G430L spectrum were shifted upward, the blue-optical slope may be better explained with a combination of Rayleigh scattering and metal opacity sources (Lothringer et al., 2020). In addition, the low data points between 0.5 and 0.6 μm would then be more in-line with the STIS G750L data near those wavelengths. Only a more complicated retrieval that includes offsets from multiple instruments will reveal whether this indeed provides better insight into our data.

Inhomogeneous cloud cover along a planet’s terminator strongly impacts our interpretation of transmission spectra (Line & Parmentier, 2016). The strong incident irradiation upon tidally locked hot Jupiters drives a strong west-to-east circulation pattern, which in turn results in a temperature gradient of several hundred degrees (e.g., Showman & Guillot, 2002). Thus, the atmospheric properties on the east and west limb of a hot Jupiter may be drastically different. Of particular importance to transmission spectroscopy, the cooler west limb may have species that have condensed to form clouds, while those same species may remain in a gaseous state along the hotter east limb. In addition, 3D general circulation models of hot Jupiter atmospheres have also shown north-south variations in the distribution of cloud cover (e.g., Parmentier et al., 2013). Since our instruments are unable to resolve the planet itself, much less specific regions along the planet’s limb, a transmission spectrum is comprised of integrated light from the entire terminator of the planet, which likely includes some regions that are clear and some that are cloudy.

Line & Parmentier (2016) showed that the effect of nonuniform clouds is nearly indistinguishable from the effect of a high mean molecular weight atmosphere on a transit forward model. This degeneracy differs from that of an opaque uniform cloud

deck, since the wavelength-dependent shape of a uniform cloud deck in a transit forward model differs from that of a high mean molecular weight atmosphere, and thus in theory could be distinguished. Both [MacDonald & Madhusudhan \(2017\)](#) and [Sheppard et al. \(2021\)](#) developed partial cloud retrieval schemes and showed their transmission spectra were most consistent with inhomogeneous cloud models. By incorporating partial clouds, [Sheppard et al. \(2021\)](#) found that their retrieved metallicity more closely aligned to hot Jupiter planet evolution models ([Thorngren & Fortney, 2019](#)). Since inhomogeneous cloud cover is expected to be a feature of hot Jupiter atmospheres, we will explore the effects of including a free parameter for partial cloud cover in future retrievals.

We briefly introduced free chemistry retrievals in Section [5.7.1](#). While PLATON determines atmospheric chemical composition using free parameters for metallicity and C/O ratio, free chemistry retrievals determine individual chemical species abundances based upon spectral features. Recently, [Welbanks et al. \(2019\)](#) examined exoplanet atmospheric metallicity trends by using a free retrieval scheme to estimate abundances of H₂O, Na, and K in a sample of 19 exoplanets. Among their findings for gas giant planets, they showed that while the Na and K abundances correlated with each other, they were often vastly different from the H₂O abundances. They suggested that the differing trends in species abundances argued against the use of chemical equilibrium models using only metallicity and C/O ratio to determine atmospheric chemistry. Different species may be differently enhanced, and variation between species may only be detected using free retrievals. In the past, other PanCET studies have successfully used PLATON alongside other free

chemistry retrieval schemes to better understand exoplanet atmospheres (e.g., [Fu et al., 2020](#); [Sheppard et al., 2021](#)). We will work with the PanCET team to better interpret our results using the free chemistry ATMO retrieval code ([Evans et al., 2017](#); [Wakeford et al., 2017](#)).

[Lothringer et al. \(2020\)](#) recently showed that opacity sources not commonly considered in exoplanet atmosphere models will increase the transit depths at wavelengths shorter than $0.5 \mu\text{m}$ in hot Jupiter exoplanets with $T_{\text{eq}} \gtrsim 2000 \text{ K}$ (see [1.3.3](#)). PHOENIX forward models, which incorporate these opacity sources, have been successfully applied in the past to explain high apparent opacity levels shortward of $0.5 \mu\text{m}$ (e.g., [Fu et al., 2020](#)), and we will work with the PanCET team to apply these forward models to the KELT-7b transmission spectrum.

5.7.3 Comparison to Previous Results

[Pluriel et al. \(2020\)](#) examined the same HST WFC3 spectra for KELT-7b, and they used the TauREx3 free retrieval scheme to determine the KELT-7b atmospheric properties ([Al-Refaie et al., 2019](#)). Their results using HST WFC3 data alone were consistent with a cloud-free (68% credible region for cloud base pressure level from 224 to 10^5 Pascals) atmosphere containing H_2O and H^- opacities. They performed additional retrievals, successively adding additional data sets. When they added Spitzer archival data ([Garhart et al., 2020](#)), their results pointed to CO detection. When they added the relatively short wavelength TESS transit depth, they no longer detected H^- opacity, but instead detected FeH to explain shorter wave-

length absorption within the G141 grism. The [Pluriel et al. \(2020\)](#) results make no statements concerning overall atmospheric metallicity or C/O ratio.

The most significant difference between our results and those of [Pluriel et al. \(2020\)](#) concerns the existence of high altitude clouds. To compare our results more directly, we performed a retrieval using WFC3 data only, and our results still indicate that high altitude clouds (68% credible region for cloud base pressure level from 8 to 589 Pascals) are required to mute the H₂O features. Our retrieved limb temperature is also over 250 K cooler than the 1385 K temperature found by [Pluriel et al. \(2020\)](#). This result is not surprising given the correlation between temperature and cloud formation (e.g., [Fu et al., 2017](#)). Although PLATON does not support direct retrieval of species abundances, we used Bayesian evidence to compare models with and without various opacity sources to determine the importance of those opacities. Overall, our results agree with those of [Pluriel et al. \(2020\)](#) in that our model containing H₂O is strongly preferred to that without. Although examination of H⁻ opacity was inconclusive, this result is in agreement with the [Pluriel et al. \(2020\)](#) retrieval including the TESS data point, which lies within the STIS G750L bandpass.

5.7.4 Implications for Planet Formation

[Zhou et al. \(2016\)](#) suggested that the spin-orbit alignment of KELT-7b is primordial. Hot Jupiters are believed to have migrated inward after formation (§1.3.2), and the well-aligned orbit of KELT-7b indicates the planet most likely migrated inward via planet-gas interactions with its protoplanetary disk ([Lin et al., 1996](#)).

[Eistrup et al. \(2018\)](#) recently demonstrated that the C/O ratio in protoplanetary disks evolves over time during the era of planet formation. If KELT-7 did indeed migrate inward via planet-gas interactions, subsolar C/O values are possible, with the lowest C/O ratios extant in the primordial gas at the latest times (~ 7 Myr). Other elemental ratios evolve differently throughout the disk over time. Thus, more precise measurement of a variety of atomic and molecular abundances may allow us to further constrain the evolutionary pathway of this interesting giant planet.

Our median retrieved metallicity for the KELT-7b fiducial model is $27.5 \times$ solar, with the 68% credible region spanning from 3.63 to $302 \times$ solar (see [Table 5.8](#)). [Thorngren & Fortney \(2019\)](#) recently combined planet evolutionary models with observed exoplanet radii, insolation, and ages within a Bayesian framework to compute the atmospheric metallicities for individual planets. For KELT-7b, they estimated a metallicity of $21.08 \times$ solar, with an uncertainty of 7.00 . Their 95% percentile upper limit on KELT-7b metallicity is $33.65 \times$ solar. Thus, our retrieved metallicity value agrees well with the [Thorngren & Fortney \(2019\)](#) predictions. In addition, [Madhusudhan et al. \(2014\)](#) showed that hot Jupiters that form via core accretion and then migrate through their protoplanetary disks will have supersolar metallicities combined with subsolar or solar C/O ratios. Thus, our findings that KELT-7b has a supersolar metallicity and subsolar C/O ratio are in agreement with [Madhusudhan et al. \(2014\)](#)'s predictions of disk-driven migration.

5.8 Summary and Conclusion

We have produced and analyzed the composite 0.3 - 5.0 μm KELT-7b transmission spectrum, comprised of HST STIS and WFC3 data, as well as TESS-band transit depth and archival Spitzer IRAC 3.6 and 4.5 μm data. We analyzed the STIS transmission spectrum for the first time.

We examined the transmission spectrum using the isothermal equilibrium chemistry PLATON retrieval code with the *dynesty* nested sampling package. Our retrieval results show the KELT-7b transmission spectrum is consistent with a subsolar $\text{C/O} = 0.35_{-0.19}^{+0.21}$, high metallicity $\log \frac{Z}{Z_{\odot}} = 1.44_{-0.88}^{+1.04}$ atmosphere with high altitude clouds condensing at a pressure level $\log \frac{P_{\text{cloud}}}{\text{Pascals}} = 1.94_{-0.78}^{+1.20}$. By comparing the Bayesian evidence for models with and without various opacity sources, we found strong evidence for H_2O opacity, corresponding to a $3.6\text{-}\sigma$ detection in frequentist terms. By analyzing the STIS spectrum only, we found moderate evidence for K opacity, corresponding to a $3\text{-}\sigma$ detection.

KELT-7b was previously shown to follow an orbital path well-aligned with its host star's spin axis, implying that it migrated to its current location through its protoplanetary disk via planet-gas interaction (Bieryla et al., 2015; Zhou et al., 2016). The planet's subsolar C/O ratio combined with supersolar metallicity are in agreement with Madhusudhan et al. (2014)'s predictions for disk-driven migration. In addition, the planet's subsolar C/O ratio may be explained by recent chemical models showing that the C/O ratio of the protoplanetary disk evolves over time during the era of planet formation (Eistrup et al., 2018). Furthermore, KELT-7b's

retrieved superstellar metallicity agrees well with the [Thorngren & Fortney \(2019\)](#) predicted value of $21.08 \times$ solar, with an uncertainty of 7.00. Future studies may help to unravel more details of the planet’s evolutionary pathway as we measure additional chemical abundances.

HST is currently programming observations through October 2022,⁹ and will maintain a stable orbit through at least the mid-2030s.¹⁰ The James Webb Space Telescope (JWST) is scheduled to launch in October 2021. As shown in Chapter 4, the unprecedented wavelength coverage and resolution of JWST, combined with new exoplanet targets discovered by TESS, heralds a new era in exoplanet atmosphere discovery. However, JWST will probe only the infrared regime. Therefore, it is incumbent upon exoplanet scientists to work together to develop observation plans that capitalize upon the upcoming unique time period, when it will be possible to simultaneously observe UV/optical bands using HST and IR bands with JWST.

5.9 Future Work

The analysis and results presented in Sections 5.1 through 5.8 rely largely upon University of Maryland analysis tools (e.g., [Deming et al., 2013](#); [Wilkins et al., 2014](#)) and publicly available codes (e.g., [Zhang et al., 2019, 2020](#)). In the future, I will work with the PanCET team to further refine our data reduction analysis and the interpretation of our results. In particular, I will complete the following work:

1. In this Chapter, the planetary system parameters used for data analysis to

⁹<https://hst-docs.stsci.edu/hsp>

¹⁰<https://www.discovermagazine.com/the-sciences/how-much-longer-will-the-hubble-space-telescope-last>

produce the KELT-7b transmission spectrum relied upon the [Bieryla et al. \(2015\)](#) discovery paper. I will update the system parameters by using EXOFASTv2 ([Eastman et al., 2019](#)) to perform a global model fit to the stellar and planetary parameters. In this analysis, I will employ our HST, TESS, and Spitzer data, as well as stellar properties from the TESS Input Catalog, version 8 (TIC-8, [Stassun et al., 2019, 2018](#)), which makes use of Gaia Data Release 2 ([Gaia Collaboration et al., 2018, 2016](#)). I will report the results of this analysis and reproduce the transmission spectrum based upon any changes to the system parameters.

2. I will compare our output STIS transmission spectra with those obtained from PanCET team members using their analysis techniques (e.g., [Nikolov et al., 2015, 2014](#)). If any large discrepancies exist between the output transmission spectra, we will identify their source to ensure that the final spectrum produced is of the highest quality possible.
3. PanCET team members have access to forward models and atmospheric retrieval codes that will yield further insight into the atmosphere of KELT-7b. For example, PHOENIX forward models self-consistently solve the radiative transfer equation layer-by-layer assuming chemical and radiative-convective equilibrium. These models have proven useful in past analyses to predict opacity sources at blue-optical wavelengths ([Fu et al., 2020](#); [Lothringer et al., 2020](#)). In addition, the ATMO retrieval code can retrieve abundances of molecular species of interest ([Evans et al., 2017](#); [Wakeford et al., 2017](#)). I will work with

PanCET team members to further analyze the output transmission spectrum of KELT-7b.

4. As part of our updated retrieval analysis, we will consider the effects of including free parameters for inhomogeneous cloud cover and instrumental offsets (for all instruments, particularly the 2 STIS gratings and WFC3 G141). In addition, if observational data are available, we will analyze the star KELT-7 for stellar activity, and model those effects in our retrievals.

Appendix A: Facilities and Software

We made use of the following facilities and software while conducting the research described in this dissertation.

A.1 Facilities

1. Exoplanet Follow-up Observing Program for TESS (ExoFOP-TESS) website (<https://exofop.ipac.caltech.edu/tess/>)
2. Mikulski Archive for Space Telescopes (MAST, <https://archive.stsci.edu/>)
3. NASA Exoplanet Archive (<https://exoplanetarchive.ipac.caltech.edu/> - [Akeson et al., 2013](#))

A.2 Software

1. astropy (<https://www.astropy.org/> - [Astropy Collaboration et al., 2018, 2013](#))
2. corner.py (<https://corner.readthedocs.io/en/latest/index.html> - [Foreman-Mackey, 2016](#))
3. DYNESTY (<https://github.com/joshspeagle/dynesty> - [Speagle, 2020](#))

4. Exo-Transit (https://github.com/elizakempton/Exo_Transmit - [Kemp-ton et al., 2017](#))
5. IDL Astronomy User's Library (<https://idlastro.gsfc.nasa.gov/>)
6. Matplotlib (<https://matplotlib.org/> - [Hunter, 2007](#))
7. MuSCAT/MuSCAT2 Python Simulation Code written by Dana Louie (Chapter 3)
8. NIRISS IDL Simulation Code written by Dana Louie (Chapter 4)
9. NumPy (<https://numpy.org/> - [Harris et al., 2020](#))
10. PLATON (<https://github.com/ideasrule/platon> - [Zhang et al., 2019, 2020](#))
11. SciPy (<https://www.scipy.org/> - [Virtanen et al., 2020](#))

Bibliography

- Abe, Y. & Matsui, T. 1985, Lunar and Planetary Science Conference Proceedings, 90, C545
- Abril-Abril, M., Nuñez-Castaín, A., Rodríguez-García, L. A., & Cabrera-Lavers, A. 2016, in Society of Photo-Optical Instrumentation Engineers (SPIE) Conference Series, Vol. 9906, , 99063U
- Adams, E. R., Seager, S., & Elkins-Tanton, L. 2008, *ApJ*, 673, 1160, arXiv:0710.4941
- Akeson, R. L., Chen, X., Ciardi, D., Crane, M., Good, J., Harbut, M., Jackson, E., Kane, S. R., Laity, A. C., Leifer, S., Lynn, M., McElroy, D. L., Papin, M., Plavchan, P., Ramírez, S. V., Rey, R., von Braun, K., Wittman, M., Abajian, M., Ali, B., Beichman, C., Beekley, A., Berriman, G. B., Berukoff, S., Bryden, G., Chan, B., Groom, S., Lau, C., Payne, A. N., Regelson, M., Saucedo, M., Schmitz, M., Stauffer, J., Wyatt, P., & Zhang, A. 2013, *PASP*, 125, 989, arXiv:1307.2944
- Al-Refaie, A. F., Changeat, Q., Waldmann, I. P., & Tinetti, G. 2019, arXiv e-prints, arXiv:1912.07759, arXiv:1912.07759
- Alam, M. K., López-Morales, M., Nikolov, N., Sing, D. K., Henry, G. W., Baxter, C., Désert, J.-M., Barstow, J. K., Mikal-Evans, T., Bourrier, V., Lavvas, P., Wakeford, H. R., Williamson, M. H., Sanz-Forcada, J., Buchhave, L. A., Cohen, O., & García Muñoz, A. 2020, *AJ*, 160, 51, arXiv:2005.11293
- Allard, F., Homeier, D., & Freytag, B. 2012, *Philosophical Transactions of the Royal Society of London Series A*, 370, 2765, arXiv:1112.3591
- Allard, N. F., Spiegelman, F., & Kielkopf, J. F. 2016, *A&A*, 589, A21
- Allard, N. F., Spiegelman, F., Leininger, T., & Molliere, P. 2019, *A&A*, 628, A120, arXiv:1908.01989
- Allart, R., Bourrier, V., Lovis, C., Ehrenreich, D., Spake, J. J., Wyttenbach, A., Pino, L., Pepe, F., Sing, D. K., & Lecavelier des Etangs, A. 2018, *Science*, 362, 1384, arXiv:1812.02189

- Almenara, J. M., Astudillo-Defru, N., Bonfils, X., Forveille, T., Santerne, A., Albrecht, S., Barros, S. C. C., Bouchy, F., Delfosse, X., Demangeon, O., Diaz, R. F., Hébrard, G., Mayor, M., Neves, V., Rojo, P., Santos, N. C., & Wünsche, A. 2015, *A&A*, 581, L7, arXiv:1509.02917
- Alonso, R., Deeg, H. J., Brown, T. M., & Belmonte, J. A. ESA Special Publication, Vol. 538, , *Stellar Structure and Habitable Planet Finding*, ed. F. Favata S. Aigrain & A. Wilson, 255–259
- Asplund, M., Grevesse, N., Sauval, A. J., & Scott, P. 2009, *ARA&A*, 47, 481, arXiv:0909.0948
- Astropy Collaboration, Price-Whelan, A. M., Sipócz, B. M., Günther, H. M., Lim, P. L., Crawford, S. M., Conseil, S., Shupe, D. L., Craig, M. W., Dencheva, N., Ginsburg, A., VanderPlas, J. T., Bradley, L. D., Pérez-Suárez, D., de Val-Borro, M., Aldcroft, T. L., Cruz, K. L., Robitaille, T. P., Tollerud, E. J., Ardelean, C., Babej, T., Bach, Y. P., Bachetti, M., Bakanov, A. V., Bamford, S. P., Barentsen, G., Barmby, P., Baumbach, A., Berry, K. L., Biscani, F., Boquien, M., Bostroem, K. A., Bouma, L. G., Brammer, G. B., Bray, E. M., Breytenbach, H., Buddelmeijer, H., Burke, D. J., Calderone, G., Cano Rodríguez, J. L., Cara, M., Cardoso, J. V. M., Cheedella, S., Copin, Y., Corrales, L., Crichton, D., D’Avella, D., Deil, C., Depagne, É., Dietrich, J. P., Donath, A., Droettboom, M., Earl, N., Erben, T., Fabbro, S., Ferreira, L. A., Finethy, T., Fox, R. T., Garrison, L. H., Gibbons, S. L. J., Goldstein, D. A., Gommers, R., Greco, J. P., Greenfield, P., Groener, A. M., Grollier, F., Hagen, A., Hirst, P., Homeier, D., Horton, A. J., Hossein-zadeh, G., Hu, L., Hunkeler, J. S., Ivezić, Ž., Jain, A., Jenness, T., Kanarek, G., Kendrew, S., Kern, N. S., Kerzendorf, W. E., Khvalko, A., King, J., Kirkby, D., Kulkarni, A. M., Kumar, A., Lee, A., Lenz, D., Littlefair, S. P., Ma, Z., Macleod, D. M., Mastropietro, M., McCully, C., Montagnac, S., Morris, B. M., Mueller, M., Mumford, S. J., Muna, D., Murphy, N. A., Nelson, S., Nguyen, G. H., Ninan, J. P., Nöthe, M., Ogaz, S., Oh, S., Parejko, J. K., Parley, N., Pascual, S., Patil, R., Patil, A. A., Plunkett, A. L., Prochaska, J. X., Rastogi, T., Reddy Janga, V., Sabater, J., Sakurikar, P., Seifert, M., Sherbert, L. E., Sherwood-Taylor, H., Shih, A. Y., Sick, J., Silbiger, M. T., Singanamalla, S., Singer, L. P., Sladen, P. H., Sooley, K. A., Sornarajah, S., Streicher, O., Teuben, P., Thomas, S. W., Tremblay, G. R., Turner, J. E. H., Terrón, V., van Kerkwijk, M. H., de la Vega, A., Watkins, L. L., Weaver, B. A., Whitmore, J. B., Willez, J., Zabalza, V., & Astropy Contributors. 2018, *AJ*, 156, 123, arXiv:1801.02634
- Astropy Collaboration, Robitaille, T. P., Tollerud, E. J., Greenfield, P., Droettboom, M., Bray, E., Aldcroft, T., Davis, M., Ginsburg, A., Price-Whelan, A. M., Kerzendorf, W. E., Conley, A., Crighton, N., Barbary, K., Muna, D., Ferguson, H., Grollier, F., Parikh, M. M., Nair, P. H., Unther, H. M., Deil, C., Willez, J., Conseil, S., Kramer, R., Turner, J. E. H., Singer, L., Fox, R., Weaver, B. A., Zabalza, V., Edwards, Z. I., Azalee Bostroem, K., Burke, D. J., Casey, A. R., Crawford, S. M., Dencheva, N., Ely, J., Jenness, T., Labrie, K., Lim, P. L.,

- Pierfederici, F., Pontzen, A., Ptak, A., Refsdal, B., Servillat, M., & Streicher, O. 2013, *A&A*, 558, A33, arXiv:1307.6212
- Auvergne, M., Bodin, P., Boissard, L., Buey, J. T., Chaintreuil, S., Epstein, G., Jouret, M., Lam-Trong, T., Levacher, P., Magnan, A., Perez, R., Plasson, P., Plessier, J., Peter, G., Steller, M., Tiphène, D., Baglin, A., Agogué, P., Appourchaux, T., Barbet, D., Beaufort, T., Bellenger, R., Berlin, R., Bernardi, P., Blouin, D., Boumier, P., Bonneau, F., Briet, R., Butler, B., Cautain, R., Chiavassa, F., Costes, V., Cuvilho, J., Cunha-Parro, V., de Oliveira Fialho, F., Decaudin, M., Defise, J. M., Djalal, S., Docclo, A., Drummond, R., Dupuis, O., Exil, G., Fauré, C., Gaboriaud, A., Gamet, P., Gavalda, P., Grolleau, E., Gueguen, L., Guivarc'h, V., Guterman, P., Hasiba, J., Huntzinger, G., Hustaix, H., Imbert, C., Jeanville, G., Johlander, B., Jorda, L., Journoud, P., Karioty, F., Kerjean, L., Lafond, L., Lapeyrere, V., Landiech, P., Larqué, T., Laudet, P., Le Merrer, J., Leporati, L., Leruyet, B., Levieuge, B., Llebaria, A., Martin, L., Mazy, E., Mesnager, J. M., Michel, J. P., Moalic, J. P., Monjoin, W., Naudet, D., Neukirchner, S., Nguyen-Kim, K., Ollivier, M., Orcesi, J. L., Ottacher, H., Oulali, A., Parisot, J., Perruchot, S., Piacentino, A., Pinheiro da Silva, L., Platzer, J., Pontet, B., Pradines, A., Quentin, C., Rohbeck, U., Rolland, G., Rollenhagen, F., Romagnan, R., Russ, N., Samadi, R., Schmidt, R., Schwartz, N., Sebbag, I., Smit, H., Sunter, W., Tello, M., Toulouse, P., Ulmer, B., Vandermarcq, O., Vergnault, E., Wallner, R., Waultier, G., & Zanatta, P. 2009, *A&A*, 506, 411, arXiv:0901.2206
- Baglin, A., Auvergne, M., Barge, P., Deleuil, M., Catala, C., Michel, E., Weiss, W., & COROT Team. The CoRoT Mission Pre-Launch Status - Stellar Seismology and Planet Finding, ed. , M. FridlundA. BaglinJ. Lochard & L. Conroy, 33
- Bakos, G. Á. The HATNet and HATSouth Exoplanet Surveys, ed. , H. J. DeegJ. A. Belmonte, 111
- Ballard, S. 2019, *AJ*, 157, 113, arXiv:1801.04949
- Barber, R. J., Tennyson, J., Harris, G. J., & Tolchenov, R. N. 2006, *MNRAS*, 368, 1087, arXiv:astro-ph/0601236
- Barclay, T., Pepper, J., & Quintana, E. V. 2018, *ApJS*, 239, 2, arXiv:1804.05050
- Barros, S. C. C., Almenara, J. M., Deleuil, M., Diaz, R. F., Csizmadia, S., Cabrera, J., Chaintreuil, S., Collier Cameron, A., Hatzes, A., Haywood, R., Lanza, A. F., Aigrain, S., Alonso, R., Bordé, P., Bouchy, F., Deeg, H. J., Erikson, A., Fridlund, M., Grziwa, S., Gandolfi, D., Guillot, T., Guenther, E., Leger, A., Moutou, C., Ollivier, M., Pasternacki, T., Pätzold, M., Rauer, H., Rouan, D., Santerne, A., Schneider, J., & Wuchterl, G. 2014, *A&A*, 569, A74, arXiv:1407.8099
- Barstow, J. K. 2020, *MNRAS*, 497, 4183, arXiv:2002.02945
- Barstow, J. K., Aigrain, S., Irwin, P. G. J., Kendrew, S., & Fletcher, L. N. 2015, *MNRAS*, 448, 2546, arXiv:1501.06349

- Barstow, J. K., Aigrain, S., Irwin, P. G. J., & Sing, D. K. 2017, *ApJ*, 834, 50, arXiv:1610.01841
- Barstow, J. K., Irwin, P. G. J., Kendrew, S., & Aigrain, S. 2016, in , Vol. 9904, *Space Telescopes and Instrumentation 2016: Optical, Infrared, and Millimeter Wave*, 99043P
- Batalha, N. E., Kempton, E. M.-R., & Mbarek, R. 2017a, *ApJL*, 836, L5, arXiv:1701.00012
- Batalha, N. E., Lewis, T., Fortney, J. J., Batalha, N. M., Kempton, E., Lewis, N. K., & Line, M. R. 2019, *ApJL*, 885, L25, arXiv:1910.00076
- Batalha, N. E. & Line, M. R. 2017, *AJ*, 153, 151, arXiv:1612.02085
- Batalha, N. E., Mandell, A., Pontoppidan, K., Stevenson, K. B., Lewis, N. K., Kalirai, J., Greene, T., Albert, L., Nielsen, L. D., & Earl, N. 2017b, *ArXiv e-prints*, arXiv:1702.01820
- Bean, J. L., Désert, J.-M., Kabath, P., Stalder, B., Seager, S., Miller-Ricci Kempton, E., Berta, Z. K., Homeier, D., Walsh, S., & Seifahrt, A. 2011, *ApJ*, 743, 92, arXiv:1109.0582
- Bean, J. L., Miller-Ricci Kempton, E., & Homeier, D. 2010, *Nature*, 468, 669, arXiv:1012.0331
- Becker, J. C., Vanderburg, A., Adams, F. C., Rappaport, S. A., & Schwengeler, H. M. 2015, *ApJL*, 812, L18, arXiv:1508.02411
- Beichman, C., Benneke, B., Knutson, H., Smith, R., Lagage, P.-O., Dressing, C., Latham, D., Lunine, J., Birkmann, S., Ferruit, P., Giardino, G., Kempton, E., Carey, S., Krick, J., Deroo, P. D., Mandell, A., Ressler, M. E., Shporer, A., Swain, M., Vasisht, G., Ricker, G., Bouwman, J., Crossfield, I., Greene, T., Howell, S., Christiansen, J., Ciardi, D., Clampin, M., Greenhouse, M., Sozzetti, A., Goudfrooij, P., Hines, D., Keyes, T., Lee, J., McCullough, P., Robberto, M., Stansberry, J., Valenti, J., Rieke, M., Rieke, G., Fortney, J., Bean, J., Kreidberg, L., Ehrenreich, D., Deming, D., Albert, L., Doyon, R., & Sing, D. 2014, *PASP*, 126, 1134
- Belu, A. R., Selsis, F., Morales, J.-C., Ribas, I., Cossou, C., & Rauer, H. 2011, *A&A*, 525, A83, arXiv:1008.0028
- Benneke, B., Wong, I., Piaulet, C., Knutson, H. A., Lothringer, J., Morley, C. V., Crossfield, I. J. M., Gao, P., Greene, T. P., Dressing, C., Dragomir, D., Howard, A. W., McCullough, P. R., Kempton, E. M. R., Fortney, J. J., & Fraine, J. 2019, *ApJL*, 887, L14, arXiv:1909.04642

- Berta, Z. K., Charbonneau, D., Désert, J.-M., Miller-Ricci Kempton, E., McCullough, P. R., Burke, C. J., Fortney, J. J., Irwin, J., Nutzman, P., & Homeier, D. 2012, *ApJ*, 747, 35, arXiv:1111.5621
- Berta-Thompson, Z. K., Irwin, J., Charbonneau, D., Newton, E. R., Dittmann, J. A., Astudillo-Defru, N., Bonfils, X., Gillon, M., Jehin, E., Stark, A. A., Stalder, B., Bouchy, F., Delfosse, X., Forveille, T., Lovis, C., Mayor, M., Neves, V., Pepe, F., Santos, N. C., Udry, S., & Wünsche, A. 2015, *Nature*, 527, 204, arXiv:1511.03550
- Bessell, M. S. 2005, *ARA&A*, 43, 293
- Bieryla, A., Collins, K., Beatty, T. G., Eastman, J., Siverd, R. J., Pepper, J., Gaudi, B. S., Stassun, K. G., Cañas, C., Latham, D. W., Buchhave, L. A., Sanchis-Ojeda, R., Winn, J. N., Jensen, E. L. N., Kielkopf, J. F., McLeod, K. K., Gregorio, J., Colón, K. D., Street, R., Ross, R., Penny, M., Mellon, S. N., Oberst, T. E., Fulton, B. J., Wang, J., Berlind, P., Calkins, M. L., Esquerdo, G. A., DePoy, D. L., Gould, A., Marshall, J., Pogge, R., Trueblood, M., & Trueblood, P. 2015, *AJ*, 150, 12, arXiv:1501.05565
- Bluhm, P., Luque, R., Espinoza, N., Pallé, E., Caballero, J. A., Dreizler, S., Livingston, J. H., Mathur, S., Quirrenbach, A., Stock, S., Van Eylen, V., Nowak, G., López, E. D., Csizmadia, S., Zapatero Osorio, M. R., Schöfer, P., Lillo-Box, J., Oshagh, M., González-Álvarez, E., Amado, P. J., Barrado, D., Béjar, V. J. S., Cale, B., Chaturvedi, P., Cifuentes, C., Cochran, W. D., Collins, K. A., Collins, K. I., Cortés-Contreras, M., Díez Alonso, E., El Mufti, M., Ercolino, A., Fridlund, M., Gaidos, E., García, R. A., Georgieva, I., González-Cuesta, L., Guerra, P., Hatzes, A. P., Henning, T., Herrero, E., Hidalgo, D., Isopi, G., Jeffers, S. V., Jenkins, J. M., Jensen, E. L. N., Ká bath, P., Kaminski, A., Kemmer, J., Korth, J., Kossakowski, D., Kürster, M., Lafarga, M., Mallia, F., Montes, D., Morales, J. C., Morales-Calderón, M., Murgas, F., Narita, N., Passegger, V. M., Pedraz, S., Persson, C. M., Plavchan, P., Rauer, H., Redfield, S., Reffert, S., Reiners, A., Ribas, I., Ricker, G. R., Rodríguez-López, C., Santos, A. R. G., Seager, S., Schlecker, M., Schweitzer, A., Shan, Y., Soto, M. G., Subjak, J., Tal-Or, L., Trifonov, T., Vanaverbeke, S., Vanderspek, R., Wittrock, J., Zechmeister, M., & Zohrabi, F. 2020, *A&A*, 639, A132, arXiv:2004.06218
- Bochanski, J. J., Hawley, S. L., Covey, K. R., West, A. A., Reid, I. N., Golimowski, D. A., & Ivezić, Ž. 2010, *AJ*, 139, 2679, arXiv:1004.4002
- Borucki, W., Koch, D., Batalha, N., Caldwell, D., Christensen-Dalsgaard, J., Cochran, W. D., Dunham, E., Gautier, T. N., Geary, J., Gilliland, R., Jenkins, J., Kjeldsen, H., Lissauer, J. J., & Rowe, J. *IAU Symposium*, Vol. 253, , *Transiting Planets*, ed. F. Pont, D. Sasselov & M. J. Holman, 289–299
- Borucki, W. J., Koch, D., Basri, G., Batalha, N., Brown, T., Caldwell, D., Caldwell, J., Christensen-Dalsgaard, J., Cochran, W. D., DeVore, E., Dunham, E. W.,

- Dupree, A. K., Gautier, T. N., Geary, J. C., Gilliland, R., Gould, A., Howell, S. B., Jenkins, J. M., Kondo, Y., Latham, D. W., Marcy, G. W., Meibom, S., Kjeldsen, H., Lissauer, J. J., Monet, D. G., Morrison, D., Sasselov, D., Tarter, J., Boss, A., Brownlee, D., Owen, T., Buzasi, D., Charbonneau, D., Doyle, L., Fortney, J., Ford, E. B., Holman, M. J., Seager, S., Steffen, J. H., Welsh, W. F., Rowe, J., Anderson, H., Buchhave, L., Ciardi, D., Walkowicz, L., Sherry, W., Horch, E., Isaacson, H., Everett, M. E., Fischer, D., Torres, G., Johnson, J. A., Endl, M., MacQueen, P., Bryson, S. T., Dotson, J., Haas, M., Kolodziejczak, J., Van Cleve, J., Chandrasekaran, H., Twicken, J. D., Quintana, E. V., Clarke, B. D., Allen, C., Li, J., Wu, H., Tenenbaum, P., Verner, E., Bruhweiler, F., Barnes, J., & Prsa, A. 2010, *Science*, 327, 977
- Borucki, W. J., Koch, D. G., Lissauer, J., Basri, G., Brown, T., Caldwell, D. A., Jenkins, J. M., Caldwell, J. J., Christensen-Dalsgaard, J., Cochran, W. D., Dunham, E. W., Gautier, T. N., Geary, J. C., Latham, D., Sasselov, D., Gilliland, R. L., Howell, S., Monet, D. G., & Batalha, N. *Astronomical Society of the Pacific Conference Series*, Vol. 366, , *Transiting Extrapolar Planets Workshop*, ed. C. Afonso, D. Wel Drake & T. Henning, 309
- Borucki, W. J. & Summers, A. L. 1984, *Icarus*, 58, 121
- Borysow, A. 2002, *A&A*, 390, 779
- Boss, A. P. 1997, *Science*, 276, 1836
- Bouma, L. G., Winn, J. N., Kosiarek, J., & McCullough, P. R. 2017, *ArXiv e-prints*, arXiv:1705.08891
- Bourrier, V., Ehrenreich, D., Wheatley, P. J., Bolmont, E., Gillon, M., de Wit, J., Burgasser, A. J., Jehin, E., Queloz, D., & Triaud, A. H. M. J. 2017, *A&A*, 599, L3, arXiv:1702.07004
- Boyajian, T. S., von Braun, K., van Belle, G., McAlister, H. A., ten Brummelaar, T. A., Kane, S. R., Muirhead, P. S., Jones, J., White, R., Schaefer, G., Ciardi, D., Henry, T., López-Morales, M., Ridgway, S., Gies, D., Jao, W.-C., Rojas-Ayala, B., Parks, J. R., Sturmann, L., Sturmann, J., Turner, N. H., Farrington, C., Goldfinger, P. J., & Berger, D. H. 2012, *ApJ*, 757, 112, arXiv:1208.2431
- Brown, T. M. 2001, *ApJ*, 553, 1006, arXiv:astro-ph/0101307
- . 2003, *ApJL*, 593, L125, arXiv:astro-ph/0307256
- Burrows, A., Marley, M., Hubbard, W. B., Lunine, J. I., Guillot, T., Saumon, D., Freedman, R., Sudarsky, D., & Sharp, C. 1997, *ApJ*, 491, 856, arXiv:astro-ph/9705201
- Burrows, A. & Sharp, C. M. 1999, *ApJ*, 512, 843, arXiv:astro-ph/9807055
- Chabrier, G. & Baraffe, I. 1997, *A&A*, 327, 1039, arXiv:astro-ph/9704118

- Chachan, Y., Knutson, H. A., Gao, P., Kataria, T., Wong, I., Henry, G. W., Benneke, B., Zhang, M., Barstow, J., Bean, J. L., Mikal-Evans, T., Lewis, N. K., Mansfield, M., López-Morales, M., Nikolov, N., Sing, D. K., & Wakeford, H. 2019, *AJ*, 158, 244, arXiv:1910.07523
- Charbonneau, D., Berta, Z. K., Irwin, J., Burke, C. J., Nutzman, P., Buchhave, L. A., Lovis, C., Bonfils, X., Latham, D. W., Udry, S., Murray-Clay, R. A., Holman, M. J., Falco, E. E., Winn, J. N., Queloz, D., Pepe, F., Mayor, M., Delfosse, X., & Forveille, T. 2009, *Nature*, 462, 891, arXiv:0912.3229
- Charbonneau, D., Brown, T. M., Dunham, E. W., Latham, D. W., Looper, D. L., & Mandushev, G. in , *American Institute of Physics Conference Series*, Vol. 713, *The Search for Other Worlds*, ed. S. S. HoltD. Deming, 151–160
- Charbonneau, D., Brown, T. M., Latham, D. W., & Mayor, M. 2000, *ApJL*, 529, L45, arXiv:astro-ph/9911436
- Charbonneau, D., Brown, T. M., Noyes, R. W., & Gilliland, R. L. 2002, *ApJ*, 568, 377, arXiv:astro-ph/0111544
- Charbonneau, D. & Deming, D. 2007, *ArXiv e-prints*, arXiv:0706.1047
- Chen, J. & Kipping, D. 2017, *ApJ*, 834, 17, arXiv:1603.08614
- Chromey, F. R. 2010, *To Measure the Sky*
- Clampin, M. *IAU Symposium*, Vol. 276, , *The Astrophysics of Planetary Systems: Formation, Structure, and Dynamical Evolution*, ed. A. SozzettiM. G. Lattanzi & A. P. Boss, 335–342
- Claret, A. 2017, *A&A*, 600, A30, arXiv:1804.10295
- Claret, A. & Bloemen, S. 2011, *A&A*, 529, A75
- Claudi, R., Benatti, S., Carleo, I., Ghedina, A., Molinari, E., Oliva, E., Tozzi, A., Baruffolo, A., Cecconi, M., Cosentino, R., Fantinel, D., Fini, L., Ghinassi, F., Gonzalez, M., Gratton, R., Guerra, J., Harutyunyan, A., Hernandez, N., Iuzzolino, M., Lodi, M., Malavolta, L., Maldonado, J., Micela, G., Sanna, N., Sanjuan, J., Scuderi, S., Sozzetti, A., Pérez Ventura, H., Diaz Marcos, H., Galli, A., Gonzalez, C., Riverol, L., & Riverol, C. 2016, in *Society of Photo-Optical Instrumentation Engineers (SPIE) Conference Series*, Vol. 9908, , 99081A
- Cloutier, R. & Menou, K. 2020, *AJ*, 159, 211, arXiv:1912.02170
- Collier Cameron, A., Pollacco, D., Hellier, C., West, R., WASP Consortium, & SOPHIE & CORALIE Planet-Search Teams. *Transiting Planets*, ed. , F. PontD. Sas-selov & M. J. Holman, Vol. 253, 29–35

- Collins, K. A., Collins, K. I., Pepper, J., Labadie-Bartz, J., Stassun, K. G., Gaudi, B. S., Bayliss, D., Bento, J., COLÓN, K. D., Feliz, D., James, D., Johnson, M. C., Kuhn, R. B., Lund, M. B., Penny, M. T., Rodriguez, J. E., Siverd, R. J., Stevens, D. J., Yao, X., Zhou, G., Akshay, M., Aldi, G. F., Ashcraft, C., Awiphan, S., Baştürk, Ö., Baker, D., Beatty, T. G., Benni, P., Berlind, P., Berriman, G. B., Berta-Thompson, Z., Bieryla, A., Bozza, V., Calchi Novati, S., Calkins, M. L., Cann, J. M., Ciardi, D. R., Clark, I. R., Cochran, W. D., Cohen, D. H., Conti, D., Crepp, J. R., Curtis, I. A., D’Ago, G., Diazeguigure, K. A., Dressing, C. D., Dubois, F., Ellingson, E., Ellis, T. G., Esquerdo, G. A., Evans, P., Friedli, A., Fukui, A., Fulton, B. J., Gonzales, E. J., Good, J. C., Gregorio, J., Gumusayak, T., Hancock, D. A., Harada, C. K., Hart, R., Hintz, E. G., Jang-Condell, H., Jeffery, E. J., Jensen, E. L. N., Jofré, E., Joner, M. D., Kar, A., Kasper, D. H., Ketten, B., Kielkopf, J. F., Komonjinda, S., Kotnik, C., Latham, D. W., Leuquire, J., Lewis, T. R., Logie, L., Lowther, S. J., Macqueen, P. J., Martin, T. J., Mawet, D., Mcleod, K. K., Murawski, G., Narita, N., Nordhausen, J., Oberst, T. E., Odden, C., Panka, P. A., Petrucci, R., Plavchan, P., Quinn, S. N., Rau, S., Reed, P. A., Relles, H., Renaud, J. P., Scarpetta, G., Sorber, R. L., Spencer, A. D., Spencer, M., Stephens, D. C., Stockdale, C., Tan, T.-G., Trueblood, M., Trueblood, P., Vanaverbeke, S., Villanueva, Steven, J., Warner, E. M., West, M. L., Yalçinkaya, S., Yeigh, R., & Zambelli, R. 2018, *AJ*, 156, 234, arXiv:1803.01869
- Colón, K. D. & Ford, E. B. 2011, *PASP*, 123, 1391, arXiv:1110.4385
- Colón, K. D., Ford, E. B., & Morehead, R. C. 2012, *MNRAS*, 426, 342, arXiv:1207.2481
- Crisp, D., Pollock, H. R., Rosenberg, R., Chapsky, L., Lee, R. A. M., Oyafuso, F. A., Frankenberg, C., O’Dell, C. W., Bruegge, C. J., Doran, G. B., Eldering, A., Fisher, B. M., Fu, D., Gunson, M. R., Mandrake, L., Osterman, G. B., Schwandner, F. M., Sun, K., Taylor, T. E., Wennberg, P. O., & Wunch, D. 2017, *Atmospheric Measurement Techniques*, 10, 59
- Crossfield, I. J. M. & Kreidberg, L. 2017, *ArXiv e-prints*, arXiv:1708.00016
- Crouzet, N., Bonfils, X., Delfosse, X., Boisse, I., Hébrard, G., Forveille, T., Donati, J.-F., Bouchy, F., Moutou, C., Doyon, R., Artigau, E., Albert, L., Malo, L., Lecavelier des Etangs, A., & Santerne, A. 2017, *ArXiv e-prints*, arXiv:1701.03539
- Dai, F., Winn, J. N., Albrecht, S., Arriagada, P., Bieryla, A., Butler, R. P., Crane, J. D., Hirano, T., Johnson, J. A., Kiilerich, A., Latham, D. W., Narita, N., Nowak, G., Palle, E., Ribas, I., Rogers, L. A., Sanchis-Ojeda, R., Shectman, S. A., Teske, J. K., Thompson, I. B., Van Eylen, V., Vanderburg, A., Wittenmyer, R. A., & Yu, L. 2016, *ApJ*, 823, 115, arXiv:1604.01413
- de Wit, J., Wakeford, H. R., Gillon, M., Lewis, N. K., Valenti, J. A., Demory, B.-O., Burgasser, A. J., Burdanov, A., Delrez, L., Jehin, E., Lederer, S. M., Queloz, D., Triaud, A. H. M. J., & Van Grootel, V. 2016, *Nature*, 537, 69, arXiv:1606.01103

- de Wit, J., Wakeford, H. R., Lewis, N. K., Delrez, L., Gillon, M., Selsis, F., Lecante, J., Demory, B.-O., Bolmont, E., Bourrier, V., Burgasser, A. J., Grimm, S., Jehin, E., Lederer, S. M., Owen, J. E., Stamenković, V., & Triaud, A. H. M. J. 2018, *Nature Astronomy*, 2, 214, arXiv:1802.02250
- Demarque, P., Woo, J.-H., Kim, Y.-C., & Yi, S. K. 2004, *ApJS*, 155, 667
- Deming, D. & Knutson, H. A. 2020, *Nature Astronomy*, 4, 453, arXiv:2005.11331
- Deming, D., Seager, S., Winn, J., Miller-Ricci, E., Clampin, M., Lindler, D., Greene, T., Charbonneau, D., Laughlin, G., Ricker, G., Latham, D., & Ennico, K. 2009, *PASP*, 121, 952, arXiv:0903.4880
- Deming, D. & Sheppard, K. 2017, *ApJL*, 841, L3, arXiv:1705.00625
- Deming, D., Wilkins, A., McCullough, P., Burrows, A., Fortney, J. J., Agol, E., Dobbs-Dixon, I., Madhusudhan, N., Crouzet, N., Desert, J.-M., Gilliland, R. L., Haynes, K., Knutson, H. A., Line, M., Magic, Z., Mandell, A. M., Ranjan, S., Charbonneau, D., Clampin, M., Seager, S., & Showman, A. P. 2013, *ApJ*, 774, 95, arXiv:1302.1141
- Demory, B.-O., Gillon, M., Madhusudhan, N., & Queloz, D. 2016, *MNRAS*, 455, 2018, arXiv:1505.00269
- Désert, J.-M., Bean, J., Miller-Ricci Kempton, E., Berta, Z. K., Charbonneau, D., Irwin, J., Fortney, J., Burke, C. J., & Nutzman, P. 2011, *ApJL*, 731, L40, arXiv:1103.2370
- Diamond-Lowe, H., Stevenson, K. B., Bean, J. L., Line, M. R., & Fortney, J. J. 2014, *ApJ*, 796, 66, arXiv:1409.5336
- Dittmann, J. A., Irwin, J. M., Charbonneau, D., Berta-Thompson, Z. K., & Newton, E. R. 2016, *ArXiv e-prints*, arXiv:1611.09848
- . 2017a, *AJ*, 154, 142, arXiv:1611.09848
- Dittmann, J. A., Irwin, J. M., Charbonneau, D., Bonfils, X., Astudillo-Defru, N., Haywood, R. D., Berta-Thompson, Z. K., Newton, E. R., Rodriguez, J. E., Winters, J. G., Tan, T.-G., Almenara, J.-M., Bouchy, F., Delfosse, X., Forveille, T., Lovis, C., Murgas, F., Pepe, F., Santos, N. C., Udry, S., Wünsche, A., Esquerdo, G. A., Latham, D. W., & Dressing, C. D. 2017b, *Nature*, 544, 333, arXiv:1704.05556
- Doyon, R., Hutchings, J. B., Beaulieu, M., Albert, L., Lafrenière, D., Willott, C., Touahri, D., Rowlands, N., Maszkiewicz, M., Fullerton, A. W., Volk, K., Martel, A. R., Chayer, P., Sivaramakrishnan, A., Abraham, R., Ferrarese, L., Jayawardhana, R., Johnstone, D., Meyer, M., Pipher, J. L., & Sawicki, M. 2012, in , Vol. 8442, *Space Telescopes and Instrumentation 2012: Optical, Infrared, and Millimeter Wave*, 84422R

- Dravins, D., Lindegren, L., Mezey, E., & Young, A. T. 1998, *PASP*, 110, 1118
- Dressing, C. D. & Charbonneau, D. 2013, *ApJ*, 767, 95, arXiv:1302.1647
- . 2015, *ApJ*, 807, 45, arXiv:1501.01623
- Eastman, J., Gaudi, B. S., & Agol, E. 2013, *PASP*, 125, 83, arXiv:1206.5798
- Eastman, J. D., Rodriguez, J. E., Agol, E., Stassun, K. G., Beatty, T. G., Vanderburg, A., Gaudi, B. S., Collins, K. A., & Luger, R. 2019, arXiv e-prints, arXiv:1907.09480, arXiv:1907.09480
- Edwards, B., Changeat, Q., Mori, M., Anisman, L. O., Morvan, M., Yip, K. H., Tsiaras, A., Al-Refaie, A., Waldmann, I., & Tinetti, G. 2021, *AJ*, 161, 44, arXiv:2011.08815
- Eistrup, C., Walsh, C., & van Dishoeck, E. F. 2018, *A&A*, 613, A14, arXiv:1709.07863
- Elkins-Tanton, L. T. & Seager, S. 2008, *ApJ*, 685, 1237, arXiv:0808.1909
- Evans, T. M., Pont, F., Sing, D. K., Aigrain, S., Barstow, J. K., Désert, J.-M., Gibson, N., Heng, K., Knutson, H. A., & Lecavelier des Etangs, A. 2013, *ApJL*, 772, L16, arXiv:1307.3239
- Evans, T. M. & Sackett, P. D. 2010, *ApJ*, 712, 38, arXiv:1002.0886
- Evans, T. M., Sing, D. K., Kataria, T., Goyal, J., Nikolov, N., Wakeford, H. R., Deming, D., Marley, M. S., Amundsen, D. S., Ballester, G. E., Barstow, J. K., Ben-Jaffel, L., Bourrier, V., Buchhave, L. A., Cohen, O., Ehrenreich, D., García Muñoz, A., Henry, G. W., Knutson, H., Lavvas, P., Lecavelier Des Etangs, A., Lewis, N. K., López-Morales, M., Mandell, A. M., Sanz-Forcada, J., Tremblin, P., & Lupu, R. 2017, *Nature*, 548, 58, arXiv:1708.01076
- Evans, T. M., Sing, D. K., Wakeford, H. R., Nikolov, N., Ballester, G. E., Drummond, B., Kataria, T., Gibson, N. P., Amundsen, D. S., & Spake, J. 2016, *ApJL*, 822, L4, arXiv:1604.02310
- Fischer, D. A., Anglada-Escude, G., Arriagada, P., Baluev, R. V., Bean, J. L., Bouchy, F., Buchhave, L. A., Carroll, T., Chakraborty, A., Crepp, J. R., Dawson, R. I., Diddams, S. A., Dumusque, X., Eastman, J. D., Endl, M., Figueira, P., Ford, E. B., Foreman-Mackey, D., Fournier, P., Fűrész, G., Gaudi, B. S., Gregory, P. C., Grundahl, F., Hatzes, A. P., Hébrard, G., Herrero, E., Hogg, D. W., Howard, A. W., Johnson, J. A., Jorden, P., Jurgenson, C. A., Latham, D. W., Laughlin, G., Loredó, T. J., Lovis, C., Mahadevan, S., McCracken, T. M., Pepe, F., Perez, M., Phillips, D. F., Plavchan, P. P., Prato, L., Quirrenbach, A., Reiners, A., Robertson, P., Santos, N. C., Sawyer, D., Segransan, D., Sozzetti, A., Steinmetz, T., Szentgyorgyi, A., Udry, S., Valenti, J. A., Wang, S. X., Wittenmyer, R. A., & Wright, J. T. 2016, *PASP*, 128, 066001, arXiv:1602.07939

- Foreman-Mackey, D. 2016, *The Journal of Open Source Software*, 1, 24
- Foreman-Mackey, D., Hogg, D. W., Lang, D., & Goodman, J. 2013, *PASP*, 125, 306, arXiv:1202.3665
- Fraine, J. D., Deming, D., Gillon, M., Jehin, E., Demory, B.-O., Benneke, B., Seager, S., Lewis, N. K., Knutson, H., & Désert, J.-M. 2013, *ApJ*, 765, 127, arXiv:1301.6763
- Fressin, F., Torres, G., Charbonneau, D., Bryson, S. T., Christiansen, J., Dressing, C. D., Jenkins, J. M., Walkowicz, L. M., & Batalha, N. M. 2013, *ApJ*, 766, 81, arXiv:1301.0842
- Fu, G., Deming, D., Knutson, H., Madhusudhan, N., Mandell, A., & Fraine, J. 2017, *ApJL*, 847, L22, arXiv:1709.07385
- Fu, G., Deming, D., Lothringer, J., Nikolov, N., Sing, D. K., Kempton, E. M. R., Ih, J., Evans, T. M., Stevenson, K., Wakeford, H. R., Rodriguez, J. E., Eastman, J. D., Stassun, K., Henry, G. W., López-Morales, M., Lendl, M., Conti, D. M., Stockdale, C., Collins, K., Kielkopf, J., Barstow, J. K., Sanz-Forcada, J., Ehrenreich, D., & Bourrier, V. 2020, arXiv e-prints, arXiv:2005.02568, arXiv:2005.02568
- Fukui, A., Narita, N., Kawashima, Y., Kusakabe, N., Onitsuka, M., Ryu, T., Ikoma, M., Yanagisawa, K., & Izumiura, H. 2016, *ApJ*, 819, 27, arXiv:1510.03997
- Fukui, A., Suzuki, D., Koshimoto, N., Bachelet, E., Vanmunster, T., Storey, D., Maehara, H., Yanagisawa, K., Yamada, T., Yonehara, A., Hirano, T., Bennett, D. P., Bozza, V., Mawet, D., Penny, M. T., Awiphan, S., Oksanen, A., Heintz, T. M., Oberst, T. E., Béjar, V. J. S., Casasayas-Barris, N., Chen, G., Crouzet, N., Hidalgo, D., Klagyivik, P., Murgas, F., Narita, N., Palle, E., Parviainen, H., Watanabe, N., Kusakabe, N., Mori, M., Terada, Y., de Leon, J. P., Hernandez, A., Luque, R., Monelli, M., Montañes-Rodriguez, P., Prieto-Arranz, J., Murata, K. L., Shugarov, S., Kubota, Y., Otsuki, C., Shionoya, A., Nishiumi, T., Nishide, A., Fukagawa, M., Onodera, K., Villanueva, S., J., Street, R. A., Tsapras, Y., Hundertmark, M., Kuzuhara, M., Fujita, M., Beichman, C., Beaulieu, J. P., Alonso, R., Reichart, D. E., Kawai, N., & Tamura, M. 2019, *AJ*, 158, 206, arXiv:1909.11802
- Fulton, B. J. & Petigura, E. A. 2018, *AJ*, 156, 264, arXiv:1805.01453
- Fulton, B. J., Petigura, E. A., Howard, A. W., Isaacson, H., Marcy, G. W., Cargile, P. A., Hebb, L., Weiss, L. M., Johnson, J. A., Morton, T. D., Sinukoff, E., Crossfield, I. J. M., & Hirsch, L. A. 2017a, *AJ*, 154, 109, arXiv:1703.10375
- Fulton, B. J., Petigura, E. A., Howard, A. W., Isaacson, H., Marcy, G. W., Cargile, P. A., Hebb, L., Weiss, L. M., Johnson, J. A., Morton, T. D., Sinukoff, E., Crossfield, I. J. M., & Hirsch, L. A. 2017b, ArXiv e-prints, arXiv:1703.10375

Gaia Collaboration, Brown, A. G. A., Vallenari, A., Prusti, T., de Bruijne, J. H. J., Babusiaux, C., Bailer-Jones, C. A. L., Biermann, M., Evans, D. W., Eyer, L., Jansen, F., Jordi, C., Klioner, S. A., Lammers, U., Lindegren, L., Luri, X., Mignard, F., Panem, C., Pourbaix, D., Randich, S., Sartoretti, P., Siddiqui, H. I., Soubiran, C., van Leeuwen, F., Walton, N. A., Arenou, F., Bastian, U., Cropper, M., Drimmel, R., Katz, D., Lattanzi, M. G., Bakker, J., Cacciari, C., Castañeda, J., Chaoul, L., Cheek, N., De Angeli, F., Fabricius, C., Guerra, R., Holl, B., Masana, E., Messineo, R., Mowlavi, N., Nienartowicz, K., Panuzzo, P., Portell, J., Riello, M., Seabroke, G. M., Tanga, P., Thévenin, F., Gracia-Abril, G., Comoretto, G., Garcia-Reinaldos, M., Teyssier, D., Altmann, M., Andrae, R., Audard, M., Bellas-Velidis, I., Benson, K., Berthier, J., Blomme, R., Burgess, P., Busso, G., Carry, B., Cellino, A., Clementini, G., Clotet, M., Creevey, O., Davidson, M., De Ridder, J., Delchambre, L., Dell’Oro, A., Ducourant, C., Fernández-Hernández, J., Fouesneau, M., Frémat, Y., Galluccio, L., García-Torres, M., González-Núñez, J., González-Vidal, J. J., Gosset, E., Guy, L. P., Halbwachs, J. L., Hambly, N. C., Harrison, D. L., Hernández, J., Hestroffer, D., Hodgkin, S. T., Hutton, A., Jasniewicz, G., Jean-Antoine-Piccolo, A., Jordan, S., Korn, A. J., Krone-Martins, A., Lanzafame, A. C., Lebzelter, T., Löffler, W., Manteiga, M., Marrese, P. M., Martín-Fleitas, J. M., Moitinho, A., Mora, A., Muinonen, K., Osinde, J., Pancino, E., Pauwels, T., Petit, J. M., Recio-Blanco, A., Richards, P. J., Rimoldini, L., Robin, A. C., Sarro, L. M., Siopis, C., Smith, M., Sozzetti, A., Süveges, M., Torra, J., van Reeveen, W., Abbas, U., Abreu Aramburu, A., Accart, S., Aerts, C., Altavilla, G., Álvarez, M. A., Alvarez, R., Alves, J., Anderson, R. I., Andrei, A. H., Anglada Varela, E., Antiche, E., Antoja, T., Arcay, B., Astraatmadja, T. L., Bach, N., Baker, S. G., Balaguer-Núñez, L., Balm, P., Barache, C., Barata, C., Barbato, D., Barblan, F., Barklem, P. S., Barrado, D., Barros, M., Barstow, M. A., Bartholomé Muñoz, S., Bassilana, J. L., Becciani, U., Bellazzini, M., Berihuete, A., Bertone, S., Bianchi, L., Bienaymé, O., Blanco-Cuaresma, S., Boch, T., Boeche, C., Bombrun, A., Borrachero, R., Bossini, D., Bouquillon, S., Bourda, G., Bragaglia, A., Bramante, L., Breddels, M. A., Bressan, A., Brouillet, N., Brüsemeister, T., Brugaletta, E., Bucciarelli, B., Burlacu, A., Busonero, D., Butkevich, A. G., Buzzzi, R., Caffau, E., Cancelliere, R., Cannizzaro, G., Cantat-Gaudin, T., Carballo, R., Carlucci, T., Carrasco, J. M., Casamiquela, L., Castellani, M., Castro-Ginard, A., Charlot, P., Chemin, L., Chiavassa, A., Cocozza, G., Costigan, G., Cowell, S., Crifo, F., Crosta, M., Crowley, C., Cuypers, J., Dafonte, C., Damerdji, Y., Dapergolas, A., David, P., David, M., de Laverny, P., De Luise, F., De March, R., de Martino, D., de Souza, R., de Torres, A., Debosscher, J., del Pozo, E., Delbo, M., Delgado, A., Delgado, H. E., Di Matteo, P., Diakite, S., Diener, C., Distefano, E., Dolding, C., Drazinos, P., Durán, J., Edvardsson, B., Enke, H., Eriksson, K., Esquej, P., Eynard Bontemps, G., Fabre, C., Fabrizio, M., Faigler, S., Falcão, A. J., Farràs Casas, M., Federici, L., Fedorets, G., Fernique, P., Figueras, F., Filippi, F., Findeisen, K., Fonti, A., Fraile, E., Fraser, M., Frézouls, B., Gai, M., Galleti, S., Garabato, D., García-Sedano, F., Garofalo, A., Garralda, N., Gavel, A., Gavras, P., Gerssen, J., Geyer, R., Giacobbe, P., Gilmore, G., Girona, S., Giuffrida, G., Glass, F., Gomes, M., Granvik, M., Gueguen, A.,

Guerrier, A., Guiraud, J., Gutiérrez-Sánchez, R., Haignon, R., Hatzidimitriou, D., Hauser, M., Haywood, M., Heiter, U., Helmi, A., Heu, J., Hilger, T., Hobbs, D., Hofmann, W., Holland, G., Huckle, H. E., Hypki, A., Icardi, V., Janßen, K., Jevardat de Fombelle, G., Jonker, P. G., Juhász, Á. L., Julbe, F., Karampelas, A., Kewley, A., Klar, J., Kochoska, A., Kohley, R., Kolenberg, K., Kontizas, M., Kontizas, E., Koposov, S. E., Kordopatis, G., Kostrzewa-Rutkowska, Z., Koub-sky, P., Lambert, S., Lanza, A. F., Lasne, Y., Lavigne, J. B., Le Fustec, Y., Le Poncin-Lafitte, C., Lebreton, Y., Leccia, S., Leclerc, N., Lecoœur-Taïbi, I., Lenhardt, H., Leroux, F., Liao, S., Licata, E., Lindstrøm, H. E. P., Lister, T. A., Livanou, E., Lobel, A., López, M., Managau, S., Mann, R. G., Mantelet, G., Marchal, O., Marchant, J. M., Marconi, M., Marinoni, S., Marschalkó, G., Marshall, D. J., Martino, M., Marton, G., Mary, N., Massari, D., Matijević, G., Mazeh, T., McMillan, P. J., Messina, S., Michalik, D., Millar, N. R., Molina, D., Molinaro, R., Molnár, L., Montegriffo, P., Mor, R., Morbidelli, R., Morel, T., Morris, D., Mulone, A. F., Muraveva, T., Musella, I., Nelemans, G., Nicaastro, L., Noval, L., O’Mullane, W., Ordénovic, C., Ordóñez-Blanco, D., Osborne, P., Pagani, C., Pagano, I., Pailier, F., Palacin, H., Palaversa, L., Panahi, A., Pawlak, M., Pier-simoni, A. M., Pineau, F. X., Plachy, E., Plum, G., Poggio, E., Poujoulet, E., Prša, A., Pulone, L., Racero, E., Ragaini, S., Rambaux, N., Ramos-Lerate, M., Regibo, S., Reylé, C., Rielet, F., Ripepi, V., Riva, A., Rivard, A., Rixon, G., Roegiers, T., Roelens, M., Romero-Gómez, M., Rowell, N., Royer, F., Ruiz-Dern, L., Sadowski, G., Sagristà Sellés, T., Sahlmann, J., Salgado, J., Salguero, E., Sanna, N., Santana-Ros, T., Sarasso, M., Savietto, H., Schultheis, M., Sciacca, E., Segol, M., Segovia, J. C., Ségransan, D., Shih, I. C., Siltala, L., Silva, A. F., Smart, R. L., Smith, K. W., Solano, E., Solitro, F., Sordo, R., Soria Nieto, S., Souchay, J., Spagna, A., Spoto, F., Stampa, U., Steele, I. A., Steidelmüller, H., Stephenson, C. A., Stoev, H., Suess, F. F., Surdej, J., Szabados, L., Szegedi-Elek, E., Tapiador, D., Taris, F., Tauran, G., Taylor, M. B., Teixeira, R., Terrett, D., Teyssandier, P., Thuillot, W., Titarenko, A., Torra Clotet, F., Turon, C., Ulla, A., Utrilla, E., Uzzi, S., Vaillant, M., Valentini, G., Valette, V., van Elteren, A., Van Hemelryck, E., van Leeuwen, M., Vaschetto, M., Vecchiato, A., Veljanoski, J., Viala, Y., Vicente, D., Vogt, S., von Essen, C., Voss, H., Votruba, V., Voutsinas, S., Walmsley, G., Weiler, M., Wertz, O., Wevers, T., Wyrzykowski, Ł., Yoldas, A., Žerjal, M., Ziaepour, H., Zorec, J., Zschocke, S., Zucker, S., Zurbach, C., & Zwitter, T. 2018, *A&A*, 616, A1, arXiv:1804.09365

Gaia Collaboration, Prusti, T., de Bruijne, J. H. J., Brown, A. G. A., Vallenari, A., Babusiaux, C., Bailer-Jones, C. A. L., Bastian, U., Biermann, M., Evans, D. W., Eyer, L., Jansen, F., Jordi, C., Klioner, S. A., Lammers, U., Lindgren, L., Luri, X., Mignard, F., Milligan, D. J., Panem, C., Poinsignon, V., Pourbaix, D., Randich, S., Sarri, G., Sartoretti, P., Siddiqui, H. I., Soubiran, C., Valette, V., van Leeuwen, F., Walton, N. A., Aerts, C., Arenou, F., Cropper, M., Drimmel, R., Høg, E., Katz, D., Lattanzi, M. G., O’Mullane, W., Grebel, E. K., Holland, A. D., Huc, C., Passot, X., Bramante, L., Cacciari, C., Castañeda, J., Chaoul, L., Cheek, N., De Angeli, F., Fabricius, C., Guerra, R., Hernández, J., Jean-Antoine-Piccolo,

A., Masana, E., Messineo, R., Mowlavi, N., Nienartowicz, K., Ordóñez-Blanco, D., Panuzzo, P., Portell, J., Richards, P. J., Riello, M., Seabroke, G. M., Tanga, P., Thévenin, F., Torra, J., Els, S. G., Gracia-Abril, G., Comoretto, G., Garcia-Reinaldos, M., Lock, T., Mercier, E., Altmann, M., Andrae, R., Astraatmadja, T. L., Bellas-Velidis, I., Benson, K., Berthier, J., Blomme, R., Busso, G., Carry, B., Cellino, A., Clementini, G., Cowell, S., Creevey, O., Cuypers, J., Davidson, M., De Ridder, J., de Torres, A., Delchambre, L., Dell'Oro, A., Ducourant, C., Frémat, Y., García-Torres, M., Gosset, E., Halbwachs, J. L., Hambly, N. C., Harrison, D. L., Hauser, M., Hestroffer, D., Hodgkin, S. T., Huckle, H. E., Hutton, A., Jasniewicz, G., Jordan, S., Kontizas, M., Korn, A. J., Lanzafame, A. C., Manteiga, M., Moitinho, A., Muinonen, K., Osinde, J., Pancino, E., Pauwels, T., Petit, J. M., Recio-Blanco, A., Robin, A. C., Sarro, L. M., Siopis, C., Smith, M., Smith, K. W., Sozzetti, A., Thuillot, W., van Reeven, W., Viala, Y., Abbas, U., Abreu Aramburu, A., Accart, S., Aguado, J. J., Allan, P. M., Allasia, W., Altavilla, G., Álvarez, M. A., Alves, J., Anderson, R. I., Andrei, A. H., Anglada Varela, E., Antiche, E., Antoja, T., Antón, S., Arcay, B., Atzei, A., Ayache, L., Bach, N., Baker, S. G., Balaguer-Núñez, L., Barache, C., Barata, C., Barbier, A., Barblan, F., Baroni, M., Barrado y Navascués, D., Barros, M., Barstow, M. A., Becciani, U., Bellazzini, M., Bellei, G., Bello García, A., Belokurov, V., Bendjoya, P., Berihuete, A., Bianchi, L., Bienaymé, O., Billebaud, F., Blagorodnova, N., Blanco-Cuaresma, S., Boch, T., Bombrun, A., Borrachero, R., Bouquillon, S., Bourda, G., Bouy, H., Bragaglia, A., Breddels, M. A., Brouillet, N., Brüsemeister, T., Bucciarelli, B., Budnik, F., Burgess, P., Burgon, R., Burlacu, A., Busonero, D., Buzzi, R., Caffau, E., Cambras, J., Campbell, H., Cancelliere, R., Cantat-Gaudin, T., Carlucci, T., Carrasco, J. M., Castellani, M., Charlot, P., Charnas, J., Charvet, P., Chassat, F., Chiavassa, A., Clotet, M., Cocozza, G., Collins, R. S., Collins, P., Costigan, G., Crifo, F., Cross, N. J. G., Crosta, M., Crowley, C., Dafonte, C., Damerdji, Y., Dapergolas, A., David, P., David, M., De Cat, P., de Felice, F., de Laverny, P., De Luise, F., De March, R., de Martino, D., de Souza, R., Debosscher, J., del Pozo, E., Delbo, M., Delgado, A., Delgado, H. E., di Marco, F., Di Matteo, P., Diakite, S., Distefano, E., Dolding, C., Dos Anjos, S., Drazinos, P., Durán, J., Dzigian, Y., Ecale, E., Edvardsson, B., Enke, H., Erdmann, M., Escolar, D., Espina, M., Evans, N. W., Eynard Bontemps, G., Fabre, C., Fabrizio, M., Faigler, S., Falcão, A. J., Farràs Casas, M., Faye, F., Federici, L., Fedorets, G., Fernández-Hernández, J., Fernique, P., Fienga, A., Figueras, F., Filippi, F., Findeisen, K., Fonti, A., Fouesneau, M., Fraile, E., Fraser, M., Fuchs, J., Furnell, R., Gai, M., Galletti, S., Galluccio, L., Garabato, D., García-Sedano, F., Garé, P., Garofalo, A., Garralda, N., Gavras, P., Gerssen, J., Geyer, R., Gilmore, G., Girona, S., Giuffrida, G., Gomes, M., González-Marcos, A., González-Núñez, J., González-Vidal, J. J., Granvik, M., Guerrier, A., Guillout, P., Guiraud, J., Gúrpide, A., Gutiérrez-Sánchez, R., Guy, L. P., Haigron, R., Hatzidimitriou, D., Haywood, M., Heiter, U., Helmi, A., Hobbs, D., Hofmann, W., Holl, B., Holland, G., Hunt, J. A. S., Hypki, A., Icardi, V., Irwin, M., Jevardat de Fombelle, G., Jofré, P., Jonker, P. G., Jorissen, A., Julbe, F., Karampelas, A., Kochoska, A., Kohley, R., Kolenberg, K., Kontizas, E., Koposov, S. E., Kordopatis, G., Koub-

sky, P., Kowalczyk, A., Krone-Martins, A., Kudryashova, M., Kull, I., Bachchan, R. K., Lacoste-Seris, F., Lanza, A. F., Lavigne, J. B., Le Poncin-Lafitte, C., Lebreton, Y., Lebzelter, T., Leccia, S., Leclerc, N., Lecoeur-Taibi, I., Lemaitre, V., Lenhardt, H., Leroux, F., Liao, S., Licata, E., Lindstrøm, H. E. P., Lister, T. A., Livanou, E., Lobel, A., Löffler, W., López, M., Lopez-Lozano, A., Lorenz, D., Loureiro, T., MacDonald, I., Magalhães Fernandes, T., Managau, S., Mann, R. G., Mantelet, G., Marchal, O., Marchant, J. M., Marconi, M., Marie, J., Marinoni, S., Marrese, P. M., Marschalkó, G., Marshall, D. J., Martín-Fleitas, J. M., Martino, M., Mary, N., Matijević, G., Mazeh, T., McMillan, P. J., Messina, S., Mestre, A., Michalik, D., Millar, N. R., Miranda, B. M. H., Molina, D., Molinaro, R., Molinaro, M., Molnár, L., Moniez, M., Montegriffo, P., Monteiro, D., Mor, R., Mora, A., Morbidelli, R., Morel, T., Morgenthaler, S., Morley, T., Morris, D., Mulone, A. F., Muraveva, T., Musella, I., Narbonne, J., Nelemans, G., Nicastro, L., Noval, L., Ordénovic, C., Ordieres-Meré, J., Osborne, P., Pagani, C., Pagano, I., Pailler, F., Palacin, H., Palaversa, L., Parsons, P., Paulsen, T., Pecoraro, M., Pedrosa, R., Pentikäinen, H., Pereira, J., Pichon, B., Piersimoni, A. M., Pineau, F. X., Plachy, E., Plum, G., Poujoulet, E., Prša, A., Pulone, L., Ragaini, S., Rago, S., Rambaux, N., Ramos-Lerate, M., Ranalli, P., Rauw, G., Read, A., Regibo, S., Renk, F., Reylé, C., Ribeiro, R. A., Rimoldini, L., Ripepi, V., Riva, A., Rixon, G., Roelens, M., Romero-Gómez, M., Rowell, N., Royer, F., Rudolph, A., Ruiz-Dern, L., Sadowski, G., Sagristà Sellés, T., Sahlmann, J., Salgado, J., Salguero, E., Sarasso, M., Savietto, H., Schnorhk, A., Schultheis, M., Sciacca, E., Segol, M., Segovia, J. C., Segransan, D., Serpell, E., Shih, I. C., Smareglia, R., Smart, R. L., Smith, C., Solano, E., Solitro, F., Sordo, R., Soria Nieto, S., Souchay, J., Spagna, A., Spoto, F., Stampa, U., Steele, I. A., Steidelmüller, H., Stephenson, C. A., Stoev, H., Suess, F. F., Süveges, M., Surdej, J., Szabados, L., Szegedi-Elek, E., Tapiador, D., Taris, F., Tauran, G., Taylor, M. B., Teixeira, R., Terrett, D., Tingley, B., Trager, S. C., Turon, C., Ulla, A., Utrilla, E., Valentini, G., van Elteren, A., Van Hemelryck, E., van Leeuwen, M., Varadi, M., Vecchiato, A., Veljanoski, J., Via, T., Vicente, D., Vogt, S., Voss, H., Votruba, V., Voutsinas, S., Walmsley, G., Weiler, M., Weingrill, K., Werner, D., Wevers, T., Whitehead, G., Wyrzykowski, L., Yoldas, A., Žerjal, M., Zucker, S., Zurbach, C., Zwitter, T., Alecu, A., Allen, M., Allende Prieto, C., Amorim, A., Anglada-Escudé, G., Arsenijević, V., Azaz, S., Balm, P., Beck, M., Bernstein, H. H., Bigot, L., Bijaoui, A., Blasco, C., Bonfigli, M., Bono, G., Boudreault, S., Bressan, A., Brown, S., Brunet, P. M., Bunclark, P., Buonanno, R., Butkevich, A. G., Carret, C., Carrion, C., Chemin, L., Chéreau, F., Corcione, L., Darmigny, E., de Boer, K. S., de Teodoro, P., de Zeeuw, P. T., Delle Luche, C., Domingues, C. D., Dubath, P., Fodor, F., Frézouls, B., Fries, A., Fustes, D., Fyfe, D., Gallardo, E., Gallejos, J., Gardiol, D., Gebran, M., Gomboc, A., Gómez, A., Grux, E., Gueguen, A., Heyrovsky, A., Hoar, J., Iannicola, G., Isasi Parache, Y., Janotto, A. M., Joliet, E., Jonckheere, A., Keil, R., Kim, D. W., Klagyivik, P., Klar, J., Knude, J., Kochukhov, O., Kolka, I., Kos, J., Kutka, A., Lainey, V., LeBouquin, D., Liu, C., Loreggia, D., Makarov, V. V., Marseille, M. G., Martayan, C., Martinez-Rubi, O., Massart, B., Meynadier, F., Mignot, S., Munari, U., Nguyen, A. T.,

- Nordlander, T., Ocvirk, P., O’Flaherty, K. S., Olias Sanz, A., Ortiz, P., Osorio, J., Oszkiewicz, D., Ouzounis, A., Palmer, M., Park, P., Pasquato, E., Peltzer, C., Peralta, J., Péturaud, F., Pieniluoma, T., Pigozzi, E., Poels, J., Prat, G., Prod’homme, T., Raison, F., Rebordao, J. M., Risquez, D., Rocca-Volmerange, B., Rosen, S., Ruiz-Fuertes, M. I., Russo, F., Sembay, S., Serraller Vizcaino, I., Short, A., Siebert, A., Silva, H., Sinachopoulos, D., Slezak, E., Soffel, M., Sosnowska, D., Straizys, V., ter Linden, M., Terrell, D., Theil, S., Tiede, C., Troisi, L., Tsalmantza, P., Tur, D., Vaccari, M., Vachier, F., Valles, P., Van Hamme, W., Veltz, L., Virtanen, J., Wallut, J. M., Wichmann, R., Wilkinson, M. I., Ziaee pour, H., & Zschocke, S. 2016, *A&A*, 595, A1, arXiv:1609.04153
- Gao, P., Thorngren, D. P., Lee, G. K. H., Fortney, J. J., Morley, C. V., Wakeford, H. R., Powell, D. K., Stevenson, K. B., & Zhang, X. 2020, *Nature Astronomy*, 4, 951, arXiv:2005.11939
- Gardner, J. P., Mather, J. C., Clampin, M., Doyon, R., Greenhouse, M. A., Hammel, H. B., Hutchings, J. B., Jakobsen, P., Lilly, S. J., Long, K. S., Lunine, J. I., McCaughrean, M. J., Mountain, M., Nella, J., Rieke, G. H., Rieke, M. J., Rix, H.-W., Smith, E. P., Sonneborn, G., Stiavelli, M., Stockman, H. S., Windhorst, R. A., & Wright, G. S. 2006, *Space Science Reviews*, 123, 485, arXiv:astro-ph/0606175
- Garhart, E., Deming, D., Mandell, A., Knutson, H. A., Wallack, N., Burrows, A., Fortney, J. J., Hood, C., Seay, C., Sing, D. K., Benneke, B., Fraine, J. D., Kataria, T., Lewis, N., Madhusudhan, N., McCullough, P., Stevenson, K. B., & Wakeford, H. 2020, *AJ*, 159, 137, arXiv:1901.07040
- Gaudi, B. S., Seager, S., & Mallen-Ornelas, G. 2005, *ApJ*, 623, 472, arXiv:astro-ph/0409443
- Gibney, E. & Castelvetti, D. 2019, *Nature*, 574, 162
- Gibson, N. P., Pont, F., & Aigrain, S. 2011, *MNRAS*, 411, 2199, arXiv:1010.1753
- Gibson, S. R., Howard, A. W., Marcy, G. W., Edelstein, J., Wishnow, E. H., & Poppett, C. L. 2016, in *Society of Photo-Optical Instrumentation Engineers (SPIE) Conference Series*, Vol. 9908, , 990870
- Gillon, M., Demory, B. O., Barman, T., Bonfils, X., Mazeh, T., Pont, F., Udry, S., Mayor, M., & Queloz, D. 2007, *A&A*, 471, L51, arXiv:0707.2261
- Gillon, M., Jehin, E., Lederer, S. M., Delrez, L., de Wit, J., Burdanov, A., Van Grootel, V., Burgasser, A. J., Triaud, A. H. M. J., Opitom, C., Demory, B.-O., Sahu, D. K., Bardalez Gagliuffi, D., Magain, P., & Queloz, D. 2016, *Nature*, 533, 221, arXiv:1605.07211
- Gillon, M., Jehin, E., Magain, P., Chantry, V., Hutsemékers, D., Manfroid, J., Queloz, D., & Udry, S. 2011, in *European Physical Journal Web of Conferences*, Vol. 11, *European Physical Journal Web of Conferences*, 06002

- Gillon, M., Triaud, A. H. M. J., Demory, B.-O., Jehin, E., Agol, E., Deck, K. M., Lederer, S. M., de Wit, J., Burdanov, A., Ingalls, J. G., Bolmont, E., Leconte, J., Raymond, S. N., Selsis, F., Turbet, M., Barkaoui, K., Burgasser, A., Burleigh, M. R., Carey, S. J., Chaushev, A., Copperwheat, C. M., Delrez, L., Fernandes, C. S., Holdsworth, D. L., Kotze, E. J., Van Grootel, V., Almléaky, Y., Benkhaldoun, Z., Magain, P., & Queloz, D. 2017, *Nature*, 542, 456
- Ginzburg, S., Schlichting, H. E., & Sari, R. 2016, *ApJ*, 825, 29, arXiv:1512.07925
- . 2018, *MNRAS*, 476, 759, arXiv:1708.01621
- Girardi, L., Barbieri, M., Groenewegen, M. A. T., Marigo, P., Bressan, A., Rocha-Pinto, H. J., Santiago, B. X., Camargo, J. I. B., & da Costa, L. N. 2012, *Astrophysics and Space Science Proceedings*, 26, 165
- Gordon, I. E., Rothman, L. S., Hill, C., Kochanov, R. V., Tan, Y., Bernath, P. F., Birk, M., Boudon, V., Campargue, A., Chance, K. V., Drouin, B. J., Flaud, J. M., Gamache, R. R., Hodges, J. T., Jacquemart, D., Perevalov, V. I., Perrin, A., Shine, K. P., Smith, M. A. H., Tennyson, J., Toon, G. C., Tran, H., Tyuterev, V. G., Barbe, A., Császár, A. G., Devi, V. M., Furtenbacher, T., Harrison, J. J., Hartmann, J. M., Jolly, A., Johnson, T. J., Karman, T., Kleiner, I., Kyuberis, A. A., Loos, J., Lyulin, O. M., Massie, S. T., Mikhailenko, S. N., Moazzen-Ahmadi, N., Müller, H. S. P., Naumenko, O. V., Nikitin, A. V., Polyansky, O. L., Rey, M., Rotger, M., Sharpe, S. W., Sung, K., Starikova, E., Tashkun, S. A., Auwera, J. V., Wagner, G., Wilzewski, J., Wcisło, P., Yu, S., & Zak, E. J. 2017, , 203, 3
- Greene, T. P., Line, M. R., Montero, C., Fortney, J. J., Lustig-Yaeger, J., & Luther, K. 2016, *ApJ*, 817, 17, arXiv:1511.05528
- Grekle-McKeon, M. & Deming, D. 2019, *AJ*, 157, 77
- Guillot, T., Burrows, A., Hubbard, W. B., Lunine, J. I., & Saumon, D. 1996, *ApJL*, 459, L35, arXiv:astro-ph/9511109
- Gupta, A. & Schlichting, H. E. 2019, *MNRAS*, 487, 24, arXiv:1811.03202
- . 2020, *MNRAS*, 493, 792, arXiv:1907.03732
- Hardegree-Ullman, K. K., Zink, J. K., Christiansen, J. L., Dressing, C. D., Ciardi, D. R., & Schlieder, J. E. 2020, *ApJS*, 247, 28, arXiv:2001.11511
- Harris, C. R., Millman, K. J., van der Walt, S. J., Gommers, R., Virtanen, P., Cournapeau, D., Wieser, E., Taylor, J., Berg, S., Smith, N. J., Kern, R., Picus, M., Hoyer, S., van Kerkwijk, M. H., Brett, M., Haldane, A., Fernández del Río, J., Wiebe, M., Peterson, P., Gérard-Marchant, P., Sheppard, K., Reddy, T., Weckesser, W., Abbasi, H., Gohlke, C., & Oliphant, T. E. 2020, *Nature*, 585, 357–362

- Haswell, C. A. 2010, *Transiting Exoplanets*
- Haynes, K., Mandell, A. M., Madhusudhan, N., Deming, D., & Knutson, H. 2015, *ApJ*, 806, 146, arXiv:1505.01490
- Haywood, R. D., Collier Cameron, A., Queloz, D., Barros, S. C. C., Deleuil, M., Fares, R., Gillon, M., Lanza, A. F., Lovis, C., Moutou, C., Pepe, F., Pollacco, D., Santerne, A., Ségransan, D., & Unruh, Y. C. 2014, *MNRAS*, 443, 2517, arXiv:1407.1044
- Helled, R., Bodenheimer, P., Podolak, M., Boley, A., Meru, F., Nayakshin, S., Fortney, J. J., Mayer, L., Alibert, Y., & Boss, A. P. H. Beuther, R. S. Klessen C. P. Dullemond & T. Henning, 643
- Heng, K. 2017, *Exoplanetary Atmospheres: Theoretical Concepts and Foundations*
- Henry, G. W., Marcy, G. W., Butler, R. P., & Vogt, S. S. 2000, *ApJL*, 529, L41
- Holzlohner, R., Kosmalski, J., & Guisard, S. 2018, in *Society of Photo-Optical Instrumentation Engineers (SPIE) Conference Series*, Vol. 10700, , 107000I
- Houck, J. R., Roellig, T. L., Van Cleve, J., Forrest, W. J., Herter, T. L., Lawrence, C. R., Matthews, K., Reitsema, H. J., Soifer, B. T., Watson, D. M., Weedman, D., Huisjen, M., Troeltzsch, J. R., Barry, D. J., Bernard-Salas, J., Blacken, C., Brandl, B. R., Charmandaris, V., Devost, D., Gull, G. E., Hall, P., Henderson, C. P., Higdon, S. J. U., Pirger, B. E., Schoenwald, J., Sloan, G. C., Uchida, K. I., Appleton, P. N., Armus, L., Burgdorf, M. J., Fajardo-Acosta, S. B., Grillmair, C. J., Ingalls, J. G., Morris, P. W., & Teplitz, H. I. 2004, in *Society of Photo-Optical Instrumentation Engineers (SPIE) Conference Series*, Vol. 5487, *Optical, Infrared, and Millimeter Space Telescopes*, ed. J. C. Mather, 62–76
- Howe, A. R., Burrows, A., & Deming, D. 2017, *ApJ*, 835, 96, arXiv:1612.01245
- Howell, S. B. 2020, *The NASA Kepler Mission*, 2514-3433 (IOP Publishing)
- Howell, S. B., Sobeck, C., Haas, M., Still, M., Barclay, T., Mullally, F., Troeltzsch, J., Aigrain, S., Bryson, S. T., Caldwell, D., Chaplin, W. J., Cochran, W. D., Huber, D., Marcy, G. W., Miglio, A., Najita, J. R., Smith, M., Twicken, J. D., & Fortney, J. J. 2014, *PASP*, 126, 398, arXiv:1402.5163
- Hubbard, W. B., Fortney, J. J., Lunine, J. I., Burrows, A., Sudarsky, D., & Pinto, P. 2001, *ApJ*, 560, 413, arXiv:astro-ph/0101024
- Hunter, J. D. 2007, *Computing in Science Engineering*, 9, 90
- Irwin, J., Charbonneau, D., Nutzman, P., & Falco, E. *IAU Symposium*, Vol. 253, , *Transiting Planets*, ed. F. Pont D. Sasselov & M. J. Holman, 37–43

- Irwin, J. M., Berta-Thompson, Z. K., Charbonneau, D., Dittmann, J., Falco, E. E., Newton, E. R., & Nutzman, P. in , Cambridge Workshop on Cool Stars, Stellar Systems, and the Sun, Vol. 18, 18th Cambridge Workshop on Cool Stars, Stellar Systems, and the Sun, ed. G. T. van Belle H. C. Harris, 767–772
- Irwin, P. G. J., Teanby, N. A., de Kok, R., Fletcher, L. N., Howett, C. J. A., Tsang, C. C. C., Wilson, C. F., Calcutt, S. B., Nixon, C. A., & Parrish, P. D. 2008, , 109, 1136
- Iyer, A. R., Swain, M. R., Zellem, R. T., Line, M. R., Roudier, G., Rocha, G., & Livingston, J. H. 2016, *ApJ*, 823, 109, arXiv:1512.00151
- Jehin, E., Gillon, M., Queloz, D., Magain, P., Manfroid, J., Chantry, V., Lendl, M., Hutsemékers, D., & Udry, S. 2011, *The Messenger*, 145, 2
- Jenkins, J. S., Pozuelos, F. J., Tuomi, M., Berdiñas, Z. M., Díaz, M. R., Vines, J. I., Suárez, J. C., & Peña Rojas, P. A. 2019, *MNRAS*, 490, 5585, arXiv:1909.00831
- Jin, S. & Mordasini, C. 2018, *ApJ*, 853, 163, arXiv:1706.00251
- John, T. L. 1988, *A&A*, 193, 189
- Jontof-Hutter, D., Rowe, J. F., Lissauer, J. J., Fabrycky, D. C., & Ford, E. B. 2015, *Nature*, 522, 321, arXiv:1506.07067
- Kasting, J. F., Whitmire, D. P., & Reynolds, R. T. 1993, *Icarus*, 101, 108
- Kelsall, T., Weiland, J. L., Franz, B. A., Reach, W. T., Arendt, R. G., Dwek, E., Freudenreich, H. T., Hauser, M. G., Moseley, S. H., Odegard, N. P., Silverberg, R. F., & Wright, E. L. 1998, *ApJ*, 508, 44, arXiv:astro-ph/9806250
- Kempton, E. M. R. IAU Symposium, Vol. 276, , *The Astrophysics of Planetary Systems: Formation, Structure, and Dynamical Evolution*, ed. A. Sozzetti M. G. Lattanzi & A. P. Boss, 212–217
- Kempton, E. M. R., Bean, J. L., Louie, D. R., Deming, D., Koll, D. D. B., Mansfield, M., Christiansen, J. L., López-Morales, M., Swain, M. R., Zellem, R. T., Ballard, S., Barclay, T., Barstow, J. K., Batalha, N. E., Beatty, T. G., Berta-Thompson, Z., Birkby, J., Buchhave, L. A., Charbonneau, D., Cowan, N. B., Crossfield, I., de Val-Borro, M., Doyon, R., Dragomir, D., Gaidos, E., Heng, K., Hu, R., Kane, S. R., Kreidberg, L., Mallonn, M., Morley, C. V., Narita, N., Nascimbeni, V., Pallé, E., Quintana, E. V., Rauscher, E., Seager, S., Shkolnik, E. L., Sing, D. K., Sozzetti, A., Stassun, K. G., Valenti, J. A., & von Essen, C. 2018, *PASP*, 130, 114401, arXiv:1805.03671
- Kempton, E. M.-R., Lupu, R., Owusu-Asare, A., Slough, P., & Cale, B. 2017, *PASP*, 129, 044402, arXiv:1611.03871

- Knutson, H. A., Dragomir, D., Kreidberg, L., Kempton, E. M. R., McCullough, P. R., Fortney, J. J., Bean, J. L., Gillon, M., Homeier, D., & Howard, A. W. 2014, *ApJ*, 794, 155, arXiv:1403.4602
- Konacki, M., Torres, G., Jha, S., & Sasselov, D. D. 2003, *Nature*, 421, 507
- Kopparapu, R. K., Ramirez, R., Kasting, J. F., Eymet, V., Robinson, T. D., Mahadevan, S., Terrien, R. C., Domagal-Goldman, S., Meadows, V., & Deshpande, R. 2013, *ApJ*, 765, 131, arXiv:1301.6674
- Kopparapu, R. K., Ramirez, R. M., SchottelKotte, J., Kasting, J. F., Domagal-Goldman, S., & Eymet, V. 2014, *ApJL*, 787, L29, arXiv:1404.5292
- Kreidberg, L., Bean, J. L., Désert, J.-M., Benneke, B., Deming, D., Stevenson, K. B., Seager, S., Berta-Thompson, Z., Seifahrt, A., & Homeier, D. 2014a, *Nature*, 505, 69, arXiv:1401.0022
- Kreidberg, L., Bean, J. L., Désert, J.-M., Line, M. R., Fortney, J. J., Madhusudhan, N., Stevenson, K. B., Showman, A. P., Charbonneau, D., McCullough, P. R., Seager, S., Burrows, A., Henry, G. W., Williamson, M., Kataria, T., & Homeier, D. 2014b, *ApJL*, 793, L27, arXiv:1410.2255
- Kreidberg, L., Koll, D. D. B., Morley, C., Hu, R., Schaefer, L., Deming, D., Stevenson, K. B., Dittmann, J., Vanderburg, A., Berardo, D., Guo, X., Stassun, K., Crossfield, I., Charbonneau, D., Latham, D. W., Loeb, A., Ricker, G., Seager, S., & Vanderpek, R. 2019, *Nature*, 573, 87, arXiv:1908.06834
- Kreidberg, L., Line, M. R., Bean, J. L., Stevenson, K. B., Désert, J.-M., Madhusudhan, N., Fortney, J. J., Barstow, J. K., Henry, G. W., Williamson, M. H., & Showman, A. P. 2015, *ApJ*, 814, 66, arXiv:1504.05586
- Kuntschner, H., Bushouse, H., Kümmel, M., & Walsh, J. R. 2009, WFC3 SMOV proposal 11552: Calibration of the G141 grism, Space Telescope WFC Instrument Science Report
- Lange, M. A. & Ahrens, T. J. 1982, *Icarus*, 51, 96
- Lee, E. J. & Chiang, E. 2016, *ApJ*, 817, 90, arXiv:1510.08855
- Lee, E. J., Chiang, E., & Ormel, C. W. 2014, *ApJ*, 797, 95, arXiv:1409.3578
- Léger, A., Rouan, D., Schneider, J., Barge, P., Fridlund, M., Samuel, B., Ollivier, M., Guenther, E., Deleuil, M., Deeg, H. J., Auvergne, M., Alonso, R., Aigrain, S., Alapini, A., Almenara, J. M., Baglin, A., Barbieri, M., Bruntt, H., Bordé, P., Bouchy, F., Cabrera, J., Catala, C., Carone, L., Carpano, S., Csizmadia, S., Dvorak, R., Erikson, A., Ferraz-Mello, S., Foing, B., Fressin, F., Gandolfi, D., Gillon, M., Gondoin, P., Grasset, O., Guillot, T., Hatzes, A., Hébrard, G., Jorda, L., Lammer, H., Llebaria, A., Loeillet, B., Mayor, M., Mazeh, T., Moutou, C., Pätzold, M., Pont, F., Queloz, D., Rauer, H., Renner, S., Samadi, R., Shporer,

- A., Sotin, C., Tingley, B., Wuchterl, G., Adda, M., Agogu, P., Appourchaux, T., Ballans, H., Baron, P., Beaufort, T., Bellenger, R., Berlin, R., Bernardi, P., Blouin, D., Baudin, F., Bodin, P., Boisnard, L., Boit, L., Bonneau, F., Borzeix, S., Briet, R., Buey, J.-T., Butler, B., Cailleau, D., Cautain, R., Chabaud, P.-Y., Chaintreuil, S., Chiavassa, F., Costes, V., Cuna Parrho, V., de Oliveira Fialho, F., Decaudin, M., Defise, J.-M., Djalal, S., Epstein, G., Exil, G.-E., Fauré, C., Fenouillet, T., Gaboriaud, A., Gallic, A., Gamet, P., Gavalda, P., Grolleau, E., Gruneisen, R., Gueguen, L., Guis, V., Guivarc'h, V., Guterman, P., Hallouard, D., Hasiba, J., Heuripeau, F., Huntzinger, G., Hustaix, H., Imad, C., Imbert, C., Johlander, B., Jouret, M., Journoud, P., Karioty, F., Kerjean, L., Lafaille, V., Lafond, L., Lam-Trong, T., Landiech, P., Lapeyrere, V., Larqué, T., Laudet, P., Lautier, N., Lecann, H., Lefevre, L., Leruyet, B., Levacher, P., Magnan, A., Mazy, E., Mertens, F., Mesnager, J.-M., Meunier, J.-C., Michel, J.-P., Monjoin, W., Naudet, D., Nguyen-Kim, K., Orcesi, J.-L., Ottacher, H., Perez, R., Peter, G., Plasson, P., Plesseria, J.-Y., Pontet, B., Pradines, A., Quentin, C., Reynaud, J.-L., Rolland, G., Rollenhagen, F., Romagnan, R., Russ, N., Schmidt, R., Schwartz, N., Sebbag, I., Sedes, G., Smit, H., Steller, M. B., Sunter, W., Surace, C., Tello, M., Tiphène, D., Toulouse, P., Ulmer, B., Vandermarcq, O., Vergnault, E., Vuillemin, A., & Zanatta, P. 2009, *A&A*, 506, 287, arXiv:0908.0241
- Lin, D. N. C., Bodenheimer, P., & Richardson, D. C. 1996, *Nature*, 380, 606
- Line, M. R., Knutson, H., Deming, D., Wilkins, A., & Desert, J.-M. 2013a, *ApJ*, 778, 183, arXiv:1310.4796
- Line, M. R. & Parmentier, V. 2016, *ApJ*, 820, 78, arXiv:1511.09443
- Line, M. R., Wolf, A. S., Zhang, X., Knutson, H., Kammer, J. A., Ellison, E., Deroo, P., Crisp, D., & Yung, Y. L. 2013b, *ApJ*, 775, 137, arXiv:1304.5561
- Liu, W., Lin, S., & Piegorsch, W. W. 2008, *International Statistical Review*, 76, 39, arXiv:<https://onlinelibrary.wiley.com/doi/pdf/10.1111/j.1751-5823.2007.00027.x>
- Lodders, K. 2003, *ApJ*, 591, 1220
- Lopez, E. D. & Fortney, J. J. 2014, *ApJ*, 792, 1, arXiv:1311.0329
- Lopez, E. D. & Rice, K. 2018, *MNRAS*, 479, 5303, arXiv:1610.09390
- Lothringer, J. D., Fu, G., Sing, D. K., & Barman, T. S. 2020, *ApJL*, 898, L14, arXiv:2005.02528
- Louie, D. R., Deming, D., Albert, L., Bouma, L. G., Bean, J., & Lopez-Morales, M. 2018, *PASP*, 130, 044401, arXiv:1711.02098
- Louie, D. R., Narita, N., Fukui, A., Palle, E., Tamura, M., Kusakabe, N., Parviainen, H., & Deming, D. 2020, *PASP*, 132, 084403, arXiv:2006.10765

- Lovis, C. & Fischer, D. 2010, *Radial Velocity Techniques for Exoplanets*, ed. S. Seager, 27–53
- MacDonald, R. J. & Madhusudhan, N. 2017, *MNRAS*, 469, 1979, arXiv:1701.01113
- Madhusudhan, N. 2018, *Atmospheric Retrieval of Exoplanets*, 104
- Madhusudhan, N., Amin, M. A., & Kennedy, G. M. 2014, *ApJL*, 794, L12, arXiv:1408.3668
- Madhusudhan, N. & Seager, S. 2009, *ApJ*, 707, 24, arXiv:0910.1347
- Magic, Z., Chiavassa, A., Collet, R., & Asplund, M. 2015, *A&A*, 573, A90, arXiv:1403.3487
- Mandel, K. & Agol, E. 2002, *ApJL*, 580, L171, arXiv:astro-ph/0210099
- Mann, A. W., Gaidos, E., Vanderburg, A., Rizzuto, A. C., Ansdell, M., Medina, J. V., Mace, G. N., Kraus, A. L., & Sokal, K. R. 2017, *AJ*, 153, 64, arXiv:1609.00726
- Mansfield, M., Bean, J. L., Oklopčić, A., Kreidberg, L., Désert, J.-M., Kempton, E. M. R., Line, M. R., Fortney, J. J., Henry, G. W., Mallonn, M., Stevenson, K. B., Dragomir, D., Allart, R., & Bourrier, V. 2018, *ApJL*, 868, L34, arXiv:1812.02214
- Marcy, G. W., Isaacson, H., Howard, A. W., Rowe, J. F., Jenkins, J. M., Bryson, S. T., Latham, D. W., Howell, S. B., Gautier, III, T. N., Batalha, N. M., Rogers, L., Ciardi, D., Fischer, D. A., Gilliland, R. L., Kjeldsen, H., Christensen-Dalsgaard, J., Huber, D., Chaplin, W. J., Basu, S., Buchhave, L. A., Quinn, S. N., Borucki, W. J., Koch, D. G., Hunter, R., Caldwell, D. A., Van Cleve, J., Kolbl, R., Weiss, L. M., Petigura, E., Seager, S., Morton, T., Johnson, J. A., Ballard, S., Burke, C., Cochran, W. D., Endl, M., MacQueen, P., Everett, M. E., Lissauer, J. J., Ford, E. B., Torres, G., Fressin, F., Brown, T. M., Steffen, J. H., Charbonneau, D., Basri, G. S., Sasselov, D. D., Winn, J., Sanchis-Ojeda, R., Christiansen, J., Adams, E., Henze, C., Dupree, A., Fabrycky, D. C., Fortney, J. J., Tarter, J., Holman, M. J., Tenenbaum, P., Shporer, A., Lucas, P. W., Welsh, W. F., Orosz, J. A., Bedding, T. R., Campante, T. L., Davies, G. R., Elsworth, Y., Handberg, R., Hekker, S., Karoff, C., Kawaler, S. D., Lund, M. N., Lundkvist, M., Metcalfe, T. S., Miglio, A., Silva Aguirre, V., Stello, D., White, T. R., Boss, A., Devore, E., Gould, A., Prsa, A., Agol, E., Barclay, T., Coughlin, J., Brugamyer, E., Mullally, F., Quintana, E. V., Still, M., Thompson, S. E., Morrison, D., Twicken, J. D., Désert, J.-M., Carter, J., Crepp, J. R., Hébrard, G., Santerne, A., Moutou, C., Sobeck, C., Hudgins, D., Haas, M. R., Robertson, P., Lillo-Box, J., & Barrado, D. 2014, *ApJS*, 210, 20, arXiv:1401.4195

- Martinez, C. F., Cunha, K., Ghezzi, L., & Smith, V. V. 2019, *ApJ*, 875, 29, arXiv:1903.00174
- Mayor, M. & Queloz, D. 1995, *Nature*, 378, 355
- Mazeh, T. in , *EAS Publications Series*, Vol. 29, *EAS Publications Series*, ed. M. J. Goupil J. P. Zahn, 1–65
- Mbarek, R. & Kempton, E. M. R. 2016, *ApJ*, 827, 121, arXiv:1602.02759
- McCullough, P. & MacKenty, J. 2012, *Considerations for using Spatial Scans with WFC3*, *Space Telescope WFC Instrument Science Report*
- McCullough, P. R., Crouzet, N., Deming, D., & Madhusudhan, N. 2014, *ApJ*, 791, 55, arXiv:1407.2462
- McLaughlin, D. B. 1924, *ApJ*, 60, 22
- Mégevand, D., Zerbi, F. M., Di Marcantonio, P., Cabral, A., Riva, M., Abreu, M., Pepe, F., Cristiani, S., Rebolo Lopez, R., Santos, N. C., Dekker, H., Aliverti, M., Allende, C., Amate, M., Avila, G., Baldini, V., Bandy, T., Bristow, P., Broeg, C., Cirami, R., Coelho, J., Conconi, P., Coretti, I., Cupani, G., D’Odorico, V., De Caprio, V., Delabre, B., Dorn, R., Figueira, P., Fragoso, A., Galeotta, S., Genolet, L., Gomes, R., González Hernández, J., Hughes, I., Iwert, O., Kerber, F., Landoni, M., Lizon, J.-L., Lovis, C., Maire, C., Mannetta, M., Martins, C. C. J. A. P., Molaro, P., Monteiro, M. A. S., Moschetti, M., Oliveira, A., Zapatero Osorio, M. R., Poretti, E., Rasilla, J. L., Santana Tschudi, S., Santos, P., Sosnowska, D., Sousa, S., Tenegi, F., Toso, G., Vanzella, E., & Viel, M. 2014, in *Society of Photo-Optical Instrumentation Engineers (SPIE) Conference Series*, Vol. 9147, , 91471H
- Ment, K., Dittmann, J. A., Astudillo-Defru, N., Charbonneau, D., Irwin, J., Bonfils, X., Murgas, F., Almenara, J.-M., Forveille, T., Agol, E., Ballard, S., Berta-Thompson, Z. K., Bouchy, F., Cloutier, R., Delfosse, X., Doyon, R., Dressing, C. D., Esquerdo, G. A., Haywood, R. D., Kipping, D. M., Latham, D. W., Lovis, C., Newton, E. R., Pepe, F., Rodriguez, J. E., Santos, N. C., Tan, T.-G., Udry, S., Winters, J. G., & Wünsche, A. 2019, *AJ*, 157, 32, arXiv:1808.00485
- Miller-Ricci, E. & Fortney, J. J. 2010, *ApJL*, 716, L74, arXiv:1001.0976
- Miller-Ricci, E., Seager, S., & Sasselov, D. 2009, *ApJ*, 690, 1056, arXiv:0808.1902
- Mollière, P., van Boekel, R., Bouwman, J., Henning, T., Lagage, P.-O., & Min, M. 2017, *A&A*, 600, A10, arXiv:1611.08608
- Morton, D. C. 1991, *ApJS*, 77, 119
- Morton, T. D. 2012, *ApJ*, 761, 6, arXiv:1206.1568

- Morton, T. D., Bryson, S. T., Coughlin, J. L., Rowe, J. F., Ravichandran, G., Pettigra, E. A., Haas, M. R., & Batalha, N. M. 2016, *ApJ*, 822, 86, arXiv:1605.02825
- Moses, J. I., Cavalie, T., Fletcher, L. N., & Roman, M. T. 2020, arXiv e-prints, arXiv:2006.11367, arXiv:2006.11367
- Moutou, C., Deleuil, M., Guillot, T., Baglin, A., Bordé, P., Bouchy, F., Cabrera, J., Csizmadia, S., & Deeg, H. J. 2013, *Icarus*, 226, 1625, arXiv:1306.0578
- Muirhead, P. S., Hamren, K., Schlawin, E., Rojas-Ayala, B., Covey, K. R., & Lloyd, J. P. 2012, *ApJL*, 750, L37, arXiv:1109.1819
- Narita, N., Fukui, A., Kusakabe, N., Onitsuka, M., Ryu, T., Yanagisawa, K., Izumiura, H., Tamura, M., & Yamamuro, T. 2015, *Journal of Astronomical Telescopes, Instruments, and Systems*, 1, 045001, arXiv:1509.03154
- Narita, N., Fukui, A., Kusakabe, N., Watanabe, N., Palle, E., Parviainen, H., Montañés-Rodríguez, P., Murgas, F., Monelli, M., Aguiar, M., Perez Prieto, J. A., Oscoz, Á., de Leon, J., Mori, M., Tamura, M., Yamamuro, T., Béjar, V. J. S., Crouzet, N., Hidalgo, D., Klagyivik, P., Luque, R., & Nishiumi, T. 2019, *Journal of Astronomical Telescopes, Instruments, and Systems*, 5, 015001, arXiv:1807.01908
- Nielsen, L. D., Gandolfi, D., Armstrong, D. J., Jenkins, J. S., Fridlund, M., Santos, N. C., Dai, F., Adibekyan, V., Luque, R., Steffen, J. H., Esposito, M., Meru, F., Sabotta, S., Bolmont, E., Kossakowski, D., Otegi, J. F., Murgas, F., Stalport, M., Rodler, F., Díaz, M. R., Kurtovic, N. T., Ricker, G., Vanderspek, R., Latham, D. W., Seager, S., Winn, J. N., Jenkins, J. M., Allart, R., Almenara, J. M., Barrado, D., Barros, S. C. C., Bayliss, D., Berdiñas, Z. M., Boisse, I., Bouchy, F., Boyd, P., Brown, D. J. A., Bryant, E. M., Burke, C., Cochran, W. D., Cooke, B. F., Demangeon, O. D. S., Díaz, R. F., Dittman, J., Dorn, C., Dumusque, X., García, R. A., González-Cuesta, L., Grziwa, S., Georgieva, I., Guerrero, N., Hatzes, A. P., Helled, R., Henze, C. E., Hoggatpanah, S., Korth, J., Lam, K. W. F., Lillo-Box, J., Lopez, T. A., Livingston, J., Mathur, S., Mousis, O., Narita, N., Osborn, H. P., Palle, E., Rojas, P. A. P., Persson, C. M., Quinn, S. N., Rauer, H., Redfield, S., Santerne, A., dos Santos, L. A., Seidel, J. V., Sousa, S. G., Ting, E. B., Turbet, M., Udry, S., Vand erburg, A., Van Eylen, V., Vines, J. I., Wheatley, P. J., & Wilson, P. A. 2020, *MNRAS*, 492, 5399, arXiv:2001.08834
- Nikolov, N., Sing, D. K., Burrows, A. S., Fortney, J. J., Henry, G. W., Pont, F., Ballester, G. E., Aigrain, S., Wilson, P. A., Huitson, C. M., Gibson, N. P., Désert, J. M., Lecavelier Des Etangs, A., Showman, A. P., Vidal-Madjar, A., Wakeford, H. R., & Zahnle, K. 2015, *MNRAS*, 447, 463, arXiv:1411.4567
- Nikolov, N., Sing, D. K., Pont, F., Burrows, A. S., Fortney, J. J., Ballester, G. E., Evans, T. M., Huitson, C. M., Wakeford, H. R., Wilson, P. A., Aigrain, S.,

- Deming, D., Gibson, N. P., Henry, G. W., Knutson, H., Lecavelier des Etangs, A., Showman, A. P., Vidal-Madjar, A., & Zahnle, K. 2014, *MNRAS*, 437, 46, arXiv:1310.0083
- Nortmann, L., Pallé, E., Salz, M., Sanz-Forcada, J., Nagel, E., Alonso-Floriano, F. J., Czesla, S., Yan, F., Chen, G., Snellen, I. A. G., Zechmeister, M., Schmitt, J. H. M. M., López-Puertas, M., Casasayas-Barris, N., Bauer, F. F., Amado, P. J., Caballero, J. A., Dreizler, S., Henning, T., Lampón, M., Montes, D., Molaverdikhani, K., Quirrenbach, A., Reiners, A., Ribas, I., Sánchez-López, A., Schneider, P. C., & Zapatero Osorio, M. R. 2018, *Science*, 362, 1388, arXiv:1812.03119
- Nutzman, P. & Charbonneau, D. 2008, *PASP*, 120, 317, arXiv:0709.2879
- Öberg, K. I. & Bergin, E. A. 2016, *ApJL*, 831, L19, arXiv:1610.07859
- Öberg, K. I., Murray-Clay, R., & Bergin, E. A. 2011, *ApJL*, 743, L16, arXiv:1110.5567
- Obermeier, C., Henning, T., Schlieder, J. E., Crossfield, I. J. M., Petigura, E. A., Howard, A. W., Sinukoff, E., Isaacson, H., Ciardi, D. R., David, T. J., Hillenbrand, L. A., Beichman, C. A., Howell, S. B., Horch, E., Everett, M., Hirsch, L., Teske, J., Christiansen, J. L., Lépine, S., Aller, K. M., Liu, M. C., Saglia, R. P., Livingston, J., & Kluge, M. 2016, *AJ*, 152, 223, arXiv:1608.04760
- O'Dell, C. W., Connor, B., Bösch, H., O'Brien, D., Frankenberg, C., Castano, R., Christi, M., Eldering, D., Fisher, B., Gunson, M., McDuffie, J., Miller, C. E., Natraj, V., Oyafuso, F., Polonsky, I., Smyth, M., Taylor, T., Toon, G. C., Wennberg, P. O., & Wunch, D. 2012, *Atmospheric Measurement Techniques*, 5, 99
- O'Donovan, F. T., Charbonneau, D., Alonso, R., Brown, T. M., Mandushev, G., Dunham, E. W., Latham, D. W., Stefanik, R. P., Torres, G., & Everett, M. E. 2007, *ApJ*, 662, 658, arXiv:astro-ph/0610603
- O'Donovan, F. T., Charbonneau, D., Torres, G., Mandushev, G., Dunham, E. W., Latham, D. W., Alonso, R., Brown, T. M., Esquerdo, G. A., Everett, M. E., & Creevey, O. L. 2006, *ApJ*, 644, 1237, arXiv:astro-ph/0603005
- Ohta, Y., Taruya, A., & Suto, Y. 2005, *ApJ*, 622, 1118, arXiv:astro-ph/0410499
- Okita, H., Hayashi, S. S., & Takato, N. 2019, *PASJ*, 71, 32
- O'Malley-James, J. T. & Kaltenegger, L. 2017, *ArXiv e-prints*, arXiv:1702.06936
- Owen, J. E. & Wu, Y. 2013, *ApJ*, 775, 105, arXiv:1303.3899
- . 2017, *ApJ*, 847, 29, arXiv:1705.10810

- Parmentier, V., Line, M. R., Bean, J. L., Mansfield, M., Kreidberg, L., Lupu, R., Visscher, C., Désert, J.-M., Fortney, J. J., Deleuil, M., Arcangeli, J., Showman, A. P., & Marley, M. S. 2018, *A&A*, 617, A110, arXiv:1805.00096
- Parmentier, V., Showman, A. P., & Lian, Y. 2013, *A&A*, 558, A91, arXiv:1301.4522
- Parviainen, H., Palle, E., Zapatero-Osorio, M. R., Montanes Rodriguez, P., Murgas, F., Narita, N., Hidalgo Soto, D., Béjar, V. J. S., Korth, J., Monelli, M., Casasayas Barris, N., Crouzet, N., de Leon, J. P., Fukui, A., Hernandez, A., Klagyivik, P., Kusakabe, N., Luque, R., Mori, M., Nishiumi, T., Prieto-Arranz, J., Tamura, M., Watanabe, N., Burke, C., Charbonneau, D., Collins, K. A., Collins, K. I., Conti, D., Garcia Soto, A., Jenkins, J. S., Jenkins, J. M., Levine, A., Li, J., Rinehart, S., Seager, S., Tenenbaum, P., Ting, E. B., Vanderspek, R., Vezie, M., & Winn, J. N. 2020, *A&A*, 633, A28, arXiv:1911.04366
- Parviainen, H., Tingley, B., Deeg, H. J., Palle, E., Alonso, R., Montanes Rodriguez, P., Murgas, F., Narita, N., Fukui, A., Watanabe, N., Kusakabe, N., Tamura, M., Nishiumi, T., Prieto-Arranz, J., Klagyivik, P., Béjar, V. J. S., Crouzet, N., Mori, M., Hidalgo Soto, D., Casasayas Barris, N., & Luque, R. 2019, *A&A*, 630, A89, arXiv:1907.09776
- Pepper, J., Gould, A., & Depoy, D. L. in , *American Institute of Physics Conference Series*, Vol. 713, *The Search for Other Worlds*, ed. S. S. HoltD. Deming, 185–188
- Pepper, J., Kuhn, R. B., Siverd, R., James, D., & Stassun, K. 2012, *PASP*, 124, 230, arXiv:1202.1826
- Pepper, J., Pogge, R. W., DePoy, D. L., Marshall, J. L., Stanek, K. Z., Stutz, A. M., Poindexter, S., Siverd, R., O'Brien, T. P., Trueblood, M., & Trueblood, P. 2007, *PASP*, 119, 923, arXiv:0704.0460
- Perryman, M. 2018, *The Exoplanet Handbook*
- Pluriel, W., Whiteford, N., Edwards, B., Changeat, Q., Yip, K. H., Baeyens, R., Al-Refaie, A., Fabienne Bieger, M., Blain, D., Gressier, A., Guilluy, G., Yassin Jaziri, A., Kiefer, F., Modirrousta-Galian, D., Morvan, M., Mugnai, L. V., Poveda, M., Skaf, N., Zingales, T., Wright, S., Charnay, B., Drossart, P., Leconte, J., Tsiaras, A., Venot, O., Waldmann, I., & Beaulieu, J.-P. 2020, *AJ*, 160, 112, arXiv:2006.14199
- Pollacco, D. L., Skillen, I., Collier Cameron, A., Christian, D. J., Hellier, C., Irwin, J., Lister, T. A., Street, R. A., West, R. G., Anderson, D. R., Clarkson, W. I., Deeg, H., Enoch, B., Evans, A., Fitzsimmons, A., Haswell, C. A., Hodgkin, S., Horne, K., Kane, S. R., Keenan, F. P., Maxted, P. F. L., Norton, A. J., Osborne, J., Parley, N. R., Ryans, R. S. I., Smalley, B., Wheatley, P. J., & Wilson, D. M. 2006, *PASP*, 118, 1407, arXiv:astro-ph/0608454

- Pollack, J. B., Hubickyj, O., Bodenheimer, P., Lissauer, J. J., Podolak, M., & Greenzweig, Y. 1996, *Icarus*, 124, 62
- Polyansky, O. L., Kyuberis, A. A., Zobov, N. F., Tennyson, J., Yurchenko, S. N., & Lodi, L. 2018, *MNRAS*, 480, 2597, arXiv:1807.04529
- Quarles, B., Quintana, E. V., Lopez, E., Schlieder, J. E., & Barclay, T. 2017a, *ApJL*, 842, L5, arXiv:1704.02261
- Quarles, B., Quintana, E. V., Lopez, E. D., Schlieder, J. E., & Barclay, T. 2017b, *ArXiv e-prints*, arXiv:1704.02261
- Rackham, B. V., Apai, D., & Giampapa, M. S. 2018, *ApJ*, 853, 122, arXiv:1711.05691
- . 2019, *AJ*, 157, 96, arXiv:1812.06184
- Reid, I. N. & Hawley, S. L. 2005, *New light on dark stars : red dwarfs, low-mass stars, brown dwarfs*
- Rice, W. K. M., Veljanoski, J., & Collier Cameron, A. 2012, *MNRAS*, 425, 2567, arXiv:1207.5970
- Ricker, G. R., Vanderspek, R., Winn, J., Seager, S., Berta-Thompson, Z., Levine, A., Villasenor, J., Latham, D., Charbonneau, D., Holman, M., Johnson, J., Sasselov, D., Szentgyorgyi, A., Torres, G., Bakos, G., Brown, T., Christensen-Dalsgaard, J., Kjeldsen, H., Clampin, M., Rinehart, S., Deming, D., Doty, J., Dunham, E., Ida, S., Kawai, N., Sato, B., Jenkins, J., Lissauer, J., Jernigan, G., Kaltenegger, L., Laughlin, G., Lin, D., McCullough, P., Narita, N., Pepper, J., Stassun, K., & Udry, S. 2016, in *Society of Photo-Optical Instrumentation Engineers (SPIE) Conference Series*, Vol. 9904, , 99042B
- Ricker, G. R., Winn, J. N., Vanderspek, R., Latham, D. W., Bakos, G. Á., Bean, J. L., Berta-Thompson, Z. K., Brown, T. M., Buchhave, L., Butler, N. R., Butler, R. P., Chaplin, W. J., Charbonneau, D., Christensen-Dalsgaard, J., Clampin, M., Deming, D., Doty, J., De Lee, N., Dressing, C., Dunham, E. W., Endl, M., Fressin, F., Ge, J., Henning, T., Holman, M. J., Howard, A. W., Ida, S., Jenkins, J. M., Jernigan, G., Johnson, J. A., Kaltenegger, L., Kawai, N., Kjeldsen, H., Laughlin, G., Levine, A. M., Lin, D., Lissauer, J. J., MacQueen, P., Marcy, G., McCullough, P. R., Morton, T. D., Narita, N., Paegert, M., Palle, E., Pepe, F., Pepper, J., Quirrenbach, A., Rinehart, S. A., Sasselov, D., Sato, B., Seager, S., Sozzetti, A., Stassun, K. G., Sullivan, P., Szentgyorgyi, A., Torres, G., Udry, S., & Villasenor, J. 2015, *Journal of Astronomical Telescopes, Instruments, and Systems*, 1, 014003
- Ricker, G. R., Winn, J. N., Vanderspek, R., Latham, D. W., Bakos, G. Á., Bean, J. L., Berta-Thompson, Z. K., Brown, T. M., Buchhave, L., Butler, N. R., Butler, R. P., Chaplin, W. J., Charbonneau, D., Christensen-Dalsgaard, J., Clampin,

- M., Deming, D., Doty, J., De Lee, N., Dressing, C., Dunham, E. W., Endl, M., Fressin, F., Ge, J., Henning, T., Holman, M. J., Howard, A. W., Ida, S., Jenkins, J., Jernigan, G., Johnson, J. A., Kaltenegger, L., Kawai, N., Kjeldsen, H., Laughlin, G., Levine, A. M., Lin, D., Lissauer, J. J., MacQueen, P., Marcy, G., McCullough, P. R., Morton, T. D., Narita, N., Paegert, M., Palle, E., Pepe, F., Pepper, J., Quirrenbach, A., Rinehart, S. A., Sasselov, D., Sato, B., Seager, S., Sozzetti, A., Stassun, K. G., Sullivan, P., Szentgyorgyi, A., Torres, G., Udry, S., & Villaseñor, J. 2014, in , Vol. 9143, Space Telescopes and Instrumentation 2014: Optical, Infrared, and Millimeter Wave, 914320
- Robinson, T. D. & Catling, D. C. 2014, *Nature Geoscience*, 7, 12, arXiv:1312.6859
- Rodgers, C. D. 2000, *Inverse Methods for Atmospheric Sounding: Theory and Practice*
- Rogers, L. A. 2015, *ApJ*, 801, 41, arXiv:1407.4457
- Rogers, L. A. & Seager, S. 2010a, *ApJ*, 712, 974, arXiv:0912.3288
- . 2010b, *ApJ*, 716, 1208, arXiv:0912.3243
- Rosenblatt, F. 1971, *Icarus*, 14, 71
- Ross, S. M. 2014, *Introduction to probability and statistics for engineers and scientists*, Fifth Edition
- Rossiter, R. A. 1924, *ApJ*, 60, 15
- Rothman, L. S., Gordon, I. E., Barber, R. J., Dothe, H., Gamache, R. R., Goldman, A., Perevalov, V. I., Tashkun, S. A., & Tennyson, J. 2010, , 111, 2139
- Salz, M., Czesla, S., Schneider, P. C., Nagel, E., Schmitt, J. H. M. M., Nortmann, L., Alonso-Floriano, F. J., López-Puertas, M., Lampón, M., Bauer, F. F., Snellen, I. A. G., Pallé, E., Caballero, J. A., Yan, F., Chen, G., Sanz-Forcada, J., Amado, P. J., Quirrenbach, A., Ribas, I., Reiners, A., Béjar, V. J. S., Casasayas-Barris, N., Cortés-Contreras, M., Dreizler, S., Guenther, E. W., Henning, T., Jeffers, S. V., Kaminski, A., Kürster, M., Lafarga, M., Lara, L. M., Molaverdikhani, K., Montes, D., Morales, J. C., Sánchez-López, A., Seifert, W., Zapatero Osorio, M. R., & Zechmeister, M. 2018, *A&A*, 620, A97, arXiv:1812.02453
- Santerne, A., Moutou, C., Tsantaki, M., Bouchy, F., Hébrard, G., Adibekyan, V., Almenara, J. M., Amard, L., Barros, S. C. C., Boisse, I., Bonomo, A. S., Bruno, G., Courcol, B., Deleuil, M., Demangeon, O., Díaz, R. F., Guillot, T., Havel, M., Montagnier, G., Rajpurohit, A. S., Rey, J., & Santos, N. C. 2016, *A&A*, 587, A64, arXiv:1511.00643
- Saumon, D., Hubbard, W. B., Burrows, A., Guillot, T., Lunine, J. I., & Chabrier, G. 1996, *ApJ*, 460, 993, arXiv:astro-ph/9510046

- Schaefer, L. & Fegley, B. 2010, *Icarus*, 208, 438, arXiv:0909.4050
- Schlichting, H. E., Sari, R., & Yalinewich, A. 2015, *Icarus*, 247, 81, arXiv:1406.6435
- Schwab, C., Rakich, A., Gong, Q., Mahadevan, S., Halverson, S. P., Roy, A., Terrien, R. C., Robertson, P. M., Hearty, F. R., Levi, E. I., Monson, A. J., Wright, J. T., McElwain, M. W., Bender, C. F., Blake, C. H., Stürmer, J., Gurevich, Y. V., Chakraborty, A., & Ramsey, L. W. 2016, in *Society of Photo-Optical Instrumentation Engineers (SPIE) Conference Series*, Vol. 9908, , 99087H
- Seager, S. 2010, *Exoplanet Atmospheres: Physical Processes*
- . 2013, *Science*, 340, 577
- Seager, S. & Deming, D. 2010, *ARA&A*, 48, 631, arXiv:1005.4037
- Seager, S., Kuchner, M., Hier-Majumder, C. A., & Militzer, B. 2007, *ApJ*, 669, 1279, arXiv:0707.2895
- Seager, S. & Mallén-Ornelas, G. 2003, *ApJ*, 585, 1038, arXiv:astro-ph/0206228
- Seager, S. & Sasselov, D. D. 1998, *ApJL*, 502, L157, arXiv:astro-ph/9805335
- . 2000, *ApJ*, 537, 916, arXiv:astro-ph/9912241
- Seifahrt, A., Stürmer, J., Bean, J. L., & Schwab, C. 2018, in *Society of Photo-Optical Instrumentation Engineers (SPIE) Conference Series*, Vol. 10702, , 107026D
- Sheppard, K. B., Welbanks, L., Mandell, A. M., Madhusudhan, N., Nikolov, N., Deming, D., Henry, G. W., Williamson, M. H., Sing, D. K., López-Morales, M., Ih, J., Sanz-Forcada, J., Lavvas, P., Ballester, G. E., Evans, T. M., Muñoz, A. G., & dos Santos, L. A. 2021, *AJ*, 161, 51, arXiv:2010.09659
- Shields, A. L., Ballard, S., & Johnson, J. A. 2016, , 663, 1, arXiv:1610.05765
- Showman, A. P. & Guillot, T. 2002, *A&A*, 385, 166, arXiv:astro-ph/0202236
- Shuvalov, V. 2009, *Meteoritics and Planetary Science*, 44, 1095
- Sing, D. K., Fortney, J. J., Nikolov, N., Wakeford, H. R., Kataria, T., Evans, T. M., Aigrain, S., Ballester, G. E., Burrows, A. S., Deming, D., Désert, J.-M., Gibson, N. P., Henry, G. W., Huitson, C. M., Knutson, H. A., Lecavelier Des Etangs, A., Pont, F., Showman, A. P., Vidal-Madjar, A., Williamson, M. H., & Wilson, P. A. 2016, *Nature*, 529, 59, arXiv:1512.04341
- Sing, D. K., Wakeford, H. R., Showman, A. P., Nikolov, N., Fortney, J. J., Burrows, A. S., Ballester, G. E., Deming, D., Aigrain, S., Désert, J. M., Gibson, N. P., Henry, G. W., Knutson, H., Lecavelier des Etangs, A., Pont, F., Vidal-Madjar, A., Williamson, M. W., & Wilson, P. A. 2015, *MNRAS*, 446, 2428, arXiv:1410.7611

- Sinukoff, E., Howard, A. W., Petigura, E. A., Fulton, B. J., Isaacson, H., Weiss, L. M., Brewer, J. M., Hansen, B. M. S., Hirsch, L., Christiansen, J. L., Crepp, J. R., Crossfield, I. J. M., Schlieder, J. E., Ciardi, D. R., Beichman, C. A., Knutson, H. A., Benneke, B., Dressing, C. D., Livingston, J. H., Deck, K. M., Lépine, S., & Rogers, L. A. 2017, *AJ*, 153, 70, arXiv:1612.04851
- Sinukoff, E., Howard, A. W., Petigura, E. A., Schlieder, J. E., Crossfield, I. J. M., Ciardi, D. R., Fulton, B. J., Isaacson, H., Aller, K. M., Baranec, C., Beichman, C. A., Hansen, B. M. S., Knutson, H. A., Law, N. M., Liu, M. C., Riddle, R., & Dressing, C. D. 2016, *ApJ*, 827, 78, arXiv:1511.09213
- Southworth, J., Hinse, T. C., Jørgensen, U. G., Dominik, M., Ricci, D., Burgdorf, M. J., Hornstrup, A., Wheatley, P. J., Anguita, T., Bozza, V., Novati, S. C., Harpsøe, K., Kjærgaard, P., Liebig, C., Mancini, L., Masi, G., Mathiasen, M., Rahvar, S., Scarpetta, G., Snodgrass, C., Surdej, J., Thöne, C. C., & Zub, M. 2009, *MNRAS*, 396, 1023, arXiv:0903.2139
- Souto, D., Cunha, K., García-Hernández, D. A., Zamora, O., Allende Prieto, C., Smith, V. V., Mahadevan, S., Blake, C., Johnson, J. A., Jönsson, H., Pinsonneault, M., Holtzman, J., Majewski, S. R., Shetrone, M., Teske, J., Nidever, D., Schiavon, R., Sobek, J., García Pérez, A. E., Gómez Maqueo Chew, Y., & Stassun, K. 2017, *ApJ*, 835, 239, arXiv:1612.01598
- Speagle, J. S. 2020, *MNRAS*, 493, 3132, arXiv:1904.02180
- Stassun, K. G., Oelkers, R. J., Paegert, M., Torres, G., Pepper, J., De Lee, N., Collins, K., Latham, D. W., Muirhead, P. S., Chittidi, J., Rojas-Ayala, B., Fleming, S. W., Rose, M. E., Tenenbaum, P., Ting, E. B., Kane, S. R., Barclay, T., Bean, J. L., Brassuer, C. E., Charbonneau, D., Ge, J., Lissauer, J. J., Mann, A. W., McLean, B., Mullally, S., Narita, N., Plavchan, P., Ricker, G. R., Sasselov, D., Seager, S., Sharma, S., Shiao, B., Sozzetti, A., Stello, D., Vanderspek, R., Wallace, G., & Winn, J. N. 2019, *AJ*, 158, 138, arXiv:1905.10694
- Stassun, K. G., Oelkers, R. J., Pepper, J., Paegert, M., De Lee, N., Torres, G., Latham, D. W., Charpinet, S., Dressing, C. D., Huber, D., Kane, S. R., Lépine, S., Mann, A., Muirhead, P. S., Rojas-Ayala, B., Silvotti, R., Fleming, S. W., Levine, A., & Plavchan, P. 2018, *AJ*, 156, 102, arXiv:1706.00495
- Stevenson, K. B., Bean, J. L., Fabrycky, D., & Kreidberg, L. 2014, *ApJ*, 796, 32, arXiv:1410.0002
- Stevenson, K. B., Lewis, N. K., Bean, J. L., Beichman, C., Fraine, J., Kilpatrick, B. M., Krick, J. E., Lothringer, J. D., Mandell, A. M., Valenti, J. A., Agol, E., Angerhausen, D., Barstow, J. K., Birkmann, S. M., Burrows, A., Charbonneau, D., Cowan, N. B., Crouzet, N., Cubillos, P. E., Curry, S. M., Dalba, P. A., de Wit, J., Deming, D., Désert, J.-M., Doyon, R., Dragomir, D., Ehrenreich, D., Fortney, J. J., García Muñoz, A., Gibson, N. P., Gizis, J. E., Greene, T. P., Harrington, J.,

- Heng, K., Kataria, T., Kempton, E. M.-R., Knutson, H., Kreidberg, L., Lafrenière, D., Lagage, P.-O., Line, M. R., Lopez-Morales, M., Madhusudhan, N., Morley, C. V., Rocchetto, M., Schlawin, E., Shkolnik, E. L., Shporer, A., Sing, D. K., Todorov, K. O., Tucker, G. S., & Wakeford, H. R. 2016, *PASP*, 128, 094401, arXiv:1602.08389
- Sullivan, P. W., Winn, J. N., Berta-Thompson, Z. K., Charbonneau, D., Deming, D., Dressing, C. D., Latham, D. W., Levine, A. M., McCullough, P. R., Morton, T., Ricker, G. R., Vanderspek, R., & Woods, D. 2015, *ApJ*, 809, 77, arXiv:1506.03845
- Swain, M. R., Vasisht, G., & Tinetti, G. 2008, *Nature*, 452, 329
- Swinyard, B. M., Rieke, G. H., Ressler, M., Glasse, A., Wright, G. S., Ferlet, M., & Wells, M. 2004, in , Vol. 5487, *Optical, Infrared, and Millimeter Space Telescopes*, ed. J. C. Mather, 785–793
- Tennyson, J. & Yurchenko, S. 2018, *Atoms*, 6, 26, arXiv:1805.03711
- Tennyson, J. & Yurchenko, S. N. 2012, *MNRAS*, 425, 21, arXiv:1204.0124
- Tennyson, J., Yurchenko, S. N., Al-Refai, A. F., Clark, V. H. J., Chubb, K. L., Conway, E. K., Dewan, A., Gorman, M. N., Hill, C., Lynas-Gray, A. E., Mellor, T., McKemmish, L. K., Owens, A., Polyansky, O. L., Semenov, M., Somogyi, W., Tinetti, G., Upadhyay, A., Waldmann, I., Wang, Y., Wright, S., & Yurchenko, O. P. 2020, , 255, 107228, arXiv:2007.13022
- Thorngren, D. & Fortney, J. J. 2019, *ApJL*, 874, L31, arXiv:1811.11859
- Tinetti, G., Deroo, P., Swain, M. R., Griffith, C. A., Vasisht, G., Brown, L. R., Burke, C., & McCullough, P. 2010, *ApJL*, 712, L139, arXiv:1002.2434
- Tinetti, G., Drossart, P., Eccleston, P., Hartogh, P., Heske, A., Leconte, J., Micela, G., Ollivier, M., Pilbratt, G., Puig, L., Turrini, D., Vandenbussche, B., Wolkenberg, P., Pascale, E., Beaulieu, J. P., Güdel, M., Min, M., Rataj, M., Ray, T., Ribas, I., Barstow, J., Bowles, N., Coustenis, A., Coudé du Foresto, V., Decin, L., Encrenaz, T., Forget, F., Friswell, M., Griffin, M., Lagage, P. O., Malaguti, P., Moneti, A., Morales, J. C., Pace, E., Rocchetto, M., Sarkar, S., Selsis, F., Taylor, W., Tennyson, J., Venot, O., Waldmann, I. P., Wright, G., Zingales, T., & Zapatero-Osorio, M. R. G. G. Fazio, M. LystrupN. BatalhaN. Siegler & E. C. Tong, 99041X
- Torres, G., Fressin, F., Batalha, N. M., Borucki, W. J., Brown, T. M., Bryson, S. T., Buchhave, L. A., Charbonneau, D., Ciardi, D. R., Dunham, E. W., Fabrycky, D. C., Ford, E. B., Gautier, Thomas N., I., Gilliland, R. L., Holman, M. J., Howell, S. B., Isaacson, H., Jenkins, J. M., Koch, D. G., Latham, D. W., Lissauer, J. J., Marcy, G. W., Monet, D. G., Prsa, A., Quinn, S. N., Ragozzine, D., Rowe, J. F., Sasselov, D. D., Steffen, J. H., & Welsh, W. F. 2011, *ApJ*, 727, 24, arXiv:1008.4393

- Trotta, R. 2008, *Contemporary Physics*, 49, 71, arXiv:0803.4089
- . 2017, arXiv e-prints, arXiv:1701.01467, arXiv:1701.01467
- Tsiaras, A., Rocchetto, M., Waldmann, I. P., Venot, O., Varley, R., Morello, G., Damiano, M., Tinetti, G., Barton, E. J., Yurchenko, S. N., & Tennyson, J. 2016, *ApJ*, 820, 99, arXiv:1511.08901
- Tsiaras, A., Waldmann, I. P., Tinetti, G., Tennyson, J., & Yurchenko, S. N. 2019a, *Nature Astronomy*, 3, 1156
- . 2019b, *Nature Astronomy*, 3, 1086, arXiv:1909.05218
- Tsiaras, A., Waldmann, I. P., Zingales, T., Rocchetto, M., Morello, G., Damiano, M., Karpouzias, K., Tinetti, G., McKemmish, L. K., Tennyson, J., & Yurchenko, S. N. 2018, *AJ*, 155, 156, arXiv:1704.05413
- Udalski, A., Paczynski, B., Zebrun, K., Szymanski, M., Kubiak, M., Soszynski, I., Szewczyk, O., Wyrzykowski, L., & Pietrzynski, G. 2002a, , 52, 1, arXiv:astro-ph/0202320
- Udalski, A., Zebrun, K., Szymanski, M., Kubiak, M., Soszynski, I., Szewczyk, O., Wyrzykowski, L., & Pietrzynski, G. 2002b, , 52, 115, arXiv:astro-ph/0207133
- Van Eylen, V., Agentoft, C., Lundkvist, M. S., Kjeldsen, H., Owen, J. E., Fulton, B. J., Petigura, E., & Snellen, I. 2018, *MNRAS*, 479, 4786, arXiv:1710.05398
- Vanderburg, A., Montet, B. T., Johnson, J. A., Buchhave, L. A., Zeng, L., Pepe, F., Collier Cameron, A., Latham, D. W., Molinari, E., Udry, S., Lovis, C., Matthews, J. M., Cameron, C., Law, N., Bowler, B. P., Angus, R., Baranec, C., Bieryla, A., Boschini, W., Charbonneau, D., Cosentino, R., Dumusque, X., Figueira, P., Guenther, D. B., Harutyunyan, A., Hellier, C., Kuschnig, R., Lopez-Morales, M., Mayor, M., Micela, G., Moffat, A. F. J., Pedani, M., Phillips, D. F., Piotto, G., Pollacco, D., Queloz, D., Rice, K., Riddle, R., Rowe, J. F., Rucinski, S. M., Sasselov, D., Ségransan, D., Sozzetti, A., Szentgyorgyi, A., Watson, C., & Weiss, W. W. 2015, *ApJ*, 800, 59, arXiv:1412.5674
- Varela, A. M., Muñz-Tuñón, C., de Gurtubai, A., & Saviron, C. *Astronomical Society of the Pacific Conference Series*, Vol. 266, , *Astronomical Site Evaluation in the Visible and Radio Range*, ed. J. VerninZ. Benkhaldoun & C. Muñoz-Tuñón, 454
- Virtanen, P., Gommers, R., Oliphant, T. E., Haberland, M., Reddy, T., Cournapeau, D., Burovski, E., Peterson, P., Weckesser, W., Bright, J., van der Walt, S. J., Brett, M., Wilson, J., Jarrod Millman, K., Mayorov, N., Nelson, A. R. J., Jones, E., Kern, R., Larson, E., Carey, C., Polat, İ., Feng, Y., Moore, E. W., VanderPlas, J., Laxalde, D., Perktold, J., Cimrman, R., Henriksen, I., Quintero, E. A., Harris, C. R., Archibald, A. M., Ribeiro, A. H., Pedregosa, F., van Mulbregt, P., & Contributors, S. . . 2020, *Nature Methods*, 17, 261

- Wakeford, H. R., Lewis, N. K., Fowler, J., Bruno, G., Wilson, T. J., Moran, S. E., Valenti, J., Batalha, N. E., Filippazzo, J., Bourrier, V., Hörst, S. M., Lederer, S. M., & de Wit, J. 2019, *AJ*, 157, 11, arXiv:1811.04877
- Wakeford, H. R., Sing, D. K., Deming, D., Gibson, N. P., Fortney, J. J., Burrows, A. S., Ballester, G., Nikolov, N., Aigrain, S., Henry, G., Knutson, H., Lecavelier des Etangs, A., Pont, F., Showman, A. P., Vidal-Madjar, A., & Zahnle, K. 2013, *MNRAS*, 435, 3481, arXiv:1308.2106
- Wakeford, H. R., Sing, D. K., Kataria, T., Deming, D., Nikolov, N., Lopez, E. D., Tremblin, P., Amundsen, D. S., Lewis, N. K., Mandell, A. M., Fortney, J. J., Knutson, H., Benneke, B., & Evans, T. M. 2017, *Science*, 356, 628, arXiv:1705.04354
- Waldmann, I. P., Tinetti, G., Rocchetto, M., Barton, E. J., Yurchenko, S. N., & Tennyson, J. 2015, *ApJ*, 802, 107, arXiv:1409.2312
- Wall, J. V. & Jenkins, C. R. 2012, *Practical Statistics for Astronomers*
- Wang, S., Wu, D.-H., Barclay, T., & Laughlin, G. P. 2017, *ArXiv e-prints*, arXiv:1704.04290
- Weiss, L. M. & Marcy, G. W. 2014, *ApJL*, 783, L6, arXiv:1312.0936
- Welbanks, L., Madhusudhan, N., Allard, N. F., Hubeny, I., Spiegelman, F., & Leininger, T. 2019, *ApJL*, 887, L20, arXiv:1912.04904
- Wheatley, P. J., Louden, T., Bourrier, V., Ehrenreich, D., & Gillon, M. 2017, *MNRAS*, 465, L74, arXiv:1605.01564
- Wildi, F., Blind, N., Reshetov, V., Hernandez, O., Genolet, L., Conod, U., Sordet, M., Segovilla, A., Rasilla, J. L., Brousseau, D., Thibault, S., Delabre, B., Bandy, T., Sarajlic, M., Cabral, A., Bovay, S., Vallée, P., Bouchy, F., Doyon, R., Artigau, E., Pepe, F., Hagelberg, J., Melo, C., Delfosse, X., Figueira, P., Santos, N. C., González Hernández, J. I., de Medeiros, J. R., Rebolo, R., Broeg, C., Benz, W., Boisse, I., Malo, L., Käuff, U., & Saddlemyer, L. 2017, in *Society of Photo-Optical Instrumentation Engineers (SPIE) Conference Series*, Vol. 10400, , 1040018
- Wilkins, A. N., Deming, D., Madhusudhan, N., Burrows, A., Knutson, H., McCullough, P., & Ranjan, S. 2014, *ApJ*, 783, 113, arXiv:1401.4464
- Winn, J. N. 2010, *Exoplanet Transits and Occultations*, ed. S. Seager, 55–77
- Wolfgang, A., Rogers, L. A., & Ford, E. B. 2016, *ApJ*, 825, 19, arXiv:1504.07557
- Wong, I., Shporer, A., Daylan, T., Benneke, B., Fetherolf, T., Kane, S. R., Ricker, G. R., Vanderspek, R., Latham, D. W., Winn, J. N., Jenkins, J. M., Boyd, P. T., Glidden, A., Goeke, R. F., Sha, L., Ting, E. B., & Yahalomi, D. 2020, *AJ*, 160, 155, arXiv:2003.06407

- Wright, J. T. & Robertson, P. 2017, *Research Notes of the American Astronomical Society*, 1, 51, arXiv:1801.05383
- Wyatt, M. C., Kral, Q., & Sinclair, C. A. 2020, *MNRAS*, 491, 782, arXiv:1910.10731
- Young, A. T. 1967, *AJ*, 72, 747
- Zeng, L., Sasselov, D. D., & Jacobsen, S. B. 2016, *ApJ*, 819, 127, arXiv:1512.08827
- Zhang, M., Chachan, Y., Kempton, E. M. R., & Knutson, H. A. 2019, *PASP*, 131, 034501, arXiv:1811.11761
- Zhang, M., Chachan, Y., Kempton, E. M. R., Knutson, H. A., & Chang, W. H. 2020, *ApJ*, 899, 27, arXiv:2004.09513
- Zheng, C. & Borysow, A. 1995, *ApJ*, 441, 960
- Zhou, G., Latham, D. W., Bieryla, A., Beatty, T. G., Buchhave, L. A., Esquerdo, G. A., Berlind, P., & Calkins, M. L. 2016, *MNRAS*, 460, 3376, arXiv:1605.01991